Development of Multifunctional Carbon Nanotube Nanocomposite Sensors for Structural Health Monitoring

by

Kenneth Jan-Hwang Loh

A dissertation submitted in partial fulfillment
of the requirements for the degree of
Doctor of Philosophy
(Civil Engineering)
in The University of Michigan
2008

Doctoral Committee:

Assistant Professor Jerome P. Lynch, Chair
Professor Sherif El-Tawil
Professor Victor C. Li
Professor Nicholas A. Kotov

"Research is to see what everybody else has seen
and to think what nobody else has thought"
– Albert Szent-Györgyi von Nagyrapolt

DEDICATIONS

To Mom, Dad, Alingo, and Sunny

ACKNOWLEDGEMENTS

Dietrich Bonhoeffer said, "it is very easy to overestimate the importance of our own achievements in comparison to what we owe others." This important milestone of my life would have been impossible without the love, guidance, and support from my family and friends. First, I would like to thank my parents (Li-Chuan Lin and Chin-Hsiung Loh) for their unconditional love and for their continuous encouragement, time, and energy that enabled me the strength and motivation to become who I am today. My achievements to date and those to come in the future serve as a testament to them successfully nurturing and educating me. My sister Alingo's everlasting support and faith are also reasons for my accomplishments thus far.

I derive my strength, perseverance, and motivation from my girlfriend, Sunny Chu. Sunny's continuous love and support over the past nine years are reasons why I am capable of facing challenges with the utmost optimism and able to enjoy success with gratitude. She is why I can look back to see a fulfilling past, can be thankful and happy for my accomplishments today, and look forward to an even brighter tomorrow.

I owe forever my sincerest gratitude to my friend and advisor, Jerry Lynch, for his guidance and intellect in research and for believing in my potentials. He has opened my eyes to the beauties of the nanotechnology world and has challenged me with novel research problems capable of solving real-world problems. His teachings and inspirations have fueled my intellectual and personal growth. Jerry's guidance and dedication of time and energy have taught me the arts of becoming a successful researcher.

The research presented in this dissertation is only possible due to the assistance and intellectual guidance provided by my committee members. Professor Nicholas Kotov's expertise in nanomaterial assembly and his selfless devotion of resources, time, and energy have been the catalysts to accelerate my research and scholarly growth. I

thank Professor Victor Li for his wealth of knowledge in mechanics and materials science and for broadening my perspective as to how research in academia evolves towards commercial adoption and applications. I would also like to thank Professor Sherif El-Tawil for his selfless sharing of his vast knowledge in finite element analysis and simulations.

During my studies at the University of Michigan, I have been privileged to work with top researchers across diverse fields of engineering. My sincere gratitude goes to Professor Michael Thouless for enabling me with theoretical tools such as thin film fracture mechanics and for assisting the characterization and optimization of nanocomposite mechanical properties. I would also like to thank Dr. Narito Kurata for giving me the opportunity to work with him and his colleagues at the Kobori Research Institute of Kajima Corporation (in 2005) to develop embedded system identification firmware for wireless sensors. I thank Dr. Andrē Taylor for our numerous discussions to incorporate various nanomaterials for improving inherent nanocomposite properties.

During my undergraduate studies at Johns Hopkins University, Professor Roger Ghanem (University of Southern California) and Professor Masanobu Shinozuka (University of California, Irvine) have had faith in my abilities and permitted my early exposure to research in smart materials and structures. I am forever indebted to them for their help and guidance throughout my undergraduate studies and for providing me with numerous research opportunities in the fields of remote sensing and structural health monitoring.

Behind the scenes, my friends and colleagues of the Laboratory for Intelligent Structural Technologies (LIST) have assisted me in numerous aspects ranging from wireless sensing, numerical simulations, to nanocomposite characterization. Dr. Tsung-Chin Hou, Andrew Swartz, Andy Zimmerman, Junhee Kim, and Niki Fanouraki have all been critical elements to my research success. In addition, Bongsup Shim, Edward Jan, and Paul Podsiadlo from Professor Nicholas Kotov's group, and Shunzhi Qian from Professor Victor Li's group have also helped me with layer-by-layer assembly and thin film mechanical load testing.

My experiences here at the University of Michigan would not have been complete without my friends, Jongwon Lee, Min-Yuan Cheng, Hsien-Chang Lin, Ares

Chen, Laura Zimmerman, Remy Lequesne, Mantia Athanasopoulou, Ekin Ekiz, and Anna Clark. Some of my most unforgettable moments in Ann Arbor have been spent with these individuals on the softball field, basketball court, or the many late nights.

I would like to thank some of my best friends I've met during my undergraduate studies at Johns Hopkins, namely, Tommy Hou, Jeff Chu, Kevin Wu, Kelly Wang, William Chang, Vicky Lin, Rose Chen, William Lao, Gabriel Chen, and James Ho, for their forever support and encouragement during tough times and for the endless supply of laughter, joy, and friendship. In addition, I would also like to thank Joseph Zhang, Charles Liao, Shaw-Ming Yang, Pierre Lin, and Jerry Tsai for their continued support and for always being there for me when I most need their strength and motivation.

This research is supported by the National Science Foundation (NSF) under Grant Number CMMI-0528867 (program manager: Dr. Shih Chi Liu). Additional support has also been provided by the University of Michigan, College of Engineering Graduate Student Research Assistantship, Karen and Paul Van Weelden Award, Michigan Space Grant Consortium (MSGC) and National Aeronautics and Space Administration (NASA), and SPIE.

TABLE OF CONTENTS

LIST OF FIGURES

LIST OF TABLES

LIST OF ABBREVIATIONS AND ACRONYMS

2D	Two-Dimensional
3D	Three-Dimensional
AC	Alternating Current
AFM	Atomic Force Microscope
ASK	Amplitude Shift Keying
CNT	Carbon Nanotube
DAQ	Data Acquisition System
DC	Direct Current
DFT-UFF	Density-Functional Theory-Universal Force Field
DWNT	Double-Walled Carbon Nanotube
EIS	Electrical Impedance Spectroscopy
EIT	Electrical Impedance Tomography
EM	Electromagnetic
FEM	Finite Element Method
FIB	Focused-Ion Beam
FRP	Fiber-Reinforced Polymers
FRA	Frequency Response Analyzer
FSK	Frequency Shift Keying
GNP	Gold Nanoparticles
IC	Integrated Circuits
Lb	Langmuir-Blodgett
LbL	Layer-by-Layer
LVDT	Linear Voltage Displacement Transducer
MAS NMR	Magic-Angle Spinning Nuclear Magnetic Resonance
MEMS	Microelectromechanical Systems

MWNT	Multi-Walled Carbon Nanotube
NDE	Non-Destructive Evaluation
PCB	Printed Circuit Board
PE	Polyelectrolyte
PECVD	Plasma-Enhanced Chemical Vapor Deposition
PSK	Phase Shift Keying
RC	Resistor-Capacitor
RLC	Resistor-Inductor-Capacitor
RF	Radio Frequency
RFID	Radio Frequency and Identification
PZT	Lead Zirconium Titanate
SA	Simulated Annealing
SDOF	Single-Degree of Freedom
SEM	Scanning Electron Microscope
SMD	Surface Mounted Device
SoC	System-on-a-Chip
STM	Scanning Tunneling Microscope
SWNT	Single-Walled Carbon Nanotube
SHM	Structural Health Monitoring
TEM	Tunneling Electron Microscope
TI	Texas Instruments, Inc.
UV	Ultraviolet
UV-Vis	Ultraviolet-Visible Absorption Spectroscopy

GLOSSARY

Fe	Iron
Fe_xO_y	Iron[X] Oxide
GaAs	Gallium Arsenide
Ge	Germanium
H^+	Hydrogen Ion
H_2O	Water
H_2SO_4	Sulfuric Acid
$HAuCl_4$	Chloroauric Acid
HCl	Hydrochloric Acid
HF	Hydrofluoric Acid
$NaBH_4$	Sodium Borohydride
NaCl	Sodium Chloride (Salt)
OH^-	Hydroxide Ion
PAA	Poly(Acrylic Acid)
PAH	Poly(Allylamine Hydrochloride)
PANI	Poly(Aniline) Emeraldine Base
PDMA	Poly(Methylacrylamide)
PEI	Poly(Ethylene Imine)
PET	Poly(Ethylene Terephthalate)
PSS	Poly(Sodium 4-Styrene Sulfonate)
PVA	Poly(Vinyl Alochol)
PVC	Poly(Vinyl Chloride)
SDS	Sodium Dodecyl Sulfate
Si	Silicon

ABSTRACT

Development of Multifunctional Carbon Nanotube Nanocomposite Sensors for Structural Health Monitoring

by

Kenneth Jan-Hwang Loh

Chair: Jerome P. Lynch

The United States is currently facing a national crisis with many of its vital civil infrastructure systems deteriorating at an alarming rate. If left unaddressed, catastrophic structural failures like that witnessed from recent events (Minneapolis' I-35 bridge collapse in August 2007, Montreal's de la Concorde Overpass collapse in September 2006, among others) are bound to occur more frequently. As a result, the field of structural health monitoring (SHM) has been pursuing new sensing technologies for monitoring the long-term performance, and for assessing the health condition of critical infrastructure systems. Unfortunately, the current set of sensing technologies available has proven inadequate for detecting structural distress for two reasons. First, most sensors are "point" sensors that measure responses to load at highly localized regions (usually not collocated with damage). Second, physics-based models or pattern recognition algorithms are necessary for inferring damage states based on indirect structural response measurements. This dissertation fundamentally solves this technology bottleneck by engineering a new generation of multifunctional materials that serve as the basis for *distributed* sensors that sense damage *directly*.

Specifically, nanomaterials such as single-walled carbon nanotubes (SWNT) and polyelectrolytes are molecularly self-assembled at the nano-scale to form homogeneous

nanocomposites with superior mechanical and electrical properties. At the forefront of this work is the use of SWNTs for intentional tailoring of the physical properties of a polymeric composite including tensile strength, bulk conductivity, and electromechanical and electrochemical responses. Taking advantage of the high aspect ratio and surface area of individual SWNTs, polyelectrolytes are chemically attached onto SWNT surfaces to *tune* the properties of the resulting macro-scale nanocomposite. Experimental results show that these SWNT-enhanced nanocomposites can also be tailored to exhibit high-performance strain (electromechanical) or pH/corrosion (electrochemical) sensing capabilities.

In order to use these materials in complex field environments, a comprehensive understanding of the material's mechanical and electrical properties is required. First, the mechanical properties of SWNT-PE composites are characterized through extensive tensile load testing. A direct result of embedding carbon nanotubes is the gain in tensile strength (*i.e.*, from ~20 MPa for pure PSS-PVA films to ~250 MPa for SWNT-enhanced PSS-PVA thin films). In addition, fracture theory elucidates the role SWNTs play in enhancing thin film fracture toughness. On the other hand, the inclusion of SWNTs simultaneously increases the electrical conductivity and sensing sensitivity of SWNT-PE thin films. In fact, the nanocomposite's piezoresistive characteristics are explored via two-point probe methods. Both time- and frequency-domain analyses are used to analytically model the electromechanical performance of these nanocomposites using an equivalent parallel RC-circuit model. The ability to model and predict thin film piezoresistivity permits the optimization of nanocomposites to offer high strain sensitivities (*i.e.*, as high as 2% change in surface resistivity per unit strain).

This dissertation also explores two different applications of SWNT-PE nanocomposites for SHM. First, an immediate extension to the aforementioned equivalent circuit analysis is the design of thin film passive wireless strain and pH sensors. Upon patterning the SWNT-PE thin film (with inherent parallel RC-circuit behavior) as an inductive coil antenna, wireless interrogation of strain and pH sensor response is accomplished. An advantage offered by the proposed sensor is that the inherent capacitive element of the SWNT-PE nanocomposite can be employed to store electrical charge for operating the wireless sensor; thus, the passive wireless sensor does

not require batteries or other forms of portable power supply and can operate indefinitely in the field. Second, as opposed to simply using these materials as point sensors, this dissertation also seeks to use these composites as a "sensing skin" that can provide two-dimensional maps of strain, crack damage, and corrosion. Mapping of composite electrical conductivity (which is designed to change in tandem with the stimulus sought for measurement) is performed through the advancement of electrical impedance tomography (EIT). Unlike traditional structural health monitoring systems, the proposed sensing skins can directly determine structural damage location and severity (*i.e.*, due to strain, impact, pH, and corrosion) since it is inherently a distributed sensor sensing the damage directly. The ability to accurately detect damage location and severity facilitates efforts to prevent future catastrophic failures from occurring.

CHAPTER 1

INTRODUCTION

1.1. Civil Infrastructure Damage and Deterioration

Civil infrastructures, such as buildings, bridges, dams, lifelines, among others, are complex engineered systems that ensure society's economic and industrial prosperity. However, many of these vital structures are susceptible to damage due to extreme loading scenarios (*e.g.*, earthquakes, hurricanes, and blast) and long-term deterioration (*e.g.*, aging, corrosion, and fatigue). Considering recent seismic events including the Loma Prieta (1989), Northridge (1994), Kobe (1995), and Chi-Chi (1999) earthquakes, it is clear that civil structures are still vulnerable to damage and failure during natural catastrophes. In fact, the direct costs suffered from the Loma Prieta earthquake is estimated to be approximately $6.5 to $10 billion with reconstruction, structural repair, and loss of facility use all representing sizable portions of this cost [1]. When structures exhibit signs of post-disaster damage, the closure of facilities until repairs can be made lead to a significant socioeconomic impact. Clearly, this impact can be dramatically reduced via quick and reliable assessments of structural performance.

Normal wear and tear is another serous issue for the civil engineering profession. Many existing structures around the world are beginning to approach (or have already exceeded) their design service lifetimes. In addition, these structures are often subjected to harsh operational and environmental conditions that further accelerate structural deterioration. Undetected long-term deterioration jeopardizes the reliability of the structural system and the safety of its occupants. In extreme cases, undiagnosed structural damage (*e.g.*, due to corrosion and fatigue) can even lead to catastrophic system failure. For example, fatigue rupture of hanger connections eventually led to the

collapse of the Sgt. Aubrey Cosens V.C. Memorial Bridge (Latchford, ON, Canada) in 2003 [2]. In addition to the costs associated with such fatal catastrophic structural failures, an abundance of economic resources are dedicated to repairing existing structures as they age. According to Njord and Meyer [3], more than $91 billion is spent annually to maintain the U.S. inventory of highways and bridges. While this cost may seem significant, it is estimated that at least an additional $128 billion is required to upgrade existing structures just to meet current standards.

The problems encountered in civil structures is not unique [4]; the same set of problems are typically encountered in other fields including aerospace, naval, and mechanical engineering. For instance, undiagnosed corrosion of aircraft fuselages can result in over-stressing of rivets and stress-corrosion crack formation; an example of what can occur if damage is left undetected is the Aloha Airlines plane which ripped apart in-flight in 1988 [5]. More recently, impact damage compromised the integrity of the thermal insulation heat shield of the Columbia Space Shuttle which exploded during re-entry [6]. Clearly, there exists the need to devise structural health monitoring solutions that prevent the occurrence of future catastrophic structural failures.

1.2. The Current State-of-Practice of Structural Health Monitoring

Civil infrastructures are inspected by trained officials on a routine or scheduled basis. In the United States, the "National Bridge Inspection Standards" set forth by the Federal Highway Administration require highway bridges to be visually inspected every 24 months [7]. Although routine bridge inspections have been deemed relatively successful in identifying significant structural damage that require immediate attention, numerous disadvantages of visual inspection have also been recognized. First, visual inspection is highly subjective since it relies on the bridge official's interpretation of severity of damage and structural deficiency [8]. Second, the fundamental nature of visual inspection only permits one to assess structural performance based on accessible areas within the structure [9]. In some cases such as the aforementioned collapse of the Sgt. Aubrey Cosens V.C. Memorial Bridge, fatigue failure of hanger connections occurred at locations within the arch bridge's enclosed steel boxes [2, 4]. Finally, the cost

of visual inspection and maintenance is extremely high, thereby further limiting the frequency of inspection.

To enhance the objectivity of inspections while simultaneously reducing the economic burden of maintaining the inventory of aging and damaged structures, the engineering community has been aggressively pursuing novel sensing technologies and analytical methods to facilitate automated damage detection. Termed structural health monitoring (SHM), this new paradigm relies on using sensing technologies combined with physics-based models or pattern recognition algorithms to infer structural damage. Typically, the most common SHM system is one that is tethered. The tethered (or cabled) structural health monitoring system employs a variety of distributed point sensors (typically 10 to 20 sensors or nodes), namely accelerometers, strain gages, linear voltage displacement transducers (LVDT), among others, connected to a centralized data repository via coaxial wires. The coaxial wires serve to deliver electrical power to sensors and are used for receiving sensor outputs.

Sensors are instrumented at a select number of structural locations where large strains, deflections, or vibrations are expected. In general, two different techniques are employed for structural monitoring, namely (1) global-based structural monitoring or (2) local-based damage detection. First, global-based structural monitoring typically employs distributed accelerometers for measuring and characterizing the overall response (*i.e.*, modal frequencies and mode shapes) of structural systems subjected to ambient or forced excitations. However, global-based structural monitoring is only sensitive to significant structural damage, and it can be argued that damage is a localized process that takes place at structural components. As a result, local-based damage detection techniques seek to identify component-level structural damage (*e.g.*, cracks in welded connections and corrosion) before it adversely affects the overall structural performance. In this case, sensors such as strain gauges or LVDTs are instrumented at critical structural locations where damage is most likely expected to occur (*e.g.*, gusset plates, expansion joints, and bridge deck mid-spans). The end result is a monitoring system that is better scaled to common structural damage phenomena. For both cases, the use of calibrated high-performance sensors enhances objectivity of inspections by providing quantified data.

1.3. Fundamental Limitations of Current Tethered SHM Systems

Central to the tethered monitoring system is the use of discrete sensors (*e.g.*, strain gages, thermocouples, accelerometers, among others) for measuring structural response parameters. However, the main disadvantage of a tethered monitoring system is that sensors are capable of only obtaining data at their locations. Since damage can be distributed throughout a structure, it is unlikely that sensor nodal positions will precisely correspond to the locations of damage. In addition, common sensors do not measure damage; rather, as mentioned in Section 1.2, sensor response data is combined with physics-based models to *infer* or estimate damage. Robust damage detection algorithms are a technology still under development in the SHM field. While many algorithms have been proposed [10] and even illustrated on test structures [11], challenges such as algorithm sensitivity to environmental factors remain.

Another fundamental limitation of tethered monitoring systems is the great lengths of coaxial wires necessary to connect sensors to a centralized data repository. While coaxial wires provide a very reliable communication link, the wires are susceptible to damage during long-term monitoring. Furthermore, the installation and maintenance of these cables are often labor intensive and expensive. For example, structural monitoring systems installed in tall buildings have been reported in the literature to cost in excess of $5,000 per sensing channel [12]. As structural monitoring systems grow in size (as defined by the total number of sensors) for monitoring larger and more complex engineered systems, the cost of the monitoring system grows faster than at a linear rate. As another example, the cost of installing over 350 tethered sensing channels upon the Tsing-Ma Suspension Bridge in Hong Kong is estimated to have exceeded $8 million [13]. It should be noted that the high cost of installing and maintaining wires is not restricted to only civil infrastructures. Others have reported similar issues with respect to the costs associated with monitoring systems installed within aircrafts, ships, and other engineered systems [14]. In addition to the costs associated with the installation of coaxial cables, current sensing transducers such as accelerometers remain expensive.

In summary, some of the disadvantages presented by the current structural health monitoring paradigm include:

- The use of point sensors can only obtain data at instrumented locations.
- Sensors cannot directly measure damage but require physics-based models to infer damage location and severity.
- Structural health monitoring systems are expensive to install and maintain.
- The current generation of sensors employs cabled sensors connected to a centralized data repository.

1.4. Emerging Sensing Technologies for Structural Health Monitoring

New sensor technology can be developed to address some of the fundamental limitations associated with the current structural monitoring paradigm. In fact, a plethora of new sensing technologies have been proposed over the past two decades for SHM applications. A brief overview of these technologies, namely wireless sensors, radio frequency and identification (RFID), ultrasonics, and micro-electromechanical systems will be presented. Undoubtedly, each of these sensors has improved the state-of-art in SHM; however, none of them have yet established themselves as the "silver bullet" solution. Hence, there remain opportunities for improvement in the sensors used for SHM.

1.4.1. Wireless Sensors and Sensor Networks

Wireless sensors represent one potential technology that can help advance the structural engineering field's ability to economically implement SHM [11]. It should be mentioned that wireless sensors are not sensors *per se*, but rather, they are autonomous data acquisition nodes to which traditional structural sensors can be attached. In fact, wireless sensors are best viewed as a platform in which mobile computing and wireless communication elements converge with the sensing transducer. Interest in wireless sensors has been primarily motivated by their low cost attributes. Specifically, the eradication of extensive lengths of coaxial wires commonly associated with the traditional tethered monitoring systems results in wireless SHM systems having comparatively lower installation costs. These low costs promise wireless monitoring systems defined by greater nodal densities [15, 16]. With potentially hundreds of wireless sensors installed in a single structure, the wireless monitoring system is better equipped

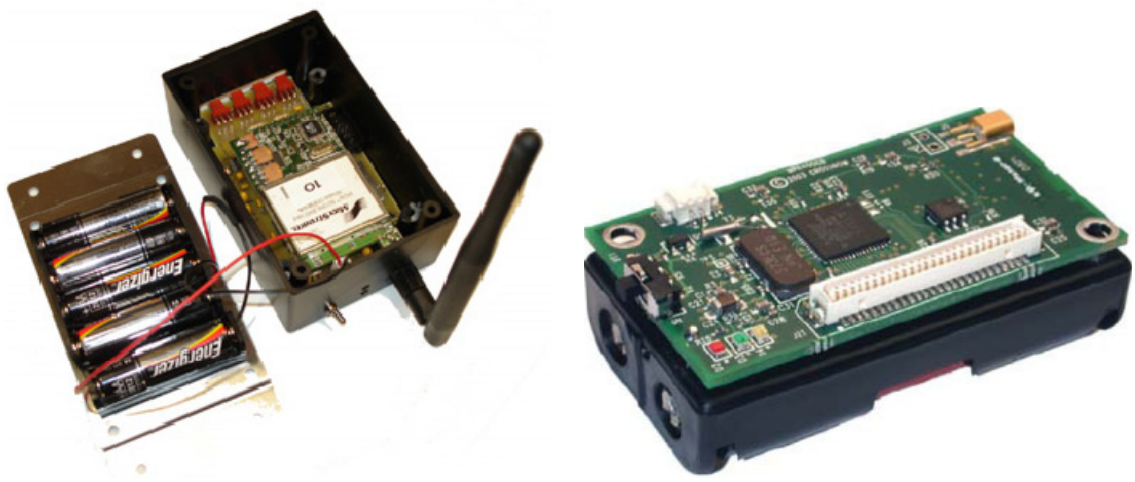

(a) (b)

Figure 1-1. (a) A picture of an academic wireless sensor prototype with its 5 AA battery pack revealed. (b) A picture of the MICA2 mote by Crossbow Technology, Inc.

to screen for structural damage by monitoring the behavior of critical structural components (*i.e.*, local damage detection) as well as the response of the entire structure (*i.e.*, global structural monitoring). Examples of an academic wireless sensor by Lynch, *et al.* [17] and a commercially available MICA2 mote (by Crossbow Technology, Inc.) [18] are shown in Figure 1-1.

While eliminating the need for coaxial cables is beneficial from a cost perspective, the lack of cables also eliminates a means of delivering power to the sensors. Wireless sensors must depend on portable power supplies such as batteries. Due to the battery's finite lifetime, an additional degree of complexity to management of the SHM system is introduced where sensor batteries need to be replaced at regular intervals (*e.g.*, 12 to 24 months). In addition, while the densely-distributed nature of wireless sensors provide more localized damage information of structures, it is still challenging to instrument wireless sensors at every structural location.

1.4.2. Passive Wireless Sensing Technologies

Due to finite power constraints of wireless sensors, new design concepts that address the issue of power are required for deploying wireless sensors in structures. One approach proposed is to employ inductively coupled wireless technologies (*e.g.*,

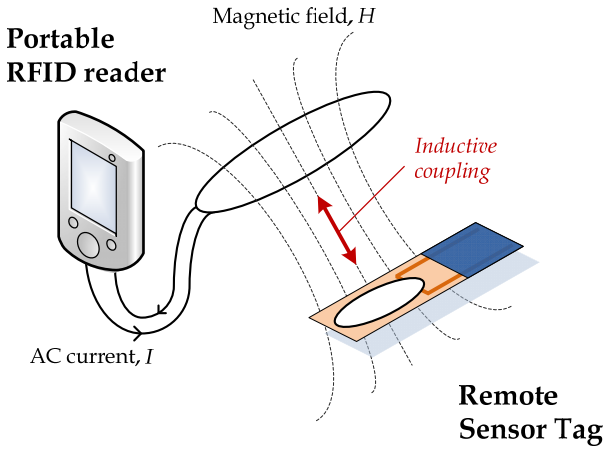

Figure 1-2. A schematic illustrating passive wireless sensing via RFID technology.

RFID) for both the delivery of power to wireless sensors as well as for data communication. Much simpler in design than ordinary wireless sensors, RFID-based wireless sensors take advantage of remote interrogators (readers) for the transmission of operational power through near-field inductive coupling (Figure 1-2). The RFID-based wireless sensor captures the delivered energy and stores it in temporary capacitive storage elements (*e.g.*, capacitors) in order to operate an ultra low-power sensor circuit [19]. Once data is collected by the sensor, the stored power is used to modulate the sensor data on a radio frequency signal readable by the remote interrogator. The advantage of such a battery-free wireless sensor is that it is low cost, can operate indefinitely in the field, and the sensor form factor can be dramatically reduced.

For example, early investigatory work in RFID sensing has been proposed by Mita and Takahira [20, 21] where they have developed a passive wireless peak strain sensor based on two concentric aluminum pipes sliding over a dielectric material. Upon installing these sensors to the base of a seven-story base-isolated building at Keio University, experimental peak strain data collected from the prototype RFID sensor coincides with those obtained from a laser displacement transducer [22]. As opposed to measuring peak strain, Jia and Sun [23] have developed a novel passive thick film strain sensor by incorporating poly(vinyl fluoride) with an interdigital capacitor to enhance the sensitivity of characteristic frequency shifts to strain. On the other hand, Watters [24] and Watters, *et al.* [25] have developed a passive wireless corrosion sensor that measures

chloride concentration and/or temperature when embedded in reinforced concrete. Similarly, to accurately monitor different thresholds of concrete corrosion, Simonen, *et al.* [26] and Dickerson, *et al.* [27] have combined their RFID corrosion sensor with an exposed switch fabricated from different gauge steel wires. When corrosion destroys the exposed wire switch, dramatic characteristic frequency shifts have been observed between initial and corroded states.

1.4.3. Ultrasonics and Guided-Waves

Two of the greatest challenges associated with SHM is: (1) to detect the location and severity of spatially distributed damage, and (2) to directly measure damage. Recent advancements in ultrasonics and guided-waves have permitted the detection of small damage features over large spatial areas [28]. In general, sets of surface-guided waves or Lamb waves are propagated along thin metallic plate structures where an array of piezoelectric sensors/actuators is employed for measuring propagated wave characteristics. For instance, Giurgiutiu, *et al.* [29] bonds multiple arrays of surface-mounted piezoelectric transducers onto aluminum alloy aircraft panels for generating Lamb waves to detect cracks and corrosion damage. Using piezoelectric sensor/actuator responses, reflected echo signals are employed for accurate detection of damage due to hairline slits, seeded cracks, and impact. Similarly, Park, *et al.* [30] has validated piezoelectric patches for identifying cracks developed in welded zones of 1/8-scale bridge truss members. Simulated damage by loose bolts and induced cracks are successfully detected via a Lamb wave-approach combined with a prescribed damage threshold index. On the other hand, when combining distributed piezoelectric sensors/actuators with a wavelet-based data processing technique, Sohn, *et al.* [31] identifies the location of delamination within large 61 x 61 cm^2 composite plates. However, in the realm of guided-wave structural health monitoring, the generated two-dimensional damage maps are still derived from wave-propagation models and provides only statistical information of damage location and severity (*i.e.*, damage is not measured directly).

1.4.4. Miniaturization of Sensors with Microelectromechanical Systems (MEMS)

There has been growing interest in the miniaturization of sensing transducers used to record structural behavior. The advantages of miniaturization are multiple; for example, reduction in sensor size and weight is critically important when considering the use of SHM systems in lightweight structures such as space-based structural systems (*e.g.*, rockets and satellites). Smaller sensors are also easier to install, particularly if the sensor is densely-distributed and embedded within structural elements; an example might be thin-film sensors installed within a layered composite material (*e.g.*, carbon fiber-reinforced polymer (CFRP) composites). In addition, miniaturization can lead to potential improvements in sensing accuracy simultaneous to significant reductions in fabrication costs. Finally, microelectromechanical systems (MEMS) sensors are more power efficient than their macro-scale counterparts.

Macro-scale sensor design concepts can be miniaturized by adopting emerging technologies associated with the MEMS field. MEMS is defined by the use of fabrication methods associated with integrated circuits (IC) to construct mechanical structures within semiconductor substrates such as silicon (Si), germanium (Ge), and gallium arsenide (GaAs) [32]. By miniaturizing macro-scale sensor transduction concepts to the micron dimensional scale, the approach is commonly termed a "top-down" design methodology. Today, a diverse collection of miniaturized sensing transducers have been proposed by the MEMS community including accelerometers, gyroscopes, gas sensors, ultrasonic transducers, among many others [33]. These examples of MEMS sensors have been shown to offer measurement accuracies on par with macro-scale counterparts. MEMS adoption of IC technologies for device fabrication allows computing and wireless communication circuits to also be collocated with the MEMS sensor, thereby offering complete system-on-a-chip (SoC) solutions [32]. Furthermore, IC-based manufacturing offers fabrication of MEMS sensors by a batch process, with hundreds of devices fabricated on a single semi-conducting wafer [33]. The market adoption of MEMS sensors has been greatest in the automotive (*e.g.*, pressure and acceleration sensing) and inertial sensing markets where high sales volume is able to amortize high fabrication costs [32, 34].

In recent years, MEMS has begun to have an impact in the SHM domain [35]. Most notably, MEMS accelerometers and ultrasonic transducers [36] have been used for structural monitoring. The cost of these sensors is low because of their use in many other applications; however, specialized MEMS sensors proposed exclusively for SHM would not have the high sale volume necessary to keep the price of individual sensors low. This limitation is a very significant one for MEMS proposed for SHM. Another limitation of MEMS is the sensitivity of MEMS sensors often does not surpass those of more traditional macro-scale sensors. For example, MEMS accelerometers have noise floors higher than force-balanced and piezoelectric accelerometers used for structural monitoring.

1.4.5. Need for New Sensing Paradigm

The emergence of wireless, RFID, and MEMS sensors has resulted in cost-effective structural monitoring systems defined by higher nodal densities. However, these sensors are still point sensors measuring structural behavior at specific locations. Accurate damage detection is extremely difficult since structural response and potential damage can only be inferred between sensor locations. What rendered guided-wave methods so attractive is their spatially large interrogation zones that provide them with spatial sensing functionality. Unfortunately, complex signal processing algorithms are often required to accurately detect damage; nevertheless, guided-wave technologies are capable of identifying the location and severity of damage over large spatial regions. Thus, more sensors consistent with a distributed sensing paradigm are needed. This thesis will take an alternative approach to that taken by guided-wave methods. Nanotechnology will be explored to produce a sensing material that can be deposited onto structural surfaces for distributed sensing.

1.5. Nanotechnology and Its Advantages

In light of the limitations of current structural health monitoring systems, the interdisciplinary nanotechnology field has emerged to offer physical tools and chemical processes that permit precise tailoring and miniaturization of sensors designed for SHM applications [37]. For instance, recent technological advancements in scanning (SEM) and

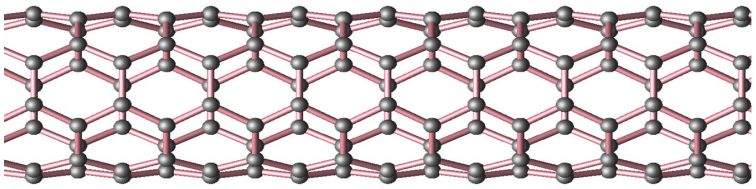

Figure 1-3. A schematic illustrating the molecular structure of a single-walled carbon nanotube (courtesy of Prof. Vincent Crespi, Pennsylvania State University).

tunneling electron microscopy (TEM), focused ion beam lithography (FIB), atomic force microscopy (AFM), and scanning tunneling microscopy (STM), to name a few, have enabled manipulation of individual atoms and molecules. On the other hand, nanomaterials such as fullerenes and nanotubes [38], nanoparticles [39], carbon black [40], and quantum dots [41] possess unique physical, electrical, thermal, and optical properties vastly different than their bulk phase. The ability to isolate, control, and assemble the aforementioned nano-scale structures into organized morphologies can yield potentially new, high-performance functional systems [42].

More specifically, among the wide variety of nanomaterials available today, carbon nanotubes (CNT) have gained considerable interest due to their unique intrinsic (*i.e.*, physical, chemical, mechanical, electrical, and thermal) properties [43] (Figure 1-3). Specifically, since the discovery of fullerenes and nanotubes by Iijima in 1991 [38], researchers have illustrated their functionality for a wide variety of applications including high-strength structural composites [44], nanoelectronics [45], various types of sensors [46, 47], among many others [48]. The widespread interest in adopting carbon nanotubes for novel applications owes to carbon nanotubes' spectacular mechanical [49] and electrical properties [48]. Mechanically, the Young's modulus and ultimate tensile strength of single-walled carbon nanotubes (SWNT) have been measured to be approximately $E \approx 1{,}054$ GPa and $\sigma_f \approx 75$ GPa, respectively, and for multi-walled carbon nanotubes (MWNTs) $E \approx 1{,}200$ GPa and $\sigma_f \approx 150$ GPa, respectively [50]. On the other hand, carbon nanotubes' high electrical conductivity stems from their nearly one-dimensional structure, thereby approaching near-ballistic transport-type electronic behavior [48].

As outlined by Devreese [42], many researchers have sought to take advantage of nanomaterials (such as SWNTs) and novel fabrication techniques to develop a new generation of physical (*e.g.*, strain, stress, and pressure), chemical (*e.g.*, gas and ionic species), and biological (*e.g.*, proteins and DNA) sensors. Due to high surface area, unique optical properties (*e.g.*, photocurrent generation), and exceptional electrical conductivity of nanotubes, sensors assembled from them are often characterized by exceptional sensitivity and resolution. For example, Stampfer, *et al.* [51] have isolated and suspended individual SWNTs over a metallic cantilever support to investigate nanotube's potential for nano-electromechanical displacement sensing. Their results indicate nonlinear changes in nanotube resistance with applied tensile deformations due to changes in the nanotube's band gap; nevertheless, the nonlinearity can be described accurately via a thermal activated transport model, and a maximum piezoresistive gauge factor of 2,900 has been obtained. The results obtained by Stampfer, *et al.* [51] confirm the advantages of nanotechnology for developing high-performance sensing devices. However, to date, the main technological challenge remains in how to scale nanomaterial and nano-sensing properties up to tangible and structural component length-scales.

Nevertheless, recent technological advancements have enabled the design of materials with specific macroscopic mechanical, electrical, and chemical properties by controlling structure and assembly at the atomistic length-scale [52]. As opposed to forming nanostructures via manipulation of individual atoms and molecules using the scanning tunneling microscope [53] or nanoindentation [54], techniques such as spin coating, Langmuir-Blodgett (Lb) [55], sol gel [56], vacuum filtration and annealing [57], layer-by-layer [58], among others, are just some of the scalable approaches to nanocomposite fabrication. Typically, nanomaterials such as carbon nanotubes are initially dispersed in surfactant, polyelectrolyte, or biochemical solutions to separate clumped particles [59]. Then, using a "bottom up" fabrication technique, nanomaterials can be structured and scaled up orders of magnitude in length scale. Clearly, future advances in miniaturized sensors will be derived from the technological advancements within the nanotechnology domain.

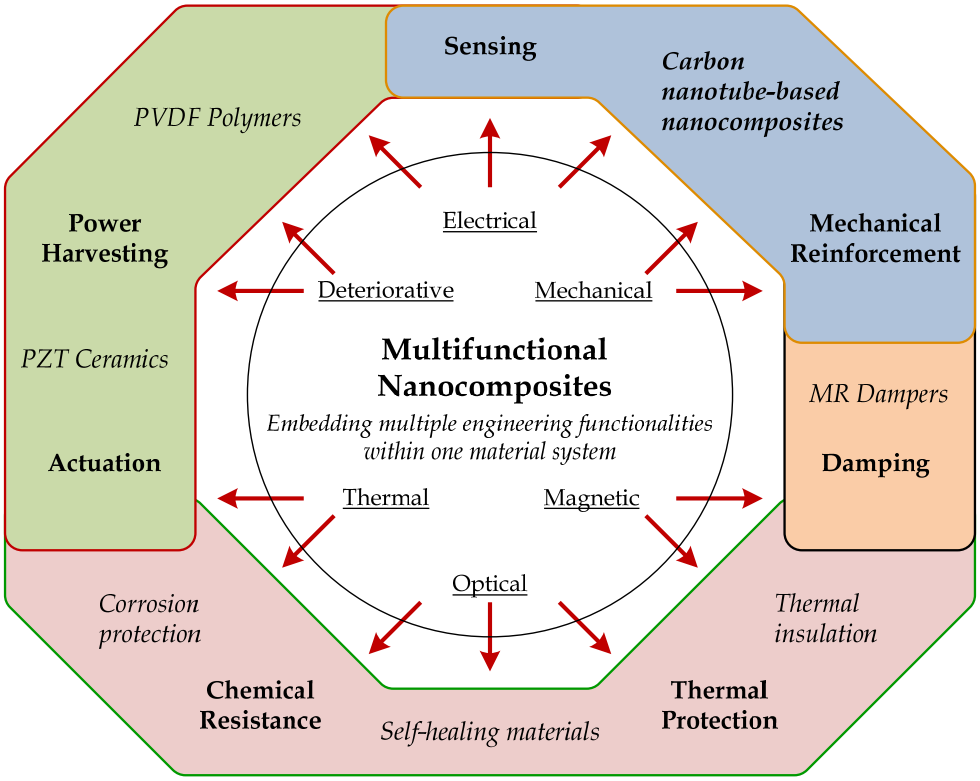

Figure 1-4. An example illustration that demonstrates the concept of multifunctional nanocomposites.

1.6. Multifunctional Nanocomposites

With the advent of nanotechnology, a new generation of engineered composites has emerged. Termed multifunctional nanocomposites, these materials are designed using a bottom up approach of intentional molecular assembly in order to embed multiple engineering functionalities within one material system. Unlike traditional composites where only one material property (namely, mechanical properties like strength, toughness, or ductility) is enhanced, multifunctional systems possess multiple functions such as structure, sensing, actuation, and power generation, among others (Figure 1-4). For example, magnetic-fluorescent nanocomposites exhibiting enhancements in magnetic and optical performance have found many biomedical

applications such as biological imaging, drug delivery, chemical sensing, and cell tracking [60]. Specifically, Veiseh, *et al.* [61] have designed a multifunctional nanoprobe sensitive to glioma (*i.e.*, brain tumor) cells by coating magnetic iron oxide nanoparticles with poly(ethylene glycol) covalently functionalized to chlorotoxin and fluorescent Cy5.5 molecules. Their results have shown the ability of the probe to target and detect glioma cells via magnetic resonant imaging and confocal (fluorescent) microscopy. With the plethora of materials fabrication tools offered by nanotechnology, multifunctional nanocomposites can be tailored to specific properties to realize a next-generation structural health monitoring system. Here, large nanocomposites can be fabricated at a low cost and be designed to be sensitive to particular damage processes. As opposed to using them as point sensors, large thin films can be coated onto structural surfaces such that each point on the thin film exhibits sensitivity to different damage processes such as strain or pH.

1.7. Research Objectives and Dissertation Outline

Based on the previous discussions focused on emerging sensing technologies for structural health monitoring, there remains the need for miniaturized sensors characterized by higher levels of performance (*e.g.*, greater accuracy and resolution) and offering data more directly correlated to damage. Thus, the primary objective of this dissertation is to take advantage of the materials and fabrication tools under development in the nanotechnology domain to design a new class of sensors for SHM based on multifunctional materials. Multifunctional materials accomplish two or more functions within the same material platform such as structure, sensing, actuation, and power generation. Specific to this body of work, multifunctional nanocomposites will be designed with various sensing mechanisms selective to specific damage phenomena while being mechanically strong. Through the use of nanotechnology, the nanocomposites will be tailored to offer desired sensitivities and resolutions, depending upon the SHM application envisioned. Moreover, these nanometer-thick composites are suitable for embedment within structural components (*e.g.*, concrete) or for depositing onto metallic surfaces without interfering with the primary load carrying function of the structure.

At the core of this thesis is the use of carbon nanotubes, one of the nano-scale structures under exploration in the nanotechnology field. CNTs are considered because of their impressive physical properties including incredible strength (~37 GPa) and high surface areas [48]. First, to fully utilize the physical properties of CNTs [43], individual nanotubes are dispersed in stable polyelectrolyte solutions to enhance their processing for inclusion in the multifunctional nanocomposite; Chapter 2 (Figure 1-5) describes the assembly method used to create CNT-polymer composites characterized by homogeneous bulk material properties. Specifically, the versatile layer-by-layer (LbL) self-assembly method is used to deposit a variety of polymers, carbon nanotubes, and nanoparticles to form thin films of controlled morphology. Multifunctionality of these carbon nanotube-based composites is demonstrated by experimentally characterizing their inherent mechanical and electrical properties. For example, the tensile stress-strain behavior and changes in thin film electrical properties (*i.e.*, conductivity) due to physical and chemical stimulus are explored. Two CNT-polyelectrolyte composites will be described with each composite using different polyelectrolytes in their matrix. One composite formulation will exhibit an electromechanical response to strain (*i.e.*, strain sensing), while the other will exhibit an electrochemical response to pH (*i.e.*, pH sensing).

Upon initial validation of the CNT nanocomposite's strength and sensing properties, Chapter 3 seeks to enhance the mechanical attributes of these carbon nanotube-based thin films to ensure they can be used within the harsh operational environments most common to civil infrastructure systems. The concentration of CNTs is varied to explore the role of nanotube contribution to the macro-scale mechanical strength, stiffness, and ultimate failure strain of the CNT-reinforced polymeric thin films. Furthermore, various post-fabrication thermal treatments are explored to avoid brittle failure mechanisms and to ensure films exhibit significant tensile ductility and strain-hardening. Similarly, Chapter 4 focuses on the analysis and optimization of the piezoresistivity of a CNT nanocomposite (Figure 1-5). Such a composite is proposed for strain sensing in SHM applications. Electrical impedance spectroscopy (EIS) is employed to derive an equivalent circuit for modeling thin film frequency domain electrical response to loading. EIS analysis will also allow the sensitivity of the thin film to be maximized for high resolution strain sensing. Again, optimization of the thin film strain

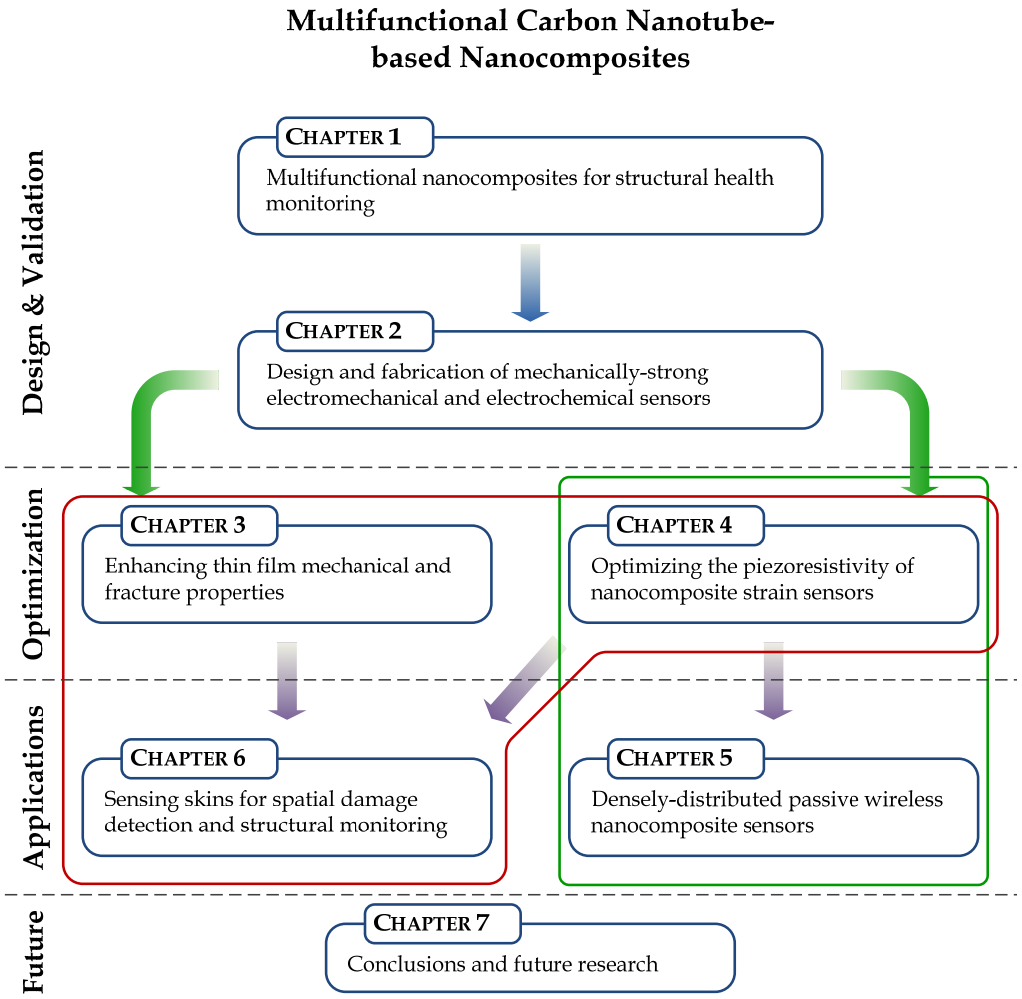

Figure 1-5. A schematic outlining the major topics presented in this dissertation.

sensitivity and bulk conductivity is achieved by varying the composition of nanotube and polymer concentrations during layer-by-layer fabrication.

As previously described, structural health monitoring requires densely distributed sensors to capture component-level damage within large structures. As monitoring systems grow, the complexities associated with wiring grows in tandem. While wireless sensors represent one solution, they remain hindered by dependence on local power sources (*e.g.*, batteries). To resolve this technological bottleneck, a passive (*i.e.*, power-source-free) wireless sensor is proposed using the CNT-based composites. Specifically, in Chapter 5, the thin film sensors characterized in Chapter 2 and optimized in Chapters 3 and 4 are coupled with coil antennas to realize a passive wireless sensing

system (similar to those described in Section 1.4.2). Miniaturization of the nanocomposite-RFID sensor is realized by employing micro-fabrication techniques (*i.e.*, printed circuit board (PCB) technology) to pattern coil antennas onto flexible FR4 laminates while thin films are directly coated onto the PCB substrate surfaces. These passive wireless sensors are validated in the laboratory for wireless communications and sensing performance (strain and pH). Successful validation would suggest that these low-cost wireless sensors could be densely instrumented and embedded within structural materials (*e.g.*, concrete) for component-level sensing.

While increasing the sensing density of future health monitoring systems through the use of passive wireless sensors is promising, structural response data gathered in such systems is still only collected at instrumented locations. To truly capture damage, an entirely new sensing paradigm based on distributed sensing is direly needed. One distinct advantage of a multifunctional sensing material is that a measurement of its conductivity can be made anywhere the material is. Hence, a multifunctional thin film covering a large area of the structure could serve as a distributed sensor. In Chapter 6, the CNT-based nanocomposites are coupled with the electrical impedance tomography (EIT) spatial conductivity mapping technique. Unlike traditional discrete sensor systems, EIT is capable of generating two-dimensional nanocomposite conductivity distribution maps. Since the electrical response of these nanocomposites have already been calibrated to stimuli (namely, strain and pH), EIT conductivity maps can be used to directly map the stimulus. Experimental studies are also presented in Chapter 6 that demonstrate the spatial detection of strain, impact damage, and corrosion. Finally, Chapter 7 concludes this dissertation by identifying potential areas for future research.

CHAPTER 2

DESIGN AND FABRICATION OF MULTIFUNCTIONAL NANOCOMPOSITES

2.1. Introduction

The primary objective of this chapter is to design and fabricate multifunctional nanocomposites that are mechanically strong and can also serve as high-performance sensors with bulk conductivities changing due to applied external stimuli. For such composites to be used in civil structures, they must be mechanically robust to withstand the harsh loadings and environments typical of such structures. In particular, the nanocomposite explored in this thesis will be assembled from polymeric materials; hence, the poor mechanical attributes of polymeric thin films must be remedied before they can be deployed in the field. For these reasons, design of a mechanically robust multifunctional nanocomposite is a key objective. To realize the distributed sensing paradigm advocated in Chapter 1, the sensing abilities of nanocomposites must be uniform across the entirety of the material's volume. In addition, the sensing capabilities of the nanocomposite must be sensitive to the parameter they seek to measure. Hence, the encoding of sensitive sensing mechanisms in a homogeneous nanocomposite is another key objective of this chapter.

Traditionally, materials endowed with desired properties are attained by physically combining more than one type of material into a composite. The concept of the composite is to incorporate the individual merits (*i.e.*, strength, ductility, high conductivity) of each material to form a composite with all of the same merits contained in one material platform. For example, reinforced concrete is a composite material that combines the high compressive strength of the concrete matrix with the high tensile

strength and ductility of the embedded steel [62]. In this thesis, a composite designed at the nano-scale will be proposed for the sensing of civil infrastructure. Two major materials will be adopted for combination in a composite form: polymeric thin films and single-walled carbon nanotubes. Polymers will provide the final composite with sensing capabilities and mechanical ductility. Unfortunately, polymeric thin films are generally weak (*e.g.*, low tensile strength) and characterized by low electrical conductivities. The SWNTs are therefore used as a filler material that mechanically reinforces the film while increasing the conductivity and sensing resolution of the composite. The result will be a mechanically robust nanocomposite capable of sensing both strain and pH.

To manufacture the nanocomposite, many different manufacturing processes are available including vacuum filtration [63], thermal annealing [64], *in situ* polymerization [65], spin coating [66], and layer-by-layer assembly [67]. Amongst these many methods, layer-by-layer assembly stands out as the most ideal for the application at hand. Specifically, LbL assembly combines monolayers of materials with alternating charge to create a multilayered composite material. Each monolayer assembles upon an existing oppositely charged substrate layer through van der Waals and electrostatic attraction. The method is known to produce homogeneous, multilayered thin films characterized by a uniform morphology at the micron and nanometer scales. In addition, this approach is cost-effective and easy to implement with a minimal amount of specialized manufacturing equipment.

This chapter begins with a detailed description of the LbL assembly process. Charged polymers (*i.e.*, polyelectrolyte or PE) and single-walled carbon nanotubes will be combined by the LbL method to yield durable SWNT-PE thin films capable of sensing. Once uniform SWNT-PE thin films have been created, three attributes are explored. First, the chapter illustrates the mechanical strength of the nanocomposite using monotonic tensile loading of free-standing thin films. Second, the electrical properties are quantitatively analyzed. Bulk conductivity of SWNT-PE thin films are measured; variation in measured conductivity is also considered for various environmental factors such as light and heat. Finally, the sensing properties of two different SWNT-PE thin films assemblies are explored. The piezoresistive properties of thin films assembled from poly(vinyl alcohol) (PVA) are analyzed, where such films can be used for strain sensing.

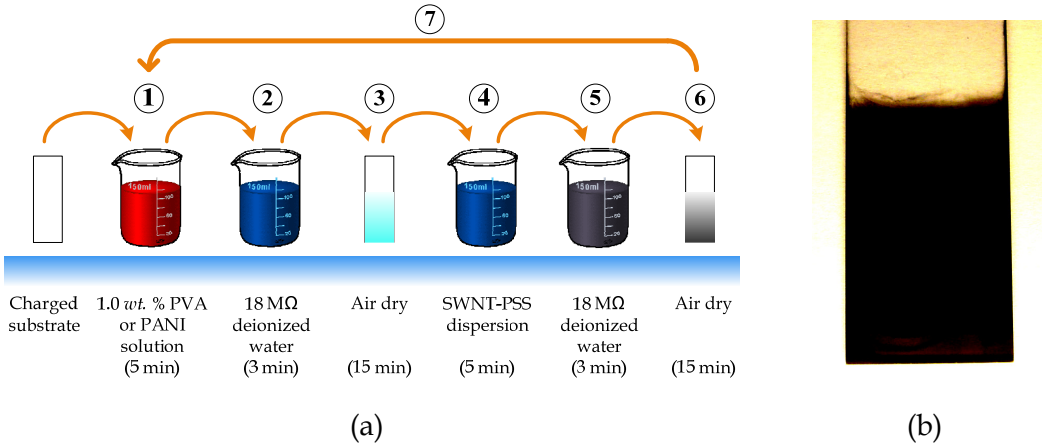

Figure 2-1. (a) Illustration of the layer-by-layer process to manufacture conformable CNT-PE nanocomposites. (b) Final 100-bilayer carbon nanotube-based composite deposited onto a transparent glass substrate.

The second thin film assembly uses poly(aniline) (PANI) as its primary PE to encode pH sensing capabilities. Such films could be used for corrosion sensing since pH is a key environmental parameter that controls the passivation of metals exposed to ionized water.

2.2. Carbon Nanotube Nanocomposite Fabrication

2.2.1. Layer-by-Layer Self-Assembly

Homogeneous multiphase carbon nanotube-polyelectrolyte composite thin films are fabricated via a systematic layer-by-layer assembly technique [58, 67-69]. The LbL method entails the sequential dipping of a charged substrate (*i.e.*, glass, silicon, among others) in oppositely-charged polyanionic (negatively charged PE) and polycationic (positively charged PE) solutions to deposit a variety of nanomaterial species one monolayer at a time (as depicted in Figure 2-1a). Selective deposition of each additional monolayer is based on opposite charge electrostatic and van der Waals force interaction with the preceding monolayer [70-72]. As opposed to creating a stratified multilayer thin film, newly adsorbed polyelectrolyte and nanomaterials are capable of interpenetrating previously deposited layers to form homogeneous nanocomposites as shown in Figure 2-1b [73]. By controlling fabrication parameters, such as the type of PE, concentration of

dipping solutions, and dipping time, thin films of variable compositions can be achieved. To date, a multitude of LbL nanocomposites for electrical, chemical, and biological applications have been developed as presented by Decher and Schlenoff [58].

The first nanocomposite fabricated by LbL is one optimized for strain sensing. This SWNT-PE thin film is primarily based on the use of poly(vinyl alcohol) (PVA, Sigma) as the polyelectrolyte in the composite. The first monolayer in the LbL assembly process is deposited by dipping a clean, charged glass microscope slide (treated with 3:7 H_2O_2:H_2SO_4 piranha solution) in a polycationic 1.0 *wt.* % PVA aqueous solution for 5 min to deposit the initial charged polyelectrolyte monolayer. Excessively large particulates and loosely-adsorbed PE species are rinsed off in 18 MΩ deionized water for 3 min, followed by a drying step for 15 min to prevent cross-contamination between the oppositely charged solutions. Using very fast magic-angle spinning nuclear magnetic resonance (MAS NMR), Rodriguez, *et al.* [74] has verified that the adsorbed polyelectrolyte remain deposited even after rinsing. Next, deposition of the carbon nanotube-based monolayer is achieved by dipping the PE-coated substrate in a stable, negatively-charged polyanionic CNT suspension (CNTs from Carbon Nanotechnologies, Inc.) for 5 min, followed by the aforementioned rinsing (3 min) and drying steps (15 min). Here, a 1.0 *wt.* % poly(sodium 4-styrene sulfonate) (PSS, $M_w \approx$ 1,000,000, Aldrich) solution is employed to achieve a stable, negatively-charged CNT dispersion. Yoo, *et al.* [75] have measured each LbL monolayer's thickness (for poly(acrylic acid)/poly(allylamine) thin films) using a Geartner ellipsometer operating at a wavelength of 633 nm and report that each monolayer's thickness can vary between 1 and 5 nm, depending on the pH of the solution. The resulting film exhibits excellent homogeneity and phase integration (*i.e.*, no stratification between monolayers is observed) [58]. This process completes one full cycle of the LbL assembly to form one bilayer of the CNT-PE nanocomposite. Multilayer thin film assembly is realized by repeating the aforementioned procedure to fabricate free-standing films of 50 and 100 bilayers of different compositions (Table 2-1). In this dissertation, an n-bilayer composite thin film fabricated with oppositely-charged species X and Y will be denoted as $(X/Y)_n$. Specifically, three different CNTs are used (unpurified SWNT (u-SWNT), purified

Table 2-1. Matrix of unique carbon nanotube-based thin films fabricated.

		Number of bilayers
Strain Sensing	**u-SWNT-PSS/PVA**[a]	50 and 100
	p-SWNT-PSS/PVA[b]	25, 50, 100, and 200
	p-DWNT-PSS/PVA[c]	50, 100, and 200
pH Sensing	**p-SWNT-PSS/PANI**[d]	50 and 100

[a] Unpurified SWNTs dispersed in 1.0 *wt.* % PSS with 1.0 *wt.* %PVA LbL counterpart.
[b] Purified SWNTs dispersed in 1.0 *wt.* % PSS with 1.0 *wt.* % PVA LbL counterpart.
[c] Purified DWNTs dispersed in 1.0 *wt.* % PSS with 1.0 *wt.* % PVA LbL counterpart.
[d] Purified SWNTs dispersed in 1.0 *wt.* % PSS with 1.0 *wt.* % PANI LbL counterpart.

SWNT (p-SWNT), and purified DWNT (p-DWNT)) to explore thin film electrical properties as a function of the types of nanotubes employed.

The second nanocomposite fabricated in this study is for pH sensing. To embed pH sensing capabilities into the nanocomposite, the PVA polyelectrolyte previously explored is replaced with a 1.0 *wt.* % PANI (1:9 *by vol.* N,N-dimethyl formamide:H_2O) (poly(aniline) emeraldine base, Aldrich, $M_w \approx 100{,}000$). Here, carbon nanotube-PANI thin films are assembled using the same LbL fabrication process previously described. It should be noted that only purified SWNTs are considered in 50 and 100 multilayered assemblies, as described in Table 2-1.

2.2.2. Suspension and Dispersion of Carbon Nanotubes

In order to fully harness the impressive electrical properties of CNTs and to transfer these properties to tangible length scales (*i.e.*, LbL thin films), a stable suspension and dispersion of CNTs in an aqueous solution is necessary. Presently, many researchers have undertaken covalent stabilization techniques to molecularly bind (or to functionalize) specific molecular species onto CNT surfaces for enhanced dispersion and functionality [59]; however, a noncovalent approach via steric stabilization of CNTs in polyelectrolyte solutions is selected for this study as this method preserves the mechanical and electrical properties of individual nanotubes [76]. A high molecular weight poly(sodium 4-styrene-sulfonate) (*i.e.*, $M_w \approx 1{,}000{,}000$) polyanion solution is

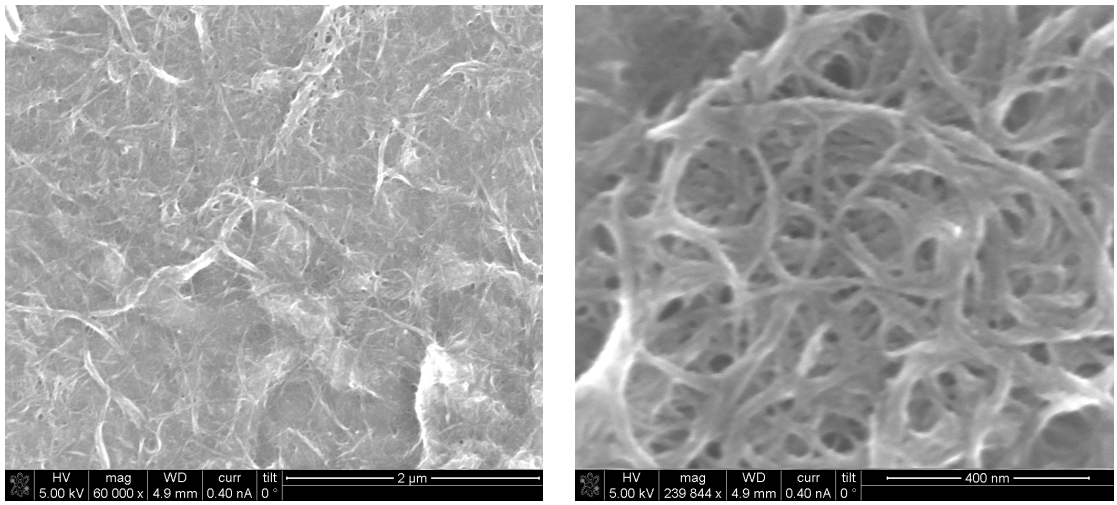

(a) (b)

Figure 2-2. (a) Low-magnification and (b) high-magnification SEM images of (p-SWNT-PSS/PVA)$_{25}$ thin film, indicating adequately dispersed p-SWNTs deposited on the LbL thin film.

employed to facilitate dispersion of single- and double-walled carbon nanotubes, previously mentioned in Section 2.2.1. Dispersion is achieved by exposing CNT-PSS mixtures to 180 min of ultrasonic excitation (135 W, 42 kHz) followed by 90 min of high-powered probe sonication (3.178 mm tip, 500 W, 22.0 kHz, 30% power amplitude). Adequate dispersion of CNTs is verified with scanning electron microscopy (SEM). Figure 2-2 shows deposition of individual and small nanotube bundles in a PVA-PSS matrix; as can be seen, the percolation threshold of SWNTs is exceeded. While it has been found in preliminary studies that PSS facilitates dispersion of SWNTs [77], Moore, *et al.* [78] validates a wide variety of polymer dispersive agents for CNTs. A key finding they report is that higher molecular weight polymers (*e.g.*, PSS) tend to suspend more SWNTs due to their longer polymeric chains and the size of their hydrophilic groups for enhanced steric stabilization [78]. In addition, various surfactants and polymers have also been shown to provide non-covalent stabilization and suspension of individual nanotubes while allowing for high concentrations of dispersed carbon nanotubes in solution [76]. Preliminary UV-Vis (ultraviolet-visible) absorption spectroscopy studies of CNT-PE thin films fabricated in this study with PSS and PVA indicate greater absorbance than films fabricated with other polyelectrolytes (namely PDMA, PAH, among others). Furthermore, measured UV-Vis absorbance is found to be well-

correlated to the amount of CNT deposition [76], thereby suggesting efficient nanotube deposition per LbL fabrication cycle when using PVA as the LbL electrolyte counterpart to PSS [77].

2.3. Inherent Nanocomposite Mechanical Properties

Upon determining the physical morphology of the proposed nanocomposite (Section 2.2), its mechanical properties, particularly, i stiffness (Young's Modulus, E), ultimate tensile strength (σ_f), and ultimate failure strain (ε_f) are of interest. These fundamental material properties govern the applicability of the multifunctional nanocomposite as a structural coating system or an embedded thin film for use in civil engineering structures. Thus, precise characterization of the nanocomposite mechanical properties permits a better understanding of the role of SWNTs in reinforcing the thin films.

2.3.1. Monotonic Tensile Testing of Free-Standing Thin Films

Experimental monotonic tensile testing of free-standing (p-SWNT-PSS/PVA)$_n$ thin films is required to determine the Young's modulus, ultimate tensile strength, and ultimate failure strain of these materials. Prior to load testing, layer-by-layer thin films deposited onto glass substrates are immersed in a hydrofluoric acid (HF) bath to release a free-standing film via chemical etching of the glass. Here, nanocomposite samples are cut into approximately 25 x 2 mm^2 specimens and loaded in a TestResources Q100 mechanical load frame (Figure 2-3). Fixed-fixed boundary conditions are ensured, and the final unsupported length of the thin film specimen is approximately 12 mm. It should be noted that precise thin film dimensions (length and width) are measured using a digital caliper with a ±0.005 mm resolution. On the other hand, the scanning electron microscope is used to determine average thin film cross-sectional thickness (where $h \approx 1.1$ μm for most specimens tested as shown in Figure 2-4). Upon sample loading, the TestResources Q100 load frame is commanded to execute a uniaxial and monotonic tensile load pattern at a displacement-controlled 10 μm-s^{-1} load rate while the embedded data acquisition system samples time, stroke displacement, and equilibrium load simultaneously at 15 Hz. It should be mentioned that stroke displacement of the

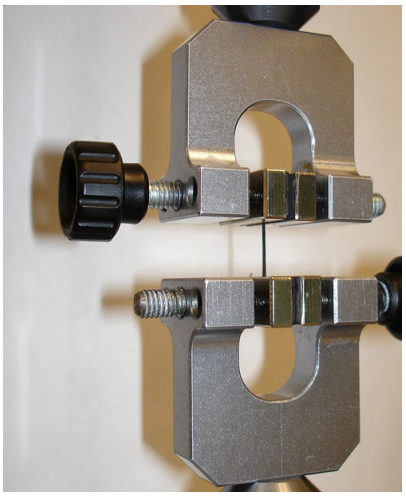

Figure 2-3. Free-standing (SWNT-PSS/PVA)$_{200}$ nanocomposite thin film is monotonically loaded in a TestResources Q100 load frame.

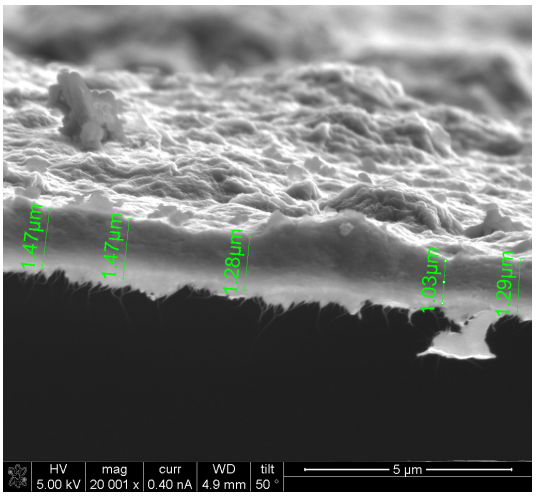

Figure 2-4. (SWNT-PSS/PVA)$_{200}$ thin film thicknesses as measured at multiple locations using SEM.

Q100 load frame is used to calculate induced strains due to the inherent difficulty of physically attaching an extensimeter onto thin films characterized by micro-meter thicknesses. Here, the assumption is that thin films do not slip during applied tensile loads and is deemed a valid assumption due to application of strong clamping forces and the use of specialized rubbery clamps for gripping. Then, the load frame is stopped as soon as film failure is observed, as shown in Figure 2-5; minimum boundary effects are observed since thin film failure occurs near the mid-section of the specimens.

2.3.2. *Nanocomposite Stress-Strain Response*

Figure 2-6 plots a representative stress-strain response of (p-SWNT-PSS/PVA)$_{200}$ thin films under applied uniaxial monotonic tensile loading. Immediately, it can be observed from Figure 2-6 that the nanocomposite's stress-strain response is dominated by an initial linear regime (to a strain of approximately 10,000 με), followed by moderate yielding, strain hardening, and ultimate film failure at ε_f = 21,000 με. The specimen's stiffness or Young's modulus is then determined to be E = 8.5 GPa by linear least-squares regression of the stress-strain curve's initial linear portion, and the ultimate failure tensile strength (immediately prior to film failure) is σ_f = 128 MPa. The experimental results reported herein are consistent with results obtained by Mamedov,

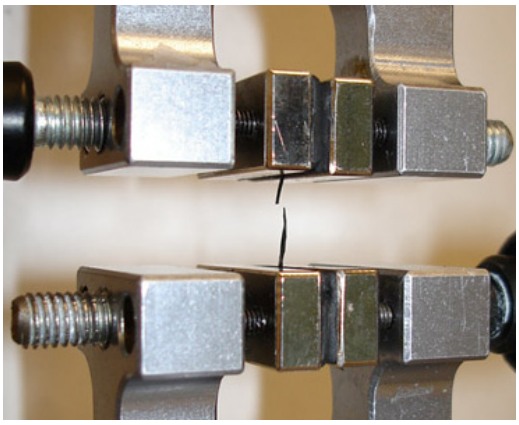

Figure 2-5. The Q100 load frame is stopped as soon as film failure occurs (where film failure occurs across the middle of the specimen). Shown is a torn sample of $(SWNT\text{-}PSS/PVA)_{200}$.

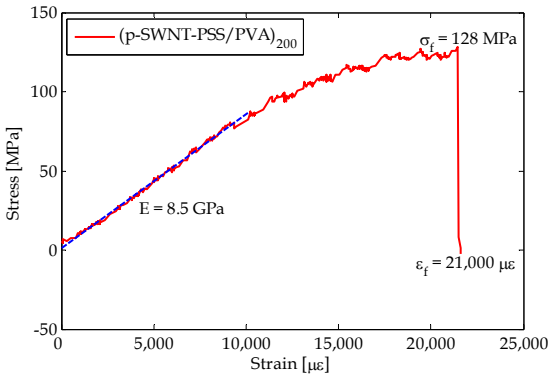

Figure 2-6. A representative stress-strain response of $(p\text{-}SWNT\text{-}PSS/PVA)_{200}$ thin films subjected to a uniaxial monotonic tensile load to failure.

et al. [70] where they report carbon nanotube LbL composites fabricated with poly(ethylene imine) (PEI) and poly(acrylic acid) (PAA) fail at 220 ± 40 MPa.

However, the stress-strain response obtained by Mamedov, *et al.* [70] is highly nonlinear and the ultimate tensile strain capacity of $((PEI/PAA)(PEI/SWNT)_5)_8$ films are approximately $\varepsilon_f \approx 10{,}000$ με; on the other hand, for all the specimens tested in this study, $(p\text{-}SWNT\text{-}PSS/PVA)_{200}$ thin films do not fail or fracture until the applied strain exceeds 20,000 με, thereby suggesting dramatic compliance enhancement of these materials by adopting a PSS/PVA polymeric matrix. It is hypothesized that the long intertwined poly(sodium 4-styrene sulfonate) polyelectrolyte (deposited during LbL) unravel under applied tensile loading to enhance the compliance of the nanocomposite; simultaneously, since unraveling of polyelectrolyte chains take place as opposed to direct stretching of carbon-carbon bonds on the polymer backbone (*i.e.*, the polymers within the composite are not aligned), the stiffness of the proposed thin film is compromised. Nevertheless, it is anticipated that the mechanical properties (*i.e.*, stiffness and strength) of the proposed carbon nanotube-based nanocomposites can be enhanced via post-fabrication treatments such as thermal annealing and polymer cross-linking as have been done by Mamedov, *et al.* [70]. In addition, it should also be mentioned that the addition of CNTs significantly improve the ultimate tensile strength and stiffness of the SWNT-polymer nanocomposite

by more than 20 and 70 times, respectively, as compared to non-reinforced polymeric free-standing thin films whose ultimate tensile strengths are well below 25 MPa [70].

2.4. Inherent Nanocomposite Electrical Properties

2.4.1. Measurement of Material Conductivity

Given any solid material body, its intrinsic electrical property is described by the material's conductivity, σ, (or its inverse which is resistivity, ρ) at a particular ambient temperature and pressure. In short, conductivity refers to the material's ability to transport charge (*i.e.*, holes and electrons) through its spatial dimensions, where the rate of charge movement can be experimentally measured and referred to as electrical current, I. Since conductivity is a material property, its value is inherent to the material and is independent of material geometry (*i.e.*, dimensions and shape).

However, in order to experimentally determine a solid material's conductivity (or resistivity), one must first determine a sample's resistance. In this case, resistance is a measurement of the material's ability to impede the flow of electrical current and can be calculated easily using Ohm's Law:

$$V = IR \tag{2-1}$$

where V is the electric field or potential drop (in units of [V]) generated as an applied DC current (direct current, I in units of [A]) is passed through a material with resistance, R (in units of [Ω]). It should be noted that a material's resistance varies with its geometry, where larger resistance values will be measured when current needs to travel longer distances than in the case when current travels shorter distances. On the other hand, a material with a larger cross-sectional area provides a greater number of paths for current flow (given the same sample lengths), thereby causing a decrease in measured resistance. By knowing a solid material's resistance and dimensions, the sample's resistance can be normalized for calculating the material's resistivity, ρ, (*i.e.*, a material property) as shown in Equation 2-2 [79]:

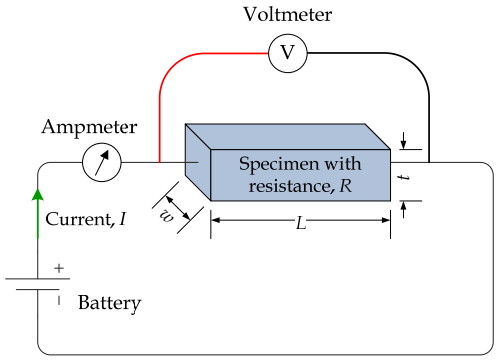

Figure 2-7. A simple technique for measuring a solid body's resistance for calculating material conductivity (or resistivity).

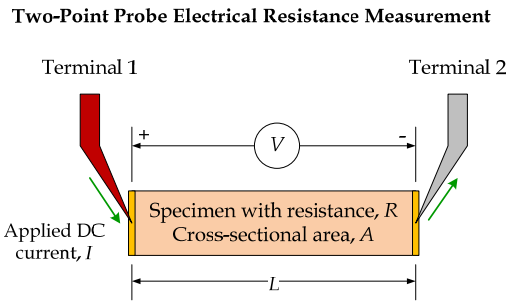

Figure 2-8. A schematic illustrating the two-point probe electrical resistance measurement technique.

$$\rho = \frac{RA}{L} \text{ in } [\Omega\text{-m}] \tag{2-2}$$

where A is the cross-sectional area (width, w times thickness, t), and L is the length of the material. In addition, the conductivity of the material is simply the inverse of resistivity.

$$\sigma = \frac{1}{\rho} \text{ in } [\text{S-m}^{-1}] \tag{2-3}$$

where the unit [S] is simply the inverse of [Ω]. A schematic is shown in Figure 2-7 to illustrate a simple technique for determining an unknown material's resistivity or conductivity.

While Figure 2-7 has demonstrated a convenient way to estimate and measure a given material's resistance, numerous scientific methods have been standardized for experimental resistance sampling [80, 81]. Similar to Figure 2-7, a two-point probe method is one of the most common measurement setups employed for determining a solid body's resistance [81]. As the name suggests, two probes (or terminals) are electrically connected to two opposite ends of a material of interest (Figure 2-8). Based on Figure 2-8, a DC current of known magnitude is injected at Terminal 1 so current flows through the specimen and exits at Terminal 2. Simultaneously, the potential drop (or voltage) is sampled using a voltmeter (*i.e.*, across Terminals 1 and 2). Then, using

Ohm's Law shown in Equation 2-1, the specimen's resistance can be calculated easily. Although this technique is simple to use and convenient, the measured resistance becomes increasingly inaccurate as specimen conductivity increases (*i.e.*, small resistance); in this case, contributions from the contact resistance between measurement terminals and the specimen becomes increasingly significant.

So as to eliminate the effect of contact resistance from electrical resistance measurements, a four-point probe measurement technique has been widely adopted for this purpose [80]. Instead of only using two electrical probes, four terminals are now attached to a specimen as shown in Figure 2-9. Here, DC current is injected at Terminal C1 and exits at Terminal C2 (Figure 2-9). Instead of measuring the potential drop across Terminals C1 and C2, an additional pair of electrodes (Terminals V1 and V2) is also electrically connected to the material body as shown in Figure 2-9. Elimination of contact resistance is achieved by using high-impedance electrodes to minimize current flow through the voltmeter via Terminal V1 to V2. Then, Ohm's Law is employed to calculate an accurate measurement of specimen resistance that is independent of contact resistance.

In this study, nanocomposite conductivities are determined by employing both two- and four-point probe electrical resistance measurement techniques. Contact resistance between measurement electrodes and the thin film is minimized by securely affixing copper tape electrodes (Ted Pella) followed by the application of highly conductive colloidal silver paste over the copper tape and thin film interface. Then, nanocomposite resistance is experimentally measured using a Agilent 34401A digital multimeter. Here, the Agilent multimeter automatically injects a DC current of known magnitude while simultaneously measuring voltage measurements to compute thin film resistance. A schematic of a two-point probe electrical resistance measurement of a nanocomposite specimen is shown in Figure 2-10.

It has been demonstrated that the minimization of contact resistance is successful since negligible measurement differences are observed between two- and four-point probe methods. Thus, the use of a two-point probe technique, as shown in Figure 2-10, is determined to be accurate. Using this measurement method, preliminary average conductivity measurements for a variety of (p-SWNT-PSS/PVA)$_n$, (p-DWNT-

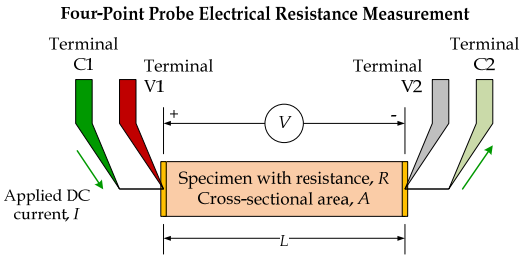

Figure 2-9. A schematic illustrating the four-point probe electrical resistance measurement technique.

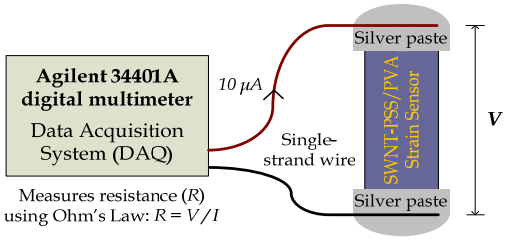

Figure 2-10. A schematic showing the experimental setup of thin film resistance measurements used in this study.

PSS/PVA)$_n$, and (p-SWNT-PSS/PANI)$_n$ thin films are tabulated in Table 2-2. In particular, maximum conductivity values for (p-SWNT-PSS/PVA)$_{200}$, (p-DWNT-PSS/PVA)$_{200}$, and (p-SWNT-PSS/PANI)$_{100}$ thin films have been determined to be approximately 1,060 ± 6 S-m^{-1}, 671 ± 20 S-m^{-1}, and 9.6 ± 0.1 S-m^{-1}, respectively (Table 2-2). The standard deviation for conductivity measurements are also provided and are determined based on 10 unique resistance measurements for each type of thin film. For instance, the dramatic differences observed between PVA-based and PANI-based SWNT nanocomposites suggest that a significantly higher density of nanotubes are deposited during (p-SWNT-PSS/PVA)$_n$ nanocomposite LbL assembly.

2.4.2. *Time-Dependent Nanocomposite Electrical Properties*

Before utilizing LbL nanocomposites for electromechanical and electrochemical sensing, it is important to quantify their electrical conductivities and to understand how such conductivities respond to variations in the approach of measurement and environment. While electrical conductivity is enabled via nanotube percolation, preliminary studies have identified two effects that adversely affect measurement of material conductivity: exponential-decay in measured film resistance during multi-point probing and light sensitivity [77]. First, it has been identified that CNT-PE thin films display time-variant exponential decay of bulk film surface resistivity [77]. While the underlying nature of this resistivity decay is unclear, it is widely known that CNT-PE thin films are strongly influenced by temperature. Valentini, *et al.* [82] have found that

Table 2-2. Summary of measured thin film bulk electrical conductivities.

Nanocomposite	Number of bilayers	Thickness [nm]	Conductivity [S-m^{-1}]
(p-SWNT-PSS/PVA)	50	240	143 ± 7
	100	480	419 ± 15
	200	950	1,060 ± 6
(p-DWNT-PSS/PVA)	50	240	176 ± 2
	100	480	671 ± 20
(p-SWNT-PSS/PANI)	100	400	9.6 ± 0.1

Note: Ten conductivity measurements are taken for every sample for obtaining a representative distribution of data.

as-grown RF-PECVD (radio-frequency pulsed plasma-enhanced chemical vapor deposited) CNT thin films exhibit a negative relationship between bulk resistivity and temperature. A similar temperature-resistance relationship has been identified by Hone, *et al.* [83] using aligned and non-aligned single-walled carbon nanotube films. Specifically, they exhibit a significant decrease in resistance with increasing temperature [82, 83]. When using two- or four-point probe methods for resistance measurements, multimeters typically supply a constant direct current (DC current of i = 500 nA to 10 mA). In our measurements, the Agilent 34401A multimeter may be causing resistive heating in the CNT-PE sample. The multimeter's current can increase the temperature of the bulk film while activating electrons at nanotube-to-nanotube junctions, both of which result in an increase in the measured film conductivity.

To illustrate this thermal-chemical conductivity behavior and to quantify the evolution of film resistance as a function of time, an experiment is conducted to measure the conductivity of the thin film over a period of five hours. The resistance of a (p-SWNT-PSS/PVA)$_{50}$ thin film is measured using the Agilent 34401A digital multimeter. A four-point probe configuration is used with the multimeter using a 100 µA DC current. The resistance is measured continuously for a period of five hours. As seen from Figure 2-11a, (p-SWNT-PSS/PVA)$_{50}$ thin films exhibit a well-defined exponential-decay in film resistance, R with increasing time. Even at small input DC current sources (*i.e.*, *5 µA*), a similar effect can be observed. Nevertheless, the exponential decay in film resistance can

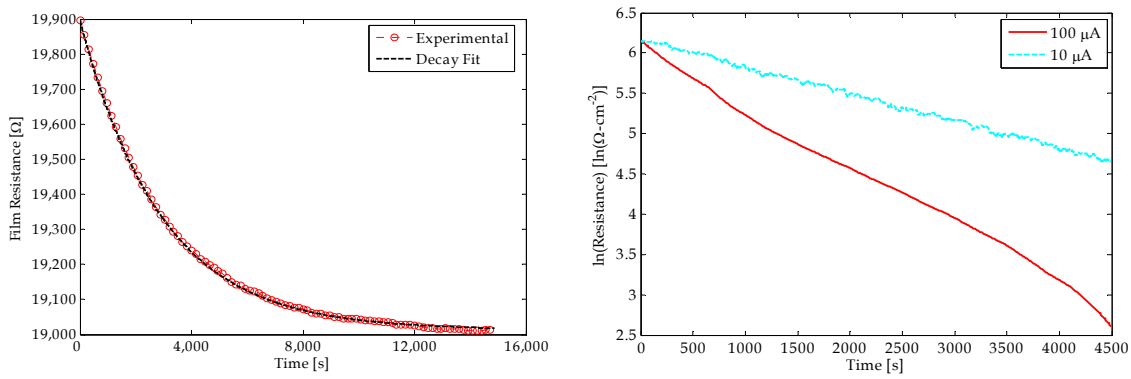

(a) (b)

Figure 2-11. (a) (p-SWNT-PSS/PVA)$_{50}$ thin film exponential decay in resistance. (b) Current-dependent bulk film resistance decay for a (p-SWNT-PSS/PVA)$_{100}$ nanocomposite when measured with 10 μA and 100 μA of DC current.

be modeled accurately. By fitting the exponential resistance decay with a numerical model of the form $R = Ae^{Bt}+C$ (where A, B, and C are model constants), a nearly perfect prediction of measured resistance is made as shown in Figure 2-11a. The existence of a calibrated model is critical since it can be used to subtract the decay from experimental resistance data. This will be critical if we use the material as a sensor whose conductivity changes due to applied external stimulus.

As mentioned before, it is hypothesized that one environmental factor contributing to the exponential decay of bulk film resistivity is a result of the resistive heating supplied by the multimeter's DC current. Naturally, with larger applied currents, heating should be more pronounced, and film resistivity should decay faster as compared to instances using smaller applied currents. Figure 2-11b plots the natural logarithm of measured film surface resistivity (normalized to film surface area) as a function of time so that film surface resistivity decay rates can be compared for two different DC supply currents (10 μA versus 100 μA) used to measure resistance of the same film. As expected, a higher applied measurement current of *100 μA* causes the temperature of the nanocomposite to increase faster, which in turn causes film resistance to decrease at a faster rate. Results from Figure 2-11b confirm (p-SWNT-PSS/PVA)$_{50}$ (and more generally, CNT-PE) thin film's sensitivity to temperature due to resistive heating induced by an applied current.

2.4.3. *Thin Film Light Sensitivity*

It has been demonstrated by Zhang and Iijima [84] that bundles of as-produced carbon nanotubes display distinct deformations including stretching, bending, and repulsion under the illumination of visible light. The measured light-induced current shows complete elastic and recoverable behavior as is also observed by Lu and Panchapakesan [85]. Furthermore, while light-induced current is insensitive to the wavelength and polarity of visible light [84], the induced photocurrent is linearly related to light intensity [85]. On the other hand, when illuminated under UV-light, Chen, *et al.* [86] have observed that individual carbon nanotubes exhibit orders of magnitude decrease in conductance due to intrinsic photoactivity, particularly from semiconducting SWNTs. Thus, to quantify LbL CNT-PE thin films' bulk resistivity changes under the illumination of light, broad-spectrum visible light is shined at increasing time intervals (namely 10, 20, 40, and 60 sec) upon $(\text{p-DWNT-PSS/PVA})_{100}$ samples enclosed in a dark experimental chamber. An Agilent 34401A multimeter is again employed to sample resistance at 1 Hz throughout the duration of testing.

Consistent with findings from Zhang and Iijima [84] and Lu and Panchapakesan [85], LbL $(\text{p-DWNT-PSS/PVA})_{100}$ thin films display decreasing resistivity upon the illumination of broad-spectrum visible light as seen from Figure 2-12a. Although CNT-PE nanocomposites show their characteristic exponential decay in bulk resistance in dark settings, the incidence of light results in an immediate decrease in film resistance (Figure 2-12a). As soon as the light is turned off, film resistance gradually increases to return to its initial exponentially-decreasing resistivity trend, thereby signifying completely recoverable behavior as have been observed by Lu and Panchapakesan [85]. By fitting the exponential decay with $R = Ae^{Bt}+C$ and then subtracting it from the experimental data, the equivalent CNT-PE light-sensitive response is extracted (Figure 2-12b). From Figure 2-12b, it is clear that as the "light on" interval is increased, the associated drop in resistance increases accordingly. Given sufficient time after the light source has been turned off, resistance recovery is fully elastic and complete. Although Figure 2-12 is of a $(\text{p-DWNT-PSS/PVA})_{50}$ sample, similar results have been observed for the other CNT-PE LbL nanocomposites under study herein. To prevent light from

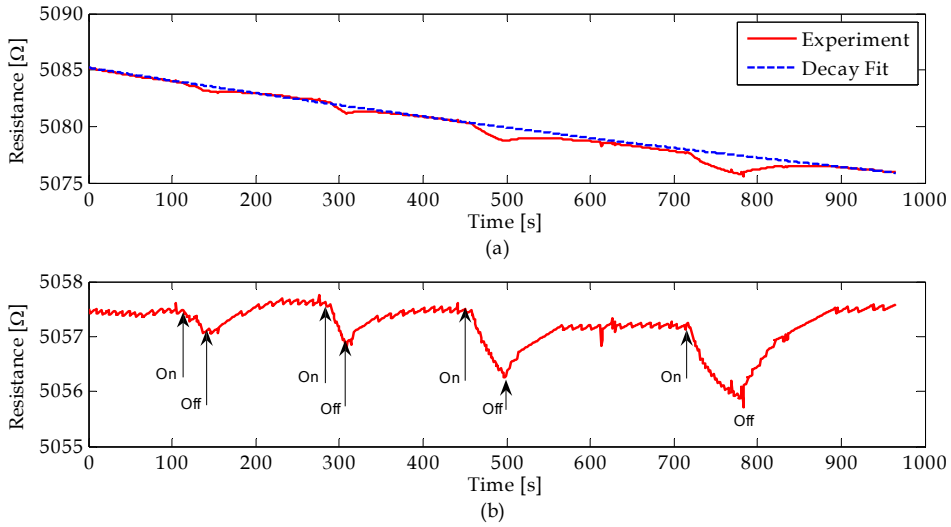

Figure 2-12. (a) (p-DWNT-PSS/PVA)$_{50}$ thin film response to broad-spectrum visible light at 10, 20, 40, and 60 s intervals along with the fitted exponential decay of film resistivity. (b) Exponential decay-removed from the thin film resistance time history.

interfering with measured data, further experiments on CNT-PE thin films are conducted by covering samples so as to ensure a completely dark environment.

2.5. Piezoresistivity of Carbon Nanotube-based Nanocomposites

Among the variety of sensing transducers used for structural health monitoring, strain sensors rank among the most important for determining long-term structural reliability and health. For example, strain sensors are widely employed to measure component level strain in both laboratory and field environments, as they correspond directly to the induced localized stress fields commonly used for damage detection. Consequently, since the development of the first strain gauges in 1936 [87], many researchers have followed suit to improve and design a broad array of strain transducers such as semiconducting strain sensors [88] and fiber optic Bragg gratings [89, 90]. Furthermore, while semiconducting and fiber optic strain sensors can achieve high sensitivities and are generally easy to use, they can suffer from high manufacturing costs and require costly data acquisition systems. Thus, it is anticipated that materials and fabrication tools derived from the nanotechnology domain can be used to design a next-

generation strain sensor that exhibits high performance (*e.g.*, sensitivity, resolution, and dynamic range) at very low costs.

In fact, early experimental investigations of CNTs as mechanical sensors have been conducted by Peng, *et al.* [91]. These researchers have sought to quantify changes in the electrical-mechanical properties of single-walled carbon nanotubes (SWNTs) suspended over patterned silicon oxide/silicon substrate trenches while the nanotubes are manipulated by an atomic force microscope (AFM) tip. Their results indicate promise for strain sensing as they have identified decreasing SWNT conductance up to two orders of magnitude of individual carbon nanotubes as AFM tips bend them [63, 91-93]. Similar numerical results using computed density-functional theory-universal force field (DFT-UFF) calculations predict similar trends [94]. Dharap, *et al.* [63] also report on changes in resistance of CNT films, called "buckypaper" (*i.e.*, fabricated by vacuum filtration and drying of a suspended CNT solution), as they are strained in low tension-compression cycles ($\varepsilon < \pm 400$ με). Extensions of their work [95] explore the Raman wavenumber shifts of the G-band of carbon nanotube films during strain. Their findings indicate that the wavenumber shifts are consistent with changes in the electrical properties of the CNTs as they are strained. Similarly, Kang, *et al*. [96] has developed a mold-casted and thermally annealed SWNT-polymer composite buckypaper exhibiting linear piezoresistivity up to strains of ±1,400 με. Their work is extended to employ MWNTs to fabricate long films for a continuous "neuron" sensor [97].

2.5.1. Monotonic Tensile Loading Experimental Details

Initial validation of the piezoresistivity of the CNT-PE thin films fabricated in this study is accomplished by applying a monotonic tensile load until ultimate failure of the nanocomposite specimens. Upon completion of layer-by-layer thin film fabrication, $(\text{p-SWNT-PSS/PVA})_{200}$ specimens along with the glass substrates used during fabrication are immersed in a 1.0 *vol.* % hydrofluoric acid bath to chemically etch off the glass substrate and to obtain conformable free-standing CNT-PE nanocomposites. The conformable thin film is allowed to dry for two hours and subsequently mounted to a 1.9-cm diameter aluminum rod for monotonic tensile testing (Figure 2-13a). Single-strand electrical wire and colloidal silver paste (Ted Pella) are employed to establish

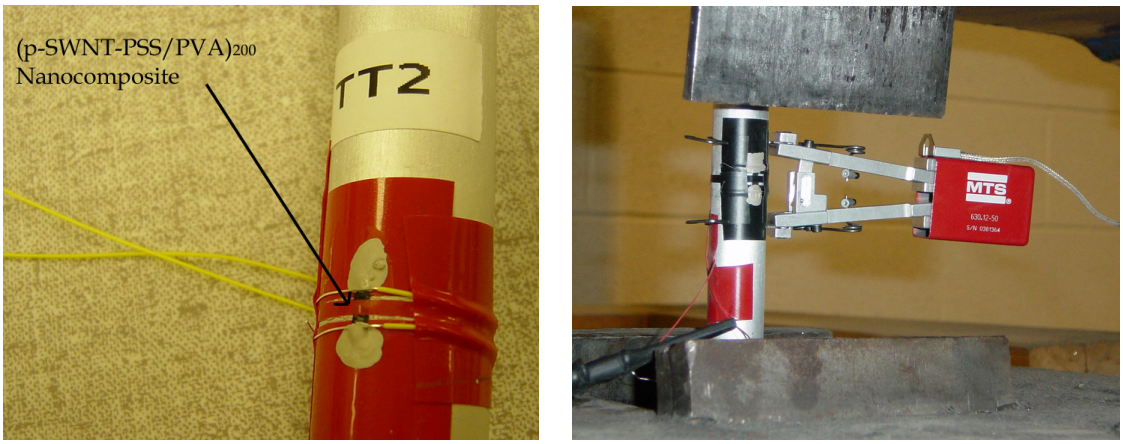

(a) (b)

Figure 2-13. (a) Free-standing (p-SWNT-PSS/PVA)$_{200}$ nanocomposite epoxy-mounted to an aluminum tensile-testing coupon. (b) Thin film strain sensor and extensimeter attached to the aluminum rod loaded in monotonic tension.

electrical connections to the thin film specimen, where an Agilent 34401A multimeter is again employed to interrogate the resistance of the material at a 1 Hz sampling rate. The mounted thin film and aluminum rod is monotonically loaded until failure (load rate is approximately 500 με-s^{-1}). As a baseline comparison, an MTS extensimeter sampled at 10 Hz is also attached firmly to the aluminum rod (Figure 2-13b).

2.5.2. *Nanocomposite Strain Sensor Validation Results*

Figure 2-14a overlays the (p-SWNT-PSS/PVA)$_{200}$ nanocomposite electrical resistance time history upon the time history plot of the specimen strain. At the initiation of loading, the nominal resistance (R_0) of the thin film is approximately 830 Ω. During monotonic loading, the film undergoes an increase in film resistance in tandem with increasing coupon strain. As can be seen, the ductile specimen undergoes a maximum tensile strain of 73,000 με before failure, at which point the electrical resistance of the thin film is greater than 1.1 kΩ. More insight can be gained by plotting the normalized change in resistance ($\Delta R/R_0$) as a function of strain measured by the MTS extensimeter. In Figure 2-14b, one can observe that the percentage change in the nanocomposite's normalized resistance is linearly proportional to applied strain. By fitting a straight line to the normalized resistance-strain data (using linear regression analysis), the

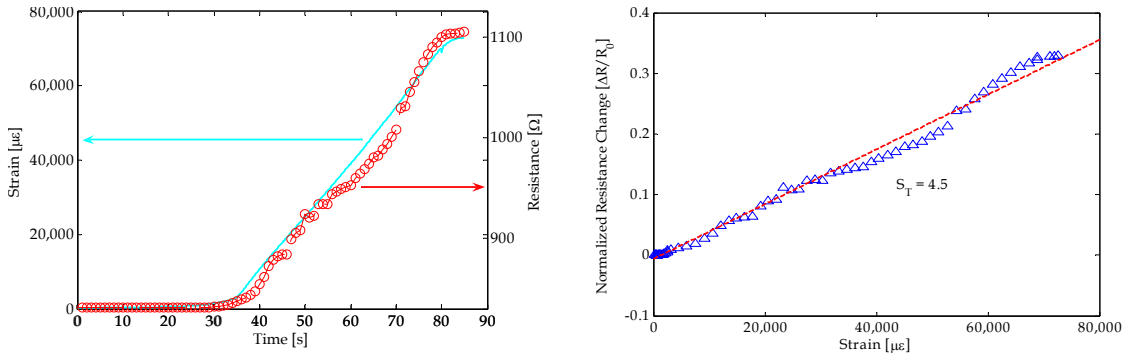

(a) (b)

Figure 2-14. (a) $(p\text{-SWNT-PSS/PVA})_{200}$ experimental resistance and MTS extensimeter strain measurement time history overlay. (b) Normalized nanocomposite change in resistance as a function of applied strain.

nanocomposite's strain sensitivity under applied monotonic tension (denoted as S_T) can be derived using Equation 2-4:

$$S_T = \frac{\Delta R/R_0}{\varepsilon} \tag{2-4}$$

For the specimen tested, the strain sensitivity is estimated at S_T = 4.5. Another observation is the well-behaved normalized resistance-strain linearity of the thin film; this behavior suggests the material has tremendous promise for strain sensing. Other preliminary tests on similar CNT-PE nanocomposites yield similar strain sensitivities.

Despite the near-linear strain sensing performance of the proposed carbon nanotube-based thin film composites (Figure 2-14b), it is crucial to identify the underlying causes for sensor non-linearity pronounced at higher strain (ε > 40,000 με). In fact, a scanning electron microscope is employed to image the micro-scale physical properties of the thin films epoxy-mounted to the aluminum testing coupons; SEM images shown in Figure 2-15 identify significant wrinkling of the thin films during mounting. In particular, unevenness to the mounted sample could be a cause for some nonlinearity in the results. The wrinkled-mounted film likely unfolds during tensile loading; this can falsely enhance the dynamic range of the sensor. Thus, to prevent wrinkling of films during mounting of free-standing films and to ensure high-quality sensor output, subsequent nanocomposites are no longer etched in an HF acid bath.

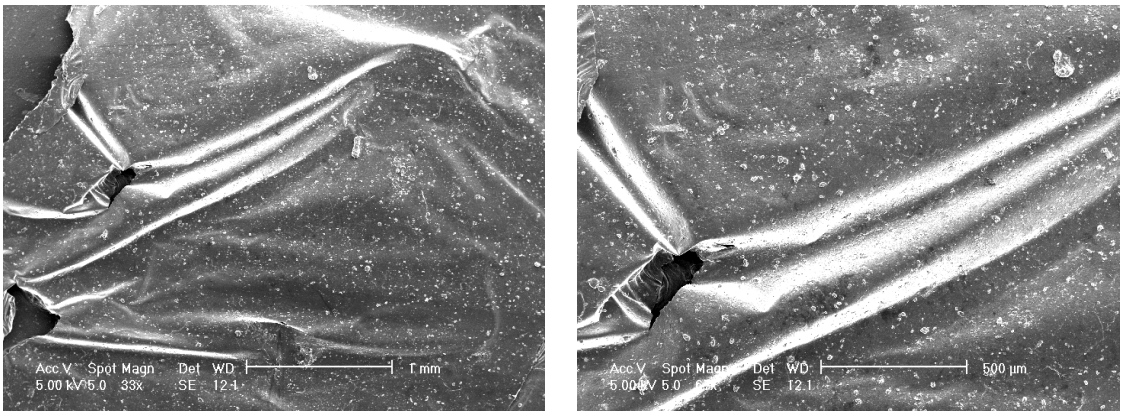

(a) (b)

Figure 2-15. (a) Low-magnification and (b) high magnification SEM images of the same free-standing (p-SWNT-PSS/PVA)$_{100}$ nanocomposite mounted on a coupon specimen showing wrinkling of films, local tearing, and uneven adhesion to the coupon.

Rather, further piezoresistive testing of these nanocomposites is conducted by epoxy-mounting both the thin film and its original glass substrate to the testing coupon. It should be noted that although glass can fail in a brittle manner under tension, the small glass substrate size (after being cut with a diamond scriber), small thickness, and low applied strain (≤ 10,000 με) ensures the integrity of the glass substrate. In addition, additional nonlinearity may be due to the inherent mechanical properties of the CNT-PE nanocomposites as have been observed from the measured stress-strain response shown in Figure 2-6.

2.5.3. Tensile-Compressive Cyclic Loading Experimental Details

Investigation of CNT-PE thin films' piezoresistivity is conducted by applying a three-cycle tensile-compressive cyclic load pattern. First, all thin films fabricated are cut from the glass substrate into small rectangles (2 x 1 cm^2) and affixed to rectangular poly(vinyl chloride) (PVC) Type I coupon samples (31 cm long, 4 cm wide, 2 cm thick) using CN-Y post-yield epoxy (Tokyo Sokki Kenkyujo). Electrical contacts are established by drying colloidal silver paste over single-strand wire to form a two-point probe measurement setup as shown in Figure 2-16. After a six-hour drying period (of the epoxy and silver paste), the coupon is loaded in an MTS-810 load frame to apply slow

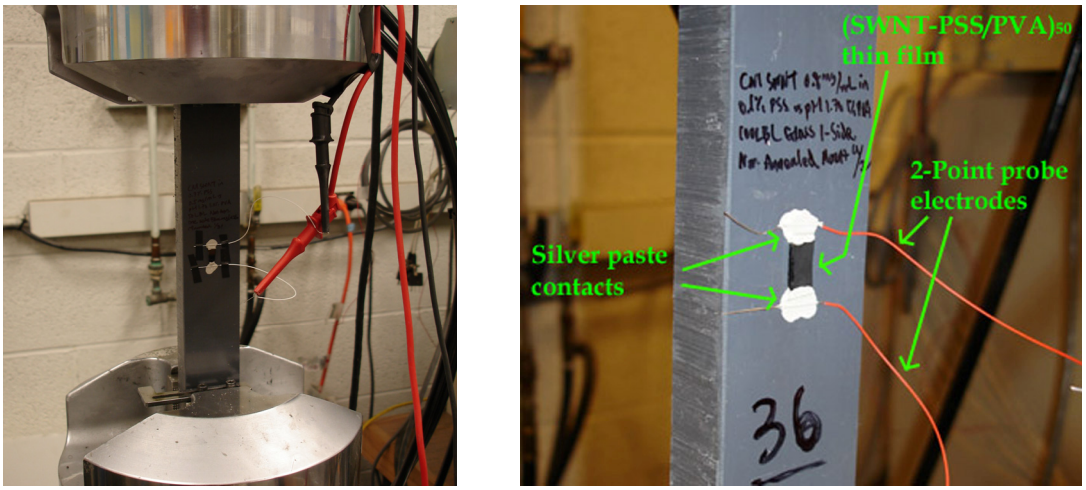

(a) (b)

Figure 2-16. (a) $(SWNT\text{-}PSS/PVA)_{50}$ strain sensor epoxy-bonded to a PVC coupon and fixed within an MTS-810 load frame for testing. (b) A close-up view of the thin film and two-point probe electrodes.

(250 με-s^{-1}) and fast (500 με-s^{-1}) saw-tooth tensile-compressive cyclic load patterns with ±5,000 με strain amplitudes (*i.e.*, within the limits of linear piezoresistive performance). Real-time resistance changes under applied loading is sampled at 1 Hz using an Agilent 34401A digital multimeter supplying 10 μA of direct current. Stroke displacement of the MTS-810 load frame and strain measurements from a traditional 120 Ω metal-foil strain gauge (Texas Measurements, Inc.) are also sampled to provide a baseline comparison of bar strain with experimental CNT-PE piezoresistive response. In addition, it should also be noted that the boundary conditions of the loaded specimens are well-controlled such that strain gauge measurements have been found to directly correlate to strains calculated from the MTS-810 load frame's stroke displacement.

2.5.4. *Nanocomposite Tensile-Compressive Piezoresistive Response*

Previous studies conducted with CNT-PE films fabricated with PSS and PVA polyelectrolyte conjugates have verified their piezoresistive response ([77] and Section 2.5.2). Here, the experimental $(CNT\text{-}PSS/PVA)_n$ (CNTs considered include u-SWNT, p-SWNT, and p-DWNT) thin film response under applied tensile-compressive strains is used to identify the strain sensing properties of thin films tabulated in Table 2-1. Most

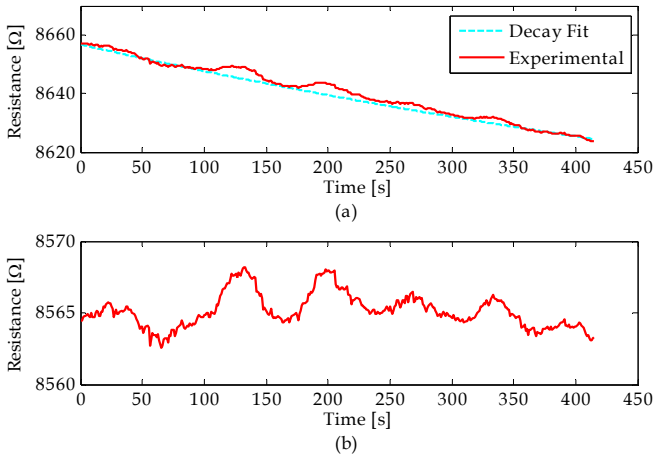

Figure 2-17. (a) (u-SWNT-PSS/PVA)$_{50}$ thin film response to a three-cycle tensile-compressive load pattern to ε = ±5,000 με. (b) Exponential decay-removed strain sensing response suggest thin film piezoresistivity cannot be accurately extracted.

importantly, the strain sensitivity for the strain sensor (denoted as S_R) is expressed as (Equation 2-5):

$$S_R = \frac{\Delta R_{peak-peak}/R_0}{\varepsilon_{peak-peak}} \tag{2-5}$$

where $\varepsilon_{peak\text{-}peak} = \Delta L/L_0$, ΔL is the change in length of the PVC element, and L_0 is the unsupported length of the PVC bar, $\Delta R_{peak\text{-}peak}$ is defined as the change in film resistance between maximum and minimum applied strains, and R_0 is the nominal (initial) resistance of the thin film. Representative u-SWNT-, p-DWNT- and p-SWNT-PSS/PVA multilayer film piezoresistive responses are shown in Figures 2-17a, 2-18a, and 2-19a. Upon identifying the resistivity decay model for each type of film, the exponential fit is numerically removed to facilitate determination of thin film strain sensitivity, S_R. Excellent model fitting can be observed as the fit-removed results show repeatable (cyclic) strain sensing response with no resistivity drifts over time (Figures 2-17b, 2-18b, and 2-19b).

Although all three types of (CNT-PSS/PVA)$_n$ thin films exhibit piezoresistive response, (u-SWNT-PSS/PVA)$_n$ thin films possess a high noise floor (low signal-to-noise ratio), making them unsuitable for strain sensing (Figure 2-17). Equivalent strain

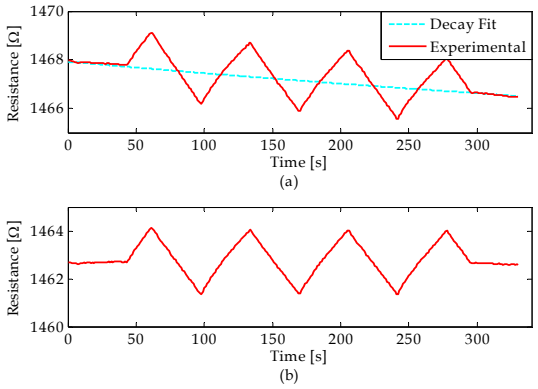

Figure 2-18. (a) $(\text{p-DWNT-PSS/PVA})_{50}$ thin film response to a three-cycle tensile-compressive load pattern to ε = ±5,000 με. (b) Exponential decay-removed strain sensing response.

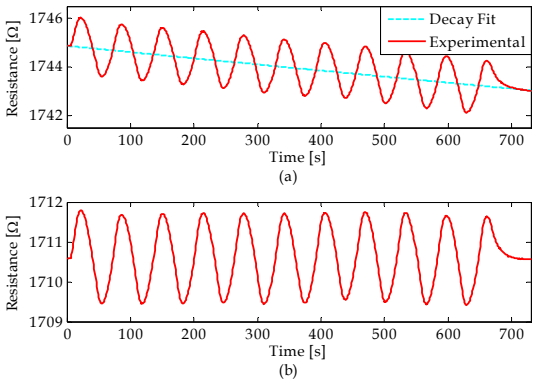

Figure 2-19. (a) $(\text{p-SWNT-PSS/PVA})_{100}$ thin film response to a ten-cycle tensile-compressive load pattern to ε = ±5,000 με. (b) Exponential decay-removed strain sensing response.

sensitivities could not be extracted accurately due to excessive noise masking the film's resistance response to applied tensile-compressive strains. Despite the fact that u-SWNTs have a large quantity of impurities (*e.g.*, amorphous carbon, iron, nickel, among others), its high noise floor may be due to premature clumping during LbL fabrication as opposed to the impurities on individual nanotubes. Efforts to disperse u-SWNTs in 1.0 *wt.* % PSS solutions have only been moderately successful; for example, precipitation occurs significantly faster than solutions of p-SWNTs and p-DWNTs. As a result, increasingly larger bundles of u-SWNTs are deposited during each additional LbL bilayer fabrication cycle. Thus, for the remainder of this chapter, performance characterization of LbL $(\text{CNT-PSS/PVA})_n$ nanocomposites will only be focused on those fabricated with purified nanotubes (p-SWNTs and p-DWNTs).

Between p-DWNT- (Figure 2-18) and p-SWNT-PSS/PVA (Figure 2-19) thin films, an obvious difference is observed. Here, $(\text{p-DWNT-PSS/PVA})_n$ thin films exhibit sharp peaks at points of maximum applied tensile-compressive strains, whereas rounded-peaks are identified for $(\text{p-SWNT-PSS/PVA})_n$ samples. Although the origins of these two different types of responses are unknown, it is hypothesized that the existence of significantly more semiconducting nanotubes in SWNTs introduces capacitance to the thin films that contributes to such behavior [96]. Chapter 4 of this dissertation will reveal the potential capacitive behavior of $(\text{p-SWNT-PSS/PVA})_n$ thin films by using frequency-

domain characterization techniques such as electrical impedance spectroscopy. In general, under applied strains, CNTs can displace in the bulk polymer matrix or deform by stretching, shrinking, or bending. Assuming an applied tensile strain, CNTs likely undergo rigid body motion due to stretching of the bulk film leading to a decrease in the number of nanotube-to-nanotube junctions, thereby increasing bulk film resistivity (the opposite applies for compression). For the latter scenario, CNT deformation under applied strain alters the inherent conductivity of individual nanotubes leading to a change in the composite's conductivity [63, 93, 96].

However, in the case of DWNT thin films (or MWNT), Qian and Dickey [98] report when MWNTs are nearly parallel to the direction of applied tensile strain, a "sword-in-sheath" atomic fracture failure is preferred with an inner tube individually translating relative to the outer tube. Due to the weak interlayer bonding of MWNTs, applied strain can induce some concentric rings of individual MWNTs to rupture first [86]. This premature failure mechanism at relatively lower strains can reduce the overall bulk strain sensitivity and dynamic range (*i.e.*, based on a lower ultimate failure strain) of $(\text{p-DWNT-PSS/PVA})_n$ nanocomposite strain sensors. Upon a "sword-in-sheath" fracture failure, inner and outer tubes can lose electrical connectivity as the inner and outer tubes separate from one another due to the applied strain. Thus, based on the experimental results presented in this section and the high performance attributes of p-SWNT-based thin films, latter portions of this dissertation will only focus on using p-SWNTs (herein referred to as SWNTs) for nanocomposite sensor designs.

2.6. Encoding pH and Corrosion Sensitivity in Nanocomposites

The ability to accurately measure and monitor pH has been critical for a variety of biological, chemical, and engineering applications; particularly, it has been demonstrated that ambient pH can be employed as an accurate and reliable corrosion indicator for health monitoring of metallic structures. For example, aluminum alloys used for aerospace structures undergo high corrosion rates when subjected to highly acidic or alkaline environments [99]; on the other hand, steel reinforcement used in civil infrastructures is normally resistant against corrosion due to concrete's inherent high alkalinity (pH > 13.5) but becomes vulnerable to corrosion when ambient pH falls below

9 (resulting in the erosion of the passivation layer on the steel) [100]. Thus, an effective way to monitor corrosion of metallic structures is to employ specie-independent pH sensors. Furthermore, long-term pH monitoring can be used to detect the onset of corrosion, thereby allowing for condition-based maintenance (as opposed to current schedule-based maintenance, which is more conservative and economically inefficient). While there exists a variety of commercially available pH sensors, most of the current pH sensors employ large liquid-filled glass tubes and are fragile, thereby confining their use in laboratory environments. In addition, current devices typically do not meet the geometric constraints and long-term durability needs of *in situ* corrosion monitoring. Thus, the ability to encode pH sensing mechanisms within nanocomposites can significantly reduce their form factor and enhance robustness for laboratory- and field-based applications.

2.6.1. Nanocomposite pH Sensing Performance

Recently, a variety of conductive and non-conductive polymers, such as polypyrrole, poly(hydroxyethyl methacrylate), poly(aniline), among others, have been shown to change optical and/or electrical properties due to pH [101]. As previously described in Section 2.2.1, in order to encode pH sensitivity within SWNT-PE thin films, PANI is employed as the primary matrix polymer to form $(\text{SWNT-PSS/PANI})_n$ LbL nanocomposites. Upon deposition of these nanocomposites onto glass substrates, the thin film and substrate are cut into small rectangular pieces (approximately 10 x 12 mm^2) via a diamond scriber. Copper tape (Ted Pella) electrodes are affixed onto two ends of the nanocomposite to achieve a two-point probe setup. In addition, contact impedance is minimized by applying colloidal silver paste (Ted Pella) over the copper tape and thin film (similar to Section 2.4.1). Then, a plastic well (7 mm diameter) is securely mounted over the thin film surface via vacuum grease (Dow Corning) as shown in Figure 2-20. Changes in thin film electrical resistance due to pH buffer solutions added to the well is measured with an Agilent 34401A digital multimeter supplying 10 nA of direct current while sampling at 1 Hz. While measuring film resistance, buffer solutions of various pH levels are pipetted in and out of the well.

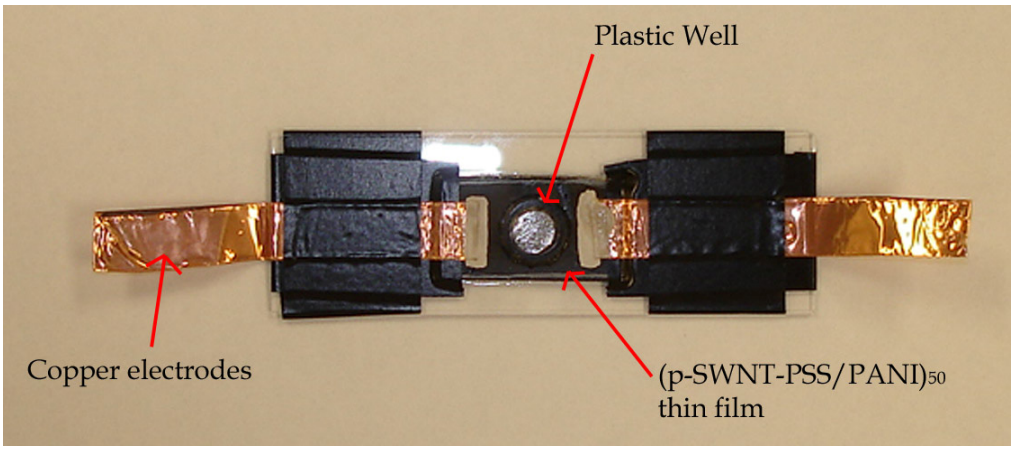

Figure 2-20. A two-point probe setup using copper tape and silver paste is electrically connected to a (SWNT-PSS/PANI)$_{50}$ specimen for characterization of thin film conductivity variation as a function of pH.

Figure 2-21 plots the time history of the thin film resistance (R) to applied pH buffer solutions. Initially, the thin film is exposed to a pH 1 buffer solution. Upon observing steady-state resistance output at (time of 175 s), the buffer solution is removed at which point the next pH buffer solution is pipeted into the well. From Figure 2-21, it can be observed that the (SWNT-PSS/PANI)$_{50}$ nanocomposite exhibits dramatic changes in resistance as a function of pH. More importantly, upon pipetting in a pH 11 solution, the immediate addition of the fresh pH 1 solution causes film resistance to decrease back to the film's original resistance, thereby suggesting that the nanocomposite response is repeatable. Furthermore, by plotting the steady-state nanocomposite resistance as a function of pH, it can be seen from Figure 2-22 that the film's pH sensitivity exhibits greatest linearity at pH extremities (*i.e.*, when subjected to acidic (pH 1 – 5) or alkaline (pH 8 – 11) buffer solutions). At neutral pH (pH 6 – 8), a large increase in nanocomposite resistance is observed when acidic buffer solutions are replaced with alkaline solutions. Nevertheless, thin film pH sensitivity (normalized by thin film surface area, A) for the presented (SWNT-PSS/PANI)$_{50}$ specimen is approximately 7.7 kΩ-pH^{-1}-cm^{-2} under the aforementioned acidic conditions and 14.8 kΩ-pH^{-1}-cm^{-2} when exposed to alkaline solutions (Figure 2-22) as calculated by Equation 2-6:

$$S_P = \frac{\Delta R/A}{\Delta pH} \tag{2-6}$$

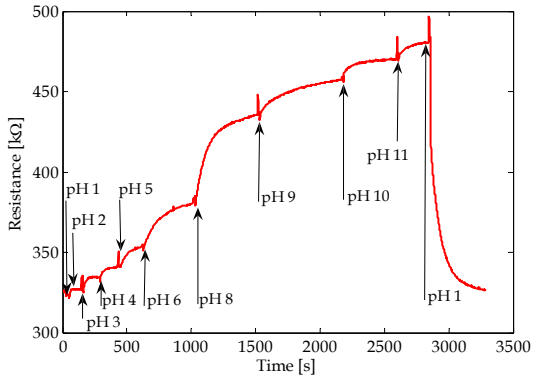

Figure 2-21. The two-point probe DC time history response of a (SWNT-PSS/PANI)$_{50}$ thin film subjected to pH 1 to 11 buffer solutions.

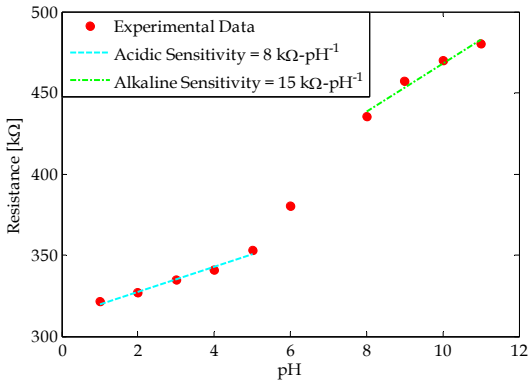

Figure 2-22. A plot of steady-state thin film resistance as a function of pH to show the bilinear pH sensitivity of a (SWNT-PSS/PANI)$_{50}$ thin film.

where ΔR is the change in nanocomposite resistance when the film is exposed to varying pH buffer solutions. These results suggest that these PANI-based thin films exhibit slightly higher sensitivity to alkaline pH buffer solutions. Nevertheless, changes in film conductivity (the inverse of resistivity) due to pH can be attributed to variations in the degree of protonization of the nitrogen atoms within the -imine groups of the PANI molecular structure [102].

2.7. Summary and Conclusions

2.7.1. Results and Discussion

In summary, this chapter has demonstrated the ability to tailor and fabricate multifunctional carbon nanotube-polyelectrolyte nanocomposites that are both mechanically strong and capable of changing their electrical properties in response to applied strain or pH. A layer-by-layer assembly method is employed to fabricate a diverse suite of (CNT-PSS/PVA)$_n$ thin films, because this specific fabrication method yields highly homogeneous composite materials at relatively low costs. First, the intrinsic mechanical performance of the proposed nanocomposites is quantified by recording their stress-strain response during uniaxial monotonic tensile loading.

Experimental results suggest that these nanocomposites exhibit high stiffness (E = 8.5 GPa), high strength (σ_f = 128 MPa), and ultra ductility (ε_f = 21,000 με). High tensile strength and ultra ductility allow these nanocomposite materials to be used in harsh settings such as those commonly experienced by civil infrastructure systems. Second, the intrinsic electrical properties of carbon nanotube-based thin films are characterized by measuring their conductivities by multi-point probing. Furthermore, the dependency of measured conductivity on environmental factors such as resistive heating and ambient broad-spectrum light are explored. For the case of resistive heating, the exponential property of the heat-induced conductivity change allows this effect to be easily removed from long-term conductivity time histories. Light induced conductivity changes can be eliminated by preventing light exposure (*e.g.*, coating the thin film with light absorbing layers).

To further investigate the application of these nanocomposites for strain sensing, free-standing films are mounted to tensile coupons for monotonic load testing. Initial results validate the piezoresistive response of $(\text{SWNT-PSS/PVA})_n$ thin films to applied monotonic tensile strain. Since a variety of carbon nanotubes (purified, unpurified, double-walled, etc.) exist, different compositions of thin films are fabricated to identify which type of CNT is best suited for strain sensing. Experimental results demonstrate the high-degree of linearity of the nanocomposite thin films, with p-SWNT-based films exhibiting the best performance (*i.e.*, low noise, high sensitivity, and high linearity). Typical strain sensitivities (S_R) are in the neighborhood of about 2 to 4. A second sensing capability is also demonstrated by incorporating PANI within the bulk polymeric matrix of the SWNT-based composite. PANI is selected since its conductivity is sensitive to pH. Experimental results obtained show that the $(\text{SWNT-PSS/PANI})_n$ thin films exhibit dramatic increases in surface resistivity in tandem with increasing levels of pH buffer solutions (pH 1 to 11). The pH sensitivity of the PANI-based thin film is about 8 to 15 $\text{k}\Omega\text{-pH}^{-1}\text{-cm}^{-2}$.

2.7.2. Contributions

The main contribution of this chapter is the successful utilization of a bottom-up materials fabrication methodology using nanotechnology-derived tools to achieve

multiple intrinsic material properties (*e.g.*, strength and sensing) within the same nanocomposites. By assembling carbon nanotubes within a bulk polymeric matrix, these thin films exhibit impressive mechanical properties, namely strength, stiffness, and ductility. Furthermore, through judicious selection of polyelectrolyte and nanomaterial species, different sensing features including strain and pH sensing are achieved. Extensive experimental characterization and validation studies have been conducted to improve current knowledge of the nanocomposite's intrinsic mechanical and electrical properties.

Despite the favorable sensing performance illustrated in this chapter, some important fundamental limitations of carbon nanotube composites have also been identified. For instance, a time variant resistance drift has been observed during probing. Although the nature of this drift has yet to be confirmed, it is hypothesized that the resistance drift may be due to resistive heating and/or physical changes at the nanotube-to-nanotube junctions. Nevertheless, the rate of resistance drift can be controlled by regulating the magnitude of the DC current employed during measurement of film resistance. In fact, this effect can be modeled accurately by fitting an exponential curve of the form $R=Ae^{Bt}+C$ to numerically remove the exponential decay. The ability to post-process experimental data and numerically remove the exponential decay still suggests potential for implementation of these nanocomposites in real structures. Since a wide variety of LbL parameters are available to control the final film's composition, an optimization study is required to further understand how the inherent mechanical properties and the sensing attributes of the films are affected by changes in LbL parameters. In particular, Chapter 3 will explore changes in the thin film's inherent strength, stiffness, and toughness when reinforced with different concentrations of SWNTs. Then, Chapter 4 will focus on control of the piezoresistivity of $(SWNT\text{-}PSS/PVA)_n$ thin films through the adjustment of various LbL parameters.

CHAPTER 3

ENHANCING MECHANICAL PROPERTIES OF CARBON NANOTUBE-BASED COMPOSITES

3.1. Introduction

As mentioned in Chapter 1, the aim of this dissertation is the design of multifunctional materials that are sensitive to external stimuli while also exhibiting superior strength, stiffness, and toughness. This multifunctionality is illustrated in Chapter 2, where it has been shown that layer-by-layer nanocomposites embedded with CNTs exhibit sensitivity to strain and pH while remaining mechanically strong. In fact, many researchers have sought to take advantage of the impressive properties (*i.e.*, stiffness and strength) of carbon nanotubes to enhance the mechanical attributes of polymeric-based thin films and nanocomposites. A recent review conducted by Coleman, *et al.* [103] has summarized efforts to incorporate carbon nanotubes within composites fabricated via epoxy-setting, thermosets, melts, *in situ* polymerization, among many others. In general, the bulk composite stiffness, strength, and hardness have found to increase in tandem with increasing SWNT and MWNT weight content [103]. More specifically, Mamedov, *et al.* [70] have also discovered that layer-by-layer PEI/PAA thin films display improved mechanical performance when reinforced with single-walled carbon nanotubes, where the ultimate failure strength and Young's modulus of bulk composites have been experimentally measured to be 220 ± 40 MPa and ~11 GPa, respectively. For the case of MWNTs employed as filler material within thin films, Olek, *et al.* [71] have observed mechanical improvements in strength and stiffness (*i.e.*, 150 MPa and 4.5 GPa, respectively). However, the proposed as-fabricated (SWNT-

PSS/PVA)$_n$ thin films exhibit strength and stiffness on the order of 128 MPa and 8.5 GPa, respectively (Section 2.3), significantly lower than results obtained by Mamedov, *et al.* [70] and Olek, *et al.* [71].

Thus, the main objective of this chapter is to explore techniques during and after layer-by-layer fabrication for enhancing the mechanical performance of (SWNT-PSS/PVA)$_n$ nanocomposites. Similar to studies presented by Coleman, *et al.* [103], thin film carbon nanotube weight content is varied from 0 to 0.50 mg-mL^{-1} to correlate SWNT content with bulk mechanical properties such as Young's modulus, ultimate tensile strength, and ultimate failure strain. In addition, nanocomposites are thermally-treated in a post fabrication step so as to induce cross-linking between polymer chains. Then, preliminary experimental studies are conducted to obtain fracture toughness measurements of these LbL nanocomposites. Imaging techniques such as scanning electron microscopy are employed to observe crack surfaces for determining how these composites behave at failure regions. Results of the mechanical and fracture study conducted herein can therefore lead to optimal design of multifunctional nanocomposites capable of sensing and providing mechanical reinforcement.

3.2. Mechanical Properties of Carbon Nanotube Nanocomposites

3.2.1. Nanocomposite Fabrication and Mechanical Testing Experimental Details

Similar to previous discussions (Section 2.2.1), the layer-by-layer technique is employed to fabricate (SWNT-PSS/PVA)$_{200}$ free-standing thin films. The bulk film nanotube weight content is controlled by precisely adjusting the initial SWNT-PSS concentration. Here, single-walled carbon nanotubes of 0.25 and 0.50 mg-mL^{-1} are dispersed in 1.0 *wt.* % poly(sodium 4-styrene sulfonate) solution following identical suspension procedures outlined in Section 2.2.2. Enhancement of the mechanical properties of as-fabricated films is conducted by thermally annealing each thin film in a furnace at 180 ^{o}C for 20 min. Then, upon thin film deposition onto glass substrates, a 1.0 *vol.* % hydrofluoric acid bath is employed for chemical etching of the glass to release free-standing (SWNT-PSS/PVA)$_{200}$ films. On the other hand, a non-SWNT-reinforced PSS-PVA thin film is also prepared to serve as the control specimen. Thus, a total of

Table 3-1. A list of nanocomposites fabricated for mechanical testing.

Thin Film Composition Name	SWNT Concentration	Polyanionic Solution	Polycationic Solution
Type A – Control	0	1.0 *wt.* % PSS	1.0 *wt.* % PVA
Type B – Low Concentration	0.25 mg-mL^{-1}	1.0 *wt.* % PSS	1.0 *wt.* % PVA
Type C – High Concentration	0.50 mg-mL^{-1}	1.0 *wt.* % PSS	1.0 *wt.* % PVA

three sets of unique films will be mechanically tested to extract their Young's modulus, ultimate failure strength, and ultimate tensile strain as shown in Table 3-1.

Upon completion of film fabrication, the three unique sets of nanocomposites (Table 3-1) are mechanically cut to 25 x 2 mm^2 specimens for monotonic tensile testing in a TestResources Q100 load frame as discussed in Section 2.3.1. Precise film dimensions (length and width) are measured using a digital caliper of ±0.005 mm precision, and thin film thickness is measured using the scanning electron microscope. Upon mounting the thin films into the Q100 load frame, the nanocomposite's unsupported length is approximately 8 to 12 mm (aspect ratio of ~4 to 6). Selection of these experimental parameters is to minimize boundary effects and slippage of films during mechanical testing. Then, the load frame is commanded to apply a uniaxial and monotonic tensile load pattern displacement-controlled at 10 μm-s^{-1}, while the embedded data acquisition system (DAQ) samples real-time stroke displacement, applied load, and time at 15 Hz. The Q100 load frame continues to load each nanocomposite specimen until film failure. It should also be noted that five to ten specimens are extracted from each type of nanocomposite composition of Table 3-1, and each specimen is experimentally tested to obtain a good distribution of the experimental data.

3.2.2. Characterization and Enhancement of Nanocomposite Mechanical Properties

In order to obtain the baseline mechanical properties of the aforementioned nanocomposites, Specimen A of Table 3-1 (no SWNT reinforcement) is mechanically tested to characterize its stress-strain response to monotonic tensile loading. A PSS-PVA specimen loaded in the Q100 load frame is shown in Figure 3-1, and its corresponding stress-strain plot is shown in Figure 3-2, where it is obvious that the PSS-PVA thin films

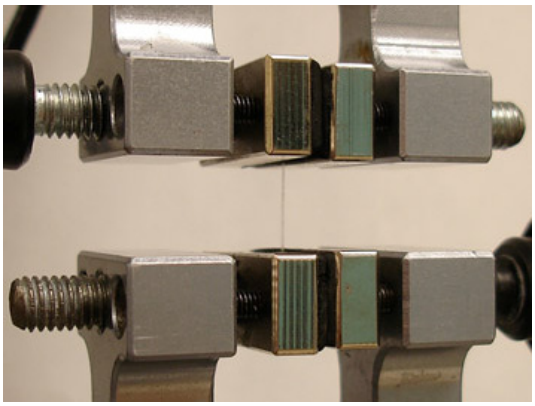

Figure 3-1. A PSS-PVA thin film is loaded in the Q100 load frame for monotonic tensile testing.

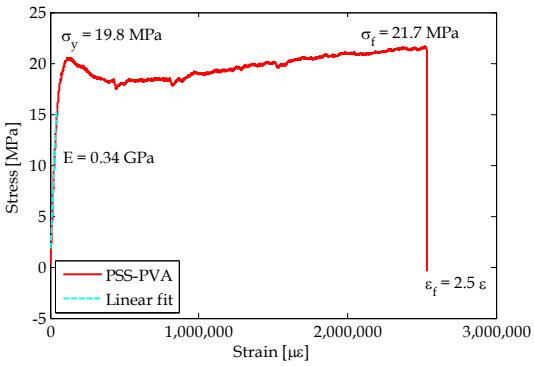

Figure 3-2. A representative stress-strain response of PSS-PVA thin films exhibiting yielding followed by strain hardening (Type A specimen).

exhibits a stress-strain response characteristic of polymeric materials. It should be noted that values for stress are determined based on engineering stress ($\sigma = F/A$, where F is the applied force of the Q100 load frame and A is the initial thin film cross-section area). Upon initial loading, Type A specimens exhibit excellent linearity up to 100,000 με (10% strain), followed by initial yielding of the polymer film and significant plasticity observed from homogeneous crazing across the entire length of the specimen (Figure 3-2). It should be noted that crazing initiates after the applied strain exceeds 1 ε or 100% strain. It should be noted that the associated plastic behavior of the PSS-PVA thin film leads to strain hardening which is expected since PSS is a high-molecular weight material [104]. In this case, strain hardening behavior is due to interlocking of physical entanglements within the PSS and PVA polymer chains. Thus, for the set of PSS-PVA specimens tested at 10 $\mu\varepsilon\text{-}s^{-1}$, linear regression of the initial stress-strain curve suggests that the average Young's modulus of PSS-PVA is approximately 0.33 ± 0.01 GPa. Since yielding is dependent on strain rate [104], the ultimate stress is a better measure of film strength, where the ultimate strength and ultimate strain is 20.7 ± 0.8 MPa and 2.53 ± 0.16 ε (253% strain), respectively. Based on these experimental measurements, it can be concluded that PSS-PVA thin films exhibit high ductility, moderate ultimate strength, but very low stiffness. Particularly, the PSS-PVA thin film's low stiffness is extremely

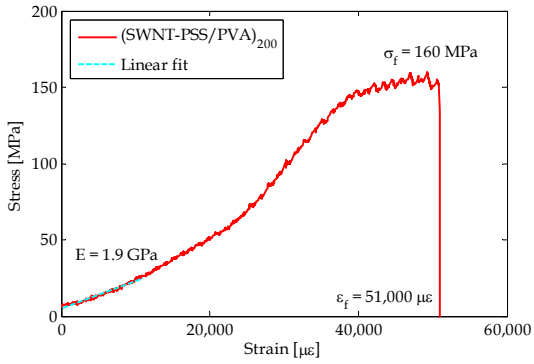

Figure 3-3. Stress-strain response of a $(SWNT\text{-}PSS/PVA)_{200}$ thin film fabricated from 0.25 mg-mL^{-1} SWNT-PSS solution (Type B specimen).

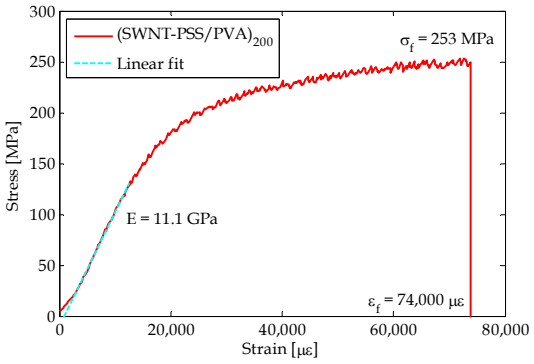

Figure 3-4. Stress-strain response of a $(SWNT\text{-}PSS/PVA)_{200}$ thin film fabricated from 0.50 mg-mL^{-1} SWNT-PSS solution (Type C specimen).

advantageous for structural health monitoring applications such that these materials are conformable and can be easily affixed onto complex structural surfaces.

Using the same procedure outlined above, Specimens B and C of Table 3-1 have also been mechanically tested for obtaining their stress-strain response. For nanocomposites fabricated with 0.25 mg-mL^{-1} SWNT-PSS solutions (*i.e.*, Specimen B), the average Young's modulus, ultimate strength, and ultimate strain are 1.9 ± 0.1 GPa, 157 ± 9 MPa, and 48,700 ± 1,000 με, respectively. For Specimen C, the corresponding mechanical properties have been determined to be 11.2 ± 0.4 GPa, 229 ± 7 MPa, and 67,000 ± 3,900 με, respectively. Representative stress-strain curves for Specimens B and C are presented in Figures 3-3 and 3-4, respectively, and a summary of thin film mechanical properties as a function of SWNT reinforcing concentration is shown in Figure 3-5.

Immediately, one can observe dramatic differences between thermally-treated nanocomposites (Figures 3-3 and 3-4) and as-fabricated $(SWNT\text{-}PSS/PVA)_{200}$ thin films (Figure 2-6). In the case where films have not been thermally annealed as a post-fabrication step, the films tested exhibited brittle fracture failure (Section 2.3.2); however, upon thermal treatment, significant polymer cross-linking is seen to enhance the thin film mechanical properties by promoting significant strain hardening after 10,000 με.

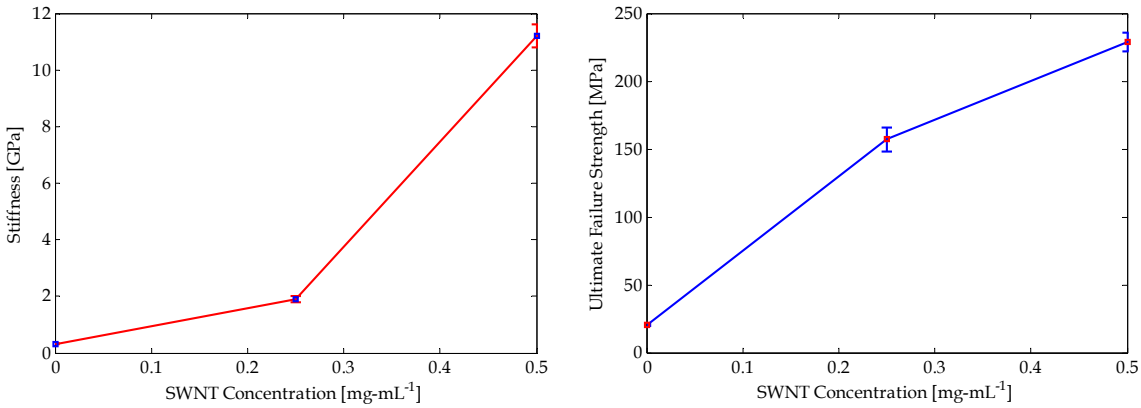

(a) (b)

Figure 3-5. (a) Average Young's modulus and (b) ultimate failure strength of nanocomposites as a function of SWNT concentration. Standard deviations of normally distributed data are also shown (for five to ten samples tested).

Furthermore, a two-fold enhancement of stiffness, ultimate strength, and ultimate strain are obtained simply by thermally treating LbL nanocomposites.

Upon plotting the summary of mechanical properties obtained for thin films fabricated from different initial SWNT concentrations, it is apparent from Figure 3-5 that enhanced mechanical properties (*i.e.*, stiffness and strength) are also attained when initial SWNT-PSS solution concentrations are increased from 0 to 0.5 mg-mL^{-1}. In fact, for both the nanocomposite's bulk Young's modulus and ultimate failure strength, an order of magnitude increase in mechanical properties can be obtained as shown in Figure 3-5. These results are consistent with findings obtained by Mamedov, *et al.* [70], where they have also observed improvements in thin film mechanical properties with increasing SWNT weight content (~50 *wt.* %). Among all of the nanocomposites tested, all specimens displayed linearity upon initial loading (up to 10,000 με for specimens reinforced with SWNTs). Beyond 10,000 με, yielding occurs, followed by moderate strain hardening for Specimen B films (low nanotube concentration) and enhanced strain hardening for Specimen C films. While no conclusive trends can be identified for nanocomposite ultimate failure strain, it can be concluded that the addition of carbon nanotubes significantly reduces the compliance of these polymeric films. Nevertheless, results from this study permit the precise tailoring of thin film mechanical properties characterized by unique stress-strain relationships.

3.3. Nanocomposite Fracture Properties

Section 3.2 has already illuminated the fact that thermal treatment induces cross-linking within the polymeric matrix to enhance bulk nanocomposite stiffness and strength. However, it is also of interest to gain further insight into the failure modes of these novel nanocomposites. Specifically, the objective of this section is to identify whether the enhancement of thin film mechanical performance is solely contributed by the polymeric matrix or by the interaction between individual nanotubes within the polymer matrix to resist crack-tip opening and fracture. Thus, preliminary experimental fracture studies are conducted to determine the fracture toughness of the proposed carbon nanotube composites. In addition, scanning electron microscopy is employed in attempts to identify SWNT bridging near crack tip openings.

3.3.1. Determining Thin Film Fracture Toughness

When considering experimental determination of fracture toughness of homogeneous isotropic materials, it is important to determine whether materials undergo plane strain or plane stress. Given a bulk material subjected to uniaxial tensile loading, a large localized stress region develops near the vicinity of a crack tip. At this localized stress region, a plastic zone is created and the material near the crack tip is at its yield stress. At such high localized stresses and strains, the inherent material response is to contract laterally due to Poisson's effect. However, such contractions are prevented if a thick material is being tested, and the material is categorized as undergoing plane strain. On the other hand, in the case of thin film materials, the size of the developed plastic zone is often comparable to the specimen thickness; consequently, the film is free to contract to relieve stresses (*i.e.*, to create zero stress in the direction of the thickness of the film); as a result, the thin film is assumed to undergo plane stress [105, 106].

In general, the stress intensity factor (K_I) describes the resistance of any bulk material to resist crack propagation. Crack propagation occurs when the stress intensity factor is equal to the material's fracture toughness (K), where this is referred to as the fracture criterion and is given in Equation 3-1 [105]:

$$K = K_{Ic} \tag{3-1}$$

When the fracture criterion is satisfied, the material reaches its critical stress intensity factor where $K_I = K_{Ic}$. However, three different critical stress intensity factors are available to describe the fracture toughness of bulk materials as shown in Equation 3-2:

$$K_{Ii} = f(a/W)\sigma_i\sqrt{a_0} \tag{3-2a}$$

$$K_{Ie} = f(a/W)\sigma_f\sqrt{a_0} \tag{3-2b}$$

$$K_{If} = f(a/W)\sigma_f\sqrt{a_f} \tag{3-2c}$$

where K_{Ii} refers to the initiation fracture toughness, K_{Ie} refers to the effective fracture toughness, K_{If} is the failure fracture toughness, σ_i is the stress at the initiation of crack propagation, σ_f is the stress at fracture instability (when the rate of crack propagation significantly increases), a_0 is the initial crack length, a_f is the crack length at fracture instability, f(a/W) is a geometric correction factor, and W is the film width [106]. The differences between initiation, effective, and failure fracture toughness are pictured in Figure 3-6.

While the failure fracture toughness (K_{If}) is the most common value employed to characterize materials, the initiation and effective fracture toughness values are also used for various engineering applications. For example, when crack growth cannot be tolerated, the initiation fracture toughness (K_{Ii}) is used as the design parameter. In the case of brittle materials and materials governed by sudden catastrophic fracture failure, all three stress intensity factors shown in Equation 3-2 are approximately the same [106]. However, it has already been shown in Figures 3-3 and 3-4 that significant yielding and strain hardening can occur; thus, the most conservative measure of fracture toughness (*i.e.*, the lowest value of fracture toughness) is obtained by considering the initiation fracture toughness (Equation 3-2a).

3.3.2. Fracture Testing Experimental Details

Here, the fracture toughness and critical stress intensity factor of (SWNT-PSS/PVA)$_{200}$ nanocomposites are determined by employing a similar experimental

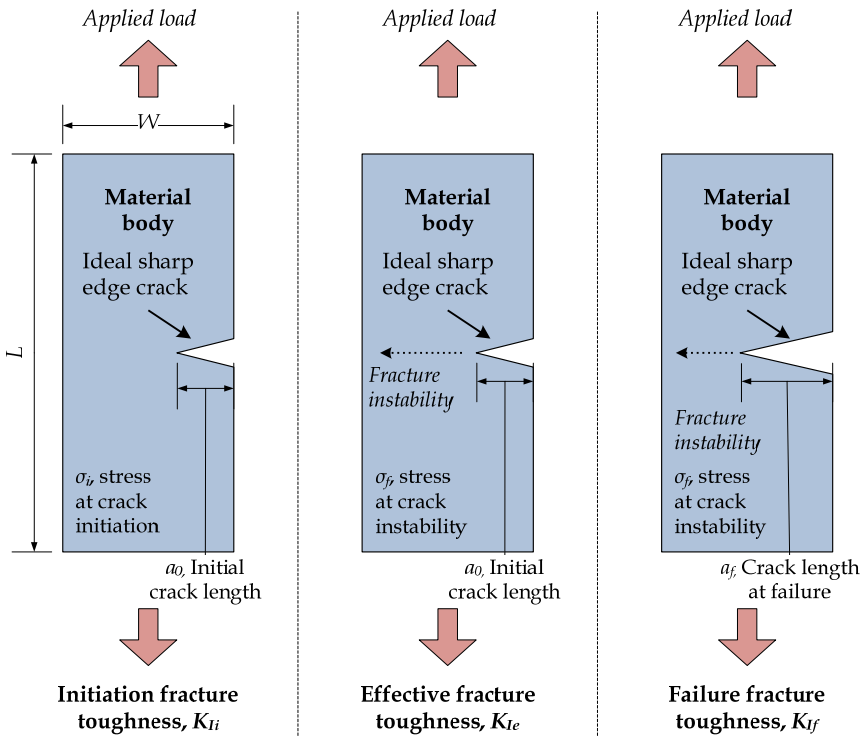

Figure 3-6. A schematic illustrating the differences between initiation, effective, and failure fracture toughness.

procedure described in Section 3.2. In this case, thermally annealed LbL-based nanocomposites are cut into approximately 25 x 4 mm^2 to 25 x 6 mm^2 specimens to preserve the specimen's high aspect ratio while simultaneously producing a wide specimen width for fracture testing. Then, an initial edge crack of approximately 0.5 to 1.0 mm long (a_0) is introduced perpendicular to one side and near the midsection of each nanocomposite specimen via mechanical cutting with a razor blade (Figure 3-7). Upon specimen preparation, the edge-cracked thin film is loaded in the TestResources Q100 load frame where a uniaxial monotonic tensile load pattern at a displacement-controlled load rate of 10 μm-s^{-1} is executed. The data acquisition system is commanded to record time, applied load, and stroke displacement at 15 Hz as before. In addition to the data logger, a high-performance JVC GZ-MG255U digital video camera is employed to optically image thin films at 30 fps (frames per second) during loading to monitor crack propagation.

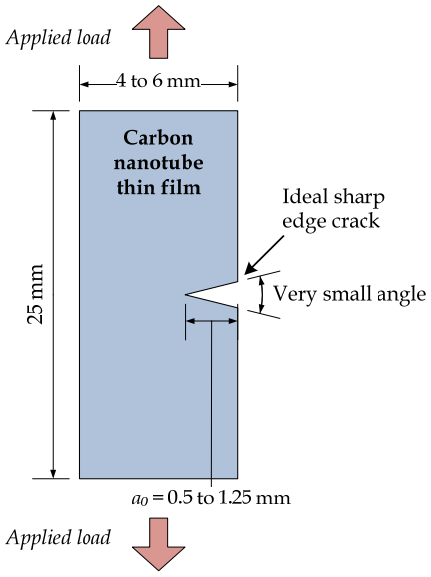

Figure 3-7. A schematic illustrating the experimental setup for determining nanocomposite fracture toughness.

3.3.3. *Determining LbL Nanocomposite Fracture Toughness*

Figure 3-8 plots the typical stress-strain responses for post-annealed (SWNT-PSS/PVA)$_{200}$ thin films fabricated with different initial SWNT concentrations and mechanically cut with an initial edge crack of length a_0 (0.5 to 1.25 mm) subjected to uniaxial monotonic tensile loading. Comparing Figure 3-8 to the previous stress-strain curves shown in Figures 3-3 and 3-4, it can be clearly seen that these edge-cut nanocomposites fail at a much lower ultimate stress and strain. Furthermore, as opposed to yielding and exhibiting strain hardening response (Figures 3-3 and 3-4), the specimens fail by sudden fracture. On the other hand, during monotonic tensile loading of edge-cracked film specimens, the high-performance JVC digital video camera has successfully captured the propagation of the crack as shown in Figure 3-9. It can be seen from Figure 3-9 that fracture indeed occurs at the location where the initial edge crack has been created; in addition, crack propagation runs through the width of the film, nearly perpendicular to the direction of the applied load.

To determine the critical stress intensity factor of layer-by-layer (SWNT-PSS/PVA)$_{200}$ nanocomposites, Equation 3-2a is employed. For the nanocomposite

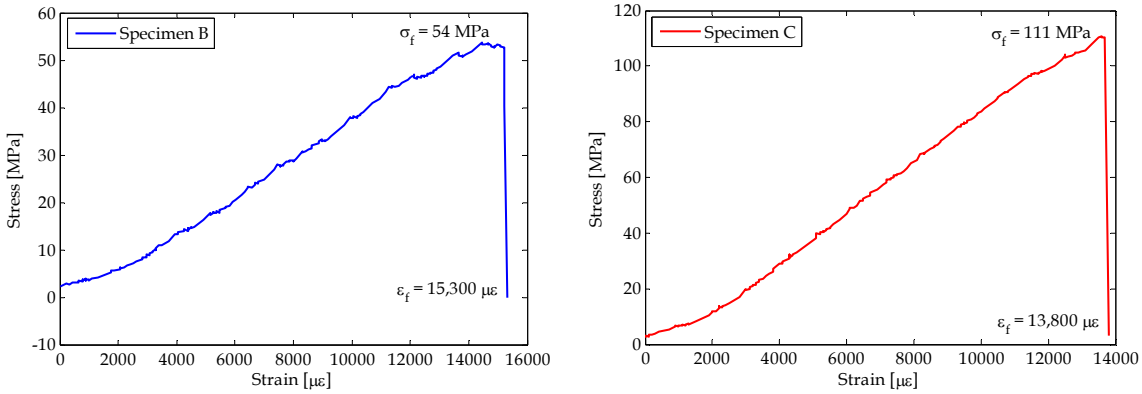

(a) (b)

Figure 3-8. Stress-strain responses of $(SWNT\text{-}PSS/PVA)_{200}$ thin films with an initial edge crack of size a_0 and fabricated with (a) 0.25 mg-mL^{-1} SWNT-PSS (Type B) and (b) 0.50 mg-mL^{-1} SWNT-PSS (Type C) concentrations.

specimens that have been fracture-tested, which are essentially finite-width plate (*i.e.*, a semi-infinite plate) materials with a pre-cut edge crack of length a_0, the geometric correction factor is given by Anderson [105] and shown in Equation 3-3:

$$f(a/W) = 1.12 \tag{3-3}$$

It should be noted that the geometric factor shown in Equation 3-3 is determined by considering the boundary conditions (*i.e.*, geometrical aspects) of the experimental setup. The geometric correction factor accounts for the edge crack opening wider than a sharp crack located within a material's body when subjected to uniaxial loading. Thus, using the geometric correction factor given in Equation 3-3, the mode-I initiation stress intensity factor is expressed in Equation 3-4 as [105]:

$$K_{Ii} = 1.12\,\sigma_i\sqrt{a_0} \tag{3-4}$$

It should be noted that only the mode-I stress intensity factor is considered in this study (where mode-I is for crack opening, mode-II is for in-plane shear, and mode-III is for out-of-plane shear) [105]. Since the nanocomposites are subjected to uniaxial monotonic tensile loading, and that the films are carefully mounted and aligned to the direction of

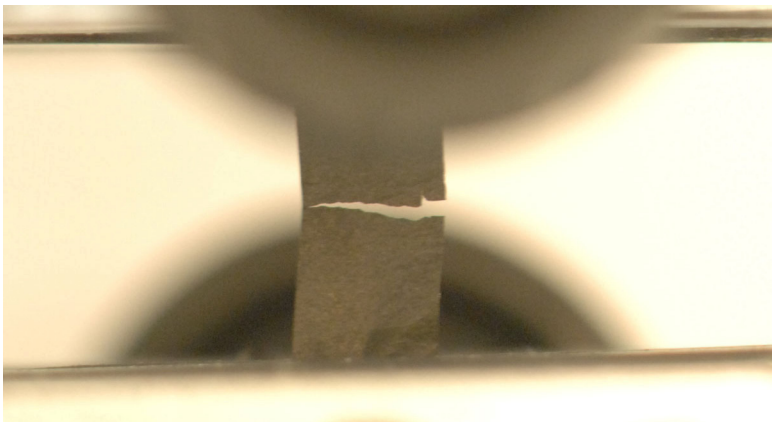

Figure 3-9. A picture of a Type C $(SWNT\text{-}PSS/PVA)_{200}$ nanocomposite fracturing under applied monotonic tensile loading.

applied load, it can be assumed that contributions from mode-II and mode-III are negligible.

For the layer-by-layer nanocomposites investigated in this study (Table 3-1), the average mode-I initiation fracture toughness is approximately 0.52, 1.55 ± 0.20, and 2.51 ± 0.12 MPa-√m for thin film Types A, B, and C (Table 3-1), respectively. It should be mentioned that the use of linear elastic fracture mechanics is valid due to the low mode-I initiation fracture toughness measured [105]. Nevertheless, Figure 3-10 plots the average mode-I initiation fracture toughness as a function of initial SWNT solution concentration, where it is obvious that fracture toughness increases near-linearly with increasing carbon nanotube content. The increase in fracture toughness with nanotube content suggests that CNTs provide enhancements to strength, stiffness, and toughness.

While previous fracture studies concluded that fracture toughness increases with nanotube content, these experimental results cannot conclusively identify nanotubes as the primary source for enhancing the nanocomposite's resistance to brittle fracture failure. In fact, fracture toughness is a local property that accounts for the behavior of a material's crack-tip under applied stress and strain [105]. However, quantification of global bulk material response to fracture necessitates calculation of the mode-I critical energy release rate (G_{Ic}). In short, the energy release rate (G) is defined by Irwin [107] as the energy available for propagating or opening a crack. Given that the nanocomposites tested are relatively thin compared to their widths and lengths, their Poisson's ratio is

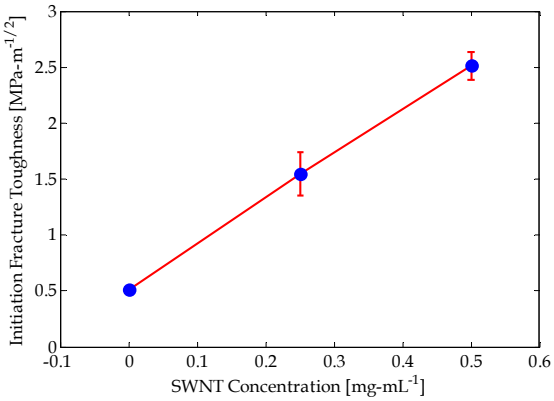

Figure 3-10. Thin film fracture toughness increases with increasing SWNT content within the nanocomposite.

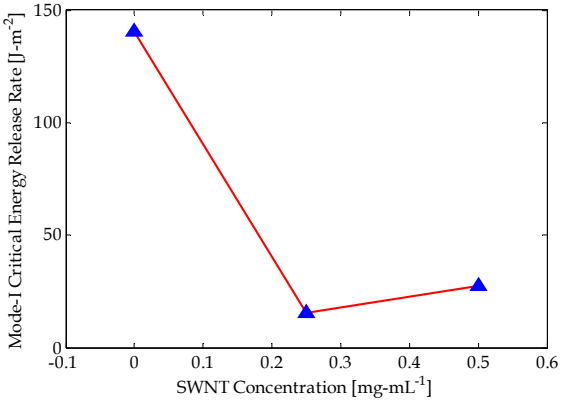

Figure 3-11. Energy release rate decreases with increasing SWNT content suggests that nanocomposites are actually more prone to sudden brittle fracture.

assumed to be $\nu = 0$ based on plane stress conditions, and G_{Ic} is determined via Equation 3-5 [105]:

$$G_{Ic} = \frac{{K_{Ic}}^2}{E} \tag{3-5}$$

Using Equation 3-5, the critical mode-I energy release rate is determined to be 141, 15.2, and 27.5 J-m^{-2} for specimen Types A, B, and C, respectively; these results are also plotted in Figure 3-11. Unlike Figure 3-10, SWNT-reinforced nanocomposites exhibit significantly lower energy release rates than pristine PSS/PVA thin films. In fact, it can be observed from Equation 3-5 that the energy release rate takes into account the material's stiffness (E); since SWNT-reinforced nanocomposites exhibit dramatic improvements in stiffness with increasing SWNT content, the energy release rate dramatically decreases, and the bulk material is in fact more prone to sudden catastrophic brittle failure with the inclusion of nanotubes. Thus, a tradeoff exists between increasing nanocomposite's strength and stiffness versus its resistance to brittle failure.

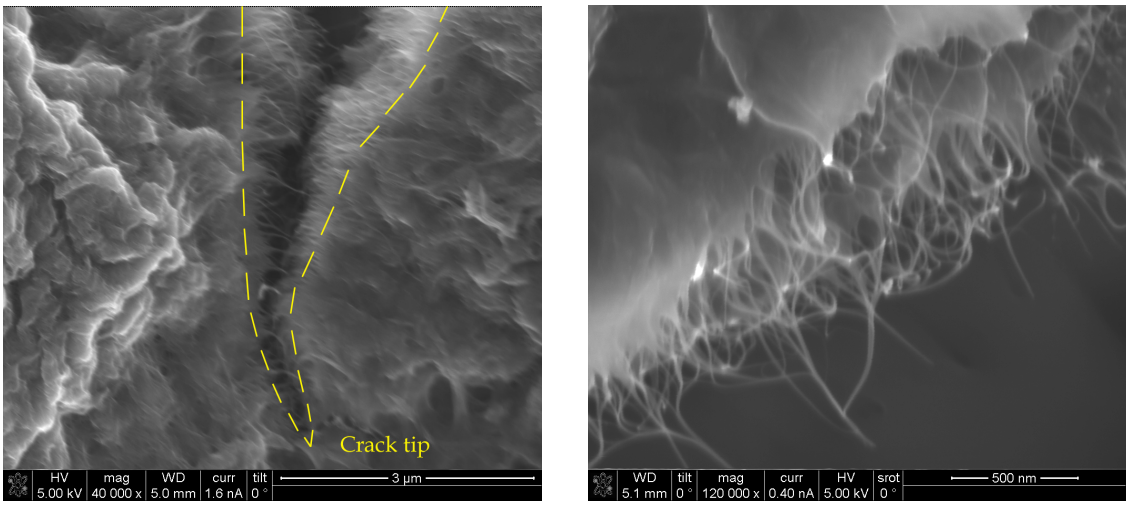

(a) (b)

Figure 3-12. (a) A scanning electron microscope image to identify crack tip nanotube bridge under at low magnification (outline of the crack tip is denoted using a solid yellow line). (b) Nanotubes are pulled-out and aligned at locations far from the sharp crack tip.

3.3.4. Crack-Tip Carbon Nanotube Bridging

While the brittleness of the bulk nanocomposite has increased with the addition of SWNTs to the polymeric matrix (Figure 3-11), fracture toughness measurements shown in Figure 3-10 suggest that nanotubes participate by resisting the opening of crack tips under applied tensile loads. Thus, it is of interest to investigate whether individual or small bundles of nanotubes actually participate to bridge sharp crack tips to provide for mechanical reinforcement. Here, experimental identification of nanotube bridging at crack tip openings are conducted using scanning electron microscopy. Upon monotonic fracture testing in Section 3.3.3, specimens that experienced crack propagation but did not fail completely are imaged using a FEI Nova Nanolab Dualbeam Focused Ion Beam scanning electron microscope.

From Figure 3-12, it can be observed from the SEM images that monotonic tensile loading induces crack propagation in the form of a sharp crack through one side of the specimen (also shown in Figure 3-9). At the crack tip, it can be clearly seen that nanotubes are straightened and aligned (Figure 3-12a), where near the tip of the crack, individual and small bundles of SWNTs bridge the crack to provide load transfer and

resist the crack opening. On the other hand, approximately 2 to 3 μm away from the sharp crack tip, carbon nanotube pull-out can be observed (Figure 3-12b). Similar results have been obtained by Malik, *et al.* [108] where they have identified crack bridging of individual nanotubes in cracked buckypaper specimens. The experimental results presented in Figure 3-12 suggests that SWNT-reinforced LbL nanocomposites behave similar to fiber reinforced materials where embedded fibers can resist crack opening and provide additional mechanisms for load transfer, thereby enhancing the bulk material's ductility. In addition, their results also indicate that small bundles of nanotubes can bridge crack openings up to 10 μm, suggesting that "yarn drawing" can occur to enable nanotubes to extend such distances. At crack openings larger than 10 μm, preliminary experimental results indicate that carbon nanotube pull-out is observed [108], as opposed to nanotube fracture observed by Ren, *et al.* [109].

3.4. Summary and Conclusions

3.4.1. Results and Discussion

In summary, the main objective of this chapter is to provide mechanical reinforcement (*i.e.*, in the form of strength, stiffness, and toughness) to nanocomposites by embedding single-walled carbon nanotubes within bulk polymeric matrices. Experimental monotonic tensile testing of pure PSS-PVA thin films and $(\text{SWNT-PSS/PVA})_{200}$ thin films fabricated with 0.25 and 0.50 mg-mL^{-1} SWNT-PSS concentrations reveal significant enhancements in the films' mechanical properties. Specifically, nanocomposites reinforced with 0.50 mg-mL^{-1} SWNTs exhibit an average stiffness, ultimate tensile strength, and ultimate failure strain of 11.2 ± 0.4 GPa, 229 ± 7 MPa, and 67,000 ± 3,900 με, respectively. Furthermore, unlike previous layer-by-layer films employed in earlier chapters of this dissertation, post-fabrication thermal annealing of the LbL-assembled nanocomposites significantly improves their ductility. Stress-strain curves obtained also demonstrate significant strain hardening after yielding.

In addition to mechanical characterization of the proposed nanocomposites, their fracture properties are investigated via tensile testing of edge-cracked specimens. It has been demonstrated that the thin films exhibit improvements in fracture toughness with increasing nanotube weight content. These results signify that increased nanotube

participation at crack tips resist the opening of cracks due to applied monotonic tension. Despite fracture toughness improvements, the bulk nanocomposite also appears to exhibit increased brittleness due to embedment of carbon nanotubes as has been revealed by energy release rate estimations. Nevertheless, having characterized the mechanical performance of SWNT-based nanocomposites to mechanical loading, one can leverage the advantages of enhancing strength and stiffness with the material's inherent brittleness simply by controlling nanotube composition within the bulk polymeric matrix.

3.4.2. Contributions

Based on material characterization results presented in this chapter, one can begin to tailor the mechanical properties (*i.e.*, stiffness, ultimate strength, ultimate strain, and fracture toughness) of nanocomposites simply by controlling carbon nanotube weight content. As opposed to simply tailoring materials via modification of nanocomposite compositions, this chapter has also identified the importance of post-fabrication techniques such as polymer cross-linking via thermal annealing to further enhance material mechanical properties. Moreover, multifunctionality is enabled such that thin films can be encoded with sensing capabilities as well as to exhibit impressive mechanical properties. Furthermore, identification of nanotube bridging at crack openings can also be used to tailor the nano- and micro-mechanical properties of these composites to exhibit enhanced ductility.

From the perspective of using nanocomposites for sensing (Chapter 2), linearity and elasticity are important properties for enhancing sensor dynamic range and performance. While the embedment of nanotubes have not been verified to improve thin film linearity and elasticity, thin film stress-strain linearity is preserved during simultaneous improvements of nanocomposite mechanical performance. By controlling carbon nanotube weight content within the nanocomposite, thin films can be tailored to exhibit specific mechanical properties suitable for the application of interest. For example, the enhancement of thin film mechanical properties can potentially improve robustness of nanocomposite sensors for long-term SHM of civil infrastructures. The advantages for enhanced mechanical properties suggest that these materials be used in

complex field environments but can also be employed for mechanical reinforcement of substrate materials. For instance, these mechanically strong films are ideally suited for integration with IC and MEMS fabrication processes such that these films can withstand large thermal and chemical stresses, strains, and deflections during fabrication. Thus, as opposed to mechanically reinforcing nanocomposites, these thin films can be used to improve the mechanical performance of the structure (*e.g.*, polymeric or MEMS devices) to which it is attached to.

While findings from this chapter provide general guidelines for improving bulk nanocomposite mechanical properties, more work is needed to further understand the nano- and micro-mechanical behaviors of these materials. For example, although carbon nanotubes resist crack tip openings during tensile loading to increase material fracture toughness, further studies are required to understand the polymer-carbon nanotube interface; theoretical and numerical simulations can illuminate the governing mechanisms that take place (*e.g.*, whether polymers unravel to allow for nanotube pullout or whether nanotubes lose their PSS coatings to slide out of the bulk matrix) at crack interfaces. On the other hand, the geometric reorientation of nanotubes during pullout at crack tips, could potentially be employed for alignment of nanotubes as have been proposed by Malik, *et al.* [108]. Thus, enhanced understanding of material behavior at multiple length scales (*i.e.*, from the nanometer to tangible length scales) permits future design of ultra-strong nanocomposites suitable for civil, mechanical, and aeronautical applications.

CHAPTER 4

OPTIMIZING THE PIEZORESISTIVITY OF CARBON NANOTUBE COMPOSITES

4.1. Introduction

Although many carbon nanotube-based strain transducers have been proposed [110], few have developed a scheme to control LbL fabrication parameters to yield desired strain sensor properties ideally suited for large deformations encountered by many civil, mechanical, and aerospace structural systems. In addition, most of the preceding work presented in the literature focuses on the nano-/micro-scale strain response of SWNTs ([63, 91-93, 95, 96]). In this chapter, the primary objective is to optimize the piezoresistivity (*i.e.*, strain sensitivity) of single-walled carbon nanotube-polyelectrolyte (SWNT-PSS/PVA)$_n$ multilayer nanocomposite strain sensors. Using the aforementioned layer-by-layer thin film fabrication methodology (Section 2.2.1), fabrication parameters can be varied to produce thin films defined by different sensor properties (*e.g.*, sensitivity, film bulk conductivity, among others). Unlike buckypaper (*i.e.*, vacuum filtrated CNTs) where linear piezoresistive response is limited to $\varepsilon < \pm 1{,}400$ $\mu\varepsilon$ [95, 96], LbL thin films are capable of high strains accompanied by linear piezoresistivity up to 10,000 με as have been demonstrated in Chapter 2 [70, 77, 111]. More importantly, this chapter presents the investigation on how changes in LbL fabrication parameters can be utilized to tailor and control the aforementioned strain sensor properties including strain sensitivity (S_R).

To aid in understanding how specific LbL parameters affect the strain sensing performance of the nanocomposite, an equivalent circuit model is pursued. Electrical impedance spectroscopy (EIS) is adopted to provide electrical measurements that can be

used to model thin film behavior by an equivalent parallel RC (resistor and capacitor)-circuit model. In particular, strain-sensitive circuit parameters will be identified using EIS on thin films mechanically strained. The advantage of using impedance spectroscopy is that it identifies frequency-dependent AC (alternating current) circuit parameters typically masked under a time-domain DC-based analysis. Upon identification of the RC-circuit in the frequency domain, the same model is utilized to fit $(SWNT\text{-}PSS/PVA)_n$ thin film strain sensors in the time-domain under an applied DC current supply. To further validate the RC-circuit model, load patterns are applied to thin film samples with the measured change in conductivity compared to the model-predicted changes. The EIS-derived circuit model will also serve as a powerful model during the design of a passive wireless sensor using SWNT-based nanocomposites (Chapter 5).

This chapter concludes with the exploration of methods that can eliminate or remove the time-based drifts observed in continuous measurement of film resistance. Two approaches are considered. First, filtering circuitry can be used to eliminate the slow exponential drift when the film is used for dynamic strain measurements. Alternatively, a novel approach where $(SWNT\text{-}PSS/PVA)_n$ nanocomposites are deposited on a poly(ethylene terephthalate) (PET) substrate is considered. This unique assembly serves as a capacitor whose capacitance changes linearly with strain.

4.2. Permutation of Layer-by-Layer Fabrication Parameters

Hidden in the previous discussions (in Chapter 2) of the LbL assembly method is the existence of various fabrication variables and parameters that directly influence the strain sensing properties of $(SWNT\text{-}PSS/PVA)_n$ nanocomposites. The power of the LbL-assisted bottom up approach is the ability to *tune* specific chemical and physical properties at the molecular-scale to control desired macro-scale sensing properties. In fact, the layer-by-layer approach can be employed to design nanocomposite strain sensors with desired properties (*e.g.*, sensitivity, linearity, dynamic range, and overall film conductivity) by varying the LbL fabrication parameters. In this study, three independent LbL fabrication parameters are varied to correlate their effects toward modifying macro-scale thin film strain sensing properties.: (1) SWNT concentration

Table 4-1. Matrix of 21 unique (SWNT-PSS/PVA)$_n$ thin films fabricated.

	0.25 mg-mL^{-1} SWNT	**0.50 mg-mL^{-1} SWNT**	**0.80 mg-mL^{-1} SWNT**
(SWNT-PSS/PVA)$_{50}$	0.4 *wt.* % PSS 0.7 *wt.* % PSS 1.0 *wt.* % PSS	0.4 *wt.* % PSS 0.7 *wt.* % PSS 1.0 *wt.* % PSS	0.4 *wt.* % PSS 0.7 *wt.* % PSS 1.0 *wt.* % PSS
(SWNT-PSS/PVA)$_{100}$	0.4 *wt.* % PSS 0.7 *wt.* % PSS 1.0 *wt.* % PSS	0.4 *wt.* % PSS 0.7 *wt.* % PSS 1.0 *wt.* % PSS	0.4 *wt.* % PSS 0.7 *wt.* % PSS 1.0 *wt.* % PSS
(SWNT-PSS/PVA)$_{200}$	-	0.4 *wt.* % PSS 0.7 *wt.* % PSS 1.0 *wt.* % PSS	-

(dispersed), (2) PSS concentration, and (3) film thickness (number of bilayers), In total, 21 unique specimens are constructed from combinations of these three fabrication parameters as shown in Table 4-1.

First, the concentration of single-walled carbon nanotubes in PSS solution is varied. Specifically, three different concentrations will be investigated: 0.25 mg-mL^{-1}, 0.50 mg-mL^{-1}, and 0.80 mg-mL^{-1} (weight per PSS solution volume). Selection of these concentrations is based on experimental studies to provide for adequate dispersion of carbon nanotubes in PSS solutions [112]. Increasing SWNT concentration results in a corresponding increase of SWNT deposition per LbL monolayer. The increase in carbon nanotube deposition creates more nanotube-to-nanotube junctions, thus providing a greater number of paths for electrical current to flow from one electrode to the other while reducing the overall resistivity of the thin film [113]. Furthermore, since SWNTs experience rigid-body motion in the flexible polymer matrix under applied strain (as opposed to deforming axially), more nanotube junctions can participate to enhance the strain sensitivity of the nanocomposite. With increasing nanotube junctions, it is hypothesized that the sensitivity of the thin film to applied strain will increase while the overall bulk film conductivity will increase.

While different polymers can facilitate suspension of carbon nanotubes for LbL fabrication, this study will focus on varying concentrations of PSS [112]. It has been determined that the concentration of PSS in solution has a direct effect on the quality of carbon nanotube dispersion. To quantify this phenomenon, ten solutions of SWNTs

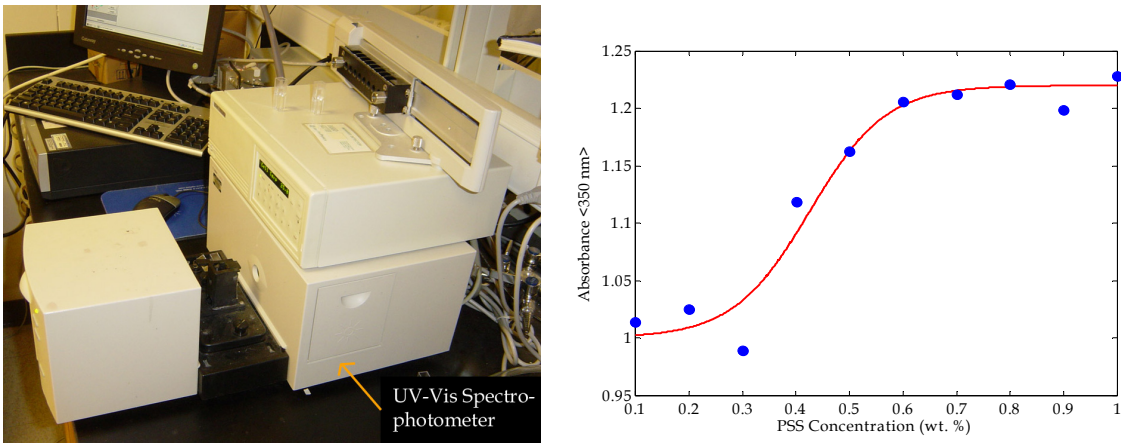

(a) (b)

Figure 4-1. (a) A picture of the UV-Vis spectrophotometer employed for determining the (b) relative absorption of 350-nm wavelength light for varying SWNT dispersed in increasing concentrations of PSS solution.

dispersed in increasing concentrations of PSS (0.1–1.0 *wt.* %) are prepared. Using a UV-Vis (ultraviolet-visible) spectrophotometer (Figure 4-1a) with 10-mm light path cuvettes, absorption spectroscopy is employed to measure the amount of light (wavelength between 300–900 nm) absorbed by the different SWNT-PSS solutions prepared using an identical processing methodology (Section 2.2.2 and [114]). In short, UV-Vis spectroscopy quantifies the interaction of photons (in the ultraviolet (200 – 400 nm) and visible wavelengths (400 – 800 nm)) with SWNTs and PSS. The spectrophotometer measures light transmittance (*i.e.*, the inverse of absorbance) to determine how different molecules interact with photons. It has been demonstrated that greater nanotube suspension is directly associated with an increase in the UV-Vis absorbance resonance peaks as well as the non-resonant background, thereby suggesting no preferential dispersion of any particular nanotube [76]. Figure 4-1b plots the absorbance at λ = 350 nm as a function of various concentrations of PSS. The results suggest that a sigmoidal relationship between absorbance and PSS concentration exists and greater nanotube suspension can be achieved by dispersing fixed amounts of SWNTs in higher concentrations of PSS (where 0.7 to 1.0 *wt.* % PSS marks a significant increase in absorbance). To investigate the effects of dispersion quality on the piezoresistivity of $(\text{SWNT-PSS/PVA})_n$ nanocomposites, three different concentrations of PSS, namely 0.4 *wt.* % (low dispersion), 0.7 *wt.* %

(moderate dispersion), and 1.0 *wt.* % PSS (high dispersion) have been selected for fabrication.

Another fabrication parameter of interest is the thickness of the (SWNT-PSS/PVA)$_n$ nanocomposites themselves. Precise control of thin film thickness can be achieved by controlling the number of LbL bilayers deposited. While thicker films can provide additional mechanical strength and reinforcement to the polymeric nanocomposite matrix, it is hypothesized that more layers decrease the overall strain sensitivity of the film due to potentially increased agglomeration during extensive LbL fabrication (*i.e.*, with larger number of bilayers deposited); clearly, a tradeoff exists between mechanical strength and electrical sensing properties. Thus, three different thicknesses, namely 50, 100, and 200 bilayer thin films, are fabricated to identify changes in (SWNT-PSS/PVA)$_n$ thin films' electronic properties as a function of film thickness. One objective of this optimization study is to identify which fabrication parameters contribute to yield the highest possible strain sensor sensitivity. Furthermore, using time- and frequency-domain analyses, an equivalent circuit model that adequately describes the piezoresistive behavior of the nanocomposite will be most useful for coupling LbL strain sensors with inductively coupled RFID devices (Chapter 5).

4.3. Experimental and Analytical Approach

Using techniques such as electrical impedance spectroscopy, one can characterize the frequency dependent electrical properties of materials and their interfaces [115]. The motivation for using EIS is to identify the frequency-dependent electrical behavior of (SWNT-PSS/PVA)$_n$ thin films which may be masked under a DC time-domain approach. Combined with physical observations from the DC time-domain approach (*i.e.*, identification of the time-dependent exponentially decaying film resistance), a simple and unique equivalent circuit (and its associated resistance, capacitance, and inductance) can be deduced from the frequency-domain response of a material under study. Subsequently, the derived circuit model from EIS can be used to validate the DC electrical response of loaded thin films previously obtained.

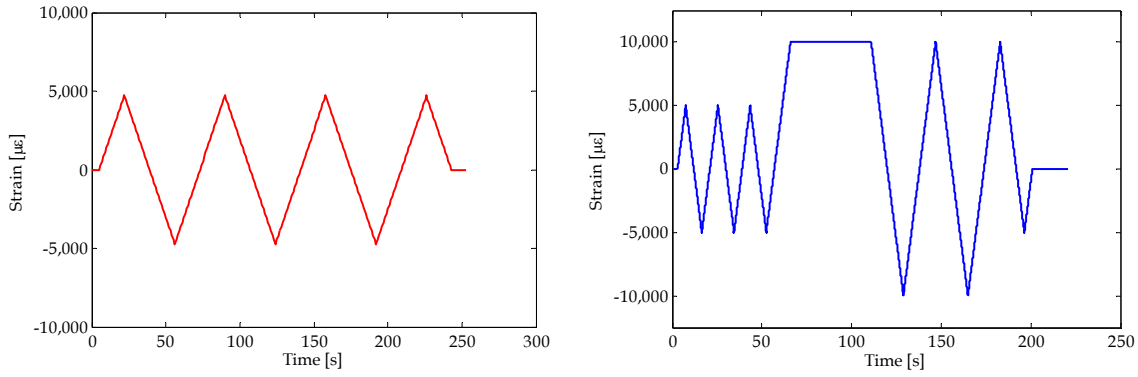

(a) (b)

Figure 4-2. (a) A three-cycle tensile-compressive load pattern to ±5,000 με (load rate 250 με-s^{-1} and 500 με-s^{-1})and (b) a three-cycle load pattern to ±5,000 με, followed by a fixed strain at 10,000 με then a final three-cycle load pattern to ±10,000 με (load rate 250 με-s^{-1} and 500 με-s^{-1}).

4.3.1. Load testing of (SWNT-PSS/PVA)$_n$ Thin Films

Prior to electrical impedance spectroscopic analysis, each nanocomposite fabricated from unique LbL compositions (as shown in Table 4-1) is tested to access its piezoresistive response to applied tensile-compressive cyclic loading. It should be noted that only p-SWNTs are considered for this study based on experimental results obtained from Chapter 2. Nanocomposite samples are cut to small rectangular elements (approximately 4 x 10 mm^2) and affixed onto PVC testing coupons via CN-Y post-yield epoxy. Upon drying of the epoxy (6 hrs), two electrodes are attached to the two ends of the thin film using single-strand wire and colloidal silver paste to form a two-point probe electrical resistance measurement setup (Figure 2-10). Then, similar to Section 2.5.3, the MTS-810 load frame is employed to execute two different load patterns to each unique nanocomposite, namely: (1) a three-cycle time history to ±5,000 με (Figure 4-2a) and (2) a three-cycle time history to ±5,000 με, followed by a 60 s fixed strain of 10,000 με and a three-cycle time history to ±10,000 με (Figure 4-2b). In addition, for the two aforementioned load patterns, the load rate is varied between 250 με-s^{-1} and 500 με-s^{-1}. Furthermore, in order to obtain accurate measurements of applied strain, a 120 Ω metal-foil strain gauge is also affixed onto the opposite side of the PVC coupon.

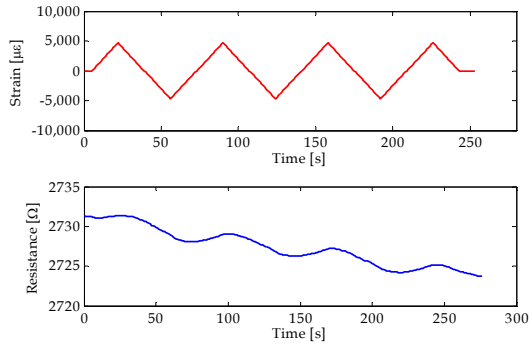

Figure 4-3. (Top) Three-cycle strain time history applied to a (SWNT-PSS/PVA)$_{100}$ thin film (0.4 *wt.* % PSS); (bottom) measured resistance during uniaxial loading (500 με-s^{-1}).

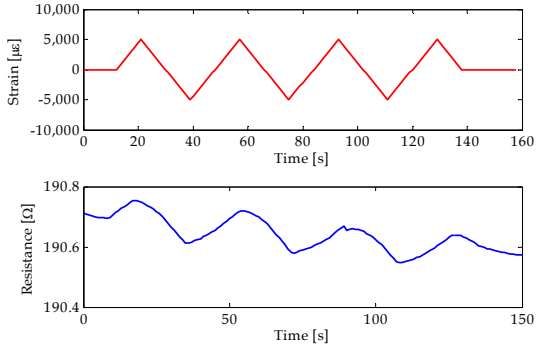

Figure 4-4. (Top) Three-cycle strain time history applied to a (SWNT-PSS/PVA)$_{100}$ thin film (0.4 *wt.* % PSS); (bottom) measured resistance during uniaxial loading (500 με-s^{-1}).

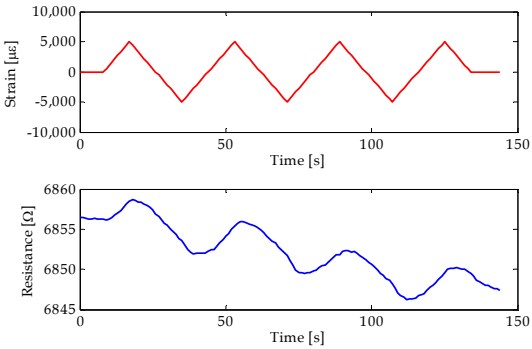

Figure 4-5. (Top) Three-cycle strain time history applied to a (SWNT-PSS/PVA)$_{50}$ thin film (0.4 *wt.* % PSS); (bottom) measured resistance during uniaxial loading (250 με-s^{-1}).

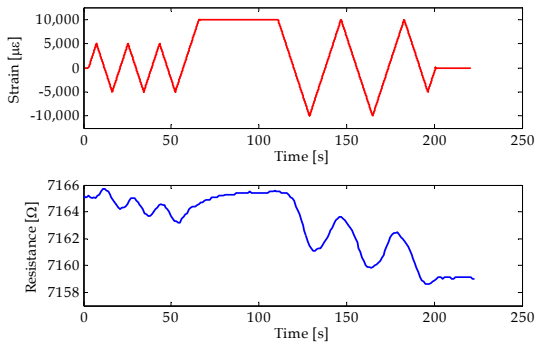

Figure 4-6. (Top) Load pattern corresponding to Figure 4-2b applied to a (SWNT-PSS/PVA)$_{100}$ thin film (0.7 *wt.* % PSS); (bottom) measured resistance during uniaxial loading (500 με-s^{-1}).

Representative time histories of nanocomposite piezoresistive response to different applied load patterns are shown in Figures 4-3 to 4-6. As expected, these carbon nanotube-based thin films exhibit dramatic changes in film resistance in tandem with applied strain. It can be seen from Figures 4-3 to 4-6 that nanocomposites manufactured from different LbL fabrication parameters exhibit vastly different "nominal" resistances (*e.g.*, 190.7 Ω for the specimen tested in Figure 4-4 and 7,165 Ω for Figure 4-6). However, as evident from these resistance time histories, it is extremely difficult to objectively compare thin film electrical properties due to different effects

taking place simultaneously (*e.g.*, piezoresistive response and simultaneous time-variant exponential decay in resistance). Thus, a frequency domain-based approach such as EIS is ideally suited for in-depth analyses of the inherent nanocomposite electrical properties.

4.3.2. Electrical Impedance Spectroscopy

In electrical impedance spectroscopy (EIS), impedance measurements are taken by applying a monochromatic AC electrical stimulus (*i.e.*, an AC signal at a particular frequency, $f = \omega/2\pi$) of known voltage ($v(t) = V_{in}sin(\omega t)$) and frequency while simultaneously measuring the corresponding steady-state current response of the system ($i(t) = I_{out}sin(\omega t+\theta)$, where θ is the phase difference between the voltage and current). While a time-domain analysis can extract material behavior due to an AC stimulus, the relationship between input stimulus and output response is inherently complex and requires differential equations to explain. On the other hand, impedance measurements (by definition a complex quantity denoted as $Z(\omega) = Z' + jZ''$), take the phase difference and attenuation between input and output into account. In rectangular coordinates, the real and imaginary components of complex impedance, $Z(\omega)$, can be expressed as Equation 4-1:

$$Re(Z) \equiv Z' = \|Z\|cos(\theta) \tag{4-1a}$$

$$Im(Z) \equiv Z'' = \|Z\|\sin(\theta) \tag{4-1b}$$

Typically, an automated frequency response analyzer (FRA) can be employed to perform impedance spectroscopy. Its operating principle is simple; a sine-wave perturbation ($P(t) = P_0sin(\omega t)$) is applied to the material, and its corresponding electrical response is correlated to two synchronous signals, where one signal is in-phase while the other is 90^o out-of-phase with the input signal. For a given frequency, ω, the complex impedance can be extracted by integrating the input-output transfer function and response over a certain number of periods (N_f) of the input sinusoidal perturbation [115]. An attractive feature of most FRAs is their ability to sweep through a set of frequencies when measuring impedance. A more in-depth discussion of electrical impedance spectroscopy can be found in Barsoukov and Macdonald [115].

The Solartron 1260 impedance gain/phase analyzer is selected to serve as an FRA for electrical characterization of (SWNT-PSS/PVA)$_n$ thin films. To measure the complex impedance of the films, the Solartron 1260 uses a four-point probe technique and outputs an AC sine-wave perturbation with amplitude of 3.0 V. The input stimuli frequency (ω) is varied between 15 – 250 kHz to capture the specimen's frequency-domain response. Upon subjecting the 21 fabricated films (Table 4-1) to EIS, all (SWNT-PSS/PVA)$_n$ multilayer nanocomposites yield a typical semicircular response in the complex impedance plane (commonly termed the Cole-Cole plot) which is consistent with the complex impedance response of a parallel RC-circuit (as opposed to being purely resistive or capacitive); an example Cole-Cole plot of a (SWNT-PSS/PVA)$_{50}$ thin film is shown in Figure 4-7.

4.3.3. Equivalent Circuit Modeling

In order to determine a unique equivalent circuit model that describes the electromechanical behavior of (SWNT-PSS/PVA)$_n$ multilayer films in both the frequency- and time-domain, a stochastic simulated annealing model-updating algorithm is employed to numerically fit different parallel RC-circuit models to the experimental Cole-Cole plots [116]. The objective function embedded in the simulated annealing model-updating method seeks to minimize the sum of the least-squares difference between numerical (derived from an equivalent circuit model) and experimental (from EIS) complex impedance data. From simulated annealing fitting of multiple variations of parallel RC-circuit models, the simplest equivalent circuit model is selected to describe the behavior of the (SWNT-PSS/PVA)$_n$ thin films. The proposed equivalent circuit model is shown in Figure 4-8, and a representative model-updated Cole-Cole plot fit is overlaid with the experimental plot presented in Figure 4-7. The equivalent circuit model identifies three discrete circuit elements: a series resistor (R_o), a parallel resistor (R_i), and a parallel capacitor (C_i).

It has been shown that the bulk (SWNT-PSS/PVA)$_n$ thin film resistance changes upon applied strain (Figures 2-13 through 2-15 and Figures 4-2 through 4-5) while also exhibiting a time-dependent exponential decay in film resistance (Figure 2-7a). Accurate incorporation of these DC time-domain observations into the EIS-derived equivalent

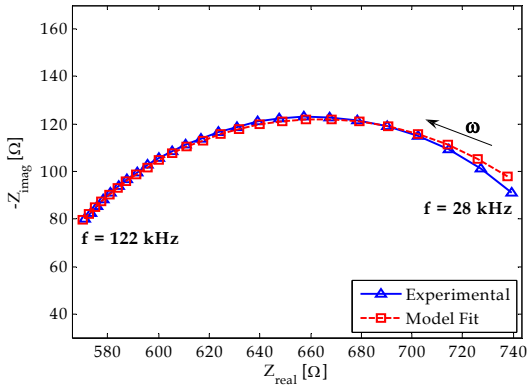

Figure 4-7. EIS experimental data (0.8 mg-mL^{-1} SWNT in 1.0 *wt.* % PSS and 1.0 *wt.* % PVA, 50 bilayers) plotted in the complex plane. Also shown is the EIS response predicted by an equivalent circuit model fitted to the experimental data.

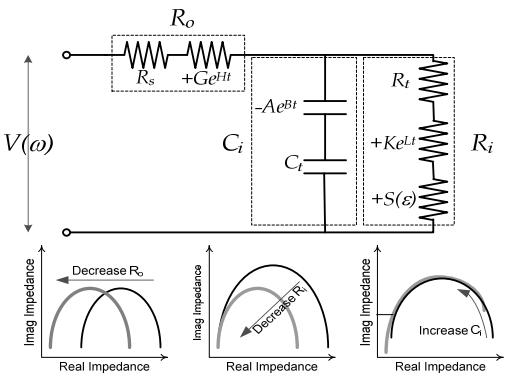

Figure 4-8. (Top) Proposed RC-circuit model form; (bottom) changes in Cole-Cole plot responses due to variations in equivalent circuit element parameters.

circuit model is accomplished by observing how changes in equivalent circuit element parameters change the overall complex impedance response in the frequency domain. Figure 4-8 shows a schematic as to how these changes (namely R_o, R_i, and C_i) lead to changes in the (SWNT-PSS/PVA)$_n$ film's frequency response.

First, in order to identify the equivalent resistor sensitive to the exponential decay effect, multiple EIS analyses are performed one after another on the unloaded (SWNT-PSS/PVA)$_n$ specimens; each sequential EIS analysis is performed a constant time (t_i) after the previous analysis. The resulting frequency response shows that as time increases, each corresponding Cole-Cole plot shifts towards decreasing real impedance (Figure 4-9). This shift also appears to slow down over time which is consistent with the exponential decay in resistance due to resistive heating of the thin film encountered in Chapter 2. By capturing the resistance change due to resistive heating, circuit elements in the equivalent circuit model sensitive to this drift can be determined. Based on the EIS plots, R_0 and R_i are identified as responsible for modeling the DC exponential decay in film resistance. Furthermore, the equivalent capacitor C_i is also modeled to exhibit some exponential decay during impedance spectroscopic analysis and can be modeled as $C_i = C_t - Ae^{Bt}$. While the nature of change in capacitance is undetermined, it is hypothesized

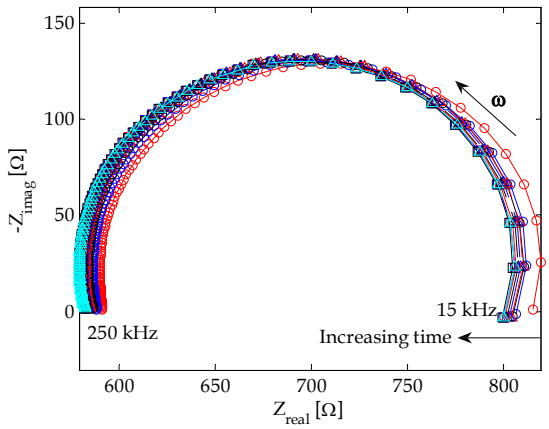

Figure 4-9. Multiple EIS analyses on an unload $(SWNT\text{-}PSS/PVA)_{50}$ thin film with increasing time.

that the applied current source (from DC resistance measurements and EIS analysis) increases the probability of electron tunneling between neighboring carbon nanotubes, thereby reducing film capacitance and resistance over time. Whereas the exponential decay in resistance (R_i) can be identified in the DC time-domain approach, changes in capacitance cannot be easily identified. The discovery of the exponentially decaying C_i illustrates the superiority of combining time- and frequency-domain analyses for the derivation of an accurate equivalent circuit model.

Secondly, identification of the strain-sensitive equivalent circuit element is conducted by applying a one-cycle tensile-compressive load pattern ($\varepsilon = \pm 5{,}000\ \mu\varepsilon$) to the thin films similar to that previously mentioned in this chapter. The load frame displacement is held at $2{,}500\ \mu\varepsilon$ intervals (0.25% strain) to capture the EIS response of the $(SWNT\text{-}PSS/PVA)_n$ thin films. A total of nine EIS analyses are taken during this one load cycle as shown in Figure 4-10. The corresponding Cole-Cole plots at each strain-state are overlaid and shown in Figure 4-11. The leftward shift of the plots is due to applied strain (*i.e.*, piezoresistance) and the exponential decay of film resistance (R_0 and R_i) caused by the applied current stimulus.

Extraction of the strain-sensitive equivalent circuit parameter is accomplished by exploring the possibility of any circuit element exhibiting strain sensitivity (*i.e.*, R_o, R_i, and C_i). Meticulous scrutiny of experimental data from the strained film confirms that the parallel resistor R_i is sensitive to strain. By calculating the time between each EIS test,

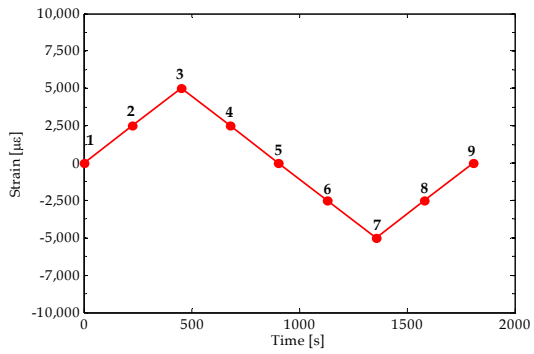

Figure 4-10. A one-cycle tensile-compressive load pattern applied to an (SWNT-PSS/PVA)$_n$ specimens for EIS analyses. Numbered points correspond to pausing of the applied load and EIS analysis.

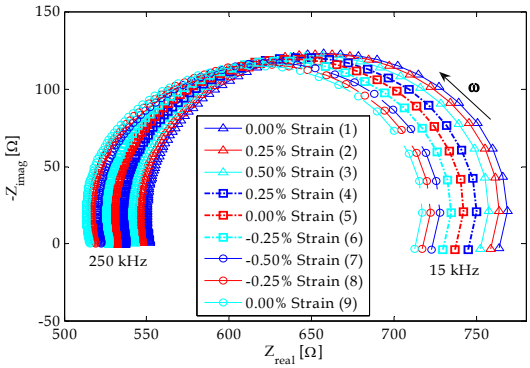

Figure 4-11. Corresponding EIS response of thin film to tensile-compressive cyclic loading (Figure 4-10) including the time-exponential decay of film resistance (Figure 4-9).

one can plot the progressive decrease of Z_{real} (Z_{real} = Z′ from Equation 4-1a) as a function of time (Figure 4-12a) with each data point corresponding to a particular strain-state experienced by the (SWNT-PSS/PVA)$_n$ nanocomposite. Upon removal of the exponential decay in Z_{real} by post-processing the experimental data, it can be shown in Figure 4-12b that (SWNT-PSS/PVA)$_n$ thin films' Z_{real} exhibit near-linear sensitivity to changes in strain. To model the piezoresistivity of R_i in the proposed equivalent circuit model (Figure 4-8), the resistive strain sensitivity (S_R) can be calculated using Equation 2-2.

In total, ten unique variables are required to accurately model the behavior of (SWNT-PSS/PVA)$_n$ thin films in both the time- and frequency-domain. These equivalent circuit parameters of Figure 4-8 are identified as: (1) the discrete circuit element values R_s, C_t, and R_t; (2) the exponential decay coefficients A and B for C_i, K and L for R_i, and G and H for R_o; and (3) S_R defined as the strain sensitivity of the (SWNT-PSS/PVA)$_n$ nanocomposite strain sensor. Using these ten parameters and the equivalent circuit model shown, the complex impedance ($Z_{eq}(\omega)$) of the equivalent circuit can be derived as:

$$Z_{eq}(\omega) = R_s + Ge^{Ht} + \frac{1}{[(R_t + Ke^{Lt})(1+S_R\varepsilon)]^{-1} + i\omega(C_t - Ae^{Bt})} \quad (4\text{-}2)$$

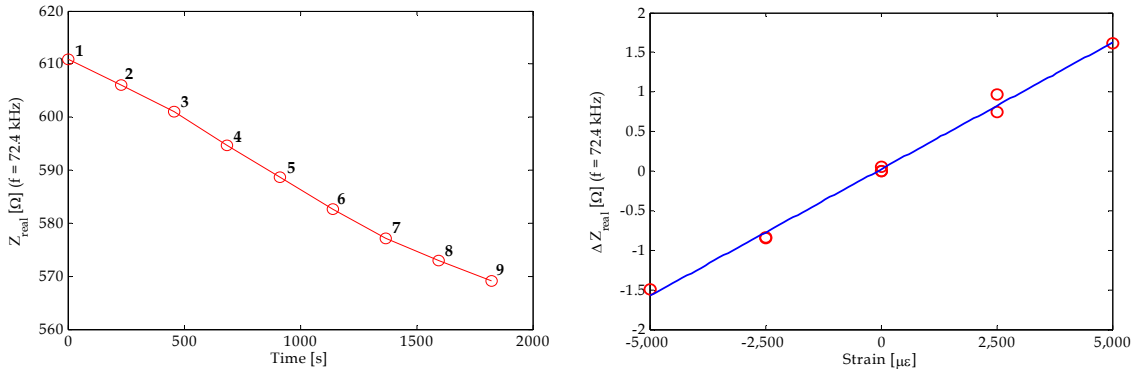

(a) (b)

Figure 4-12. (a) Impedance-real (Z_{real}) at 72.4 kHz from EIS analyses sampled over time (numbers correspond to the series of load states shown in Figure 4-10). (b) Relative change in Z_{real} as a function of applied strain after post-processing to show near-linear $(SWNT\text{-}PSS/PVA)_n$ piezoresistive response.

Equation 4-2 is then employed within a simulated annealing model-updating process where all circuit parameters are stochastically searched. The "best-fit" model parameters are those that minimize the difference between the complex impedance predicted and that experimentally derived for all the frequencies swept by the FRA during EIS analysis.

4.3.4. Frequency-Domain EIS Analysis on Unloaded Nanocomposites

Using a Solartron 1260 impedance gain/phase analyzer coupled with the same experimental setup mentioned earlier, EIS analysis is conducted for all 21 films fabricated (Table 4-1). The purpose for conducting frequency-domain analyses on unloaded $(SWNT\text{-}PSS/PVA)_n$ multilayer films is to identify the correlation between LbL fabrication parameters and equivalent circuit parameters. All EIS experimental data is fitted to the equivalent circuit model (Figure 4-8) through the simulated annealing algorithm. By calculating the equivalent complex impedance (Equation 4-2) and minimizing the sum of the least-squares difference between numerical and experimental data, simulated annealing converges to output values for the ten unique equivalent circuit parameters (R_s, R_t, C_t, A, B, G, H, K, L, and S_R).

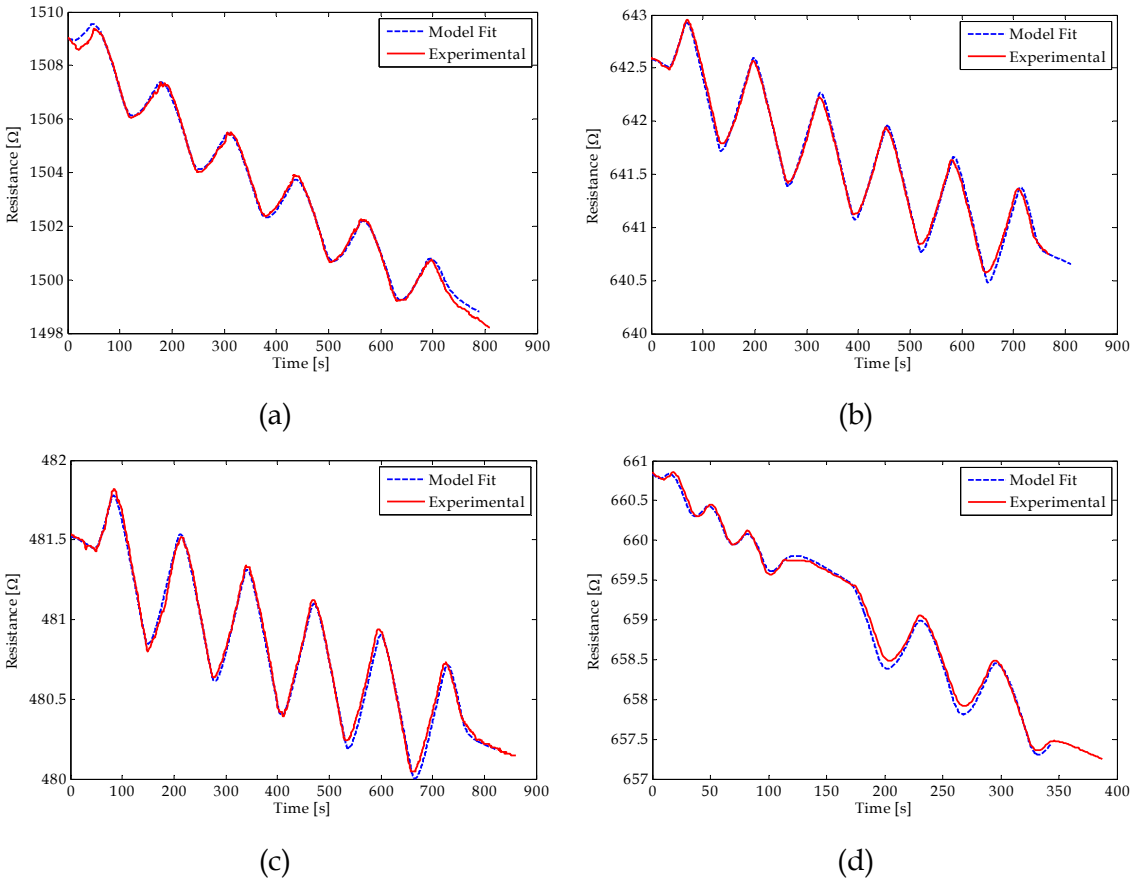

Figure 4-13. (a) Overlay of RC-parallel circuit model fit and experimental data for 0.50 mg-mL^{-1} SWNT in 0.4 *wt.* % PSS 100-bilayer thin film, (b) 0.80 mg-mL^{-1} SWNT in 0.4 *wt.* % PSS 50-bilayer thin film , and (c) 0.80 mg-mL^{-1} SWNT in 0.4 *wt.* % PSS 100-bilayer thin film under 250 με-s^{-1} cyclic loading. (d) Overlay of RC-parallel circuit model fit and experimental data for (SWNT-PSS/PVA)$_{100}$ thin film under nonuniform loading to ±*10,000 με*.

4.3.5. *Validation of Equivalent Circuit Model in the Time-Domain*

The model updating procedure yields an equivalent circuit model of the (SWNT-PSS/PVA)$_n$ thin films in the frequency domain. To validate the model, the model is used to simulate time-domain resistance time histories to the two loading cases (Figure 4-2) loaded at the two different load rates. It should be noted that, although the load case shown in Figure 4-2a refers to a three-cycle load pattern, this load case is modified to a six-cycle load pattern (±5,000 με) to generate longer time history results suitable for validation. Some representative simulated experimental resistance time histories are overlaid with experimental data and are shown in Figure 4-13. It is apparent that the

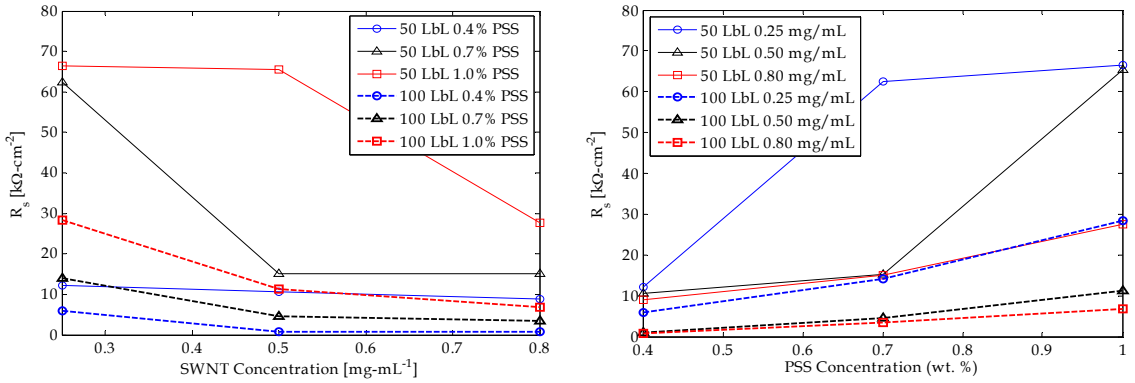

(a) (b)

Figure 4-14. (a) Series resistor R_s decreases surface resistivity as carbon nanotube concentration is increased (a similar effect is observed for R_t) while PSS concentration is fixed. (b) Plot of R_s showing increasing resistance with greater PSS concentration while SWNT concentration is fixed.

equivalent RC-circuit model derived can be used to model the resistance response of nanocomposites under applied strain and shows good agreement between numerical and experimental data. In addition, the results shown in Figure 4-13 indicate that the thin film piezoresistive response is not load rate-dependent. Thus, based on the aforementioned frequency- and time-domain based analyses, it is verified that the proposed RC-circuit model (Figure 4-8) is suitable for modeling $(SWNT\text{-}PSS/PVA)_n$ thin film electrical performance.

4.4. Variation of Thin Film Electrical Properties to Fabrication Parameters

As mentioned in Section 4.2, the layer-by-layer technique is ideally suited for tailoring nanocomposites with specific inherent electrical and sensing properties. First, the numerically-derived equivalent circuit parameters (*i.e.*, individual circuit elements) exhibit consistent trends with changes in the LbL fabrication parameters. For example, consider Rs and Rt; results from the frequency-domain model fitting are tabulated in Table 4-2 and graphically shown in Figure 4-14. Valid side-by-side comparisons between fitted circuit parameters for different films are made possible by normalizing film resistance with its surface area (*i.e.*, surface resistivity, R_{fitted} = [Ω-cm^{-2}]). This normalization is necessary since films might be mechanically cut to slightly different

Table 4-2. (a) Model-updated equivalent circuit model fitted R_s values [Ω-cm^{-2}].

0.4 *wt.* % PSS	**0.25 mg-mL^{-1} SWNT**	**0.50 mg-mL^{-1} SWNT**	**0.80 mg-mL^{-1} SWNT**
50 bilayers	12,107.0	10,557.6	8,920.7
100 bilayers	5,921.8	891.9	854.0
0.7 *wt.* % PSS	**0.25 mg-mL^{-1} SWNT**	**0.50 mg-mL^{-1} SWNT**	**0.80 mg-mL^{-1} SWNT**
50 bilayers	62,472.2	15,183.6	15,063.5
100 bilayers	14,083.8	4,589.7	3,370.2
1.0 *wt.* % PSS	**0.25 mg-mL^{-1} SWNT**	**0.50 mg-mL^{-1} SWNT**	**0.80 mg-mL^{-1} SWNT**
50 bilayers	66,489.0	65,470.7	27,595.8
100 bilayers	28,412.9	11,241.2	6,889.9

(b) Model-updated equivalent circuit model fitted R_t values [Ω-cm^{-2}].

0.4 *wt.* % PSS	**0.25 mg-mL^{-1} SWNT**	**0.50 mg-mL^{-1} SWNT**	**0.80 mg-mL^{-1} SWNT**
50 bilayers	5,303.9	5,084.4	4,850.6
100 bilayers	2,661.7	422.6	380.9
0.7 *wt.* % PSS	**0.25 mg-mL^{-1} SWNT**	**0.50 mg-mL^{-1} SWNT**	**0.80 mg-mL^{-1} SWNT**
50 bilayers	28,043.4	7,334.8	6,929.9
100 bilayers	7,580.5	2,022.6	1,519.1
1.0 *wt.* % PSS	**0.25 mg-mL^{-1} SWNT**	**0.50 mg-mL^{-1} SWNT**	**0.80 mg-mL^{-1} SWNT**
50 bilayers	17,340.3	36,369.7	12,941.4
100 bilayers	15,640.9	5,572.4	3,331.2

sizes (*i.e.*, surface areas). In general, the results show that the model-fitted values for R_s and R_t follow well-defined trends. First, as carbon nanotube concentration is increased from 0.25 mg-mL^{-1} to 0.80 mg-mL^{-1}, a progressive decrease in R_s and R_t is observed due to increased nanotube-to-nanotube junctions corresponding to greater carbon nanotube concentration (in solution) (Figure 4-14a). Also, increasing PSS concentrations causes increasing equivalent resistances potentially due to greater and more efficient polyelectrolyte adsorption during LbL (Figure 4-14b). Despite higher PSS concentrations corresponding to better nanotube suspension in aqueous solutions, the competition between PSS and nanotube adsorption favors that of PSS to increase bulk film surface

resistivity. Finally, with increasing film thicknesses, resistance decreases; this phenomenon can be explained by assuming each bilayer as a parallel resistor, where every additional resistor to the parallel network causes an overall decrease in resistance. Using this insight derived from EIS analysis on unloaded $(SWNT\text{-}PSS/PVA)_n$ nanocomposites, one can begin to tailor thin films with specific impedance and frequency-dependent properties simply by varying LbL fabrication parameters.

Of greatest interest is the dependency of LbL fabrication parameters to changes in $(SWNT\text{-}PSS/PVA)_n$ nanocomposite strain sensitivity (S_R, given in Equation 2-5). As one of the ten unknown variables during model fitting, S_R can be extracted and compared for all 21 films fabricated with a different combination of LbL fabrication parameters (Table 4-1). Among the various thin films load-tested, strong trends can be identified between strain sensitivity (S_R) and the LbL fabrication parameters (namely SWNT concentration, PSS concentration, and the thin film thickness) (Table 4-3).

First, as SWNT concentration is increased from 0.25 to 0.80 mg-mL^{-1}, the strain sensitivity of the thin film increases irrespective of the number of layers and PSS concentration; this can be observed by considering each row of Table 4-3 and Figure 4-15. Stadermann, *et al.* [113] show that as carbon nanotube content is increased, local conductance of the thin film relies heavily on the number of nanotube-to-nanotube junctions. The increased nanotube junctions present in thin films manufactured with higher SWNT concentrations allow for higher strain sensitivity as the films are stretched or compressed axially. Not only does thin film nominal resistance decrease due to greater nanotube deposition during LbL assembly to give rise to higher sensitivity (*i.e.*, larger relative change in resistance to nominal film resistance), but also, it is hypothesized that deformations due to strain will cause rigid-body motion of nanotubes in this flexible polymer composite matrix (as opposed to SWNTs deforming axially due to strain). For instance, upon applying tensile strain, individual SWNTs displace in the polymer matrix, thereby reducing the number of nanotube-to-nanotube junctions to cause an increase in resistance to give rise to the piezoresistive nature of these $(SWNT\text{-}PSS/PVA)_n$ thin films (the contrary is applicable for compressive strains). Therefore, with increasing nanotube deposition, more nanotube-to-nanotube junctions can participate during applied strain to cause changes in film resistance to increase strain

Table 4-3. Strain sensitivity (S_R) of (SWNT-PSS/PVA)$_n$ thin films fabricated with SWNT dispersed in different PSS concentrations (first number denotes strain sensitivity for a load rate of 500 με-s^{-1} and the second for a load rate of 250 με-s^{-1}).

(a)

0.4 *wt.* % PSS	**0.25 mg-mL^{-1} SWNT**	**0.50 mg-mL^{-1} SWNT**	**0.80 mg-mL^{-1} SWNT**
50 bilayers	0.573 / 0.520	0.542 / 0.521	0.653 / 0.272
100 bilayers	0.193 / 0.209	0.199 / 0.309	0.472 / 0.412
200 bilayers	-	0.172 / 0.164	-

(b)

0.7 *wt.* % PSS	**0.25 mg-mL^{-1} SWNT**	**0.50 mg-mL^{-1} SWNT**	**0.80 mg-mL^{-1} SWNT**
50 bilayers	1.016 / 1.397	1.132 / 1.404	1.805 / 1.448
100 bilayers	0.389 / 0.229	0.421 / 0.325	0.808 / 0.483
200 bilayers	-	0.299 / 0.100	-

(c)

1.0 *wt.* % PSS	**0.25 mg-mL^{-1} SWNT**	**0.50 mg-mL^{-1} SWNT**	**0.80 mg-mL^{-1} SWNT**
50 bilayers	1.220 / 1.464	1.293 / 1.531	1.516 / 1.565
100 bilayers	0.915 / 1.066	1.022 / 1.254	1.161 / 1.266
200 bilayers	-	0.813 / 1.250	-

sensitivity. This trend exists for films fabricated with different thicknesses and PSS concentrations and is consistent between the two different applied load rates of 250 and 500 με-s^{-1} (Figure 4-15).

Furthermore, (SWNT-PSS/PVA)$_n$ nanocomposites exhibit increasing strain sensitivity as the PSS dispersing agent concentration (*wt.* %) is increased. From the UV-Vis plot of absorbance as a function of PSS concentration (Figure 4-1b), it has been shown that suspension of carbon nanotubes is facilitated with higher PSS concentrations. Due to the weak electrostatic and van der Waals force attraction between each additional monolayer, large nanotube bundles cannot be deposited during the LbL fabrication

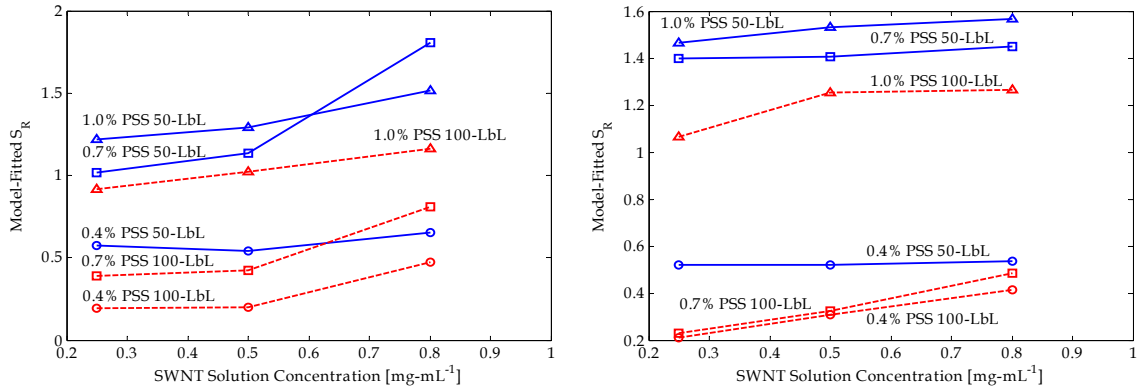

Figure 4-15. Strain sensitivity (S_R) for different (SWNT-PSS/PVA)$_n$ thin film strain sensors as a function of dispersed SWNT solution concentration for the (a) 500 με-s^{-1} and (b) 250 με-s^{-1} load rates.

process. Thus, greater dispersion of nanotubes in higher PSS concentration solutions allow for more individually suspended or small bundles of nanotubes to adsorb onto the thin film while creating more nanotube-to-nanotube junctions to achieve higher strain sensitivity. From each column of Table 4-3 and Figure 4-16, an interesting phenomenon can be observed; 50-bilayer thin films' strain sensitivities are plateauing as the dispersing agent's (PSS) concentration is increased from 0.4 to 1.0 *wt.* %. On the contrary, 100- and 200-bilayer thin films exhibit remarkable increases in strain sensitivity as PSS concentration is increased. While strain sensitivity for these films may eventually plateau, further increasing PSS concentration can potentially achieve even higher sensitivities while simultaneously increasing the mechanical properties of the proposed nanocomposites. It should be noted that a more detailed analysis with additional specimens needs to be conducted to provide greater resolution of trends in Figure 4-16.

Finally, as film thickness is increased, the strain sensitivity for films of the same PSS and SWNT concentration progressively decreases. Yet, experiments conducted with free-standing LbL films suggest an increase in mechanical strength and ultimate strength with increasing film thickness. Clearly, a tradeoff exists between optimizing (SWNT-PSS/PVA)$_n$ thin films for higher sensitivity at the cost of lower ultimate strength or vice versa. Nevertheless, the ability to tailor both the electrical and mechanical properties is advantageous for the development of novel multifunctional nanocomposites suitable for structural health monitoring in complex field environments.

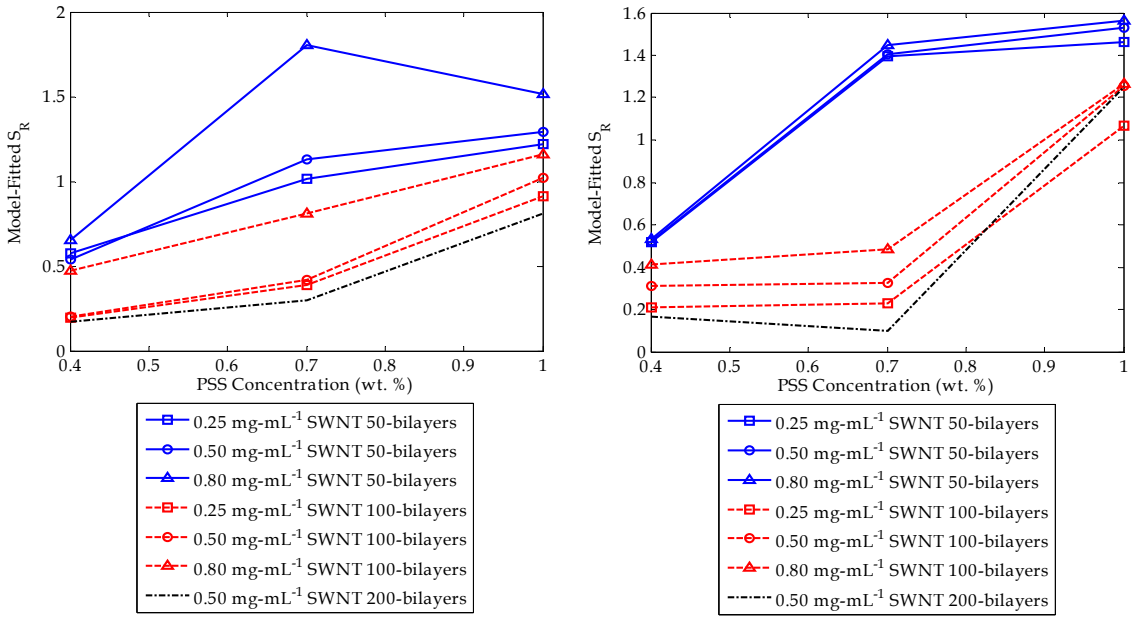

Figure 4-16. (a) Strain sensitivity for different (SWNT-PSS/PVA)$_n$ thin films as a function of PSS concentration (*wt.* %) (500 με-s^{-1} load rate) and (b) 250 με-s^{-1} load rate.

4.5. Drift-Free Dynamic Strain Measurements

4.5.1. Pass-Band Circuit Connection

The inherent time-dependent resistance decay (as observed in both the time- and frequency-domains) appears to be a limitation of the (SWNT-PSS/PVA)$_n$ nanocomposite strain sensor. However, the resistance decay rate is relatively slow, such that a band-pass circuit can be used to remove the undesirable decay. For this purpose, a low-pass (4-pole Bessel) and high-pass filter are combined upon a single signal conditioning circuit board to offer a pass-band between 0.014 and 25 Hz (Figure 4-17a) [117]. Validation of this experimental setup is conducted by applying another 20-cycle tensile-compressive cyclic load pattern to strain (SWNT-PSS/PVA)$_n$ thin films using the band-pass circuit. Before using the band-pass filter, the thin film is included within a traditional Wheatstone Bridge circuit to convert resistance changes (due to strain) into voltage variations. A representative portion of the time history is presented in Figure 4-

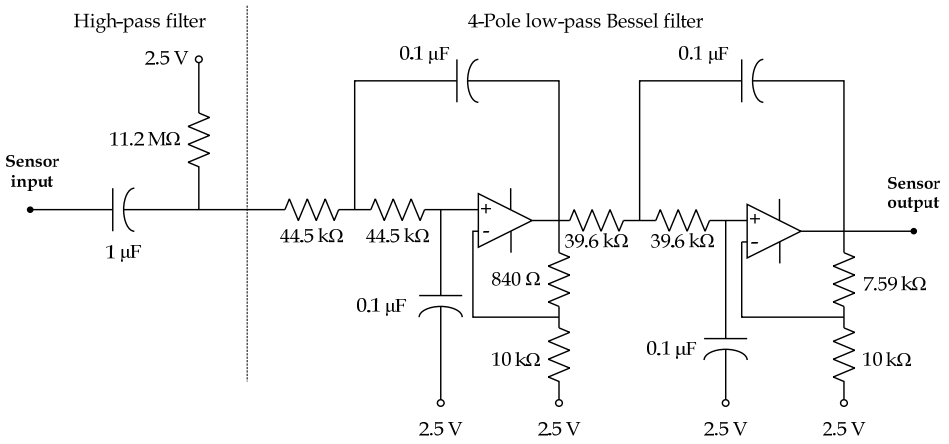

(a)

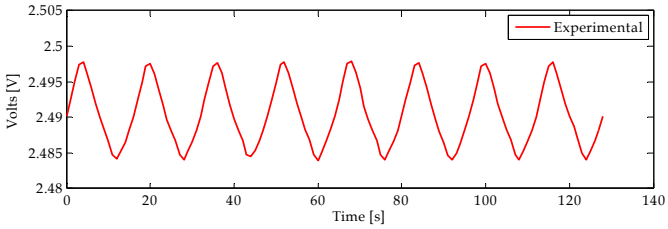

(b)

Figure 4-17. (a) Schematic of the pass-band filter used to filter out low-frequency exponential decay of nanocomposite resistance over time and (b) pass-pass filtered $(SWNT\text{-}PSS/PVA)_{50}$ experimental time history response to applied cyclic tensile-compressive loading to ±5,000 με (film is fabricated with 0.8 mg-mL^{-1} SWNT dispersed in 1.0 *wt.* % PSS).

17b; the band-pass circuit is effective in removing the resistance decay without distorting the strain measurement signal.

4.5.2. Capacitive Strain Sensor

Obviously, through the use of a pass-band filter, which requires some circuitry, the resulting SWNT-PSS/PVA thin film strain sensor loses its characteristics as a miniature thin film sensor. Since one of the goals of this research is to develop a compact layer-by-layer-assembled sensor, an alternative approach to be used in lieu of the cumbersome circuitry is proposed to attain a drift-free sensor. Instead of using a charged glass substrate during LbL self-assembly, a poly(ethylene terephthalate) (PET, 3M) thin film (0.127 mm thick) can be employed as the LbL substrate. Following the same

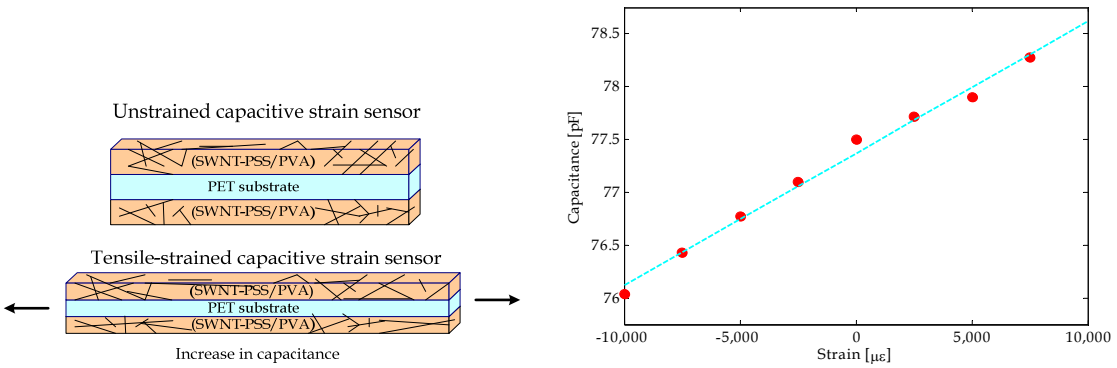

(a) (b)

Figure 4-18. (a) Schematic illustrating SWNT-on-PET capacitive strain sensor behavior such that the PET's Poisson's ratio under applied tension will decrease film width and thickness while increasing length to cause an increase in capacitance. (b) Preliminary results suggest that when measuring SWNT-on-PET capacitance with applied strain, sensor capacitance increases linearly in tandem with applied strain as expected.

experimental thin film fabrication procedure, a carbon-nanotube based parallel-plate capacitor is formed (where PET acts as the dielectric that separates the two conducting $(\text{SWNT-PSS/PVA})_n$ thin films on each side of the substrate as shown in Figure 4-18a). The capacitance of this SWNT-based parallel-plate capacitor (denoted as SWNT-on-PET) can be calculated via Equation 4-3.

$$C_{SWNT-on-PET} = \frac{\varepsilon_r \varepsilon_0 w L}{g}(1 + \varepsilon_s) \tag{4-3}$$

where ε_r is the relative dielectric permittivity of PET, ε_0 is the permittivity of vacuum or "free-space" ($\varepsilon_0 = 8.854 \cdot 10^{-12}$ $F\text{-}m^{-1}$), w (width) and L (length) are the dimensions of the SWNT-on-PET capacitor, g is 0.127 mm (PET thickness), and ε_s is the applied strain. From Equation 4-3, it is obvious that SWNT-on-PET capacitance is linearly related to strain, while capacitance can be adjusted by controlling sample dimensions. Upon affixing a SWNT-on-PET capacitive strain sensor to a PVC (Type I) bar and subsequently measuring sensor response with the Solartron 1260 impedance gain/phase analyzer to an applied tensile-compressive cyclic load pattern (Figure 4-10), it can be seen from Figure 4-18b that capacitance change is linearly related to applied strain. Thus, SWNT-

on-PET thin films can be utilized as capacitive strain sensors in order to obtain drift-free strain measurements without complex circuitry.

4.6. Summary and Conclusions

4.6.1. Results and Discussion

Results from this study allow one to begin tailoring the design of an (SWNT-PSS/PVA)$_n$ thin film strain sensor using a bottom up design approach. In this study, a layer-by-layer method is employed to fabricate a diverse suite of (SWNT-PSS/PVA)$_n$ thin films composed of varying combinations of SWNT concentration, PSS concentration, and film thickness. The purpose of this chapter is to experimentally characterize changes in LbL fabrication parameters and correlate them to bulk material strain sensing properties with the aim of enhancing strain sensing performance (*i.e.*, strain sensitivity). Based on identified trends between fabrication parameters and thin film piezoresistivity, one can begin to fabricate nanotube-based strain sensors with desired sensing properties attained by simple manipulation of the processing of SWNTs at the molecular-scale. The results obtained indicate that the (SWNT-PSS/PVA)$_n$ thin film strain sensitivities can vary between 0.193 to 1.805 by adjusting SWNT and PSS concentrations and film thickness. The ability to control the nanocomposite's electrical and mechanical properties permits the tailoring of thin films for specific SHM applications. For example, thin films that are ultra-ductile but exhibit moderate piezoresistivity may be required for monitoring structures undergoing large deformations during strong ground motions, whereas high strain sensitivity is more desirable for continuous long-term monitoring of civil infrastructures.

An RC-circuit model is devised from frequency-domain electrical impedance spectroscopy to fit experimental data to numerical results in both the frequency- and time-domains. Circuit parameters such as the strain-sensitive resistance, film capacitance, and exponentially decaying parameters that simulate the exponential decay of film resistance are all fitted using a simulated annealing algorithm to minimize the sum of the least-squares difference between experimental EIS results and those predicted by an analytical equivalent circuit model. Upon successful derivation of the proposed equivalent RC-circuit, the model is validated in the time-domain by comparing (SWNT-

PSS/PVA)$_n$ thin films' time histories with model-predicted results. Here, (SWNT-PSS/PVA)$_n$ thin films fabricated on glass substrates are cut into small rectangles and mounted to PVC bars subjected to tensile-compressive cyclic loading to ±10,000 με. Results of the fit from both the frequency- and time-domains suggest the equivalent RC-circuit model describes the strained (SWNT-PSS/PVA)$_n$ thin films well. Despite the presence of a time-dependent exponential decay of film resistance, two methods can be employed to obtain a drift-free sensor response. First, a band-pass (between 0.014 – 25 Hz) signal-conditioning circuit is included to experimentally filter out the slow decay in (SWNT-PSS/PVA)$_n$ thin film resistance. Alternatively, (SWNT-PSS/PVA)$_n$ thin films can be deposited onto PET substrates to form a capacitive strain sensor whose capacitance is strain sensitive. Most importantly, unique trends are observed, where increasing carbon nanotube and/or PSS concentration during LbL fabrication increases the overall film strain sensitivity. The increase in nanotube concentration and subsequent LbL deposition creates more nanotube-to-nanotube junctions, allowing the (SWNT-PSS/PVA)$_n$ film to be more sensitive to strain. Enhanced dispersion for higher PSS concentrations allows for larger quantities of individual nanotubes to be deposited on the substrate, thus increasing the (SWNT-PSS/PVA)$_n$ nanocomposite strain sensitivity.

4.6.2. Contributions

The main contribution of this chapter is two-fold: namely, (1) an equivalent circuit model capable of estimating and predicting (with high accuracy) thin film electrical response to applied strain has been derived and (2) SWNT-based nanocomposite piezoresistive sensitivity and inherent resistivity can be easily tailored by controlling layer-by-layer fabrication parameters. An experimental optimization study has been conducted to vary SWNT concentration, dispersing agent (*i.e.*, PSS) concentration, and film thickness; these fabrication parameters are correlated to the resulting nanocomposite's piezoresistive response. Using the derived equivalent circuit model, nanocomposite strain sensitivity and inherent resistivity have been obtained and compared between all the unique films fabricated. Specific trends have been identified which serve as future guidelines for tailoring macro-scale sensor properties for various applications. For instance, high nanocomposite resistivity (*i.e.*, low current draw) is

desirable when power consumption is a severe limitation. Nevertheless, the versatility of the fabrication process permits the optimization of the balance between sensor performance and material intrinsic properties. Secondly, as opposed to outfitting nanocomposite sensors with external circuitry (*e.g.*, band-pass circuits or post-data acquisition numerical fitting), the proposed equivalent circuit adequately describes the undesirable time-domain resistance drift. Furthermore, identification of the parallel circuit-type behavior of these thin films will permit direct application of these materials to applications where circuit modeling in the frequency domain is necessary (*e.g.*, radio frequency identification).

CHAPTER 5

APPLICATION OF MULTIFUNCTIONAL NANOCOMPOSITES FOR PASSIVE WIRELESS SENSING

5.1. Introduction

A key motivation of this dissertation is to develop novel multifunctional nanocomposites that are suitable for monitoring different damage processes (*e.g.*, cracking, yielding, and corrosion) in various civil, mechanical, and aerospace structures. However, structural damage is a complex phenomenon that can be distributed throughout various locations in the structure. Following the existing structural health monitoring paradigm (*i.e.*, distributed "point" sensors) as mentioned in Chapter 1, the objective of this chapter is to design and validate a high performance yet low cost passive (*e.g.*, without a power source) wireless sensor. Having identified an equivalent circuit model that adequately describes the electrical properties of the SWNT-based nanocomposite, it will be shown in this chapter that the RC-circuit model is ideally suited for integration with wireless devices.

In fact, many researchers have developed low-cost wireless sensors based on inductive coupling, also known as radio frequency identification (RFID) or inductively-coupled wireless sensors. Interest in RFID-based sensors is driven by the fact that these sensors do not require power sources, such as batteries. However, since these sensors have no power source, they depend on a "reader" at short-range (sub-meter) delivering power through inductive coupling. While many RFID-type wireless sensors have been successfully validated in structural monitoring applications, current academic prototypes still possess large form factors, thereby preventing their embedment within

reinforced concrete structures where sensor sizes should be comparable to the size of concrete aggregates [20-22, 24-27]. Miniaturization of passive wireless sensors would also extend their applications for monitoring structural systems constructed from composite laminates (*e.g.*, fiber-reinforced polymer (FRP) composites).

In this chapter, prototype thin film RFID-style wireless sensors are proposed for localized strain and pH monitoring. This chapter begins with a theoretical overview of inductively coupled wireless systems. When multifunctional nanocomposite sensors are coupled with a coil antenna, the final sensor package is capable of wirelessly detecting strain and pH (or corrosion) variations via changes in the characteristic frequency and bandwidth of the sensor, respectively. In total, three generations of inductively coupled nanocomposite sensors are designed and presented. First, SWNT-based thin films are electrically connected to a coil antenna formed by winding magnetic wire. Upon successful experimental validation of the RFID system, the objective of the second generation passive wireless sensors is to explore wireless communication capabilities of planar thin film coil antennas obtained from Texas Measurements, Inc. Finally, the third generation sensor combines nanotechnology-derived thin film fabrication techniques with micro-fabrication tools for the development of miniature printed circuit board (PCB) passive wireless strain and corrosion sensors. Preliminary experimental laboratory validation studies are presented to characterize the performance attributes of the wireless multifunctional SWNT-PE composite sensors.

5.2. Inductively Coupled Sensing Systems

In general, near-field radio frequency identification (or more generally, inductively coupled systems) are comprised of two main components: (1) a reader connected to a constant power source and (2) a passive sensor tag. The reader serves as the data acquisition system and is responsible for wirelessly transmitting power to an RFID tag in close proximity via inductive coupling (Figure 1-2) [19]. Two types of RFID sensor tags exist. First, digital tags include digital circuitry and capacitive circuit elements for short-term power storage. When the digital sensor tag is interrogated by an RFID reader, simple onboard computations can take place before the sensor tag transmits data back (or uplinks) to the reader base station using techniques such as

amplitude (ASK), frequency (FSK), or phase shift keying (PSK) [118]. To date, these types of RFID sensors have found application in smart cards, security systems, package tracking, sensors, and among many others. While many commercial and academic RFID tags are coupled with digital electronics for use in a variety of smart card applications, digital electronics will not be used in this study due to their cost and the need for increased form factor. The second type of RFID sensors are analog tags. Analog RFID tags do not attempt to capture power like the digital tags; in addition, no computations are executed by the tag. The analog RFID-sensor takes advantage of the properties of the electromagnetic (EM) coupling between the reader and tag to encapsulate data. In this study, the characteristics of the inductive coupling (namely, characteristic frequency and bandwidth) are designed to vary as a function of the stimulus we seek to measure (*e.g.*, strain and pH). The advantage inherent to analog RFID sensors is that it requires passive circuit elements (*i.e.*, resistors and capacitors) only, thereby keeping form factors small.

5.2.1. The Reader for Analog Tags

In its simplest form, a typical RFID reader consists of a coil antenna connected to an automatic frequency response analyzer (FRA). In this study, the Solartron 1260 impedance gain/phase analyzer is selected for its ease of use and its ability to measure electrical impedance in a frequency range between 100 mHz to 32 MHz (well within the operating frequency range of the proposed RFID sensor system, as will be discussed later). When measuring the complex-valued impedance, Z ($Z = A+jB$ where A and B are the real and imaginary components of the impedance, respectively), the FRA generates a regulated AC voltage signal that is applied to the reader coil; simultaneously, the FRA measures the corresponding AC current response in the coil as AC frequency, f, is varied. As the AC sinusoidal signal passes through the reader coil antenna, a magnetic field, H, is generated in the vicinity of the reader's coil as can be calculated by Equation 5-1 and depicted in Figure 5-1 (for a circular reader coil based on Faraday's Law) [19]:

$$H = \frac{I \cdot N \cdot r^2}{2\sqrt{(r^2+x^2)^3}} \tag{5-1}$$

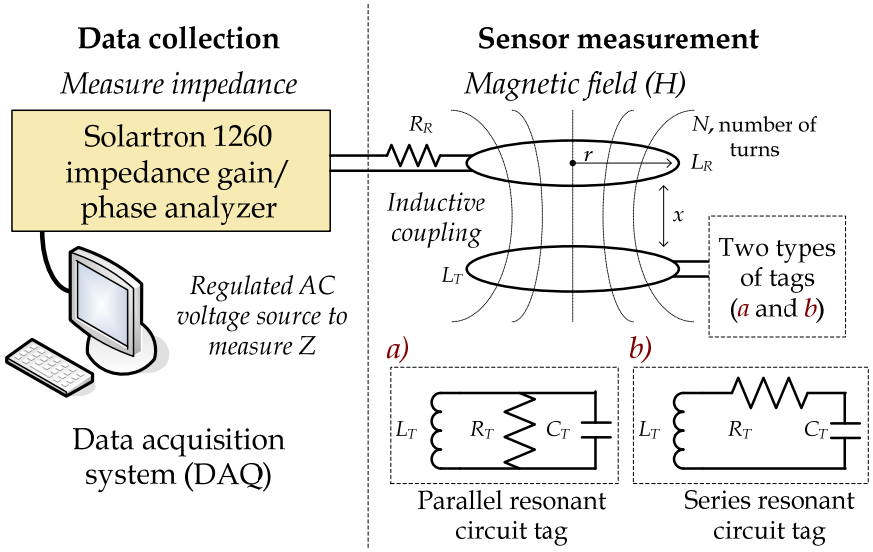

Figure 5-1. A schematic illustrating RFID wireless interrogation of a (a) parallel and (b) series resonant tag circuit.

where I is the current passing through the coil, r is the antenna radius, N is the number of turns, and x is the read-distance along the central axis of the coil (Figure 5-1). This resulting magnetic field is employed to induce current and a potential drop in an RFID tag within close proximity. From Equation 5-1, it can be observed that a tradeoff exists between different size antennas such that smaller antennas are capable of generating higher EM fields at the coil axis but larger antennas generate higher fields over greater distances (x).

5.2.2. *Sensor Tag*

Typically, the circuitry of a basic sensor tag consists of a resistor (R_T), inductor (coil antenna) (L_T), and capacitor (C_T) in a parallel or series resonant circuit configuration, also known as an RLC-circuit (Figure 5-1). Inherent to each parallel or series resonant circuit are two quantities, namely its characteristic (or resonant) frequency (f_n) and bandwidth (B). While the characteristic frequency of an RLC-circuit does not change with circuit configuration, bandwidth varies between a parallel and series resonant circuit as shown in Equations 5-2 and 5-3:

$$f_n = \frac{1}{2\pi\sqrt{L_T C_T}} \tag{5-2}$$

$$B_{series} = \frac{R_T}{2\pi L_T} \tag{5-3a}$$

$$B_{parallel} = \frac{1}{2\pi R_T C_T} \tag{5-3b}$$

Selection of sensor tag circuit configuration depends on whether characteristic frequency shift or bandwidth change is more desirable. Furthermore, certain voltage and current requirements for powering onboard electronics governs the type of resonant circuit configuration used. At resonance (f_n), series and parallel tags provide maximum current (minimum impedance) or maximum voltage (maximum impedance), respectively as shown in Figure 5-2 [119].

5.2.3. Coupled Reader and Tag System

If the Solartron 1260 FRA measures the complex impedance response of the reader coil antenna, the measured impedance would be governed by Equation 5-4.

$$Z(\omega) = R_R + j\omega L_R \tag{5-4}$$

where R_R is the inherent series resistance of the coil, L_R is the inductance of the reader coil antenna, and ω (in rad-s^{-1}) is the natural cyclic frequency of the input AC sinusoidal signal (Figure 5-2a). However, when a sensor tag comes in the vicinity of the reader coil, an additional complex impedance term (due to inductive coupling, Z_T') is superimposed onto the impedance of the measured coil antenna.

$$Z(\omega) = R_R + j\omega L_R + Z_T' \tag{5-5}$$

In order to calculate Z_T', one can begin by calculating the equivalent impedance of each circuit element in the series or parallel sensor tag: namely, the inductor (Z_L), resistor (Z_R), and capacitor (Z_C) impedances:

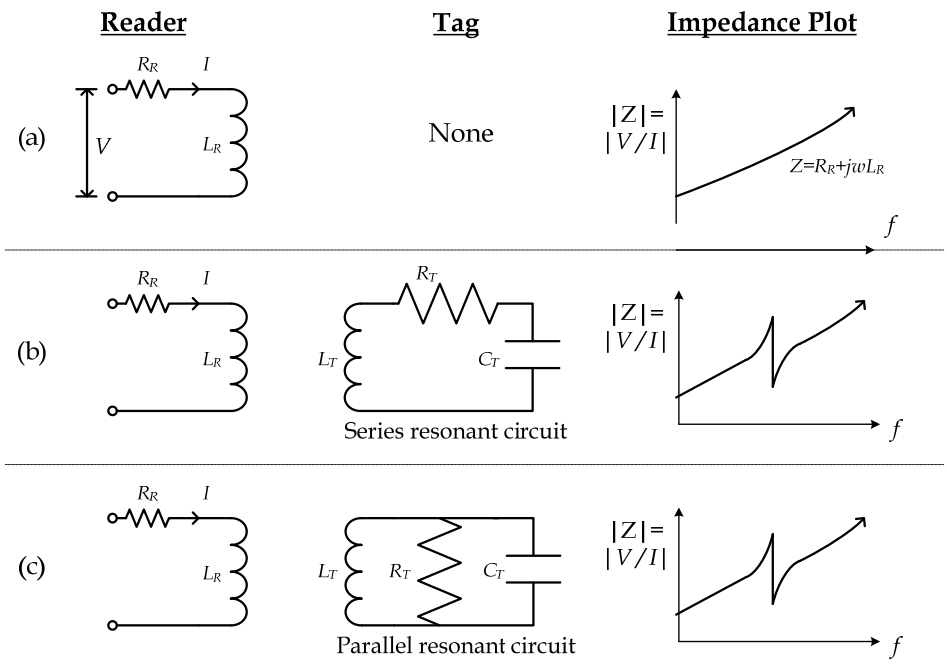

Figure 5-2. A schematic illustrating RFID reader impedance (Z) response when (a) no sensor tag is in the vicinity or when present with a (b) series or (c) parallel resonant circuit.

$$\begin{aligned} Z_L &= R_S + j\omega L_T \\ Z_R &= R_T \\ Z_C &= \frac{1}{j\omega C_T} \end{aligned} \tag{5-6}$$

Note, the resistance R_S is the inherent series resistance of the sensor tag's inductive coil. Using the equivalent impedance of each circuit element as given in Equation 5-6, the total impedance measured at the reader can be determined. For example, when a series resonant circuit tag comes into close proximity to the RFID reader, the measured impedance can be calculated by Equation 5-7:

$$Z(\omega) = R_S + j\omega L_R + \frac{k^2\omega^2 L_R L_T}{Z_L + Z_C + Z_R} \tag{5-7}$$

Similarly, for a parallel resonant circuit:

$$Z(\omega) = R_S + j\omega L_R + \frac{k^2\omega^2 L_R L_T}{1/Z_L + 1/Z_C + 1/Z_R} \quad (5\text{-}8)$$

The plot of impedance, Z, as a function of frequency, ω, for both the parallel and series resonant circuits differs from that of the reader alone (Figure 5-2a) due to a zig-zag portion of the curve (Figure 5-2b and 5-2c). From Equations 5-7 and 5-8, a coupling factor (k, a number between 0 and 1) qualitatively describes the mutual inductance between the reader and sensor coil antennas. Theoretically, $k = 1$ when the reader and tag coil antennas are of the same size, the same inductance, perfectly aligned by their coil axes, and separated by a distance of zero. However, the coupling factor is strongly dependent on coil geometry, operating conditions, range, among other factors. In the event that no sensor tag is present (where the distance between the coils can be approximated by infinity), $k = 0$, and Equations 5-7 and 5-8 reduce back to Equation 5-4.

It is obvious from Equations 5-7 and 5-8 that the as-measured RFID reader's complex impedance response is governed by the RFID tag's discrete circuit elements (*i.e.*, R_T, C_T, and L_T). Thus, an RFID sensor tag can be realized by the careful design of its individual circuit elements (*i.e.*, resistor, capacitor, or inductor) to change in response to an applied external stimulus (*e.g.*, strain or pH). Any electrical changes observed by the RFID sensor tag due to an applied external stimulus are detectable by an RFID reader in close proximity. In this study, a parallel resonant circuit configuration is employed for the design of RFID sensor tags. For example, if the resistive element of wireless sensor is designed to change in response to strain or pH, the RFID system bandwidth will change according to Equation 5-3b. Figure 5-3 illustrates an exaggerated complex impedance response measured wirelessly by the RFID reader as a wireless sensor tag's resistance changes.

5.3. Passive Wireless Sensor Fabrication

Provided that LbL-fabricated carbon nanotube composite thin films are electrically equivalent to RC-parallel circuits, they can be employed as integral elements of a passive wireless sensor. Two types of sensors are specifically proposed, namely strain and pH sensors. Following results obtained in Chapters 2 and 4, (SWNT-

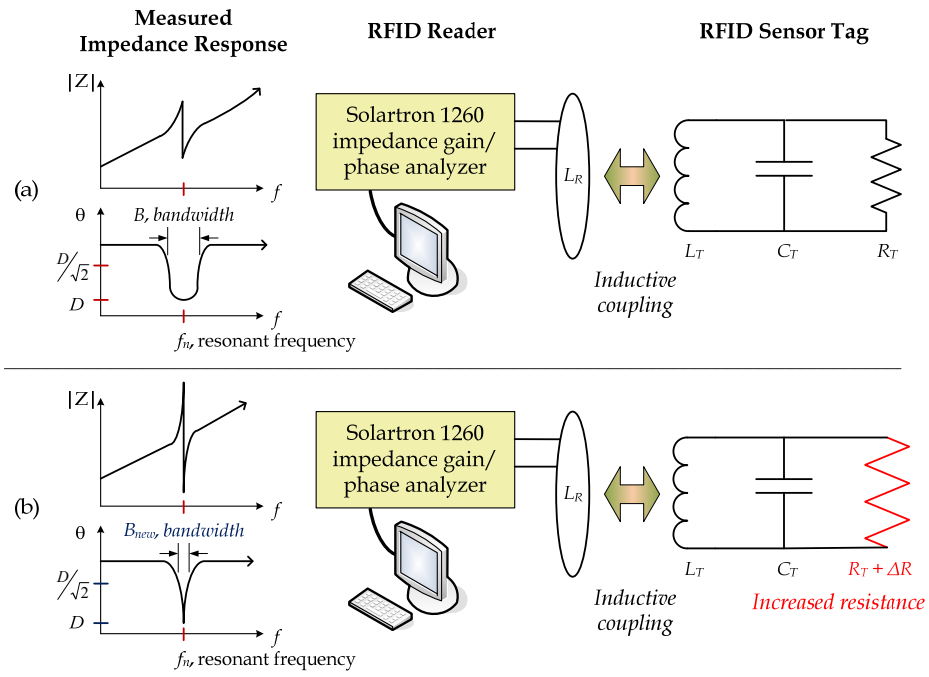

Figure 5-3. (a) An illustration of typical complex impedance magnitude and phase plots measured by an RFID reader interrogating a remote parallel sensor tag. (b) As the resistance of the RFID sensor tag decreases, a corresponding decrease in bandwidth is measured by the reader.

PSS/PVA)$_n$ films are employed as piezoresistive strain sensors; in addition, these nanocomposites can also be deposited onto both sides of a flexible substrate to realize a capacitive strain sensor. Secondly, passive wireless pH sensing is accomplished by depositing (SWNT-PSS/PANI)$_n$ nanocomposites upon a variety of substrates.

As mentioned in Section 5.1, the main objectives of this chapter are, first, to validate passive wireless sensing capabilities of nanocomposite RFID sensors, and second, to miniaturize sensors for embedment within structural components. Miniaturization of sensor form factor is demonstrated through the design and validation of three generations of nanocomposite-based multifunctional passive wireless sensors. First, Generation-I passive wireless sensors are realized by coupling carbon nanotube-based composites with traditional inductive coil antennas constructed from 28 AWG magnetic coil wire. The study focuses upon experimentally validating that sensor resonant frequency and bandwidth change due to applied stimulus (*e.g.*, tensile-compressive strains and pH, respectively). Upon successful validation of sensor

Table 5-1. A summary of components employed for fabrication of nanocomposite-based passive wireless sensors.

Sensor Type	Nanocomposite	LbL Substrate	Sensing Mechanism	Antenna Type	Antenna Size
Generation-I:					
Strain	$(SWNT\text{-}PSS/PVA)_n$	PET	Capacitive	28 AWG wire coil	4.5 cm diameter
pH	$(SWNT\text{-}PSS/PANI)_n$	Glass	Resistive	28 AWG wire coil	8.0 cm diameter
Generation-II:					
Strain	$(SWNT\text{-}PSS/PVA)_n$	PET/glass	Resistive	TI Planar	2.5 x 5 cm^2 6-turns
pH	$(SWNT\text{-}PSS/PANI)_n$	PET/glass	Resistive	TI Planar	2.5 x 5 cm^2 6-turns
Generation-III:					
Strain	$(SWNT\text{-}PSS/PVA)_n$	FR4	Resistive	PCB Planar	2.3 x 2.4 cm^2 10-turns
pH	$(SWNT\text{-}PSS/PANI)_n$	FR4	Resistive	PCB Planar	2.3 x 2.4 cm^2 10-turns

performance, the layer-by-layer technique is then employed to directly deposit nanocomposites on planar coil antennas printed on poly(ethylene terephthalate) (PET) (Texas Instruments, Inc.) to realize Generation-II wireless sensors. In order to tune the resonant frequency of the Generation-II RFID sensor, a leaded ceramic capacitor is connected to the planar coil antenna via single-stranded wire and colloidal silver paste. Thus, further miniaturization is accomplished with Generation-III where microfabrication and printed circuit board technologies (PCB) are employed for the patterning of coil antennas onto FR4 laminate substrates. Nanocomposites are directly deposited over these PCB coil antennas and miniature surface mount capacitors are soldered directly onto the board surface to realize an embeddable passive wireless sensor. Table 5-1 outlines the various components required for each generation of sensor.

5.4. Generation-I Passive Wireless Sensor Experimental Validation

Two Generation-I sensors are proposed: strain and pH sensors (Table 5-1). First, a carbon nanotube composite film is deposited on a soft PET substrate to act as the variable capacitor (sensitive to strain) within a parallel RFID sensor tag. Second, a PANI-based thin film is employed as the pH-sensitive circuit element within an RFID tag. However, to investigate whether PANI-based nanocomposites exhibit capacitive sensitivity to pH, electrical impedance spectroscopy is employed as a frequency-domain characterization tool similar to Chapter 4. Both sensors proposed employ traditional inductive coils constructed from 28 AWG magnetic coil wire.

5.4.1. Wireless Strain Sensing

As previously illustrated, (SWNT-PSS/PVA)$_n$ thin films exhibit piezoresistive responses under applied strain. Despite the ability to precisely tailor strain sensor sensitivity by adjusting LbL fabrication parameters (Chapter 4), the thin film strain sensor exhibits a time-dependent exponential decay in film resistance over long measurement periods. Thus, to avoid the time-dependent gradual thin film conductivity variations from interfering with sensor output, capacitive-based SWNT-on-PET strain sensor is introduced. This sensor will take the place of a traditional capacitor in the parallel RC-circuit. Upon coupling this capacitive strain sensor with a parallel resonant tag circuit (where $L \approx 235\ \mu H$ and $R \approx 1.2\ M\Omega$), any applied strain will result to an inversely proportional shift in resonant frequency as given in Equation 5-2. The inductive tag element is assembled by a wire coil approximately 45 mm in diameter and 50 turns connected in parallel to a resistor ($R \approx 1.2$ MΩ) and the SWNT-on-PET film.

Validation of this wireless strain sensor is conducted by applying one cycle of a tensile-compressive load pattern ($\varepsilon = \pm 10{,}000\ \mu\varepsilon$) while wirelessly measuring its response using the Solartron 1260 impedance gain/phase analyzer coupled with a coil antenna (identical to the one used in the sensor tag) to form the RFID reader. Prior to mechanical loading, the wireless strain sensor is mounted to a poly(vinyl chloride) (PVC Type I) rectangular tensile coupon (31 cm long, 4 cm wide, 2 cm thick) via standard CN-E strain gauge epoxy (Tokyo Sokki Kenkyujo) as shown in Figure 5-4. Upon sufficient drying (6

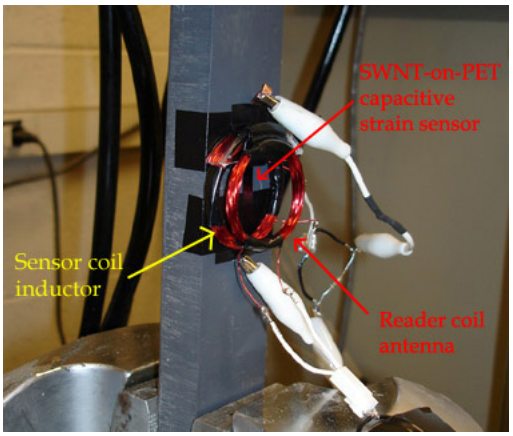

Figure 5-4. SWNT-on-PET capacitive strain sensor (epoxy-bonded to a PVC coupon) in a parallel resonant circuit configuration loaded by the MTS-810 load frame. Coil antennas associated with the sensor and reader are shown.

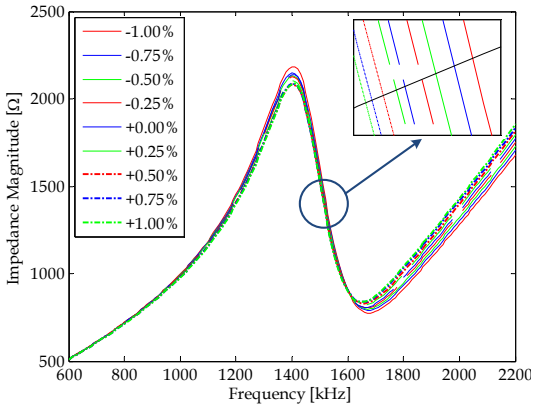

Figure 5-5. Experimental RFID reader response of SWNT-on-PET capacitive strain sensor under one-cycle tensile-compressive cyclic loading to ±10,000 με (inset shows zoomed in plot near resonant frequency).

hours), an MTS-810 load frame is employed to apply the one-cycle tensile-compressive load pattern at 2,500 με increments. At each strain increment, the load frame is held at constant displacement and load (for approximately 5 min) to allow the RFID reader (*i.e.*, the reader coil antenna coupled to the Solartron 1260 impedance gain/phase analyzer) to wirelessly interrogate the strain sensor tag. The distance between the reader and tag coils is fixed at approximately 3 cm.

Figure 5-5 represents a typical experimental data plot of the wireless strain sensor's coupled impedance as collected by the RFID reader. Identification of sensor characteristic frequency can be accomplished by observing a dip in the phase angle or the inflection point in the impedance magnitude-frequency plot (as shown in Figure 5-5) [26]. Figure 5-6a plots the calculated resonant frequency as a function of applied strain. From substituting Equation 5-9 into Equation 5-2 to yield Equation 5-10, it is apparent that resonant frequency shift is nonlinearly related to applied strain (*i.e.*, by a $1/\sqrt{(1+\varepsilon_s)}$ relationship).

$$f_n = \frac{1}{2\pi\sqrt{L_T\varepsilon_r\varepsilon_0 wL(1+\varepsilon_s)/g}} \tag{5-10}$$

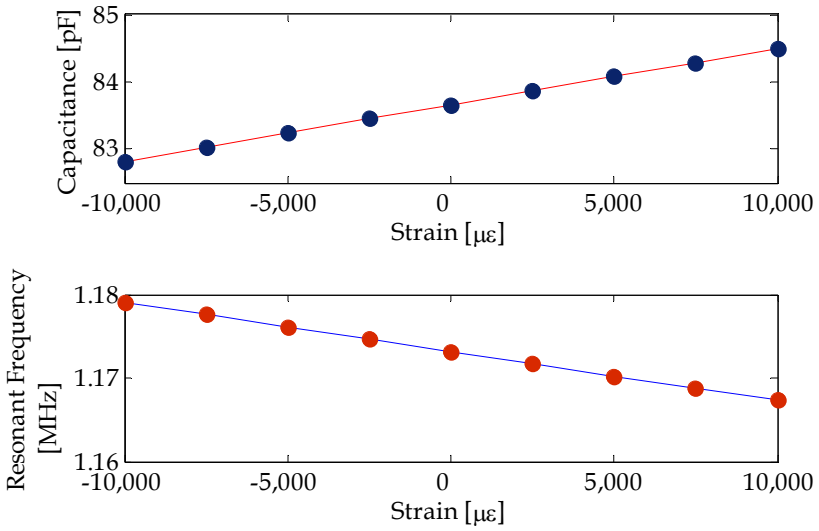

Figure 5-6. (a) Top: resonant frequency shift of SWNT-on-PET capacitive strain sensor under one-cycle tensile-compressive cyclic loading to ±10,000 με; (b) Bottom: corresponding SWNT-on-PET capacitance change.

Nevertheless, since the degree of nonlinearity is small, strain sensor sensitivity (S_C=($\Delta C/C_0$)-ε^{-1}) can be approximated by fitting a linear least-squares best-fit line to Figure 5-6a to yield S_C = 0.427 Hz-$\mu\varepsilon^{-1}$. It should be noted that because the differential frequency step during impedance measurement is small (Δf = 1 kHz), linear interpolation is employed between data points to extract sensor resonant frequency at each applied strain increment. Furthermore, upon determining the characteristic frequency of the sensor, capacitance is back-calculated using Equation 5-2 and plotted in Figure 5-6b. Apparent in Figure 5-6b is that capacitance does increase linearly in tandem with applied strain.

5.4.2. Frequency-domain pH Sensing Characterization

While DC time-domain electrical characterization has already revealed the high sensitivity of (SWNT-PSS/PANI)$_n$ nanocomposite's surface resistivity to pH (Section 2.6.1), frequency-domain evaluation can reveal other changes in the film's electrical properties (*e.g.*, capacitance or inductance). In fact, the Solartron 1260 impedance gain/phase analyzer can be employed to conduct electrical impedance spectroscopy for characterizing frequency-domain electrical properties of the pH-sensitive nanocomposites [115]. EIS is conducted by directly connecting the FRA to the thin film

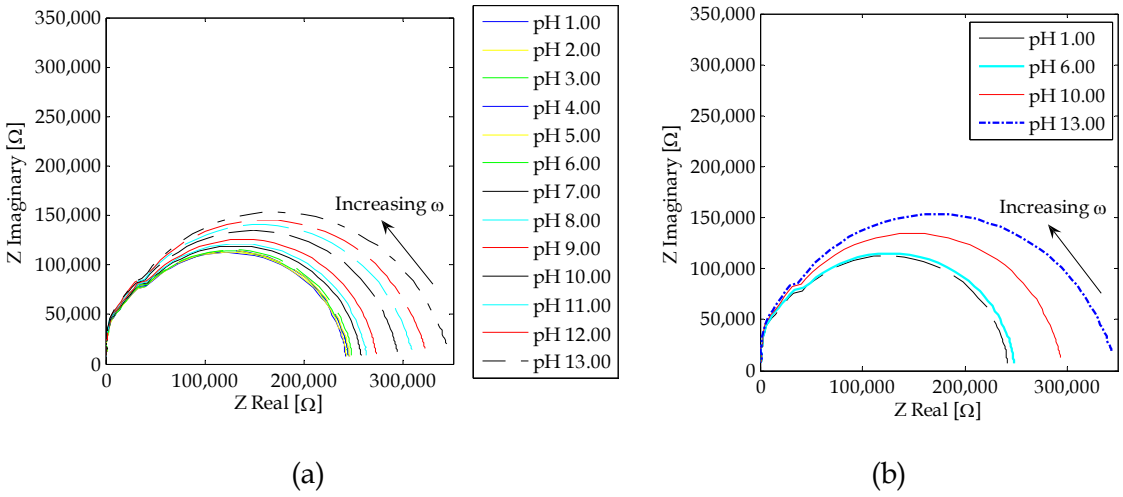

Figure 5-7. (a) Electrical impedance spectroscopic plots showing that (SWNT-PSS/PANI)$_{50}$ nanocomposite's increase in parallel resistance with increasing pH (pH from 1 to 13). (b) Select plots of Figure 4-5a shown for clarity purposes.

specimen. Then, the Solartron impedance analyzer is commanded to measure nanocomposite impedance between applied AC signal frequencies from 1 to 10 MHz.

Figure 5-7 plots the experimental response of EIS measurements of an (SWNT-PSS/PANI)$_{50}$ nanocomposite subjected to buffer solutions ranging from pH 1 to 13. The semicircular thin film EIS response in the complex impedance plane (termed the Cole-Cole plot) suggests that these thin films exhibit a resistor-capacitor (RC) parallel circuit-type behavior (Figure 5-8) [115]. It is expected that an increase in the Cole-Cole semicircular plot radius with increasing pH suggests an increase in the parallel resistance of an equivalent parallel-RC circuit (Figure 5-8).

Thus, each Cole-Cole plot is numerically fitted to an equivalent circuit schematically shown in Figure 5-8 using a stochastic simulated annealing model-updating algorithm; values for the equivalent resistance and capacitance of the (SWNT-PSS/PANI)$_{50}$ nanocomposite are dedicated during updating. Upon model-fitting of EIS thin film response to applied pH buffer solutions, the results are summarized in Figure 5-9. The LbL thin film's frequency-domain equivalent resistance exhibits a bilinear response to pH, where lower sensitivity is observed for acidic pH solutions (0.9 kΩ-pH^{-1}-cm^{-2}) but dramatically increases when exposed to alkaline solutions (12.5 kΩ-pH^{-1}-cm^{-2}). The parallel circuit capacitance is fairly constant and appears to be insensitive to pH.

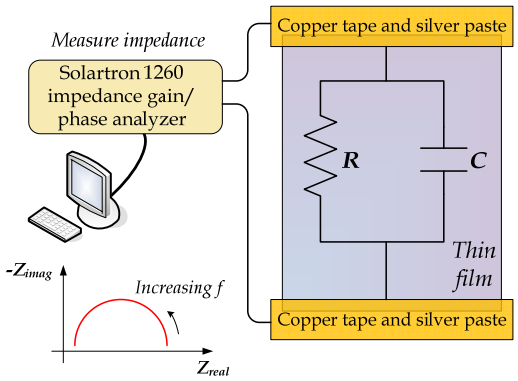

Figure 5-8. An equivalent parallel-RC circuit model is derived for simulated annealing model-fitting of thin film EIS Cole-Cole plot response.

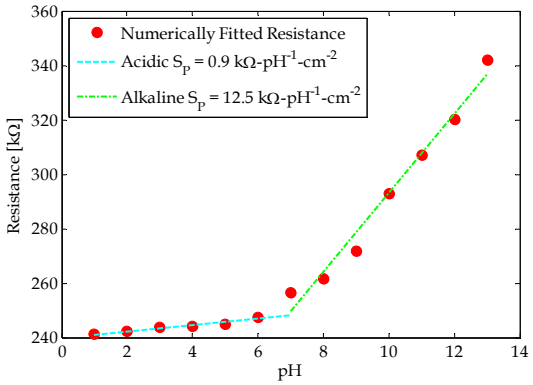

Figure 5-9. A plot of model-fitted equivalent circuit resistance as a function of applied pH buffer solutions indicating bilinear sensitivity.

5.4.3. *Wireless pH Sensing*

Passive wireless sensors are fabricated by electrically connecting (SWNT-PSS/PANI)$_{50}$ thin films to a tuning capacitor and a magnet wire coil antenna to form a parallel resonant circuit. The result is an RFID and carbon nanotube-based passive wireless sensor that measures bandwidth change as a function of pH buffer solutions. In this case, the 11 x 7 mm^2 (SWNT-PSS/PANI)$_{50}$ nanocomposite acts as the pH-sensitive resistor (whose nominal resistance is on the order of 10,000 kΩ) while connected in parallel to a 2,100 µH inductive coil antenna (where the inductive coil is an 80 mm diameter coil consisting of 90 turns) and a 220 pF tuning capacitor. To control the amount of pH solution exposed to the (SWNT-PSS/PANI)$_{50}$ thin film, a plastic well is mounted on top of the thin film via high vacuum grease (Dow Corning). It is expected that this circuit configuration will cause a change in system bandwidth due to changes in thin film resistance responding to different pH buffer solutions (from Equation 5-3b). The resulting pH sensor response is nonlinear, exhibiting a $1/R_T$ relationship between bandwidth and film resistance.

Again, for wireless sensor interrogation, the Solartron 1260 impedance gain/phase analyzer connected to an inductive coil antenna is employed as the RFID reader. Individual pH buffer solutions (pH 1 to 10 and 1 mL) are pipetted into the plastic

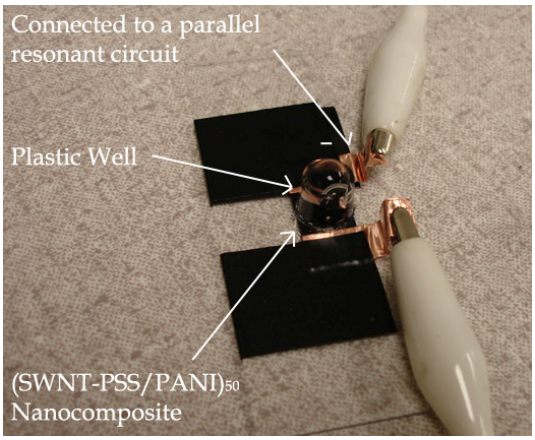

Figure 5-10. $(SWNT\text{-}PSS/PANI)_{50}$ thin film with a plastic well mounted for pipetting pH buffer solutions.

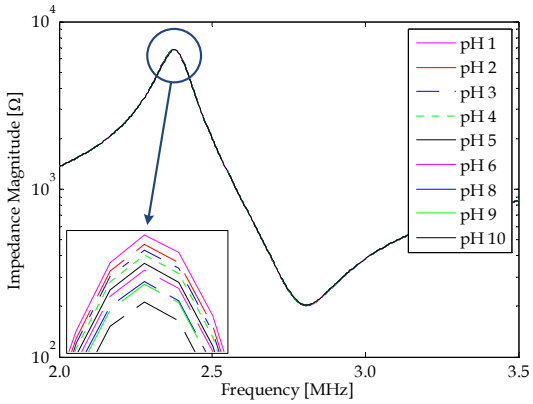

Figure 5-11. Impedance magnitude-frequency response as measured by the Solartron 1260 FRA RFID reader to capture the wireless pH sensor performance with different pH buffer solutions.

well as shown in Figure 5-10. Upon the addition of a pH buffer solution, the RFID reader is employed to measure the complex impedance over a range of frequencies. Once the RFID reader completes interrogating the pH sensor tag, the pH buffer solution in the plastic well is removed, and immediately, a different pH buffer solution is pipetted in. A representative experimental overlay is shown in Figure 5-11.

The inset of Figure 5-11, which shows a zoomed-in portion of the experimental impedance magnitude-frequency overlay, indicates that system bandwidth decreases with increasing pH buffer solution. However, bandwidth is inherently difficult to quantify; although one can subjectively select frequency limits and calculate bandwidth, this method does not correlate with theory as given in Equation 5-3b. In order to accurately calculate system bandwidth from experimental data, the stochastic simulated annealing model-updating algorithm is again employed to numerically fit experimental data to theory (Equation 5-8) [116]. The model-updating algorithm updates individual circuit elements for both the tag and reader expressed in the complex impedance frequency domain. A typical model-fitting is shown in Figure 5-12 for one set of experimental data; it can be observed that the model fit adequately identifies the sensor equivalent circuit parameters to achieve accurate numerical fitting to experimental data. Upon determining the resistance, capacitance, and inductance of the sensor tag under

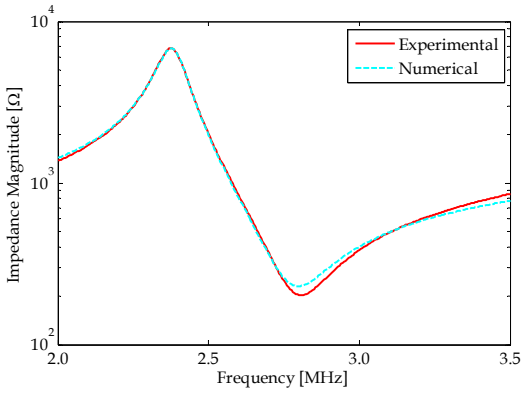

Figure 5-12. Validation of stochastic simulated annealing model-fitting between numerical and experimental (for pH = 3.00) RFID reader response indicating good fit.

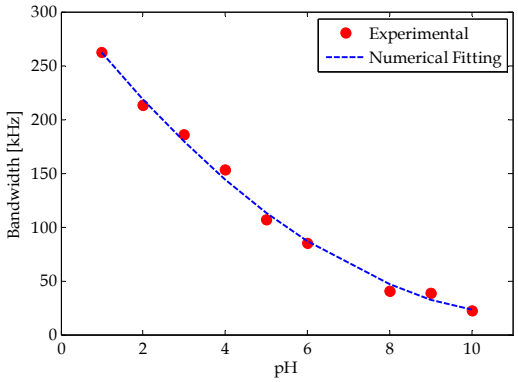

Figure 5-13. $(SWNT\text{-}PSS/PANI)_{50}$ thin film parallel resonant circuit tag shows considerable bandwidth change due to applied pH buffer solutions.

different pH buffer solutions, one can then calculate, using Equation 5-3b, the change in bandwidth of the RFID system, where the results are plotted in Figure 5-13. From Figure 5-13, it is apparent that the bandwidth of the wireless pH sensor changes from 270 to 25 kHz as pH increases from 1 to 10.

5.4.4. Generation-I Accomplishments and Challenges

As demonstrated in this section, Generation-I sensor's passive wireless communications and strain and pH sensing performance have been successfully validated. First, by depositing $(SWNT\text{-}PSS/PVA)_n$ nanocomposites onto a conformable PET substrate, a capacitive strain sensor is produced. When coupled to a 28 AWG magnet wire coil antenna and strained to ±10,000 με, the passive wireless strain sensor can be wirelessly interrogated while exhibiting decreasing resonant frequency with increasingly applied strain at a strain sensitivity of 0.427 Hz-$\mu\varepsilon^{-1}$. On the other hand, wireless pH sensing is accomplished by electrically connecting a $(SWNT\text{-}PSS/PANI)_{50}$ nanocomposite to a parallel resonant tag circuit. As different pH buffer solutions are pipetted into a plastic well mounted above the film surface, the resistive thin film sensor induces a tag bandwidth change from 270 to 25 kHz as pH scales from 1 to 10.

Despite satisfactory performance obtained for both the Generation-I passive wireless strain and pH sensors, a significant disadvantage is their large coil antennas (*i.e.*,

45 mm and 80mm for the strain and pH sensors, respectively). Such large antenna form factors will prevent these sensors from being embedded within structural materials such as composites or concrete. In addition, even if these sensors can be used in outdoor environments, its large form factor also masks the merits of using unobtrusive multifunctional thin films. Thus, a different approach is required to eliminate the use of traditional coil antennas before these passive wireless sensors can be validated for structural monitoring applications. It should also be noted that a tradeoff exists between coil geometry (*i.e.*, the coil antenna's diameter, number of turns, and thickness) and wireless read range [19] such that larger coil geometries are accompanied by longer sensor interrogation lengths.

5.5. Generation-II Sensor Miniaturization Using Planar Antennas

In Section 5.4, it has been shown that nanocomposites coupled with traditional magnet wire coil antennas can be utilized as passive wireless sensors for structural monitoring. Despite favorable sensor characteristic frequency and bandwidth changes to applied strain and pH, respectively, the large form factor of tag coil antennas is one significant limitation that prevents field applications of these sensing systems. As a result, the objective of this section is to miniaturize the sensor while maintaining performance attributes observed in Section 5.4. Towards this end, commercially available 25 x 50 mm^2 6-turn TI planar coil antennas (printed on a flexible PET substrate) are selected to offer RFID wireless communications while also serving as the layer-by-layer substrate. In general, nanocomposite thin films will be directly assembled onto these planar PET-based coil antennas and electrically connected to a tuning capacitor via single-stranded wire and colloidal silver paste. Similar to Section 5.4, the miniaturized multifunctional sensor is validated for wireless strain and pH sensing as shown in Table 5-1.

5.5.1. Generation-II Passive Wireless Sensor Fabrication

Fabrication of the Generation-II wireless strain sensor begins by depositing $(SWNT\text{-}PSS/PVA)_{50}$ thin films onto TI coil antennas (Figure 5-14). It should be noted that since these TI coil antenna traces are printed on a very flexible PET substrate, they

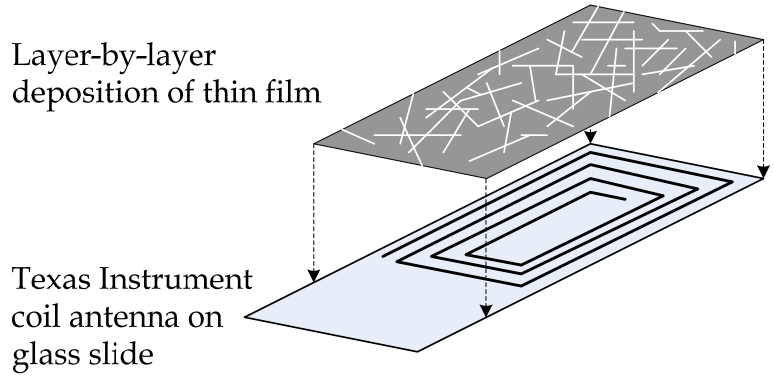

Figure 5-14. A schematic illustrating the layer-by-layer deposition of multifunctional thin film sensors onto planar TI coil antenna substrates (printed on PET and epoxy-mounted to a glass microscope slide).

are initially epoxy-mounted to a glass microscope slide (Fisher Scientific) for ease of use during LbL fabrication. Unlike the Generation-I passive wireless sensors, the Generation-II wireless sensor platform seeks to take advantage of the piezoresistivity of $(SWNT\text{-}PSS/PVA)_{50}$ thin films; thus, they are employed as strain-sensitive resistive elements within the RFID tag circuitry. Next, to ensure that the nanocomposite and coil antenna are electrically isolated, a thin coating of insulating Ted Pella Aerodag G (graphite aerosol) is sprayed onto the surface of the coil prior to LbL fabrication. Upon film deposition, realization of a parallel resonant tag circuitry is accomplished by drying colloidal silver paste (Ted Pella) over two ends of the $(SWNT\text{-}PSS/PVA)_{50}$ antenna and connecting it to the inductor (TI coil antenna) in parallel with a 1,500 pF tuning capacitor.

Similarly, realization of the Generation-II passive wireless pH sensor is accomplished by assembling the $(SWNT\text{-}PSS/PANI)_{100}$ nanocomposites onto Aerodag G-coated TI coil antennas. A 1,000 pF tuning capacitor is included in the sensor tag's parallel circuit design to achieve a resonant frequency of approximately 3.28 MHz. In addition, since the pH sensor is required to be exposed to a variety of pH solutions, a small plastic well is mounted on the film surface using high-vacuum grease. The small well is capable of containing approximately 1 mL of pH buffer solutions while holding its contents without leakage onto other areas of the sensor tag.

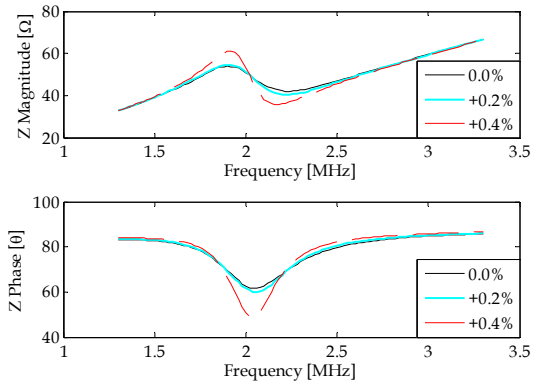

Figure 5-15. The corresponding impedance (a) magnitude and (b) phase response as measured by the RFID reader when $(SWNT\text{-}PSS/PVA)_{50}$ thin films are strained (only showing tensile strain responses for clarity).

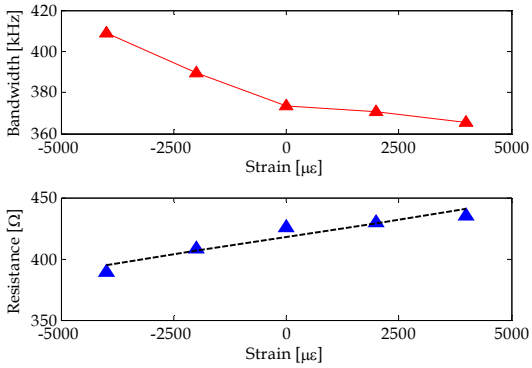

Figure 5-16. (a) Top: system bandwidth of the strain sensor tag decreases with increasing applied strain. (b) Bottom: the film resistance is back-calculated using Equation 5-3b to validate its near-linear increase in resistance with increasing strain.

5.5.2. Generation-II Wireless Strain Sensor Evaluation

Upon sensor fabrication, the Generation-II passive RFID sensor tag is epoxy-mounted (using CN-Y post-yield epoxy) to a PVC bar element for strain testing. After waiting six hours for the epoxy to dry, the PVC coupon and sensor tag are mounted in an MTS-810 load frame. The load frame is then commanded to execute an increasing monotonic strain (±4,000 με at 2,000 με intervals) to the specimens; at each interval, the load frame holds its displacement and load to allow time for the RFID reader to interrogate the strain sensor tag (similar to Section 5.4.1).

From Figure 5-15, it can be seen that the impedance magnitude and phase response wirelessly measured by the RFID reader varies depending on the level of induced strains. The piezoresistive thin film in the parallel resonant circuit causes system bandwidth changes due to applied strain, as governed by Equation 5-3b and shown in Figure 5-16a. Upon back-calculating the thin film resistance (Figure 5-16b), once again, the thin film resistance increases near-linearly in tandem with applied strain. The near-linear response of $(SWNT\text{-}PSS/PVA)_{50}$ thin film resistance to applied strain is consistent with previous results obtained from two-point probe resistance measurements presented in Chapter 2.

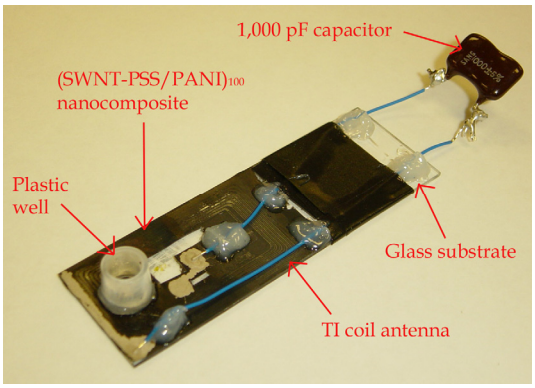

Figure 5-17. A $(SWNT\text{-}PSS/PANI)_{100}$ thin film is deposited directly onto a TI planar coil antenna to form a parallel resonant sensor tag (f_n = 3.28 MHz using a 1,000 pF tuning capacitor). A plastic well is mounted on top of the thin film to hold different pH buffer solutions.

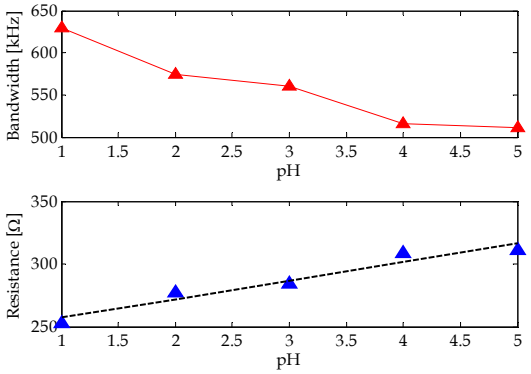

Figure 5-18. (a) Top: upon wireless sensor interrogation via the RFID reader, the system bandwidth is extracted and shown as different pH buffer solutions are pipetted into the plastic well. (b) Bottom: the film resistance is back-calculated using Equation 5-3b to validate its near-linear increase in resistance with increasing pH.

5.5.3. Generation-II Wireless pH Sensor Evaluation

Validation of the Generation-II pH sensor shown in Figure 5-17 begins by pipetting various pH buffer solutions (pH 1 to 5) one at a time into the plastic well. Since Section 5.4 has already validated the performance of Generation-I pH sensing capabilities for pH buffer solutions ranging from pH 1 to 10, only acidic solutions are employed in the study of the Generation-II sensor. Solutions are kept in the well for 5 min to allow the resistance of the $(SWNT\text{-}PSS/PANI)_{100}$ thin film to stabilize before the Solartron 1260 impedance gain/phase analyzer and its reader coil antenna is employed to wirelessly interrogate the remote sensor.

From Figure 5-18a, it can be seen that the passive wireless pH sensor's bandwidth decreases nonlinearly with increasing pH. This inherent nonlinearity is expected, since, from Equation 5-3b and as mentioned in Section 5.4, it is apparent that RFID system bandwidth is inversely proportional to the $(SWNT\text{-}PSS/PANI)_{100}$ nanocomposite resistance. However, based on the results obtained in Chapter 4, it is expected that $(SWNT\text{-}PSS/PANI)_{100}$ resistance should increase near-linearly in tandem

with increasing pH. Therefore, upon back-calculating thin film resistance using Equation 5-3b, it can be observed from Figure 5-18b that film resistance indeed varies near-linearly with pH.

5.5.4. Generation-II Accomplishments and Challenges

Here, the design objective of Generation-II is to miniaturize the passive wireless sensor form factor using commercially available planar TI coil antennas. Taking advantage of the versatility of the layer-by-layer technique to deposit nanocomposites onto a variety of substrates, $(\text{SWNT-PSS/PVA})_n$ and $(\text{SWNT-PSS/PANI})_n$ thin films are directly deposited onto TI planar antennas printed on a PET substrate. By doing so, the large magnet wire coil antennas used in the Generation-I sensor platform become obsolete, and the sensor form factor (*i.e.*, length, width, and thickness) can be dramatically reduced.

Upon film deposition, the nanocomposite and TI antenna is connected in parallel to a leaded ceramic tuning capacitor (using single-stranded wire and colloidal silver paste) for realizing passive wireless communication. The first objective of this section has been attained where Generation-II RFID sensors exhibit the same wireless communication capabilities when compared to Generation-I. Second, this study has also validated wireless strain and pH sensing; experimental results from both strain sensing and pH detection suggest nonlinear changes in RFID system bandwidth as a function of the applied external stimuli. Nevertheless, upon back-calculating thin film resistance, both films exhibit near-linear changes in resistance in tandem with strain or pH.

It should be mentioned that these Generation-II RFID devices have potential for future field applications. Despite the low power output of the Solartron 1260 impedance gain/phase analyzer (1 V), the typical read range of the aforementioned passive wireless sensors is approximately 10 cm (in air). The read range diminishes to about 3 to 5 cm if a 2-cm concrete plate is placed between the RFID reader and sensor tag (to simulate typical conditions if sensors are embedded and covered with the minimum amount of concrete cover). In addition, if metal such as reinforcement bars are within the vicinity of the tag, a reference circuit can be included within the sensor design to minimize interference and eddy currents as have been done by Simonen, *et al.* [26]. Nevertheless,

higher powered commercial portable readers exist and can be employed to dramatically extend sensor interrogation distances.

Despite potential field applicability, one severe limitation of Generation-II sensors is that electrical connections still require single-strand wire and colloidal silver paste. Particularly, and as can be seen from Figure 5-17, the tuning capacitor is loosely connected to the sensor platform; such connections are likely fragile and can be damaged during embedment within structural components. Furthermore, manual soldering of the tuning capacitor to the Generation-II sensor platform is not a scalable approach for commercializing these passive wireless sensors for structural monitoring. As a result, an even more compact and robust sensor design is required.

5.6. Generation-III Embeddable PCB Passive Wireless Sensor

5.6.1. Generation-III PCB Passive Wireless Sensor Fabrication

Based upon the limitations observed in Generation-I and Generation-II sensor platforms, a miniature, embeddable, and robust Generation-III passive wireless sensing system is proposed. First, the same small form factor and interrogation read-range is preserved by employing a coil antenna of similar dimensions. Instead of using commercially available Texas Instruments, Inc. RFID thin film tags, printed circuit board technology is adopted to electroplate a 10-turn coil antenna with an inductance of approximately 2.6 μH (2.3 x 2.4 cm^2 as shown in Table 5-1) onto an FR4 laminate substrate (Figure 5-19). The design of this miniature PCB coil antenna substrate is accomplished using computerized software (*i.e.*, CircuitMaker and TraxMaker) to precisely lay out traces and coils to obtain the desired geometry and dimensions. Coil antennas of specific inductance (in this case 2.6 μH) are obtained by controlling the coil dimensions (*i.e.*, width and length), trace widths, and spacing [119]. In addition, undesirable skin effects are limited by designing coil traces and spacing to be both 0.3 mm [120]. Upon design completion, the prototype is fabricated and electroplated by AP Circuits. A picture of the final fabricated board is shown in Figure 5-20a.

It should also be noted that, as opposed to connecting a tuning capacitor with single-stranded wire and colloidal silver paste, the board design incorporates patterned electrodes for soldering surface mounted device (SMD) 1,000 pF ceramic capacitors (4.7

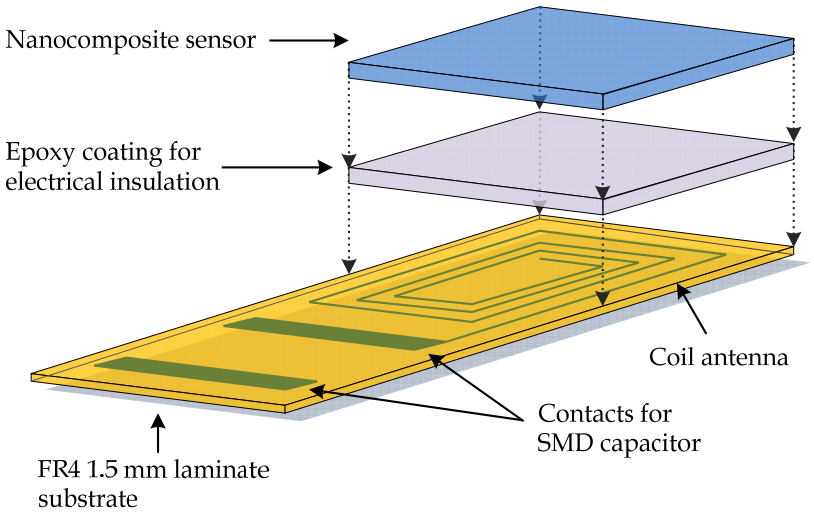

Figure 5-19. A schematic illustrating the design and fabrication of the Generation-III PCB passive wireless sensor.

mm long, 2.0 mm wide, 1.5 mm thick). These surface-mounted capacitors are significantly smaller than traditional leaded capacitors (*i.e.*, those used in Generation-II sensors). As a result, the use of SMD capacitors significantly reduces the form factor of this passive wireless sensor design. Then, these FR4 laminate substrates and the coil antenna are coated with a thin layer of epoxy for electrical insulation and are utilized as LbL substrates for depositing nanocomposite sensors. Similar to Section 5.5.1, strain sensing via sensor bandwidth changes is accomplished by depositing (SWNT-PSS/PVA)$_{100}$ thin films, whereas pH sensing employs the (SWNT-PSS/PANI)$_{100}$ film. The final form factor of the Generation-III passive wireless sensor is approximately 37 mm long, 24 mm wide, and 1.6 mm thick. A schematic of the Generation-III passive wireless system is presented in Figure 5-19.

5.6.2. Generation-III Wireless Strain Sensing

The as-fabricated Generation-III passive wireless strain sensor (Figure 5-20) is epoxy-mounted to PVC testing coupons for mechanical loading consistent with the experimental setup presented in Sections 5.4.2 and 5.5.2. Upon mounting the Generation-III wireless strain sensor and PVC bar in an MTS-810 load frame, a monotonic tensile load pattern (-5,000 to 5,000 με) is executed, and the load frame is paused at every 1,000 με interval for wireless data acquisition. On the other hand, the

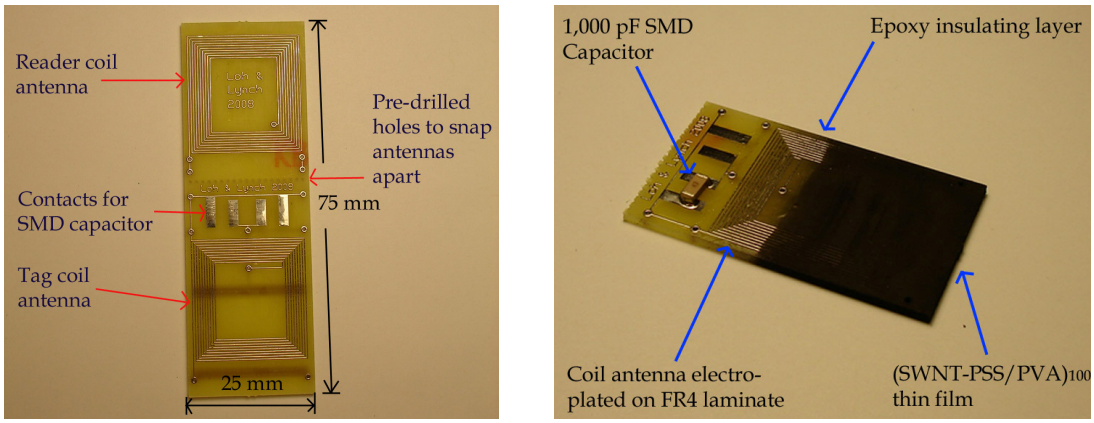

(a) (b)

Figure 5-20. A picture of the (a) designed and fabricated Generation-III electroplated FR4 laminate and (b) a Generation-III passive wireless strain sensor.

RFID reader employs the same 10-turn planar coil antenna for wireless communications; complex impedance measurements of the coil antenna are measured by the Solartron 1260 impedance gain/phase analyzer.

First, to validate wireless communications, the RFID reader is employed to interrogate an unloaded Generation-III passive wireless strain sensor. Complex impedance magnitude and phase measurements as measured by the RFID reader (Figure 5-21) show excellent communication capabilities despite the smaller sensor form factor. Second, upon mechanical load testing, the summary of results is shown in Figure 5-22. It can be clearly observed from Figure 5-22 that the passive wireless strain sensor's bandwidth, as measured wirelessly via impedance phase changes by the reader, decreases with increasingly applied tensile strain. In addition, the strain sensor's bandwidth varies near-linearly to applied strain (the strain sensitivity is estimated to be 0.57 Hz-$\mu\varepsilon^{-1}$). Similar to previous RFID strain sensing studies presented in this chapter, the nanocomposite's resistance to applied strain is back-calculated using Equation 5-3b and plotted in Figure 5-23. As expected, the $(SWNT\text{-}PSS/PVA)_{100}$ thin film increases its resistance in tandem with increasing strain ($S_R \approx 1$).

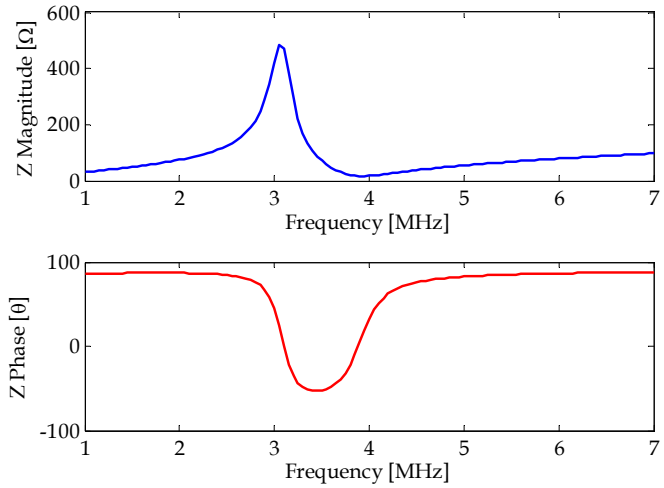

Figure 5-21. The (top) impedance magnitude and (bottom) phase response of the unloaded Generation-III passive wireless strain sensor as measured wirelessly by the RFID reader.

5.6.3. Generation-III Wireless pH Sensing

The Generation-III passive wireless pH sensor is realized by depositing (SWNT-PSS/PANI)$_{100}$ thin films onto PCB coil antennas. To maximize thin film exposure to pH buffer solutions, epoxy is applied onto areas where the thin film is electrically connected to the parallel resonant tag circuitry. The main reason for applying epoxy at electrodes is to prevent the RFID sensor's bandwidth from being influenced by the pH buffer solution's inherent conductivity. Thus, any bandwidth changes associated with applied pH variations will be solely caused by changes in the nanocomposite's resistance response. Then, pH sensing studies are conducted by dipping the entire pH sensor tag into pH buffer solution baths (pH 1 to 11) while wirelessly measuring changes using the aforementioned RFID reader.

Figure 5-24 plots the passive wireless pH sensor's impedance-frequency response as determined by the RFID reader. It should be noted that only select plots are presented to enhance the clarity of the printed figure. From Figure 5-24, it can be clearly seen that inductive coupling between the reader and tag is observed near the sensor tag's 3.0 MHz characteristic frequency as expected. As the sensor tag is exposed to increasing alkaline pH buffer solutions (1 to 11), the maximum detected impedance magnitude decreases

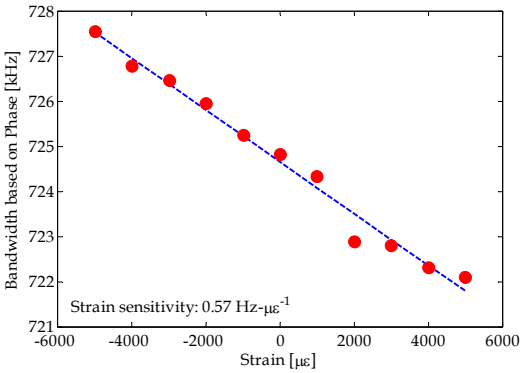

Figure 5-22. The Generation-III passive wireless strain sensor's bandwidth decreases near-linearly with applied tensile strain.

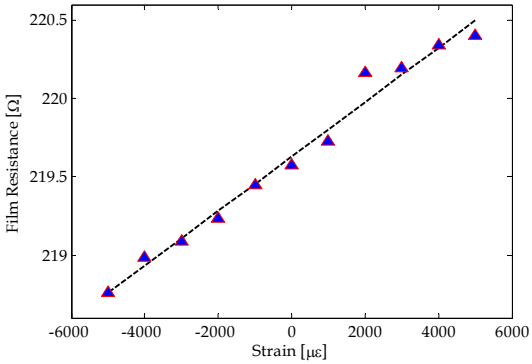

Figure 5-23. Upon back-calculating the $(SWNT\text{-}PSS/PVA)_{100}$ thin film's resistance, near-linear resistance changes to applied strain is observed ($S_R \approx 1$).

while the bandwidth of the reader-tag system increases; Figure 5-25 summarizes system bandwidth dependency to applied pH. Thus, as the nanocomposite's resistance increases with increasing pH (Figure 2-21), RFID bandwidth decreases in accordance with Equation 5-3b. Theoretically, although bandwidth change is nonlinearly related to pH, a linear least-squares fit can be obtained to estimate the inductively coupled sensor sensitivity to be 3.9 kHz-pH^{-1}. This high estimated pH sensitivity suggests that these passive wireless sensors hold promise for applications in field environments to monitor pH (and corrosion environments).

5.6.4. Generation-III Accomplishments and Challenges

The proposed Generation-III strain and pH sensors have accomplished all the objectives set forth for the design of passive wireless sensing systems. First, instead of using magnet wire coil antennas or single strand wire for electrical connections, the entire sensor design and coil antenna is electroplated onto FR4 laminate substrates via PCB technology. The size of the circuit elements is dramatically reduced through the use of SMD capacitive components to tune the sensor resonant frequency. Finally, strain and pH sensing is enabled by using the printed circuit board as the LbL substrate to deposit $(SWNT\text{-}PSS/PVA)_{100}$ and $(SWNT\text{-}PSS/PANI)_{100}$ thin films, respectively. The end result is an RFID sensor that is low in cost and has a small form factor.

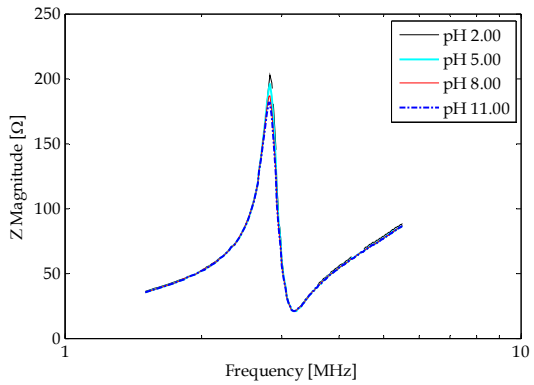

Figure 5-24. Select impedance magnitude-frequency plots measured by the RFID reader are presented to illustrate sensor response to various applied pH buffer solutions.

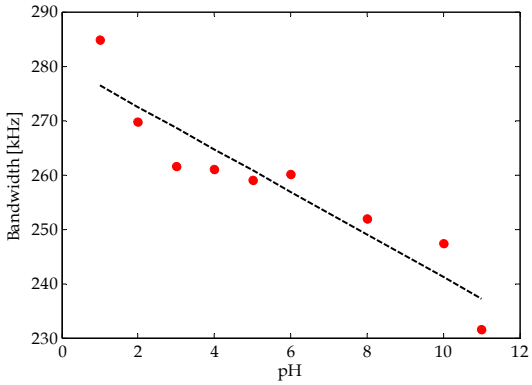

Figure 5-25. The RFID system bandwidth decreases with increasing pH buffer solutions; the sensitivity of the proposed system is approximately 3.9 kHz-pH^{-1}.

First, upon loading the Generation-III passive wireless sensors in uniaxial and monotonic tensile loading (±5,000 με and pausing at every 1,000 με intervals), the experimental results reveal extremely high sensor linearity, sensitivity, and resolution. In this case, strain is detected via bandwidth changes due to piezoresistive response of the $(SWNT\text{-}PSS/PVA)_{100}$ thin film. The sensitivity of the RFID strain sensor is estimated to be approximately 0.57 Hz-με^{-1}. Similarly, for wireless pH sensing, $(SWNT\text{-}PSS/PANI)_{100}$ films deposited onto PCB substrates also exhibit excellent and near-linear pH sensing performance. Similar to the proposed strain sensor, the wireless pH sensor decreases its system bandwidth with increasingly alkaline pH buffer solutions. This sensor has been validated to detect pH solutions ranging from 1 to 11, and the overall sensitivity of the sensor is 3.9 kHz-pH^{-1}. For both sensors proposed, the significantly smaller form factor suggests that these sensors are now suitable for embedment within structural components such as concrete (*e.g.*, to monitor strain or corrosion). However, in order to incorporate these sensors for distributed sensing of composites such as carbon-fiber reinforced polymers, greater ductility (*i.e.*, not based on brittle FR4 PCB).

5.7. Patterning of Coil Antennas in SWNT-based Thin Film Sensors

Thus far, three generations of passive wireless pH and corrosion sensors have been presented. While significant performance improvements have been achieved and sensor form factors have been dramatically reduced with increasing sensor generations, the fundamental designs still rely on using nanocomposites as an RC-circuit element (*e.g.*, a resistor or capacitor). In addition, every sensor design has required the use of a leaded or surface-mounted capacitor in order to tune the resonant frequency of the passive wireless RFID sensor. On the other hand, electrical impedance spectroscopic studies conducted in Chapter 4 have already revealed the RC-circuit behavior of $(SWNT\text{-}PSS/PVA)_n$ thin films. In fact, the equivalent circuit derived (Figure 4-8) represent a parallel resonant RFID circuit that is missing an inductor component. In fact, patterning technologies (*e.g.*, mechanical etching, focused ion beam, and photolithography) can be employed to pattern nanocomposites to coil antenna shapes, thereby embedding the inductor element with its inherent RC-circuit parallel. Thus, the final sensor design is an LbL-assembled RFID wireless sensor without the need for any external parts (*e.g.*, resistors, capacitors, or inductors).

However, in order to achieve a thin film that exhibits sensitivity to applied external stimuli and be able to communicate wirelessly via inductive coupling, the patterned thin film coil antenna must possess extremely high conductivity for passive wireless communications [121]. Thus, research to fabricate highly conductive thin films using the layer-by-layer self-assembly method is currently underway. It is hypothesized that while carbon nanotubes exhibit near-ballistic transport-type electronic behavior [48], the deposition of other polyelectrolyte species during LbL greatly reduces bulk film conductivity [77]. However, through the incorporation of metallic nanoparticles (*e.g.*, gold) within a polymer matrix, Liu, *et al.* [122] have successfully fabricated LbL films with bulk metal conductivity. Furthermore, through the addition of carbon nanotubes and a variety of polyelectrolyte species, it is hoped that an LbL-assembled passive wireless sensor can be achieved.

Fabrication of carbon nanotube-gold nanoparticle LbL thin films begins by preparing a new set of polycationic and polyanionic solutions. First, by dissolving 1.0 $mg\text{-}mL^{-1}$ of $HAuCl_4$ (Alfa Aesar) in a 1.0 *wt.* % PVA polycationic solution, gold

nanoparticles are formed upon reducing $HAuCl_4$ with 0.1 M sodium borohydride ($NaBH_4$) solution (similar to the procedure reported by Zhang, *et al.*, [123]). Upon vigorous stirring for 10 min, a pink solution is formed, indicating the completion of preparing the polycationic gold nanoparticle solution (denoted as GNP-PVA). As opposed to using PSS for surfactant steric stabilization of SWNTs, sodium dodecyl sulfate (SDS, $M_w \approx 288.38$, Sigma-Aldrich) is employed for its smaller molecular size and high nanotube deposition density during LbL. Furthermore, preparation of SWNT-SDS dispersed suspensions only require the use of 180 min of ultrasonication bath (no need for using the high-energy probe sonicator), thereby preserving the mechanical and electrical properties of these carbon nanotubes.

Once the polycationic GNP-PVA and polyanionic SWNT-SDS solutions are prepared, the LbL method continues by sequentially dipping a charged glass substrate in these solutions (as described in Section 2.2.1 of this dissertation). The SEM image of an $(SWNT\text{-}SDS/GNP\text{-}PVA)_2$ thin film is presented as evidence for the successful deposition of both carbon nanotubes and gold nanoparticles even only after two LbL bilayers (Figure 5-26). Upon film fabrication, these $(SWNT\text{-}SDS/GNP\text{-}PVA)_{50}$ thin films are patterned into conductive coil antennas via high-precision mechanical cutting as shown in Figure 5-27. In fact, preliminary two-point resistance measurements of these $(SWNT\text{-}SDS/GNP\text{-}PVA)_{50}$ thin film coil antennas suggest 4 to 5 times lower resistance than the aforementioned strain and pH thin film sensors [77]. Although film conductivity is greatly enhanced through the incorporation of GNPs and the SDS surfactant for nanotube dispersion and deposition, the coil antenna remains limited by a moderate resistance. After connecting the $(SWNT\text{-}SDS/GNP\text{-}PVA)_{50}$ coil antenna in series with a 0.1 μF capacitor to form a series resonant circuit (Figure 5-27), the bandwidth of this system still remains too high for any potential wireless communications (as governed by Equation 5-3a).

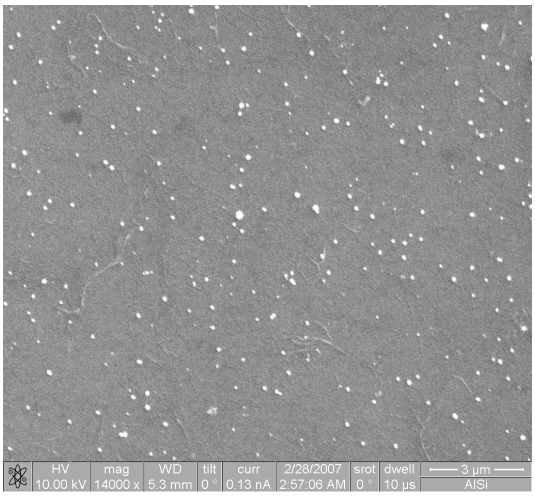

Figure 5-26. An SEM image of a (SWNT-SDS/GNP-PVA)$_2$ thin film showing deposition of both nanotubes and gold nanoparticles (white dots) even after the formation of two bilayers.

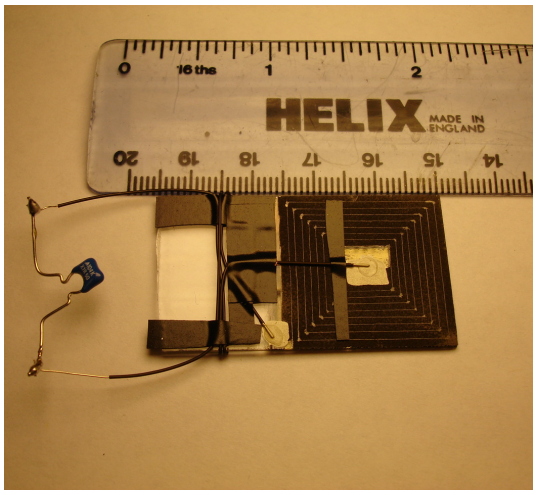

Figure 5-27. A picture of a (SWNT-PSS/GNP-PVA)$_{50}$ thin film patterned into a coil antenna to realize a series resonant RFID circuit.

Nevertheless, to validate that the patterned coil antenna indeed does behave as an inductor, the series resonant circuit of Figure 5-27 is connected to the Solartron 1260 impedance gain/phase analyzer to measure its complex impedance over a range of frequencies. From Equation 5-6, one can then deduce the equivalent complex impedance of a series resonant circuit (which is simply the summation of the impedances of the inductor, its series resistance, and the capacitor) as given in Equation 5-11:

$$Z = Z_L + Z_R + Z_C \tag{5-11}$$

where Z_L, Z_R, and Z_C is given in Equation 5-6. From Equation 5-11 and Figure 5-28, it is apparent that resonance will occur when a dip is observed in the impedance magnitude-frequency plot. For the aforementioned series resonant circuit, the resonant frequency is identified as approximately 417 kHz.

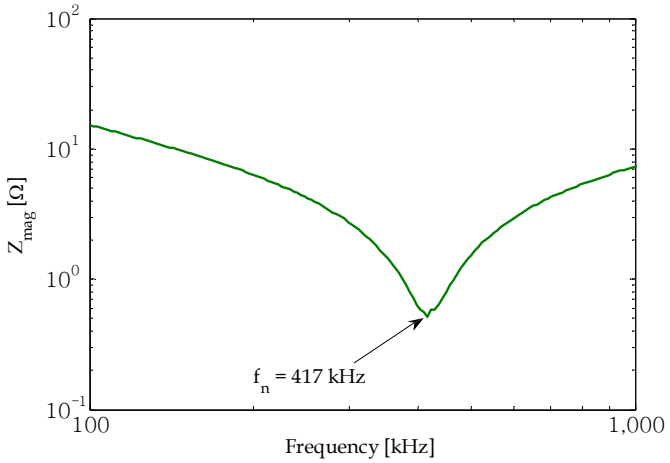

Figure 5-28. Experimental RFID reader response collected from (SWNT-SDS/GNP-PVA)$_{50}$ thin film coil antenna coupled with a 0.1 µF capacitor.

In the near future, the fabrication of highly conductive GNP-based LbL thin films will continue. As evident from the SEM image of Figure 5-26, the deposition of GNPs is sparse throughout the film surface. It is anticipated that by synthesizing smaller-sized GNPs with diameters between 2 to 25 nm using thiocyanate or sodium citrate, dense GNP deposition (up to 1800 nanoparticles per µm^2) can be achieved resulting in films characterized by higher conductivity [124]. Alternatively, MEMS processes can be employed to sputter thin copper coils on the LbL substrates to form a wireless antenna upon which thin films can be adsorbed.

5.8. Summary and Conclusions

5.8.1. Results and Discussion

In this study, three generations of passive wireless sensors for monitoring strain and pH are proposed. First, Generation-I strain and pH sensors are fabricated by physically connecting (SWNT-PSS/PVA)$_n$ and (SWNT-PSS/PANI)$_n$ thin films to magnet wire coil antennas to validate wireless communications via inductive coupling. The experimental results shown in this chapter successfully demonstrate the ability of inductive coupling to measure strain and pH via sensor resonant frequency and

bandwidth changes, respectively. However, in order to achieve wireless communications, magnet wire coil antennas with diameters of 5 to 80 mm are required.

To miniaturize the overall passive wireless sensor design, commercially available antennas printed on PET thin films are obtained from Texas Instruments, Inc. Furthermore, instead of electrically connecting thin films to the TI coil antenna, the coil antenna printed on the PET substrate is utilized as the substrate material during layer-by-layer assembly. As a result, piezoresistive and pH sensitive nanocomposites can be directly deposited onto the coil antenna to achieve a device characterized by a small thickness. However, circuit elements, such as the tuning capacitor, need to be soldered and connected to the sensor tag via colloidal silver paste. Although wireless communications along with strain and pH sensing have been validated, the device is relatively fragile and is unsuitable for use in laboratory and field environments.

Thus, to preserve the sensor miniaturization (achieved in Generation-II devices) while simultaneously optimizing sensor performance (Generation-I sensors), printed circuit board technology is employed to design the Generation-III sensor platform. Here, the entire parallel resonant circuitry of the sensor tag, along with a 10-turn planar coil antenna, is electroplated onto FR4 laminate substrates. Then, LbL assembly is employed to deposit $(\text{SWNT-PSS/PVA})_n$ and $(\text{SWNT-PSS/PANI})_n$ thin films for strain and pH sensing, respectively. The final sensor device is characterized by a small form factor. Upon conducting monotonic tensile tests to explore the sensor's strain sensing response, high linearity, sensitivity, and resolution has been observed. Similarly, carbon nanotube-PANI films deposited onto the Generation-III platform also exhibit enhanced pH sensing capabilities. In short, the Generation-III sensor platform encompasses advantages offered by Generation-I (*i.e.*, wireless communications) and Generation-II (*i.e.*, sensing performance and small form factor). In addition, the sensing system is fabricated on a mechanically-strong FR4 laminate, thereby possessing great potential for embedment within structural materials (*e.g.*, concrete) for structural health monitoring.

5.8.2. Contributions

In the beginning of this chapter, it has been stated that the main objective is to design and develop a high performance and low cost passive wireless sensor using

multifunctional nanocomposites. Furthermore, the goal is to achieve a sensor platform that is suitable for embedment within structures and can be densely-distributed for component-level structural health monitoring as discussed in Chapter 1. Through three generations of passive wireless sensors, the Generation-III sensor platform combines the advantages offered by nano- and micro-fabrication technology and exhibits favorable characteristics such as low cost, small form factor, excellent strain and pH sensing performance, and reliable wireless communications.

More importantly, this chapter presents a strategy for overcoming one of the fundamental limitations of nanotechnology – that is its scalability. First, based on findings presented in Chapters 2 and 4, nanocomposites are molecularly encoded with specific sensing capabilities (*i.e.*, strain and pH sensing). However, as opposed to simply using these nanocomposites as point sensors connected to a centralized data repository via coaxial cables, wireless communication capabilities are enabled through micro-fabrication (*i.e.*, PCB technology) of coil antennas suitable for inductive coupling. Since PCB technology has already been widely adopted in industry, this technique for sensor fabrication is ideally suited for industry adoption. Furthermore, to enhance scalability, structural health monitoring can be achieved by embedding these sensors in structures in a densely-distributed fashion. On the other hand, preliminary results for a complete nanotechnology-driven wireless sensor have also been presented, where highly conductive thin films can simultaneously provide wireless communications and sensing. These ultra-thin sensors can then find applications where sensor form factor and weight is crucial (*e.g.*, within composite materials in aerospace systems, among others).

Unfortunately, the proposed RFID-based sensors are still based on the premise of the current generation of structural health monitoring paradigm (*i.e.*, to utilize densely distributed point sensors to infer the location and severity of structural damage). Furthermore, although wireless communications have been successfully validated, RFID-based technologies have short read ranges often less than a meter. This severe limitation prevents their applicability in complex structural systems such as tall buildings. Thus, an alternative approach is still required to be able to directly measure damage over large spatial areas.

CHAPTER 6

APPLICATION OF SENSING SKINS FOR SPATIAL DAMAGE DETECTION

6.1. Introduction

As highlighted in previous chapters of this dissertation, structural health monitoring has been undergoing a paradigm shift from global-based vibration monitoring to component-level damage detection. While traditional metal-foil strain gages or even the aforementioned multifunctional nanocomposite sensors can be installed to obtain local strain measurements, their main disadvantage is that they can only provide response data at one discrete location in the structure. Accurate damage detection requires either a dense network of these point-sensors or accurate models that extrapolate localized strain fields to the remainder of the structure. On the other hand, multifunctional nanocomposite sensors can be coupled with radio frequency identification (or inductively-coupled) communication technologies to realize passive wireless sensing for densely-distributed structural monitoring (Chapter 5). While densely-distributed sensors provide more detailed information regarding structural response to ambient or forced excitations, damage detection still requires data interrogation algorithms that hypothesize damage in locations away from the sensors.

Novel distributed sensing technologies are needed to offer SHM systems improved resolutions for damage detection. One emerging distributed sensing paradigm are "active" sensors based on ultrasonic nondestructive evaluation (NDE) techniques. Specifically, guided-waves show tremendous promise for accurate damage detection and localization in thin walled structures [28, 125]. With ultrasonic waves able

to propagate over long distances, this sensing approach provides the sensor with alarge interrogation zone.

Multifunctional materials, such as the nanocomposites at the center of this dissertation, also offer exciting new methods for distributed sensing. Since the material senses everywhere the material is, it is by its very nature a distributed sensor. Hence, the objective of this chapter is to again employ SWNTs as a building block for the design and fabrication of multifunctional "sensing skins" capable of monitoring structural damage without having to probe multiple discrete sensor locations to infer the characteristics (*i.e.*, type, location, and severity) of damage. The proposed sensing skin seeks to: (1) spatially image deformation (*i.e.*, strain), (2) identify and locate foreign object and blast debris impact, and (3) observe the formation of corrosion byproducts or changes in pH which is indicative of corrosion. Using the aforementioned layer-by-layer self-assembly process (Section 2.2.1), individual SWNTs are functionalized with various polyelectrolyte species for embedding multiple sensing transduction mechanisms within the composite's morphology as discussed in Chapter 4 [77]. Here, SWNT-based LbL nanocomposites are embedded with strain sensitivity and corrosion detection capabilities [77, 111]. It will be shown that applied strain, impact damage, corrosion byproduct formation, and pH alter thin film conductivity, thereby enabling a multifunctional composite capable of monitoring common structural damage processes. Realization of a sensing skin with spatial resolution is achieved by coupling the nanocomposites with the well-established electrical impedance tomographic (EIT) spatial conductivity imaging technique [126-129]. In short, the EIT conductivity mapping technique relies on repeated electrical measurements at the film boundary so as to inversely reconstruct the skin's spatial conductivity distribution. Since the LbL-based sensing skin is embedded with specific sensing transduction mechanisms, changes in film conductivity can be directly correlated to strain, impact, corrosion, pH, among others. This chapter begins with a brief summary of electrical impedance tomography; interested readers are referred to more extensive treaties on the method [127]. Then, the EIT method is validated by intentionally manufacturing films with defects consistent with non-uniform conductivity distributions. In addition, the accuracy and resolution of nanocomposites' EIT spatial conductivity maps are also validated. Finally, upon EIT

validation, the sensing skins are experimentally demonstrated to detect: (1) tensile-compressive cyclic strains, (2) impact damage, (3) corrosion byproduct formation in metallic plates, and (4) pH exposure.

6.2. Electrical Impedance Tomography

6.2.1. Forward Problem: Background and Theoretical Foundations

Given any two- (2D) or three-dimensional (3D) linear isotropic medium (**Ω**) described by a time-invariant conductivity distribution (σ), Faraday's Law of Induction states,

$$\nabla \times \boldsymbol{E} = -\frac{\partial}{\partial \mathrm{t}}\mathbf{B} \tag{6-1}$$

and Ampere's Law states:

$$\nabla \times \boldsymbol{H} = \sigma \boldsymbol{E} + \boldsymbol{J}^{S} \tag{6-2}$$

where $\boldsymbol{E}$ is the electric field, $\boldsymbol{H}$ is the magnetic field strength, $\boldsymbol{B}$ is the magnetic field ($\boldsymbol{B}=\mu_0\boldsymbol{H}$), μ_0 is the magnetic permeability, and $\boldsymbol{J}^s$ is the current density of current sources within the body **Ω** [129, 130]. By neglecting the magnetic field when using static or low-frequency currents, Equations 6-1 and 6-2 can be combined to yield Equation 6-3, which is termed the Laplace Equation. This equation is widely used to model the flow of electrical current and the development of electrical potential, ϕ, within conductive and semiconducting bodies:

$$\nabla \cdot (\sigma \nabla \phi) = I \tag{6-3}$$

Here, it is assumed that current I is neither supplied nor generated within **Ω** and hence, the right hand side of the Laplace equation is set to zero. The flow of current within the body is therefore due to current supplied at the boundary of **Ω**. For a two-dimensional body (*e.g.*, idealized thin film materials) with direct current applied to the body's

boundary, Equation 6-3 can be rewritten as the 2D Laplace equation (Equation 6-4) to describe current flow at every location within **Ω** (based on a two-dimensional (x, y) Cartesian coordinate system) [129].

$$\nabla \cdot [\sigma(x,y)\nabla\phi(x,y)] = 0 \tag{6-4}$$

Similarly, if an alternating current of cyclic frequency ω is applied to the medium, then the 2D Laplace equation is expressed as:

$$\nabla \cdot [\gamma(x,y,\omega)\nabla\phi(x,y,\omega)] = 0 \tag{6-5}$$

where the conductivity (σ) of **Ω** is replaced with the complex admittance, γ, to account for the body's conductivity, AC signal frequency, and material permittivity (ε) as shown in Equation 6-6.

$$\gamma = \sigma + i\omega\varepsilon \tag{6-6}$$

However, it is generally assumed that the applied electric signal's frequency is sufficiently low, such that $\omega\varepsilon$ is infinitesimally small and $\gamma \approx \sigma$. In that case, Equation 6-4 is generally adopted in EIT formulation. From a continuum model's perspective, it is assumed that there are no discrete electrodes and that the applied current is defined as a continuous function along the body boundary, $\partial\Omega$ [129]. Regardless, if the potential of the boundary (ϕ) can be measured, the Dirichlet boundary condition states that

$$\phi(x,y) = v(x,y) \text{ at } \partial\Omega \tag{6-7}$$

where v is the measured boundary voltage (or potential) drop. In addition, if the sum of input and output current, I, along the entire medium's boundary is zero (*i.e.*, if the line integral of current along $\partial\Omega$ is zero), then the Neumann's boundary condition is satisfied as shown in Equation 6-8.

$$\oint I(\omega)\, \partial\Omega = 0 \tag{6-8}$$

Herein, the combination of the 2D Laplace equation (Equation 6-4) and Dirichlet-Neumann boundary conditions (Equations 6-7 and 6-8) is referred to as the forward problem for the EIT continuum model. The forward problem guarantees that the boundary potential (v) can be determined theoretically via a known and continuous boundary current function applied to a body's boundary, $I|_{\partial\Omega}$, where the body is characterized by a conductivity distribution function, $\sigma(x, y)$ [131].

6.2.2. Finite Element Method (FEM) Formulation

Often, the EIT forward problem cannot be solved in the continuum domain since a continuum spatial conductivity distribution function and an applied boundary current function are practically unobtainable. Furthermore, the solution to the continuum 2D Laplace equation is mathematically rigorous and at times implausible. As a result, a discretized weak form of the forward problem (Section 6.2.1) is obtained using variational mechanics and techniques such as the finite element method (FEM). Here, FEM discrete elements of constant properties (*e.g.*, conductivity) are employed to approximate the continuous 2D conductivity distribution function (σ) [129, 132]. Similarly, as opposed to relying on a continuous boundary current function which is also practically unobtainable, the complete electrode model, which discretizes the boundary into a finite number of electrodes (L), is implemented for finite element analyses [129, 133].

For the FEM formulation employed in this chapter, n triangular elements with second-order parabolic basis functions, w_i, are employed. The potential along the boundary of each element ($\phi|_{\partial\Omega_E}$) can then be obtained by taking the sum of the three nodal (*i.e.*, the vertices of the triangular element) potentials of each i^{th} element multiplied by each of its corresponding basis functions as shown in Figure 6-1a and Equation 6-9:

$$\phi|_{\partial\Omega_E} = \sum_{i=1}^{3} \phi_i w_i \tag{6-9}$$

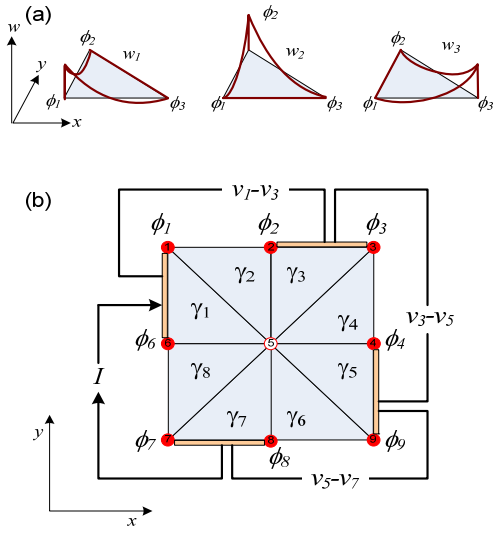

Figure 6-1. Discretized FEM formulation of the Laplace equation: (a) second-order polynomial basis functions, w_i, corresponding to a triangular element; (b) eight-element body with boundary current, I, and voltages, v.

Since the basis functions are not differentiable at the i^{th} node, the weak formulation of the Laplace equation is derived using variational methods:

$$\int_v V[\nabla \cdot (\sigma \nabla \phi)] dV = 0 \tag{6-10}$$

where V is an arbitrary function and Equation 6-10 is integrated over the body **Ω**. The combination of the weak form of the Laplace equation (Equation 6-10), the discretization of potential (Equation 6-9), and the Dirichlet-Neumann boundary conditions, results in a linear set of equations. When combined in a single matrix equation, the equation is a linear equation of the classical $Ax=b$ form:

$$\begin{bmatrix} \mathbf{A}_M + \mathbf{A}_Z & \mathbf{A}_W \\ \boldsymbol{A}_W^T & \mathbf{A}_D \end{bmatrix} \begin{bmatrix} \Phi \\ E \end{bmatrix} = \begin{bmatrix} 0 \\ I \end{bmatrix} \tag{6-11}$$

where $\Phi = (\phi_1, \ldots, \phi_n)^T$ is a vector that includes all elemental nodal potentials, $E = (v_1, v_2, \ldots, v_p)^T$ is a vector that contains all measured boundary electrode voltages, and **A** is a square matrix calculated from the basis functions (w) and element conductivities (σ) [127].

Thus, Equation 6-11 provides the foundation for determining the measured boundary voltage, E, due to the application of a known boundary current, I, to the numerically meshed body.

For example, the thin film body in Figure 6-1b is meshed using eight elements defined by nine nodes. If a current I is sourced at element 1 and drained at element 7, then Equation 6-11 can be solved for the electric potential at the nine nodes $\Phi = (\phi_1,\ldots, \phi_9)^T$ and for the voltage measured across the three adjacent electrodes, $E = (v_1, v_3, v_5, v_7)^T$. It should be noted that, in this example, **A** is a 13 x 13 square matrix. Provided the system matrix is often sparse, LU decomposition is generally required to solve the forward problem. The reader is referred to Hou, *et al.* [128] for a more detailed discussion regarding the implementation of triangular elements and the finite element method for electrical impedance tomography of thin film composites.

6.2.3. Inverse Problem: Electrical Impedance Tomographic Conductivity Mapping

In short, electrical impedance tomography relies on a complete set of simultaneous current injection and voltage measurements along a body's boundary (*i.e.*, at its electrodes) to reconstruct its spatial conductivity distribution (herein termed the inverse problem and illustrated in Figure 6-2). By its nature, the aforementioned inverse problem is ill-posed such that a unique solution may not exist for a data set corresponding to a single current pattern [127, 129]. Therefore, current is injected on all possible sets of adjacent electrodes, with voltage measurements taken for each current pattern, thereby yielding an over-determined data set. The inverse problem then seeks to determine the optimal spatial conductivity distribution by minimizing the difference between predicted boundary electrode potentials (as calculated by an assumed σ distribution based on the FEM model) with actual experimental boundary voltage measurements, E. More specifically, each step of the iterative inverse problem updates each FEM element's conductivity and solves the forward problem to determine the set of predicted boundary potentials. The predicted boundary potentials are compared to experimental boundary voltage measurements, and the EIT forward problem seeks to minimize a quadratic least-squares objective function such as Equation 6-12 [131].

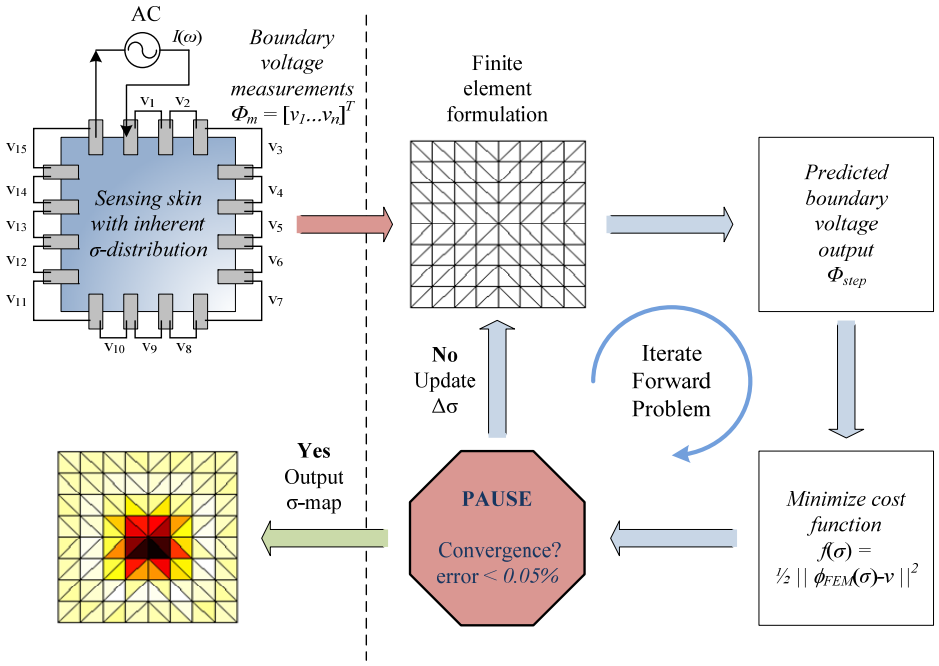

Figure 6-2. A schematic illustrating the electrical impedance tomography spatial conductivity reconstruction process. The left side of the schematic shows the nature of the inverse problem (*i.e.*, using boundary electrical measurements and known current inputs to find the conductivity distribution of the sensing skin). In order to solve for the spatial conductivity distribution, an iterative process utilizing the finite element method is employed to repeatedly solve the forward problem until the solution converges (minimization of the cost function).

$$f(\sigma) = \frac{1}{2}\|\phi(\sigma)|_{\partial\Omega} - v\|^2 \tag{6-12}$$

Here, to solve the EIT spatial conductivity reconstruction, a regularized Gauss-Newton algorithm is employed to minimize a similar but augmented least-square functional that takes into account regularization. The iterative algorithm is executed until the difference between the predicted boundary potential, $\phi(\sigma)$, and experimental boundary voltage measurements are within an acceptable error threshold (*i.e.*, when $f(\sigma) \leq 0.05\%$). Upon convergence of the iterative Gauss-Newton inverse problem (*i.e.*, when the error threshold criterion is met), the final conductivity map is derived. Unlike techniques such as backprojection which only provide relative spatial conductivity changes between successive EIT boundary electrical measurements, this algorithm reconstructs the absolute film conductivity and will be verified experimentally in Section

6.4.2. In fact, the estimated FEM discrete element conductivities have been compared to experimental two- and four-point probe surface conductivity measurements to verify a maximum error bound of 2.1%. The small experimental error obtained suggests that most of the conductivity variations resulting from EIT spatial conductivity mapping can be attributed to contact impedance uncertainties and measurement error during surface probing [128].

6.3. Multifunctional Sensing Skin Fabrication

6.3.1. Sensing Skin Fabrication and Sample Preparation

Similar to previous chapters presented in this dissertation, multifunctional nanocomposites or sensing skins are fabricated via a layer-by-layer self-assembly thin film fabrication methodology. As opposed to only using glass or silicon as LbL substrates for film deposition, this chapter also employs aluminum 6061-T6 alloy and carbon steel plates as substrate materials. However, to achieve optimal nanocomposite deposition using these metallic substrates, metallic plates are first cleaned with acetone to remove oil residue and then spray-coated with a thin uniform layer of primer to electrically isolate the sensing skins from the conductive substrates. On the other hand, glass substrates are treated with piranha solution to remove surface oil residue and microbes as mentioned in Section 2.2.1. Upon completion of substrate preparation, the LbL process begins by immersing the substrate in the polycationic 1.0 *wt.* % PVA or 1.0 *wt.* % PANI solution for 5 min. The substrate is then rinsed with 18 MΩ Milli-Q deionized water for 3 min and dried with compressed air for 10 min. Then, the substrate, along with its adsorbed PVA or PANI monolayer, is dipped into a SWNT-PSS suspension for 5 min, followed by rinsing (3 min) and drying (10 min). This process completes the adsorption of one nanocomposite bilayer and is repeated 50 or 100 times to achieve a mechanically-strong nanocomposite sensing skin.

6.3.2. EIT Electrode Preparation and Data Collection

As opposed to two- or four-point surface conductivity measurements, electrical impedance tomography relies on a series of boundary electrical measurements for

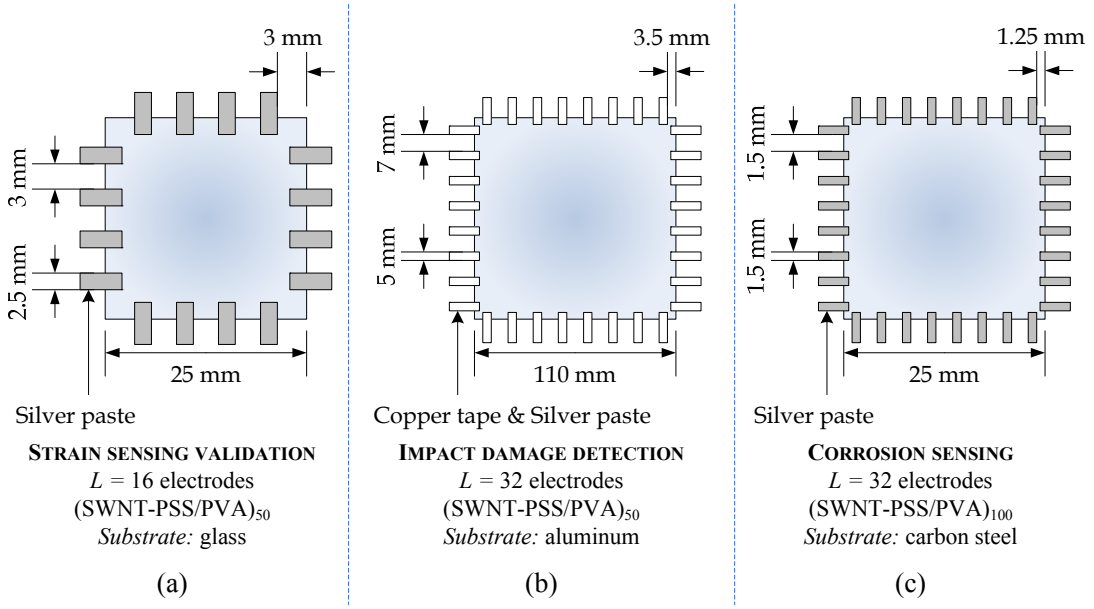

Figure 6-3. A schematic illustrating the EIT electrode configuration. (a) (SWNT-PSS/PVA)$_{50}$ and (SWNT-PSS/PANI)$_{100}$ thin films are deposited on glass substrates for strain sensing and pH sensing validation, respectively. (b) (SWNT-PSS/PVA)$_{50}$ thin films are deposited on 110 x 110 mm^2 primer-coated aluminum 6061-T6 alloy plates for impact damage detection. (c) (SWNT-PSS/PVA)$_{100}$ thin films are deposited onto 25 x 25 mm^2 primer-coated carbon steel plates for accelerated corrosion tests.

reconstructing the 2D (or even 3D) spatial conductivity image of any body, $\boldsymbol{\Omega}$ (as described in Section 6.2). Prior to data collection, sensing skins are instrumented with 16, 32, or 40 electrodes around their boundaries (with equal number of electrodes equidistantly spaced along each boundary of the square/rectangular sensing skin specimens as shown in Figure 6-3). For skins deposited on glass substrates for EIT validation analysis (Section 6.4), strain sensing validation (Section 6.5.1), and those deposited on primer-coated carbon steel for corrosion detection (Section 6.5.3), accurate and precise electrode placement is ensured by using header pins with a fixed spacing. Colloidal silver paste is used to electrically connect the header pins to the nanocomposite surface. On the other hand, electrodes for impact damage identification (Section 6.5.2) are provided using 32 copper tape electrodes; minimization of contact impedance is accomplished by drying colloidal silver paste between the copper tape and nanocomposite skin. The colloidal silver paste is allowed to dry for six hours prior to any experimental tests.

In order to obtain the reconstructed EIT spatial conductivity image, current flow is introduced into the skin at two adjacent electrodes on the skin boundary, while voltage is measured at all remaining electrodes. In this study, the neighboring or adjacent electrode measurement technique is employed [129]. Experimentally, a Keithley 6221 current generator is commanded to inject a regulated AC or DC current into a pair of adjacent electrodes, while a National Instruments (NI) data acquisition system (DAQ) is employed to measure the potential drop across all other adjacent electrode pairs. Using the neighboring electrode measurement technique, a total of $L(L\text{-}1)/2$ measurements are derived (where L is the number of electrodes). While this technique has been demonstrated to produce non-uniform current density within the body leading to reduced sensitivity to conductivity changes located away from the boundary [129], this technique is implemented for its simplicity and fast data acquisition attributes. Furthermore, it will be demonstrated in Section 6.5 that the high damage sensitivity of the proposed nanocomposite skins are unaffected by the neighboring electrode measurement technique.

6.4. EIT Spatial Conductivity Validation

6.4.1. EIT Validation of Conductivity Inhomogeneity

Validation of EIT spatial conductivity mapping of LbL nanocomposites is conducted by assessing conductivity homogeneity variations among four separate $(\text{SWNT-PSS/PVA})_{50}$ thin film specimens deposited on glass (whose dimensions are similar to those in Figure 6-3c). Following LbL fabrication, EIT is performed to obtain baseline conductivity maps (σ_{base}) for each thin film specimen. After the baseline conductivity maps are reconstructed, intentional inhomogeneity is introduced within the film structure by physically etching straight, diagonal, and L-shaped cuts into the film surface (Figures 6-4a, 6-4c, and 6-4e) to create regions of zero conductivity. After etching, EIT is performed again on each thin film specimen to obtain the etched conductivity maps (σ_{etch}). These maps are then subtracted from σ_{base} to obtain associated pattern conductivity maps, $\sigma_{pattern}$. From Figures 6-4b, 6-4d, and 6-4f, it can be observed that EIT can clearly identify the change in conductivity within the thin film structure.

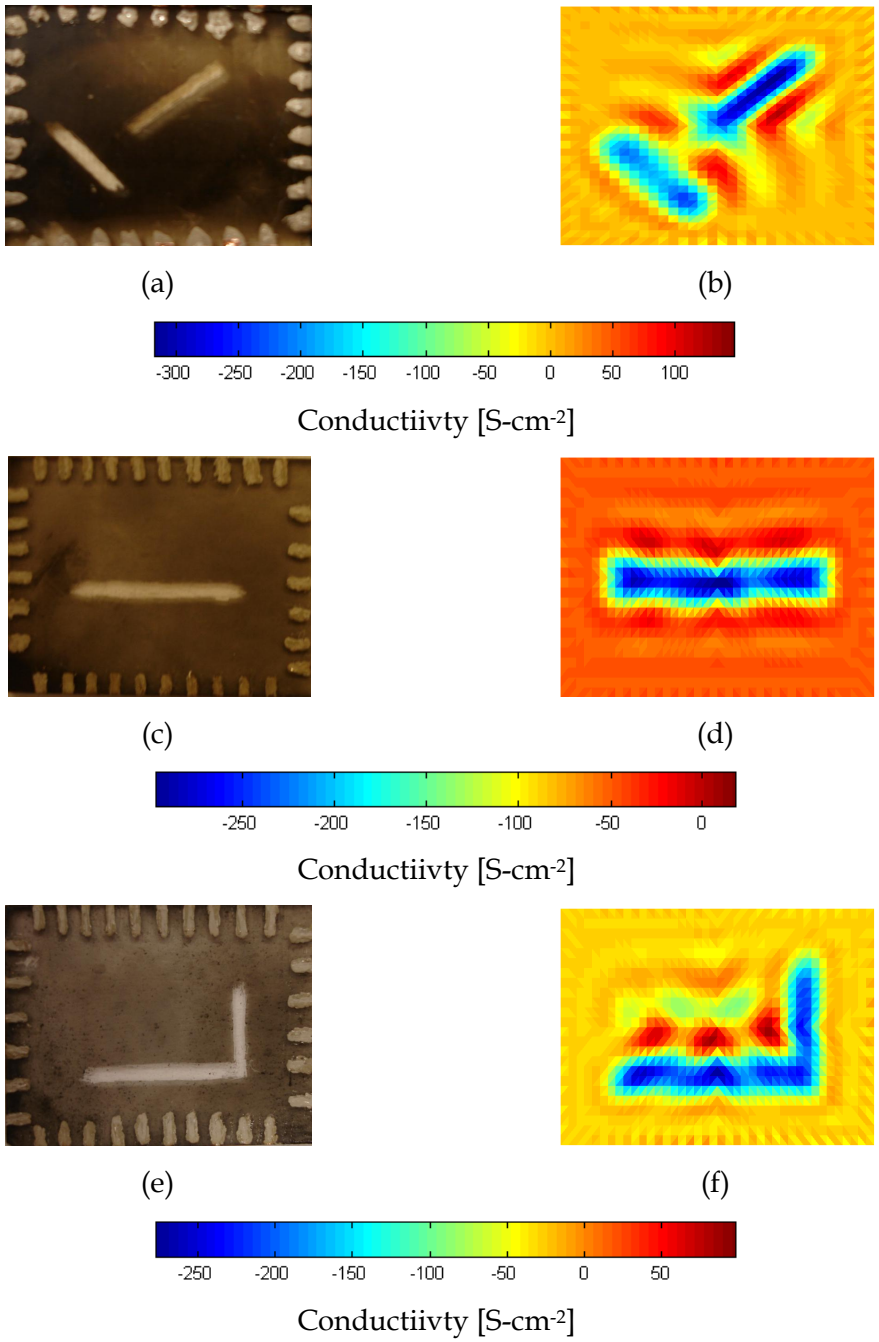

Figure 6-4. Pattern conductivity maps ($\sigma_{pattern}$) of three types of physically etched thin film specimens. (a), (c), and (e) are optical pictures of thin films with double slashes, straight line, and L-shaped etchings; (b), (d), and (f) are the corresponding pattern conductivity maps of (a), (c), and (e).

When compared with the back-lighted photographs of the three aforementioned thin film specimens, the experimental EIT conductivity maps (Figures 6-4b, 6-4d, and 6-4f) correspond precisely with the photographs (Figures 6-4a, 6-4c, and 6-4e).

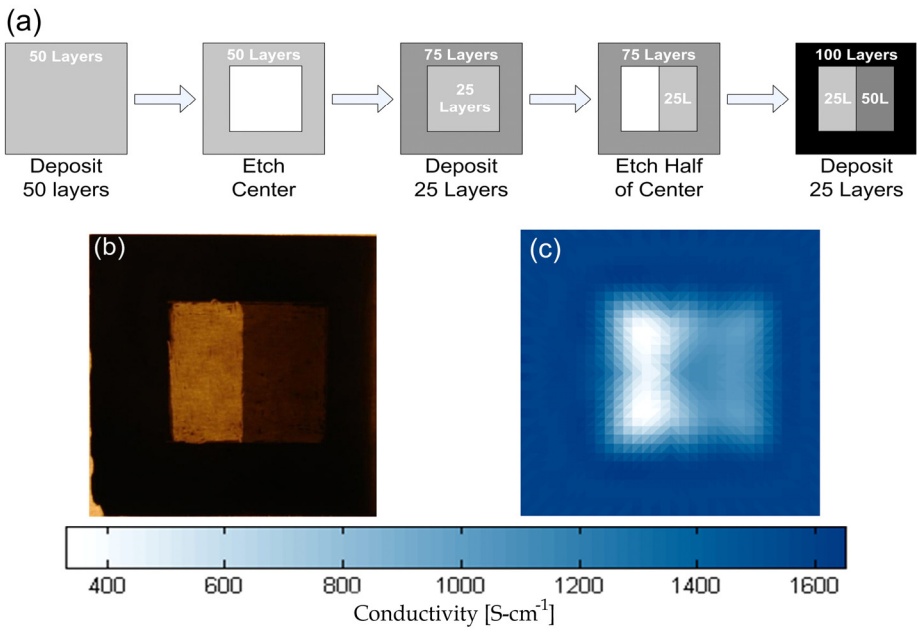

Figure 6-5. (a) Sequential deposition and etching process to structure three regions of different conductivity in a single thin film; (b) back-lighted image of thin film specimen with three dipping layers, 25 (left center), 50 (right center), and 100 bilayers (outer field); (c) is the conductivity map of (b).

In order to demonstrate that the EIT technique can identify subtle changes in conductivity within the thin film structure, three levels of conductivity are encoded into a fourth specimen by controlling the number of bilayers deposited (Figure 6-5a). From a previous study conducted by Loh, *et al*. [77] and in Section 3.3, thin film conductivity increases in tandem with increasing number of bilayers deposited. Thus, fabrication of this fourth specimen with varied conductivity is accomplished by initially fabricating a $(SWNT\text{-}PSS/PVA)_{50}$ thin film. Upon mechanical etching of an 18 by 18 mm^2 window in the middle of the film to form a region of zero conductivity, the LbL process continues to fabricate another $(SWNT\text{-}PSS/PVA)_{25}$ thin film structure over the etched 50-bilayer film. Again, mechanical etching is employed to remove a 9 by 18 mm^2 window before another 25-bilayer thin film is deposited (Figure 6-5a); the final thin film structure consists of three different magnitudes of conductivity. Generally, darker regions of the back-lighted image (Figure 6-5b) suggest greater carbon nanotube deposition consistent with more layers in the nanocomposite and corresponding to increasing film conductivity. Using

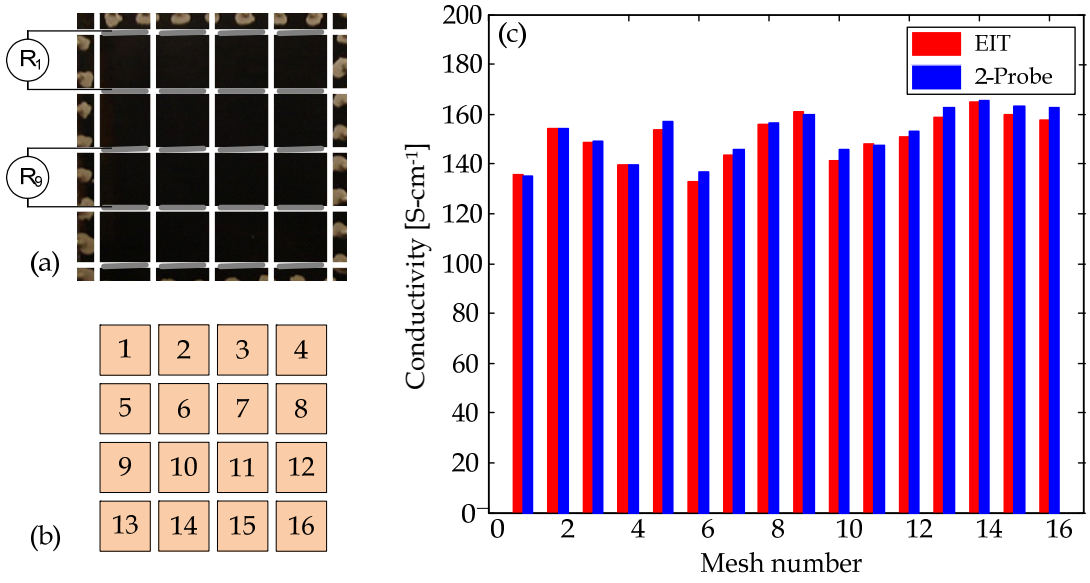

Figure 6-6. Thin film conductivity validation: (a) thin film specimen is equally meshed into 16 individual elements by physical slicing of the thin film; (b) the mesh number of (a); (c) the conductivity comparison of (a) between EIT and the two-point probe method (average error is 2%).

only a 32-electrode setup, EIT successfully identifies major and minor conductivity variations due to different CNT deposition density (Figure 6-5c).

6.4.2. EIT Validation of Measured Absolute Conductivity

As presented in Section 6.2, the EIT method can reconstruct an absolute measure of thin film conductivity distribution relying on only boundary potential measurements. While it has been demonstrated that relative conductivity change can be accurately identified via EIT (Section 6.4.1), no experimental data suggest the calculated conductivity map corresponds to the true conductivity of the thin film. Here, a validation case study is presented to directly compare EIT conductivity estimates to experimental data obtained using traditional DC two-point probing [80].

Similar to Section 6.4.1, the validation of absolute thin film spatial conductivity is conducted using 25 mm by 25 mm $(SWNT\text{-}PSS/PVA)_{50}$ thin films fabricated on a silicon substrate (Figure 6-6a). The pristine film is subjected to EIT to obtain its corresponding spatial conductivity map (where a total of 32 electrodes are used as described in Section 6.3.2). Upon boundary potential measurements and EIT reconstruction, the thin film is

physically sliced to form a four by four element grid with each element electrically isolated from all others. By drying colloidal silver paste between each grid element (as identified in Figure 6-6b), individual element resistance (R) is measured via an Agilent 64401A digital multimeter connected in a two-point probe fashion. Once resistance is obtained for a grid element, the multimeter electrodes are removed and applied to the corresponding electrodes of the next element. This is repeated until all 16 mesh resistances have been determined. Since film resistivity, ρ, (or equivalently conductivity, $\sigma=1/\rho$) is dependent on thin film thickness (h), the thickness of each thin film element is measured using ellipsometry. Resistivity, ρ, is calculated:

$$\rho = \frac{1}{\sigma} = \frac{R}{wh} l \tag{6-13}$$

where w is the element's width and l is the distance between the two-point probe electrodes.

The EIT reconstructed conductivity map using 32 boundary electrodes is compared to the conductivity measured for each of the mesh elements by two-point probing. To make a direct comparison, the triangular elements of the EIT conductivity map that fall within the domain of each grid element are averaged. As presented in Figure 6-6c, the average conductivity measured by EIT reconstruction is within 2% error of those measured by using two-point probe methods for each grid element. These results suggest the conductivity maps offered by EIT reconstruction are accurate as compared with more traditional conductivity measurement methods [128].

6.4.3. EIT Sensing Skin Resolution Analysis

It has been shown in Equation 6-4 that the two-dimensional Laplace equation is capable of modeling the flow of electrical current and the development of a boundary potential via a continuum conductivity distribution function (σ). With a continuum approach to electrical impedance tomography, the sensing skin's sensitivity and resolution to damage features are governed by inherent nanocomposite sensor properties. However, for practical applications, the EIT conductivity mapping approach employed herein relies on a discretized weak formulation using the finite element

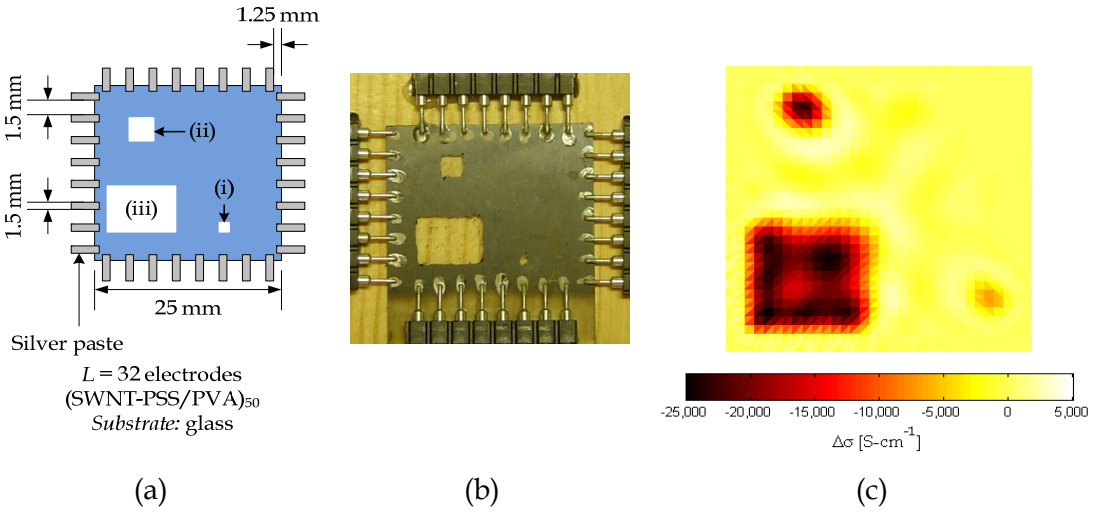

Figure 6-7. (a) A schematic and (b) photograph showing a $(SWNT\text{-}PSS/PVA)_{50}$ nanocomposite fabricated onto a glass substrate with three mechanically-etched windows. Eight EIT electrodes (header pins and colloidal silver paste) are established on each of the four boundaries of the 25 x 25 mm² thin film. (c) EIT spatial conductivity map showing the change in conductivity due to etching.

method (Section 6.2). Solution to the discretized EIT inverse problem yields a computed conductivity map comprised of a set of finite elements, where each element is described by an average conductivity representation of real space. In particular, the number of boundary electrodes directly determines the number of finite elements. Thus, the sensing skin's damage detection resolution and sensitivity are no longer determined by the skin's material and sensor properties, but rather, by the ratio of number of boundary electrodes to specimen size.

Thus, to investigate the damage detection limits (*i.e.*, resolution) of electrical impedance tomographic conductivity mapping of sensing skins, a $(SWNT\text{-}PSS/PVA)_{50}$ skin is fabricated onto a 25 x 25 mm² glass substrate (similar in dimension to the specimen presented in Figure 6-3c). Three regions of zero conductivity are created by mechanically etching the nanocomposite to form three rectangular windows of size: i) 1 x 1 mm², ii) 2.5 x 2.5 mm², and iii) 8 x 6 mm² (width x height) as illustrated in Figure 6-7a. Using header pins, eight 1.5 mm boundary electrodes are mounted onto each side of the nanocomposite boundary. Colloidal silver paste is employed to electrically connect the header pins to the nanocomposite surface as discussed in Section 6.3.2 (Figure 6-7b). The

8 x 8 electrode configuration results to 512 isosceles triangular finite elements (with an edge size of 1.5 mm).

Upon mechanical etching to remove the thin film at three distinct rectangular regions, EIT is executed again to compute the relative spatial conductivity change (Figure 6-7c). From Figure 6-7c, it can be clearly observed that the sensing skin successfully identifies three distinct rectangular regions (*i.e.*, (i), (ii), and (iii) corresponding to Figure 6-7a) with a significant drop in conductivity due to the removal of the nanocomposite skin. While the sensing skin is capable of accurately identifying the size and location of etched regions (ii) and (iii), it can be seen from Figure 6-7c that the magnitude of conductivity change near etched window (i) is smaller than regions (ii) and (iii). Since each EIT boundary electrode and electrode spacing are both 1.5 mm wide, the size of this damage feature (region (i) is 1 x 1 mm^2), is smaller than or equal to a pair of triangular finite elements within the reconstructed EIT spatial conductivity map. As a result, damage feature (i) represents the detection limit or resolution of the sensing skin. It is anticipated that the sensing skin is insensitive to damage features smaller than the size of one finite element of the reconstructed EIT image.

In order to provide a more quantitative analysis of the sensing skin's accuracy to identify damage location, at each area where the nanocomposite skin has been etched, the photograph (Figure 6-7b) and EIT spatial conductivity map (Figure 6-7c) of the skin is assembled into normalized n-by-m matrices **[P]** and **[C]**, respectively. In this case, **[P]** is a binary representation of the actual specimen photo; P_{xy} is 1 at locations where the nanocomposite is intact, and P_{xy} is 0 where the thin film is mechanically etched. On the other hand, each element of the conductivity map matrix **[C]** is scaled between 0 and 1 to represent the computed sensing skin conductivity (where zero corresponds to the non-conductive case, and unity represents maximum electrical conductivity). Thus, the correlation between the computed EIT conductivity map and specimen is obtained by computing the least-squares error matrix (**[E]**) between each pair of corresponding pixels as shown in Equation 6-14:

$$\begin{bmatrix} E_{11} & \cdots & E_{1m} \\ \vdots & \ddots & \vdots \\ E_{n1} & \cdots & E_{nm} \end{bmatrix} = \begin{bmatrix} 1-\sqrt{(P_{11}-C_{11})^2} & \cdots & 1-\sqrt{(P_{1m}-C_{1m})^2} \\ \vdots & \ddots & \vdots \\ 1-\sqrt{(P_{n1}-C_{n1})^2} & \cdots & 1-\sqrt{(P_{nm}-C_{nm})^2} \end{bmatrix} \tag{6-14}$$

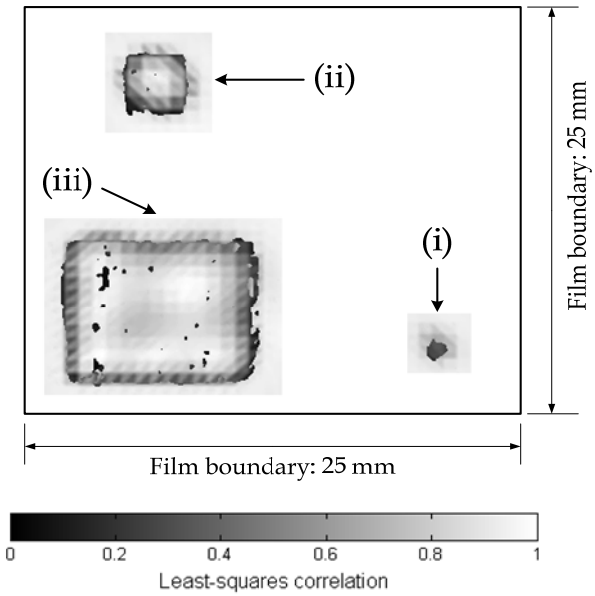

Figure 6-8. Least-squares correlation matrix **[E]** is computed at the three rectangular areas where the skin has been etched. The plot shows the difference between the computed EIT spatial conductivity map (Figure 6-7c) and the actual specimen (Figure 6-7b). It should be noted that perfect correlation is shown as white (E_{xy} = 1).

By definition, each element of **[E]** also spans between 0 and 1, such that maximum correlation is obtained when E_{xy} is 1 (and E_{xy} is 0 when there is no correlation).

The least-squares error matrix at each area where the sensing skin has been etched is computed and plotted together in Figure 6-8 to illustrate the degree of correlation between the EIT conductivity map and specimen. From Figure 6-8, it can be seen that the sensing skin is capable of accurately identifying the location, size, and geometry of different etched regions. Evaluation of correlation is achieved by computing the average least-squares error of each etched region's (*i.e.*, regions "i", "ii", and "iii") error matrix, $\mathbf{[E]}_i$, where $E_{avg,(i)}$ = 0.69, $E_{avg,(ii)}$ = 0.76, and $E_{avg,(iii)}$ = 0.82 (corresponding to regions (i), (ii), and (iii) respectively). The computed average correlation suggests that, as the etched feature size decreases from region (iii) to region (i), the degree of correlation also decreases (as also evident in Figure 6-8). At the limit where etched feature (i) is only 1 x 1 mm^2, it can be seen from Figure 6-8 that the correlation obtained is only an average. The lack of correlation obtained at etched region (i) is expected since each EIT boundary electrode is 1.5 mm wide and is larger than this particular damage feature (1 mm^2

square). Thus, results from this analysis show that the sensing skin resolution is limited by the EIT boundary electrode dimensions. Nevertheless, for spatial conductivity changes larger than each EIT boundary electrode, the sensing skin can accurately identify damage.

6.4.4. Time-Invariant EIT Conductivity Mapping

Previous studies conducted by Loh, *et al.* [77, 111] have validated $(SWNT\text{-}PSS/PVA)_n$ films' change in electrical properties to applied strain. In general, nanocomposite electrical properties respond linearly to applied strain, where film resistivity ($\rho=1/\sigma$) is proportional to strain and has been modeled accurately using a parallel resistor-capacitor (RC) circuit [111]. The typical strain sensitivity (S_S) is estimated to be approximately 2.0, comparable to those of traditional metal-foil strain gages and is calculated using Equation 6-15 (in terms of conductivity) [77, 111],

$$S_S = (\Delta\sigma/\sigma_0)\,/\varepsilon \tag{6-15}$$

where $\Delta\sigma$ is the conductivity change due to applied strain ε, and σ_0 is the nominal (*i.e.*, no strain) conductivity of the sensing film. However, it has been determined that these LbL nanocomposites exhibit an undesirable exponential decrease in nominal film resistivity (R_0) over time (~10 hrs) (Figure 2-3a) [77]. Nevertheless, the application of electrical impedance tomographic spatial conductivity imaging avoids having to account for the nanocomposite's time-variant nominal conductivity (or its inverse, resistivity). Results obtained from Section 2.3.1 and shown in Figure 2-3b have demonstrated that the resistivity decay rate is proportional to applied current (for measuring film conductivity or resistivity), where a larger current input increases the decay rate. In addition, upon removal of the applied current source, the nominal conductivity of the film recovers to its initial pristine state. Thus, applied AC or DC current waveforms injected into two adjacent electrodes for EIT spatial conductivity mapping are limited in amplitude (~0.1 mA) and duration (~1 ms). In fact, experimental results have validated the time-invariant conductivity maps generated by repeated EIT reconstruction [128].

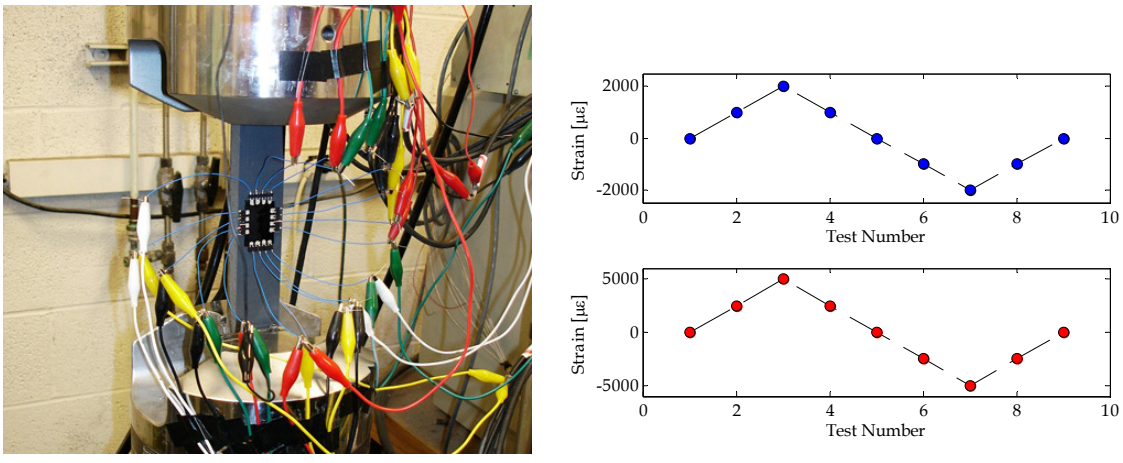

(a) (b)

Figure 6-9. (a) $(SWNT\text{-}PSS/PVA)_{50}$ skins deposited on glass (with a total of 16 electrodes along the film's boundary) are epoxy mounted to PVC coupons and mechanically loaded in an MTS-810 load frame. (b) Two different one-cycle tensile-compressive load patterns to (top) ±2,000 με and (bottom) ±5,000 με applied to $(SWNT\text{-}PSS/PVA)_{50}$ skin specimens.

6.5. Application of Sensing Skins for Structural Damage Detection

6.5.1. Sensing Skin Strain Sensing Validation

First, to demonstrate that these 2D sensing skins capture changes in film conductivity (*i.e.*, the inverse of resistivity) with applied strain, $(SWNT\text{-}PSS/PVA)_{50}$ skins deposited onto 25 x 25 mm^2 glass substrates are affixed onto PVC (polyvinyl chloride) Type I tensile coupons (31 cm long, 4 cm wide, 2 cm thick) via CN-Y post-yield epoxy (Tokyo Sokki Kenkyujo). Upon sufficient drying of the epoxy (6 hours), eight header pins are also epoxy-mounted to each of the four sides of the square skin (Figure 6-3a). Colloidal silver paste is dried between adjacent pairs of header pins to form equidistantly-spaced equal-size EIT boundary electrodes. Finally, each $(SWNT\text{-}PSS/PVA)_{50}$ sensing skin (on glass), along with the PVC coupon, is mounted in an MTS-810 load frame where it is programmed to execute a tensile-compressive cyclic load pattern to ±2,000 or ±5,000 με at a fixed load rate of 50 $\mu\varepsilon\text{-}s^{-1}$ so as to prevent cracking of the glass substrate (Figure 6-9a). The load frame is paused at 1,000 με or 2,500 με

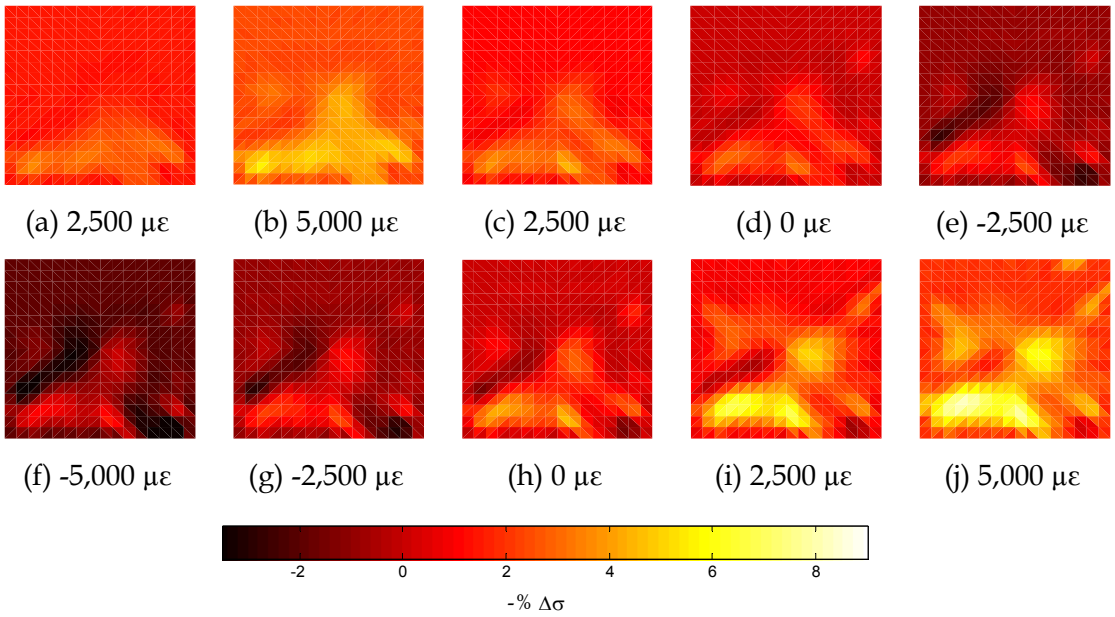

Figure 6-10. (SWNT-PSS/PVA)$_{50}$ skins deposited onto glass substrates and epoxy-mounted to PVC coupons for load testing. A one-cycle tensile-compressive load pattern (±5,000 με) is executed. (a) to (j) EIT spatial conductivity mapping is conducted at 2,500 με increments to monitor the sensing skin's 2D conductivity change. It can be seen that the sensing skin's negative percent change in conductivity (*i.e.*, percent change in resistivity varies in tandem with increasingly applied strain).

intervals (Figure 6-9b) while the EIT DAQ is commanded to inject current and measure boundary electrode potentials as described in Section 6.3.2.

Figure 6-10 plots the set of sequential EIT spatial conductivity maps of an (SWNT-PSS/PVA)$_{50}$ thin film strained at 2,500 με intervals during the application of a one-cycle tensile-compressive load pattern to ±5,000 με. From Figure 6-10, it can be clearly identified that the overall change in skin conductivity varies inversely with applied strain (*i.e.*, the negative change in conductivity changes in tandem with increasingly applied strain). In addition, the spatial conductivity maps obtained at every 2,500 με interval suggests non-uniform deformation and conductivity change with applied strain. From Figures 6-10c, 6-10f, and 6-10j (peak tensile and compressive applied strains), it can be observed that the non-uniform changes in conductivity distribution are more pronounced than cases when zero strain is applied to the specimen (Figures 6-10a, 6-10e, and 6-10h).

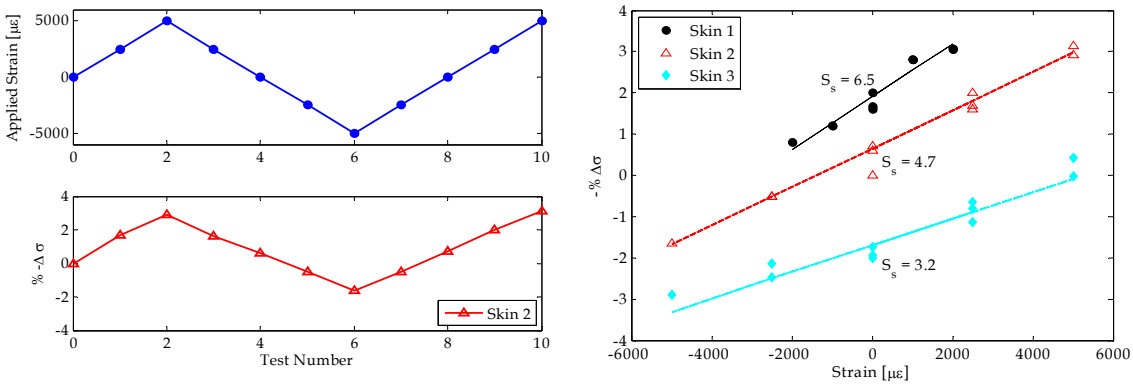

Figure 6-11. (a) (Top) A one-cycle tensile-compressive load pattern to ±5,000 με is applied to each sensing skin specimen. The load frame is paused at 2,500 με to allow EIT data acquisition. (Bottom) It can be seen that the strained sensing skin's percent change in average film conductivity changes in tandem with applied strain. (b) Upon plotting the normalized change in average conductivity (-% Δσ) against the applied strain for all the specimens, the results confirm the skin's linear strain sensing performance. In addition, by fitting a least-squared line to the obtained data, the strain sensing sensitivity (S_S) is approximately between 3.2 and 6.5. Note: The plots for Skin 1 and Skin 3 are translated in the ±y-direction (by 2.5%) for better visualization.

However, to evaluate the skin's strain sensing performance (*i.e.*, linearity and sensitivity), the average change in conductivity corresponding to all elements of the EIT conductivity map is computed and compared to the applied load pattern as shown in Figure 6-11a. It can be seen from Figure 6-11a that the negative change in average EIT skin conductivities are directly proportional to applied strain. In addition, the results obtained validate the sensing skin's ability to capture both tensile and compressive strains. By plotting the negative change in conductivity as a function of applied strain, it can be seen from Figure 6-11b that the proposed sensing skins exhibit linear strain sensing response. In addition, results shown in Figure 6-11a confirm that the sensing skin approach eliminates the time-variant nominal conductivity drift observed in previous studies [77, 111]. Furthermore, the slope of the least-squares fitted line for all specimens tested is computed to quantify the strain sensor sensitivity (Equation 6-15). The computed strain sensitivities (S_S) presented in Figure 6-11b range from 3.2 to 6.5, thereby suggesting higher sensitivity than traditional metal-foil strain gauges ($S_S \approx 2$). The sensing skin's high strain sensitivity and high resolution are ideally suited for

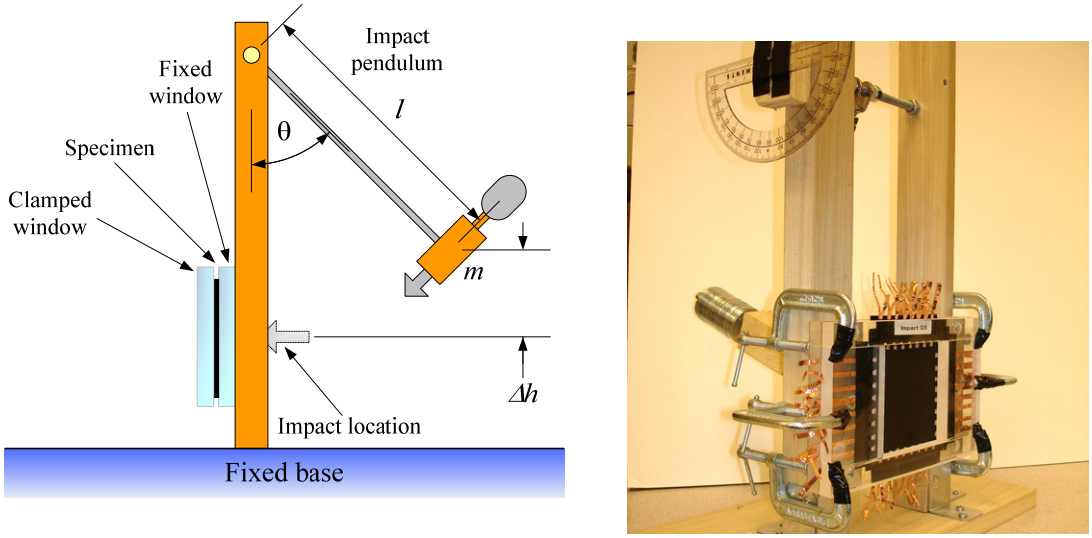

(a) (b)

Figure 6-12. (a) The impact testing apparatus is equipped with an adjustable arm pendulum (of length, l) and mass block (m). By controlling the height (Δh) of the pendulum arm, a specific amount of potential energy can be transferred to the plate during impact. (b) $(SWNT\text{-}PSS/PVA)_{50}$ skins deposited on aluminum 6061-T6 alloy are mounted onto an impact-loading test apparatus. Fixed boundary conditions are ensured by clamping a plexiglass frame over the skin and plate.

structural monitoring applications to detect small changes in a structure's induced strains.

6.5.2. *Spatial Impact Damage Detection*

This study is extended to detect spatially-distributed impact damage on metallic plate elements using the proposed LbL carbon nanotube-based skins. As mentioned in Section 6.3.2, $(SWNT\text{-}PSS/PVA)_{50}$ deposited on 110 x 110 mm^2 primer-coated aluminum 6061-T6 alloys are used for impact-damage detection validation tests (Figure 6-3b). In order to induce controlled-energy impacts on various locations on the large substrate, a pendulum impact testing apparatus is constructed in the laboratory. The pendulum test structure consists of an adjustable swinging arm (variable between 20 to 30 cm), a sharp aluminum tip (termed the striker), and a rod connected to the striker to hang washers for controlling the pendulum mass as shown in Figure 6-12. In addition, the test apparatus is configured such that the pendulum arm can be rotated between 0° and 180°

Table 6-1. Controlled impact damage on skin- and primer-coated aluminum plates for specimen IM-01.

Impact Number	Location (Front)	Arm Length [cm]	Pendulum Angle [°]	Impact Energy [J]
Impact-[i]	Top right	24	20	0.09
Impact-[ii]	Bottom left	27.5	40	0.38
Impact-[iii]	Bottom right	27.5	60	0.81
Impact-[iv]	Top left	24	80	1.17

to control the magnitude of the initial potential energy that is converted to the final impact-deformation strain energy (where 0° corresponds to the situation when the tip of the striker is in contact with the skin specimen).

Each skin-coated aluminum alloy specimen is mounted with fixed-fixed boundary conditions on the testing apparatus (Figure 6-12). Two sturdy plexiglass windows are securely mounted to the pendulum structure, and a total of six C-clamps are used to secure plate specimens between the two windows. In this series of tests, the pendulum is adjusted to impact two plate specimens at various locations with different initial potential energies (*i.e.*, the striker mounted on the pendulum is released at different initial angles and arm lengths). To demonstrate sensing skins' ability to capture the location of damage and severity of impact (*i.e.*, the amount of strain energy absorbed for plate deformation) across large structural surfaces, four different magnitudes of impact damage are introduced at various locations on each of the two plate specimens (herein referred to as IM-01 and IM-02). From Table 6-1 and 6-2, it can be seen that the lowest applied impact energy is labeled as [i], while the highest impact energy is referred to as [iv]. Since sensing skins are deposited on both sides of the metallic plate specimens, the "back" side of the plate is where the impact striker physically contacts and impacts the skin, and the "front" side is the opposite non-contact face. Prior to any induced impact damage, boundary electrical measurements are obtained and the EIT inverse problem is solved to reconstruct the baseline undamaged conductivity distribution of the pristine plate.

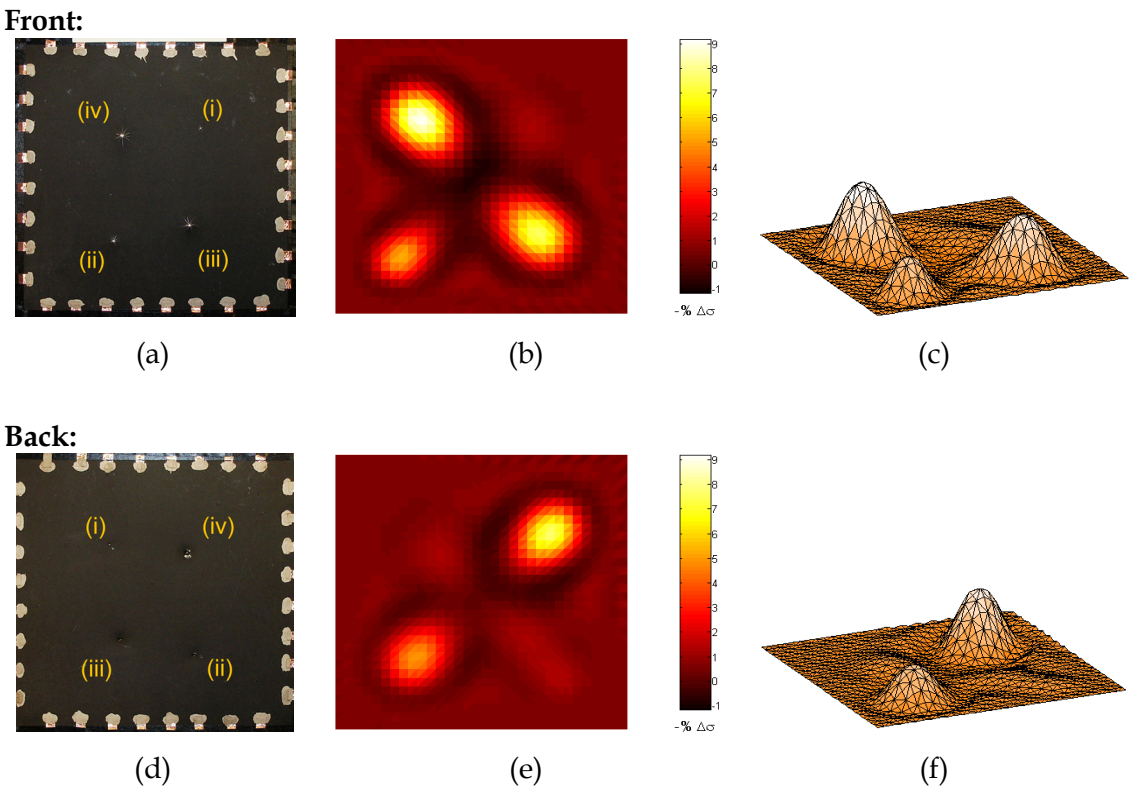

Figure 6-13. Specimen IM-01: EIT is employed to reconstruct the spatial conductivity distribution of the skins after four different magnitudes of controlled pendulum impacts [(i) – (iv)] have occurred as shown in (a) and (d) for the front and back sides, respectively. Damage can be visually identified from photographs taken from the (a) front and (d) back sides of the plate. In addition, the reconstructed front-side (b) 2D and (c) 3D representation and back-side (e) 2D and (f) 3D representation EIT spatial conductivity images all verify the sensing skin's impact damage detection capabilities.

In order to evaluate the sensing skin's ability to detect both the location and severity of structural impact damage, the first plate specimen (IM-01) is mounted in the pendulum test apparatus (Figure 6-12) and impacted four times (as shown in Figures 6-13a (front) and 6-13d (back)). Each of the four controlled impacts is conducted at different locations and have different initial impact energies (*i.e.*, controlled by the arm length and initial pendulum angle) as listed in Table 6-1. Once all four impact damages have occurred, EIT spatial conductivity mapping is executed to obtain a "damaged" sensing skin conductivity map. From Figures 6-13b (front) and 6-13e (back), it can be seen that the relative negative conductivity change for both the front and back sides clearly identify damage location and severity. From Section 6.5.1, it has been validated

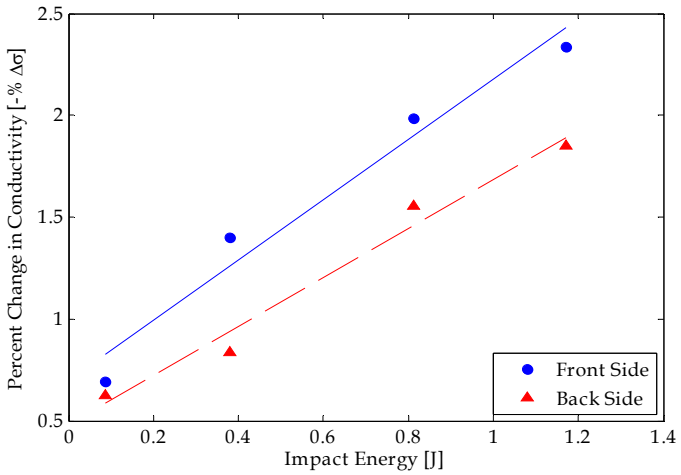

Figure 6-14. The percent change in average film conductivity of specimen IM-01 increases near-linearly with increasing impact energy (as controlled by the initial potential energy of the impact test apparatus pendulum). In addition, the similarity in the fitted lines' slopes suggests that the sensing skin exhibits similar sensitivity to strain and impact.

that higher levels of applied strain causes greater change in skin conductivity. With higher initial applied impact energies (*e.g.*, damage locations [iii] and [iv]), the plate and skins undergo higher levels of deformation and strain. Thus, with greater initial impact energies (*i.e.*, severe damage), the change in sensing skin conductivity is expected to be higher as shown in Figures 6-13b (front) and 6-13e (back).

It should be noted that small damage thresholds (impact locations [i] and [ii]) are hard to detect in the 2D reconstructed EIT conductivity maps; however, damage is accurately detected but is masked within the color bar to better illustrate larger induced damages (impact locations [iii] and [iv]). To better make this point, the 2D maps are plotted in 3D to facilitate damage identification (see Figures 6-13c and 6-13f). Upon computing the average change in skin conductivity within the vicinity of induced impact damage for the front- and back-side skins, it can be observed from Figure 6-14 that small levels of damage can be detected. In addition, the change in conductivity varies near-linearly with respect to initial impact energy.

Table 6-2. Controlled impact damage on skin- and primer-coated aluminum plates for specimen IM-02.

Impact Number	Location (Front)	Arm Length [cm]	Pendulum Angle [°]	Impact Energy [J]
First test (0 days)				
Impact-[ii]	Middle right	25.7	60	0.71
Impact-[iii]	Bottom center	28.5	90	1.63
Second test (14 days)				
Impact-[i]	Top left	23.6	30	0.19
Impact-[iv]	Center	25.4	180	3.25

For sensing skins to demonstrate potential applicability for long-term structural health monitoring, it is important to begin characterization of sensor long-term performance. For instance, structural damage typically occurs continuously throughout the service life of engineered systems. Thus, in addition to being able to detect pristine and damaged structural states, it is worthwhile to investigate the sensing skin's response to damage induced over time. Thus, upon obtaining boundary electrical measurements for specimen IM-02 to determine the initial baseline conductivity map, two additional impact tests are conducted. First, two different magnitudes of pendulum hits (damage levels [ii] and [iii] tabulated in Table 6-2 and shown in Figures 6-15a and 6-15d) are conducted at different locations on the aluminum alloy plate. Similarly, impact damage location and severity can be identified precisely from the 2D (Figures 6-15b and 6-15e) and 3D (Figures 6-15c and 6-15f) EIT conductivity images for the front and back sides of the plate, respectively.

Upon completion of the aforementioned test, the plate specimen is stored in ambient conditions for approximately 14 days prior to the next damage occurrence. Here, two additional controlled impacts ([i] and [iv] shown in Figures 6-16a and 6-16d) are conducted; the location and initial impact energies are tabulated in Table 6-2. It should be noted that the pendulum striker penetrated the entire plate at impact-[iv] (*i.e.*, the most severe case of damage). Then, the EIT inverse problem is executed to obtain the 2D

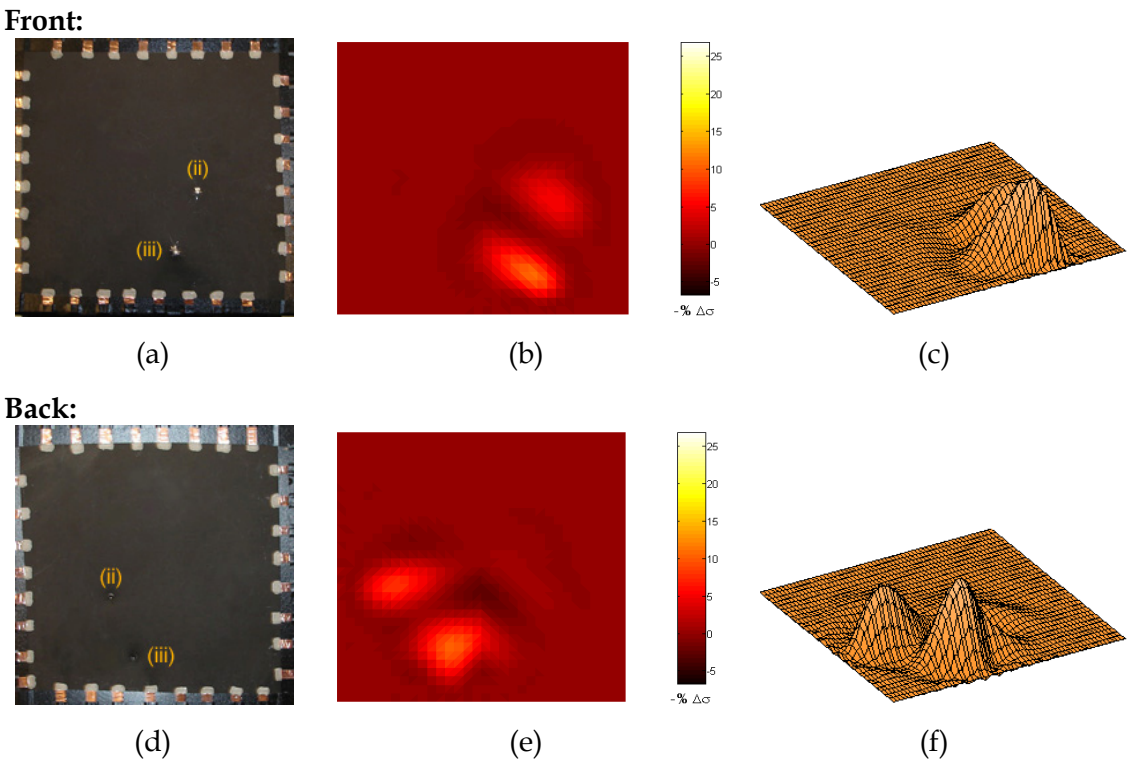

Figure 6-15. Specimen IM-02 (*first test*): Two different magnitudes ([ii] 60° and [iii] 90°) of pendulum hits are conducted. From the (a) front of the plate, the corresponding (b) 2D and (c) 3D EIT conductivity maps identify changes in film conductivity due to impact; the same is observed for the back side of the plate from the (d) photograph, (e) 2D, and (f) 3D EIT images.

(Figures 6-16b and 6-16e) and 3D (Figures 6-16c and 6-16f) EIT spatial conductivity images. From Figures 6-15 and 6-16, it can be concluded that, not only did the sensing skins capture new damage sustained on the aluminum alloy plates, but also, the EIT images also preserve damage which occurred 14 days ago. Finally, when the average conductivity at each impact location is determined and plotted against initial impact energy, the response is near-linear as expected (Figure 6-17).

6.5.3. Spatial Accelerated Corrosion Monitoring

To further showcase the multifunctional features of carbon nanotube-based sensing skins for structural damage detection, sensing skins have been deposited onto carbon steel substrates for long-term electrochemical monitoring of corrosion byproduct formation. Following skin fabrication and electrode preparation details provided in

Front:

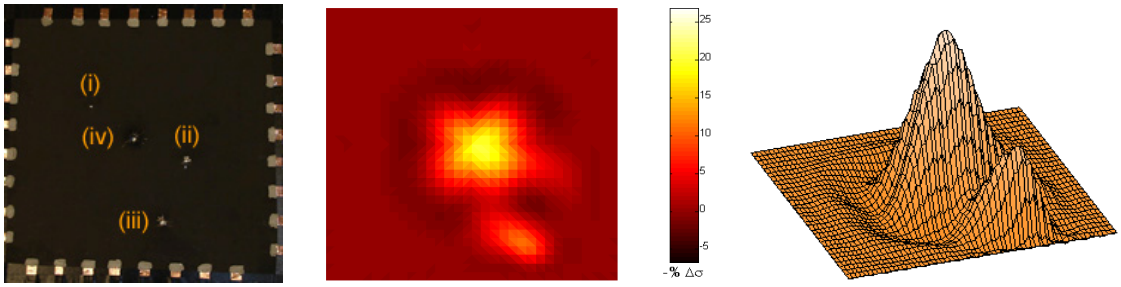

(a) (b) (c)

Back:

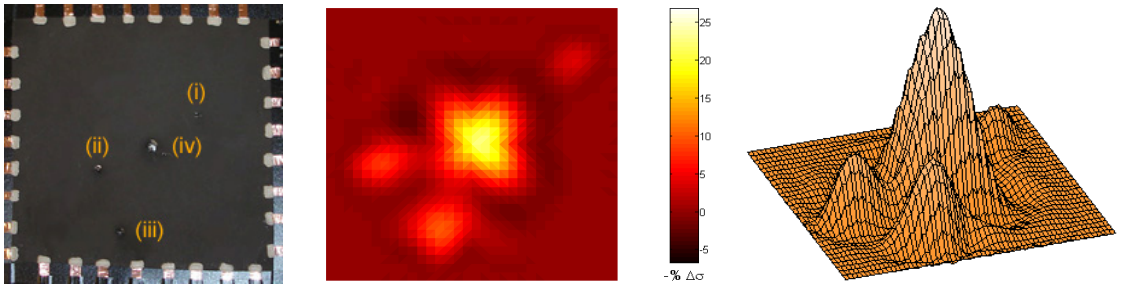

(d) (e) (f)

Figure 6-16. Specimen IM-02 (*second test*): The same plate from Figure 6-15 is impacted another two more times ([i] 30° and [iv] 180°) at the top-right corner and middle of the plate as seen from the (a) front and (d) back side photographs. The (b) front-side 2D and (c) 3D EIT images, as well as the (e) back-side 2D and (f) 3D EIT conductivity maps, all verify that the proposed sensing skins are capable of detecting different magnitudes of induced damage and their corresponding locations.

Section 6.5.1, accelerated corrosion testing is conducted by exposing 25 x 25 mm^2 carbon steel substrates to different concentrations of sodium chloride (0.1 M and 1.0 M NaCl) solutions. In efforts to control the region of accelerated corrosion and corrosion byproduct (*i.e.*, iron oxide or rust) formation, two 7 mm circular regions of exposed steel are formed by mechanically etching away the sensing skin and primer coatings. Then, two 7 mm diameter plastic wells are securely mounted over the exposed circular holes using high-vacuum grease (Dow Corning); these plastic wells are used to contain salt solutions to selectively facilitate corrosion at etched circular regions (Figure 6-18). Instead of exposing the entire substrate to concentrated NaCl solutions which can potentially alter electrode contact impedance, the technique used in this study confines solution exposure and corrosion regions. Furthermore, to demonstrate the sensing skin's

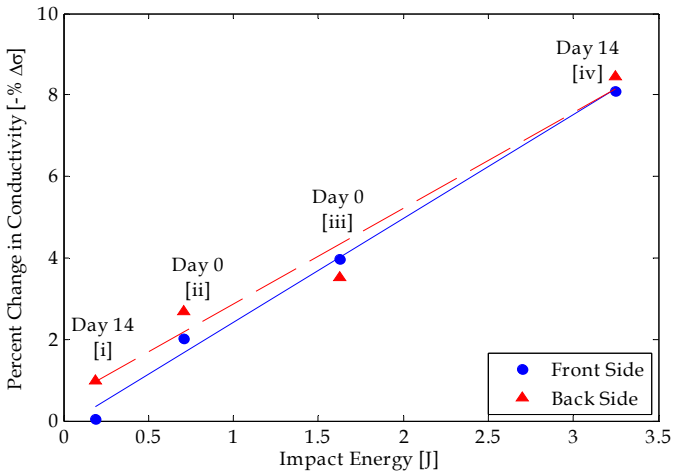

Figure 6-17. The percent change in average film conductivity of specimen IM-02 increases near-linearly with increasing impact energy (as controlled by the initial potential energy of the impact test apparatus). Times of inflicted impact damage are also denoted with each data point.

ability to detect progressive corrosion byproduct formation, the salt solutions are pipetted out of each well after 5 min of exposure time. Then, the specimens are allowed sufficient time to dry (3 hrs) prior to EIT spatial conductivity imaging. The aforementioned steps are repeated for a total corrosion time (*i.e.*, NaCl solution exposure time) of 90 min.

As before, an initial EIT spatial conductivity map is obtained to serve as the undamaged baseline. Upon acquiring successive time-lapsed EIT maps due to application of concentrated sodium chloride solutions, it can be seen from Figure 6-19 that the spatial conductivity within the wells drop over time as rust begins to accumulate within the wells. It is known that corrosion of steel occur due to oxidation of iron (within steel) to form iron oxide (*i.e.*, rust) [134]:

$$3Fe + 4H_2O \rightarrow Fe_3O_4 + 8H^+ + 8e^- \quad \text{(6-16a)}$$

$$2Fe + 3H_2O \rightarrow Fe_2O_3 + 6H^+ + 6e^- \quad \text{(6-16b)}$$

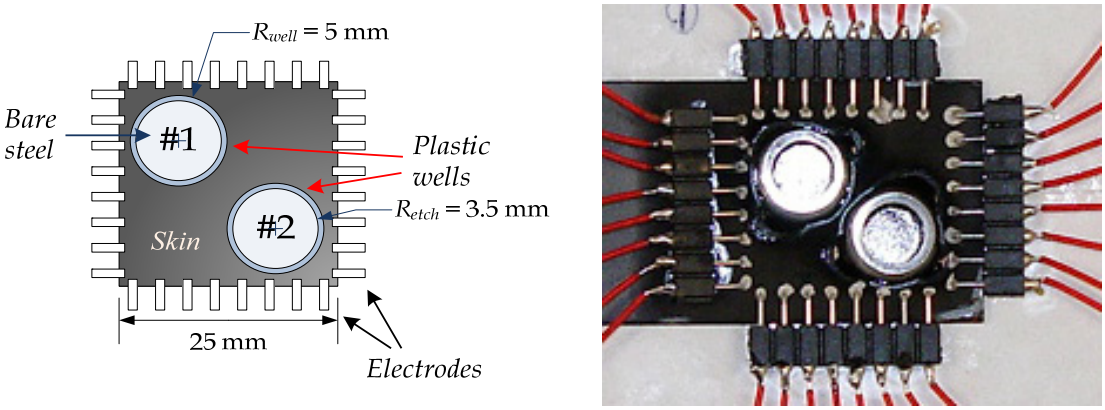

(a) (b)

Figure 6-18. (a) Two etched circular regions (Wells #1 and #2) on the sensing skin-coated carbon steel substrate. (b) Photograph of the actual accelerated corrosion testing specimen with 32 boundary electrodes and two plastic wells mounted over the etched circular holes.

When water is available for oxidation of iron, the reaction kinetics highly favors the formation of iron oxide. As a result, with increased water exposure time, rust will continue to form as long as the chemical reaction is not rate-limited by iron availability. With increased salt solution (or water) time-of-exposure, iron oxide continues to form on exposed-steel surfaces. Similarly, upon computing the average change in conductivity at Wells #1 and #2 (Figure 6-18a) at every 5 min interval, the plot of average change in well conductivity as a function of time is obtained (Figure 6-20). With increasing salt solution exposure time, the average conductivity change for both Wells #1 (1.0 M NaCl solution) and #2 (0.1 M NaCl solution) follow the same trend; initially, a sudden drop in conductivity is observed, followed by a decreasing rate until eventual plateauing of conductivity change when t = 90 min. The plateauing effect is observed, because as the thickness of iron oxide increases, the area of bare steel is reduced to limit iron oxidation. The results obtained in Figure 6-20 agree with those obtained by Yonemoto and Shida [135], where they have determined that their proposed corrosion sensor impedance increases in a similar fashion with increasing rust thickness.

In fact, the experimental results obtained in Figure 6-20 can be easily fit to an exponential decay model of the form $-\Delta\sigma=-Ae^{-Bt}+C$ via regression analysis. Results from numerical fitting suggest that the average change in thin film conductivity due to

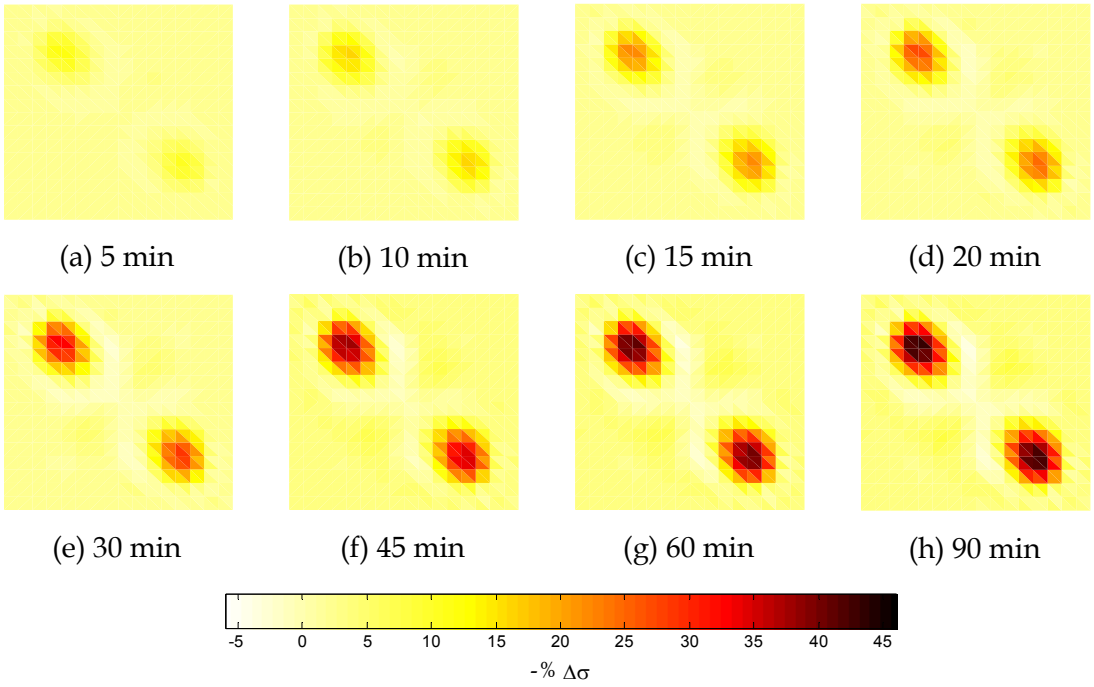

Figure 6-19. Sensing skins deposited onto primer-coated carbon steel are employed to detect corrosion byproduct formation due to short-term exposure to sodium chloride solutions in two circular wells. NaCl solutions are pipetted into each well for 5 min intervals, and the total exposure time varies between (a) 5 min to (h) 90 min. (a-h) EIT conductivity images between salt exposures show decreasing well conductivity, thereby verifying build-up of non-conductive iron oxide or rust.

corrosion byproduct formation is well-behaved. The nanocomposite conductivity decreases at an exponential rate of 0.031 min^{-1} at Well #1 (1.0 M NaCl) and 0.024 min^{-1} at Well #2 (0.1 M NaCl). The faster corrosion rate at Well #1 is consistent with the higher concentration of salt solution employed to accelerate corrosion. Current work is in progress to determine the underlying electrochemical sensing transduction mechanisms that take place during iron oxide formation.

6.5.4. Spatial pH Sensing

In Chapter 4, it has been demonstrated that electrochemical pH sensitivity can be encoded within thin films using SWNTs and a poly(aniline) emeraldine base solution. Different levels of charge injection from pipetted pH buffer solutions (pH 1 to 10) lead to dramatic conductivity variations at areas where the pH buffer solutions come into direct contact with the $(SWNT\text{-}PSS/PANI)_n$ nanocomposite. With a pH sensitivity of

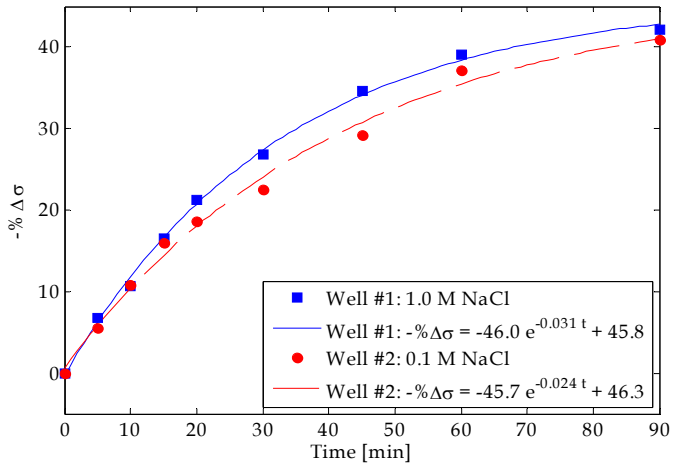

Figure 6-20. Average EIT-computed well conductivities versus accelerated corrosion times. Clearly, both wells undergo similar corrosion rates. In addition, the delay in corrosion rate suggests plateauing of corrosion byproduct formation after 60 to 90 min.

approximately 20.66 kΩ-cm^{-2}/pH, these thin films serve as ideal candidates for pH sensing in a wide variety of applications (*e.g.*, corrosion monitoring). The electrochemical response of (SWNT-PSS/PANI)$_n$ thin films have been characterized with entire films exposed to a single pH environment while two-point probe measurements are conducted [77]. In contrast, EIT conductivity mapping offers a direct method of sensing pH variations across the entire thin film.

To demonstrate the potential for two-dimensional pH sensing, the fabricated (SWNT-PSS/PANI)$_n$ thin films (roughly 25 x 60 mm^2 in area) are modified by mounting five plastic wells to its surface using high-vacuum grease (Figure 6-21a). Each plastic well serves as a chamber for containment of the pH buffer solutions while boundary potentials are measured for 2D EIT conductivity mapping of the specimen, thereby allowing simultaneous sensing of different pH solutions on a single thin film specimen. In this EIT experimental set-up, to enhance the resolution of the reconstructed EIT spatial conductivity maps, a total of 48 boundary electrodes are employed.

Prior to the application of pH buffer solutions in the 5 wells, the conductivity map of the pristine thin film is reconstructed by EIT. This map will serve as a baseline map to which further conductivity maps will be compared. To illustrate the use of (SWNT-PSS/PANI)$_n$ thin films for biological applications, a small range of pH buffer

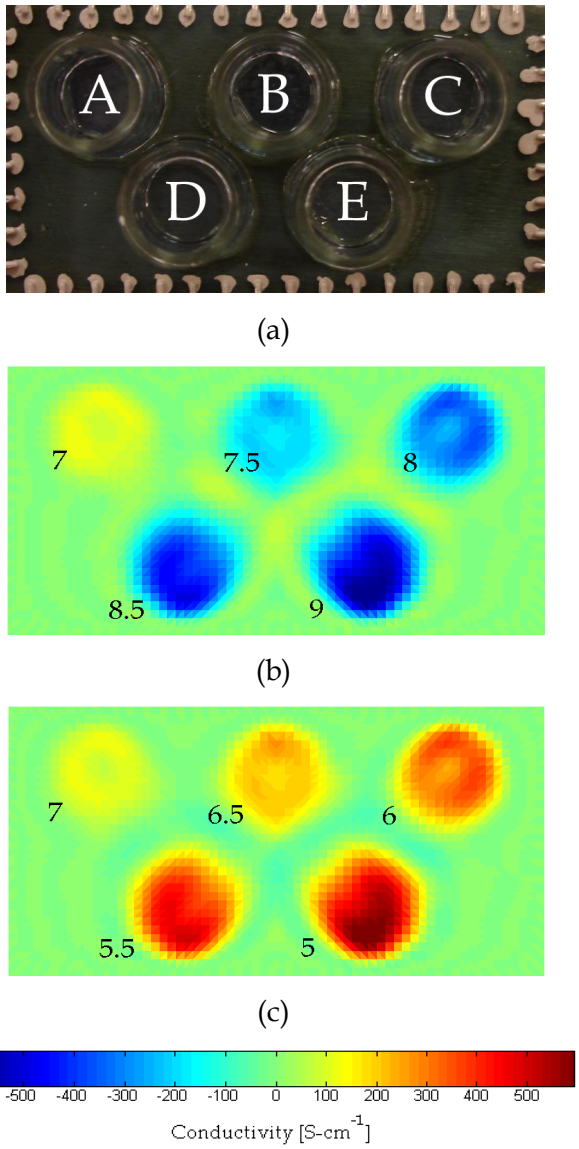

Figure 6-21. (a) $(SWNT\text{-}PSS/PANI)_{100}$ thin film under several magnitudes of pH stimuli; (b) change in spatial conductivity when pH in well A, B, C, D, and E is 7, 7.5, 8, 8.5, and 9, respectively; (c) change in spatial conductivity when pH in well A, B, C, D, and E is 7, 6.5, 6, 5.5, and 5, respectively.

solutions ranging from 5 to 9 are pipettted into the 5 wells. The EIT-derived conductivity maps of the thin film exposed to pH buffer solutions are subtracted from the baseline conductivity, thereby revealing changes in conductivity due to pH. First, the surface of the thin film is exposed to pH buffer solutions corresponding to pH values of 7, 7.5, 8, 8.5 and 9; Figure 6-21b reveals the conductivity of the $(SWNT\text{-}PSS/PANI)_{100}$ thin film decreases in linear proportion to pH. Second, the basic solutions are removed and acid

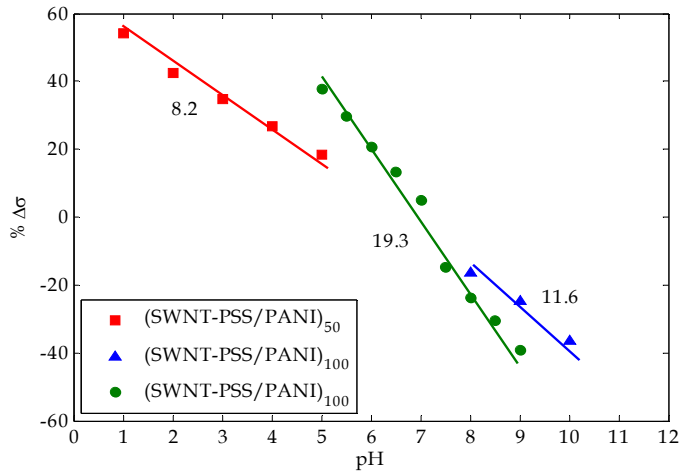

Figure 6-22. Sensitivity of three different $(SWNT\text{-}PSS/PANI)_n$ nanocomposites under pH stimuli. All three films exhibit similar linear variations in conductivity as a result of pH buffer solutions applied to the film surface.

buffer solutions with pH values 7, 6.5, 6, 5.5, and 5 are applied to the film surface. Figure 6-21c confirms the thin film undergoes an increase in the film conductivity in tandem with acidic pH. Figure 6-22 summarizes the sensitivity of $(SWNT\text{-}PSS/PANI)_n$ thin films composites to pH stimuli including earlier work conducted by the same group [128]. As shown, a linear relation exists in the pH sensitivity of electro-chemcially active $(SWNT\text{-}PSS/PANI)_n$ thin films.

6.6. Summary and Conclusions

6.6.1. Results and Discussion

In this chapter, piezoresistive and pH-sensitive LbL nanocomposites are coupled with an electrical impedance tomographical spatial conductivity mapping technique to realize two-dimensional distributed sensors. Unlike traditional "point" sensors, these "sensing skins" have been validated to detect the location and severity of spatially distributed strain, impact, pH, and corrosion. Using only boundary electrical measurements, the EIT technique reconstructs the 2D spatial conductivity distribution of the nanocomposites. It should be noted that EIT seeks to solve an inverse problem (*i.e.*, similar to techniques such as computerized tomography and radar scattering) in order to accurately estimate a thin film's spatial conductivity. Since skin electrical properties

have been calibrated for specific applied external stimuli, changes in spatial film conductivities are directly correlated to damage.

First, (SWNT-PSS/PVA)$_{50}$ films are affixed onto PVC coupons for strain sensing. A tensile-compressive cyclic load pattern to ±5,000 με is applied to specimens, and the load frame is paused at 2,500 με increments for EIT data acquisition. Results obtained confirm the skin's ability to detect non-uniform strain fields during applied strain. When the average conductivity change at each applied strain is computed, the results confirm the skin's linearity, stability, and high sensitivity (S_S = 6.5).

It should be reiterated that this strain sensing validation is conducted with applied uniaxial stresses and strains. Since the nanocomposite morphology is based on a homogeneous percolated network of randomly oriented intertwined SWNTs, changes in film conductivity does not distinguish between the directionality of strains (*e.g.*, during biaxial loads) but rather outputs an averaged conductivity change. In order to enable identification of the directionality of strain, carbon nanotubes could be aligned within the polymeric matrix such that the sensor is insensitive to deformations occurring perpendicular to the aligned CNTs. Using the layer-by-layer technique, two perpendicularly aligned sensing layers can be fabricated within one multilayer thin film structure. By measuring the change in conductivity of each individual aligned-SWNT layer, one can infer both the magnitude and direction of applied strain. Alignment of CNTs is still a technology under development [136]. As a result, it will be some time before intentional CNT alignment will be possible during LbL assembly of SWNT-based nanocomposites.

Upon strain sensing validation, the study is extended to utilize sensing skins for spatial impact damage detection. The LbL technique is employed to deposit carbon nanotube-based composites onto large (110 x 110 mm^2) aluminum alloy substrates. Using a pendulum impact testing apparatus, controlled impacts are delivered onto sensing skin-coated aluminum specimens. Experimental results confirm that the skins are capable of identifying distributed impact damage location and severity. In addition, the impact damage sensing performance does not degrade over time (*i.e.*, damage occurred over time is adequately detected via successive EIT measurements over a 14 day period), suggesting potential for long-term structural health monitoring.

To further showcase the multi-functionality of these skins, concentrated sodium chloride solutions have been employed to accelerate corrosion at select circular regions on skin-coated steel substrates. Time-lapsed EIT conductivity maps taken at every 5 min interval demonstrate the effectiveness of monitoring progressive corrosion byproduct (*i.e.*, iron oxide) formation.

6.6.2. Contributions

Unlike most commercially-available and academic prototype sensing transducers that can only measure data at instrumented structural locations, the sensing skin approach to damage identification is capable of directly detecting damage over large spatial areas. Damage detection is direct, whereas most techniques use interpolation schemes and algorithms to infer damage between sensor locations. Moreover, the computational demand required for detecting damage over large surfaces does not grow exponentially (as with systems such as acoustic wave emissions or ultrasonic systems), but rather, is limited by the number of boundary electrodes instrumented. More importantly, the proposed sensing skins are not simple data acquisition systems that only collect data from a structure; in fact, they are autonomous structural health monitoring systems that encompass data acquisition (*i.e.*, via nanocomposite conductivity changes to applied external stimuli), data processing (*i.e.*, EIT spatial conductivity mapping), and structural/damage prognosis (*i.e.*, identify the location and severity of damaged regions based on the conductivity maps).

CHAPTER 7

CONCLUSIONS

7.1. Summary of Results

The main focus of this dissertation is to present the design, characterization, and application of multifunctional nanocomposites for structural health monitoring. Here, multifunctionality refers to the ability of a single material to possess multiple engineering functions such as enhanced mechanical strength, sensing, actuation, and/or self-healing capabilities. Unlike traditional composite design, this dissertation highlights the use of a nanotechnology-driven "bottom up" fabrication approach, where molecular species are autonomously assembled at the nano-scale to dictate macro-scale bulk properties (*e.g.*, tensile strength, conducting, sensing sensitivity). In particular, carbon nanotubes have been selected as the material of choice due to their impressive mechanical, electrical, and thermal properties.

In Chapter 2, details regarding nanocomposite fabrication using the layer-by-layer self assembly technique are presented. Upon thin film fabrication, the inherent mechanical and electrical properties of these novel composites are characterized. First, monotonic tensile testing of free-standing $(SWNT\text{-}PSS/PVA)_{200}$ thin films reveal dramatic ultimate tensile strength and stiffness improvements as compared to pristine polymer materials. For example, thermally annealed SWNT-enhanced films have exhibited tensile strengths as high as 250 MPa as compared to 20 MPa which is typical of unreinforced PSS/PVA composites. Second, the inherent electrical properties of these materials are characterized. It has been experimentally demonstrated via two-point probe electrical resistance measurements that the average conductivity of (p-SWNT-

PSS/PVA)$_n$ and (p-SWNT-PSS/PANI)$_n$ is approximately 1,060 ± 6 S-m^{-1} and 9.55 ± 0.05 S-m^{-1}, respectively. However, these thin films exhibit time-variant electrical properties where (1) resistive heating due to applied current and (2) light-induced photocurrent in nanotubes increases apparent film conductivity. Fortunately, the decay can be analytically removed from time-history resistance measurements. An advantage of the LbL assembly technique is the ease in which different sensing transduction mechanisms can be embedded; (SWNT-PSS/PVA)$_n$ nanocomposites are shown to exhibit piezoresistivity while (p-SWNT-PSS/PANI)$_n$ changes its conductivity in response to pH.

Having identified that these nanocomposites exhibit multifunctionality, Chapter 3 first seeks to characterize the bulk nanocomposite's mechanical and fracture properties. Through monotonic tensile load testing, it has been shown that the addition of carbon nanotubes within a PSS-PVA polymeric matrix dramatically enhances its mechanical strength and stiffness. Examples of (SWNT-PSS/PVA)$_{200}$ thin films fabricated with a 0.5 mg-mL^{-1} SWNT-PSS solution resulted to films characterized by an ultimate tensile strength and stiffness of 229 ± 7 MPa and 11.2 ± 0.4 GPa, respectively. In addition, the fracture toughness of these materials also increases due to nanotube bridging at crack interfaces. However, further testing reveals that increasing nanotube concentrations decrease the composite's ductility and reduces the entire material's energy release rate (*i.e.*, the material becomes more brittle). Nonetheless, these analyses suggest that these thin films can be tailored to possess desirable strength, stiffness, ductility, and fracture, simply by controlling carbon nanotube weight content within the composite.

Chapter 4 then seeks to characterize and optimize the strain sensing properties of the proposed multifunctional nanocomposites. Here, initial layer-by-layer fabrication parameters are varied to produce films of different constituents. More specifically, the initial SWNT concentration (in PSS solution), PSS (dispersing agent) concentration, and film thickness are varied. As opposed to characterizing these materials using a DC time-domain approach, a frequency-domain analysis using electrical impedance spectroscopy is conducted. The main advantage of using EIS is that frequency-dependent characteristics such as capacitance or inductance are only visible during EIS. In fact, results from this chapter conclude that an equivalent parallel resistor-capacitor circuit model can be used to model the inherent thin film properties of (SWNT-PSS/PVA)$_n$

nanocomposites. This model is also validated in the time domain to show that the RC-circuit can adequately model thin film piezoresistivity. Furthermore, by conducting equivalent circuit modeling for all films of different compositions, it has been found that nanotube strain sensitivity and conductivity increases with the addition of carbon nanotubes, and conductivity decreases with increasing PSS concentration.

To demonstrate that these high-performance nanocomposites can be used for structural health monitoring, the thin films are coupled with inductively coupled wireless systems for the design of a passive wireless sensor. Chapter 5 presents three iterative designs of strain- and pH-sensitive passive wireless sensors, where the ultimate goal is to produce a sensor that is low cost, high-performance (*i.e.*, high sensitivity to applied external stimuli), small form factor, and can communicate wirelessly with a remote RFID reader. Through sensor design optimization coupled with knowledge of inductively coupled systems, the final passive sensor platform achieves all of the aforementioned goals. In general, a coil antenna and the fundamental parallel resonant circuit are electroplated onto FR4 laminate substrates using PCB technology. Then, nanocomposites are LbL-assembled directly onto this board to realize a miniaturized passive wireless sensor. Validation studies conducted have shown that these materials exhibit near-linear changes in system bandwidth as a function of applied strain or pH. It has been shown that these sensors are ideal for embedment within structural components for densely-distributed SHM.

However, to achieve a sensor that can monitor damage directly over large spatial areas, the SWNT-based multifunctional nanocomposites are coupled with an electrical impedance tomographic spatial conductivity mapping technique (Chapter 6). In short, EIT (electrical impedance tomography) relies on boundary electrical measurements to estimate the two-dimensional spatial conductivity of a conductive material. Since different types of thin films have already been calibrated to different applied external stimuli (*e.g.*, strain and pH), any change in film conductivity can be correlated to structural damage. Termed "sensing skins," this material is ideally suited for SHM where it can be used to easily identify the location and severity of damage. First, validation studies have been conducted to verify the accuracy and precision of EIT-derived spatial conductivity maps. The results shown suggest that EIT is an effective

technique suitable for mapping the true surface conductivity of these nanocomposites. However, the resolution of the sensor is directly limited by the density of boundary electrodes. Upon successful validation, $(SWNT\text{-}PSS/PVA)_n$ thin films have been demonstrated for spatial strain and impact monitoring. In addition, spatially distributed pH variations and corrosion damage have been successfully detected using $(SWNT\text{-}PSS/PANI)_n$ sensing skins.

7.2. Contributions

Despite the tremendous effort dedicated to the development of sensing technologies over the past several decades (*e.g.*, wireless sensors, RFID sensors, MEMS, ultrasonics, among others), structural health monitoring and damage detection have had limited commercial success. As has been discussed in Chapter 1, the current structural health monitoring paradigm relies on two fundamental operating principles (*i.e.*, the use of point sensors and inferring damage from sensor response) that have been logical given the sensing technologies available at the time; however, this SHM paradigm has had limited success in reliably identifying damage in large, complex structural systems.

Alternatively, the main contribution of this dissertation is to illustrate a novel sensing paradigm for SHM that addresses the aforementioned limitations of current SHM systems. As opposed to the miniaturization of sensor designs, a new class of composite materials can be designed from materials and fabrication tools offered by nanotechnology to exhibit multifunctionality (*i.e.*, possessing more than one engineering functionalities). One of the main differences between the new paradigm proposed and the traditional techniques is that these ultra-thin film composites are designed to be coated onto an entire structure to serve as a true distributed sensing paradigm. Monitoring is no longer conducted by interrogating distributed point sensors, but rather, the entire thin film directly monitors damage at every location on the structural system. Realization of a composite material that can directly sense damage everywhere in a structure is accomplished by adopting a "bottom-up" fabrication methodology to tailor materials at the finest length scales (*i.e.*, nano- and micrometer dimensions) for controlling macro-scale material properties. In particular, judicious selection of

nanomaterials and polyelectrolytes leads to the embedment of specific electromechanical and electrochemical sensing transduction mechanisms.

First, in order to design a material that is capable of being coated onto structural surfaces, there are three requirements: it must be (1) mechanically strong, (2) conformable, and (3) low cost. Using a layer-by-layer technique, carbon nanotube composites proposed in this study have been shown to exhibit incredible mechanical properties (*i.e.*, strength and stiffness). Unlike traditional composites, these novel materials take advantage of the high surface-to-volume ratio of carbon nanotubes (as well as their impressive intrinsic properties) to control the nanomaterial-to-polymer matrix interface for achieving bulk materials characterized by impressive mechanical response. In fact, the high tensile strength and stiffness of SWNT-PE thin films are the direct result of embedding dispersed SWNTs within a high-molecular weight and cross-linked polymeric matrix. Simultaneously, these materials are also highly ductile and can conform to complex structural surfaces without interfering with structural performance. More importantly, despite requiring expensive material constituents such as carbon nanotubes and conductive polymers, these ultra-thin composites require very little material for thin film fabrication and are, hence, low in cost.

In this dissertation, the concept of "sensing skins" directly addresses two other limitations of the current/traditional SHM paradigm (*i.e.*, the use of point sensors and complex algorithms for inferring damage). As alluded to in previous discussions, these sensing skins are coated onto entire structural surfaces to directly monitor damage at every location on a structure. Since thin films can be *tuned* to exhibit changes in conductivity to specific applied external stimuli, changes in film conductivity can be directly associated with damage incurred at any point on a structure. This accomplishment permits the simultaneous direct detection of damage over large spatial areas which could not have been achieved using the traditional SHM paradigm. It should also be noted that, while guided-wave SHM techniques can also identify damage across large spatial dimensions, structural damage is still *inferred* from piezoelectric sensor/actuator measurements. Thus, as damage features become more complex, computational demand increases dramatically as more sensor/actuator measurements are required. Unlike guided-waves, the proposed sensing skins can directly detect

damage (*i.e.*, strain, impact, corrosion, or pH) at multiple locations as has been demonstrated by experimental results presented in this dissertation.

7.3. Future Work

7.3.1. Short-Term Future Research

In the near future, the proposed sensing skins will be validated for damage detection on actual structural components to illustrate their potential for field applications. However, prior to field implementation, long-term sensor stability tests need to be conducted; here, skins will be exposed to varying ambient conditions (*e.g.*, humidity, temperature, and different gases) to identify potential environmental factors that may adversely affect sensor performance. In particular, outdoor use will be explored with skins exposed to weathering, ultraviolet (UV) sun light, among other factors. So as to facilitate commercialization of this novel spatial sensing approach, the layer-by-layer skin fabrication technique will also be aerosolized to facilitate efficient application onto existing structural elements such as gusset plates, steel girders, airfoils, among many other structures. Other variations of LbL include spin-assisted deposition to fabricate large nanocomposite sheets at the expense of higher raw material consumption [137].

Nanocomposite sensing skin designs can also be extended to realize a true multilayer multifunctional system, thereby capable of simultaneously identifying different damage processes at redundant locations on a structure. It is of interest to deposit $(\text{SWNT-PSS/PVA})_n$ and $(\text{SWNT-PSS/PANI})_n$ thin films on top of one another and to detect and isolate structural damage due to strain and/or corrosion. For example, such a sensing approach could elucidate the complex correlation between corrosion and stress corrosion cracking in actual structures. Simultaneous to enabling multi-sensing capabilities is the need to design multi-layered boundary electrodes; it is likely that MEMS and micro-fabrication techniques can offer unique, cost-effective boundary electrode design methodologies and scalability. Finally, in addition to detecting the magnitude of damage (*e.g.*, strain, pH, and corrosion), the ability to differentiate directionality is also of great importance (*i.e.*, to determine the strain/stress tensor). For example, a highly directional/uniaxial strain sensor can be fabricated via precise

alignment of nanotubes within the nanocomposite system; a double-layered perpendicularly aligned SWNT-based thin film can be employed for sensing biaxial and shear strain during structural deformation.

In addition to experimental validation of these nanocomposites for SHM, a fundamental theoretical understanding of nanocomposite behavior is necessary. Here, molecular dynamics simulations [138, 139] can be employed as a useful tool for enhancing the current understanding of SWNT-to-polymer interactions. For example, the understanding of SWNT and polymer interfacial behavior can facilitate the tailoring of next-generation nanocomposites that simultaneously optimize mechanical and electrical properties. Furthermore, percolation theory can be applied for deriving constitutive relationships that dictate macro-scale SWNT-PE nanocomposite performance.

7.3.2. Long-Term Research Objectives

Ultimately, the field of structural health monitoring seeks to take advantage of sensing technologies (e.g., tethered sensors, wireless systems, RFID, and sensing skins) to better understand a structure's performance and to use the acquired data for autonomously recommending the next course of action (*i.e.*, whether a structure requires, repair, rehabilitation, or reconstruction). To date, few researchers have demonstrated such an ability to autonomously perform damage prognosis on complex structural systems. In particular, damage prognosis has been extremely difficult due to the uncertainties associated with damage detection based on data acquired from a small network of distributed sensors. However, the proposed sensing skins offer the field of SHM a more realistic way to autonomously detect damage. With the ability to understand damage at every location on a structure, it is important to consider how this information can be incorporated with reliability models for estimating structural performance and projecting remaining service lifetimes. Furthermore, it is also important to explore how different damage processes (*i.e.*, cracks, corrosion, among others) collectively affect structural performance.

On the other hand, despite the plethora of multi-sensing features presented in this dissertation, the nascent field of nanotechnology offers a diverse suite of materials

and fabrication tools suitable for extending the design of thin films to possess various engineering capabilities. For instance, actuation and power harvesting represent one area where current sensing technologies have had limited success due to fundamental material constraints of piezoelectric ceramics and polymers. Here, nanomaterials such as piezoelectric zinc oxide nanowires can be molecularly aligned to yield high-performance piezoelectric nanocomposites capable of interrogating structures via generation of surface Lamb waves (*i.e.*, active sensing) or to convert ambient mechanical vibrations to electrical energy (*i.e.*, power harvesting). Other areas where nanotechnology offers significant advantages include the design of high-damping, self-healing, corrosion protection thin films, among many others. In general, the non-intrusive nature and their ultra-thin characteristics permit the deposition of nanocomposites onto large complex structural surfaces. In addition to potential structural engineering applications, such nanostructures can also find applications in environmental engineering (*e.g.*, pollutant detection and mitigation) and bioengineering (*e.g.*, biosensing and implantable devices) to name just a few.

REFERENCES

[1] Olson, R.A., Mattingly, S., Scawthorn, C., Pantelic, J., Mileti, D., Fitzpatrick, C., Helmericks, S., Breck, C.R., Olson, R.S., Tierney, K., Andrews, R., Flores, P., Jones, N., Noji, E., Krimgold, F., O'donoghue, D., Comfort, L., Oaks, S., Michaels, S. and Tobriner, S.: Socioeconomic Impact and Emergency Response. Earthquake Spectra, **6**(S1), 393-431 (1990).

[2] Bagnariol, D.: Sgt. Aubrey Cosens V.C. Memorial Bridge over the Montreal River at Latchford - Investigation of Failure. Ontario Ministry of Transportation, Canada, 1-25 (2003).

[3] Njord, J.R. and Meyer, M.D.: Critical Issues in Transportation. Transportation Research Board of the National Academics, 1-13 (2006).

[4] Biezma, M.V. and Schanack, F.: Collapse of Steel Bridges. Journal of Performance of Constructed Facilities, **21**(5), 398-405 (2007).

[5] Samsonov, P.: Nondestructive Inspection of Aging Aircraft. Proceedings of SPIE, **2001**, 257-261 (1993).

[6] Oberg, J.: The Shuttle Puzzle [Space Shuttle Columbia Disaster]. IEEE Spectrum, **40**(3), 22-24 (2003).

[7] National Bridge Inspection Standards. Federal Highway Administration (FHWA), FHWA-2001-8954, 74419-74439 (2004).

[8] Moore, M., Phares, B., Graybeal, B., Rolander, D. and Washer, G.: Reliability of Visual Inspection for Highway Bridges. Federal Highway Administration, FHWA-RD-01-020, Washington, DC, (2001).

[9] Hartle, R.A., Amrhein, W.J., Iii, K.E.W., Baughman, D.R. and Tkacs, J.J.: Bridge Inspector's Training Manual/90. Federal Highway Administration, FHWA-PD-91-015, McLean, VA, 1-24 (1990).

[10] Doebling, S.W., Farrar, C.R. and Prime, M.B.: Summary Review of Vibration-Based Damage Identification Methods. Shock and Vibration Digest, **30**(2), 91-105 (1998).

[11] Lynch, J.P. and Loh, K.J.: A Summary Review of Wireless Sensors and Sensor Networks for Structural Health Monitoring. Shock and Vibration Digest, **38**(2), 91-128 (2006).

[12] Celebi, M.: Seismic Instrumentation of Buildings (with Emphasis on Federal Buildings). United States Geological Survey (USGS), Technical Report No. 0-7460-68170, Menlo Park, CA, (2002).

[13] Farrar, C.R.: Historical Overview of Structural Health Monitoring Using Statistical Pattern Recognition. Los Alamos Dynamics: Los Alamos, NM (2001).

[14] Macgillivray, P. and Goddard, K.: Advanced Sensor Technology for Marine Propulsion Control Systems. Proceedings of 11th Ship Control Systems Symposium, **2**, 245-257 (1997).

[15] Spencer, B.F.: Opportunitites and Challenges for Smart Sensing Technology. Proceedings of International Conference on Structural Health Monitoring and Intelligent Infrastructure, **1**, 65-71 (2003).

[16] Spencer Jr., B.F., Ruiz-Sandoval, M.E. and Kurata, N.: Smart Sensing Technology: Opportunities and Challenges. Journal of Structural Control and Health Monitoring, **11**(4), 349-368 (2004).

[17] Lynch, J.P., Wang, Y., Loh, K.J., Yi, J.H. and Yun, C.B.: Performance Monitoring of the Geumdang Bridge Using a Dense Network of High-Resolution Wireless Sensors. Smart Materials and Structures, **15**(6), 1561-1575 (2006).

[18] Kurata, N., Spencer, B.F. and Ruiz-Sandoval, M.: Risk Monitoring of Buildings with Wireless Sensor Networks. Structural Control and Health Monitoring, **12**(3-4), 315-327 (2005).

[19] Finkenzeller, K.: Rfid Handbook: Fundamentals and Applications in Contactless Smart Cards and Identification. John Wiley & Sons: West Sussex, England (2003).

[20] Mita, A. and Takahira, S.: Health Monitoring of Smart Structures Using Damage Index Sensors. Proceedings of SPIE - Smart Structures and Materials, **4696**, 92-99 (2002).

[21] Mita, A. and Takahira, S.: A Smart Sensor Using a Mechanical Memory for Structural Health Monitoring. Smart Materials and Structures, **12**(2), 204-209 (2003).

[22] Mita, A. and Takahira, S.: Damage Index Sensors for Smart Structures. Structural Engineering and Mechanics, **17**(3-4), 331-346 (2004).

[23] Jia, Y. and Sun, K.: Thick Film Wireless and Powerless Strain Sensor. Proceedings of SPIE - Smart Structures and Materials, **6174**, 61740Z/61741-61740Z/61711 (2006).

[24] Watters, D.G.: Wireless Sensors Will Monitor Bridge Decks. Better Roads, **73**(2), 74-75 (2003).

[25] Watters, D.G., Jayaweera, P., Bahr, A.J., Huestis, D.L., Priyantha, N., Meline, R., Reis, R. and Parks, D.: Smart Pebble: Wireless Sensors for Structural Health Monitoring of Bridge Decks. Proceedings of SPIE - Smart Structures and Materials, **5057**, 20-28 (2003).

[26] Simonen, J.T., Andringa, M.M., Grizzle, K.M., Wood, S.L. and Neikirk, D.P.: Wireless Sensors for Monitoring Corrosion in Reinforced Concrete Members. Proceedings of SPIE - Smart Structures and Materials, **5391**, 587-596 (2004).

[27] Dickerson, N.P., Andringa, M.M., Puryear, J.M., Wood, S.L. and Neikirk, D.P.: Wireless Threshold Sensors for Detecting Corrosion in Reinforced Concrete Structures. Proceedings of SPIE - Smart Structures and Materials, **6174**, (2006).

[28] Raghavan, A. and Cesnik, C.E.S.: Review of Guided-Wave Structural Health Monitoring. Shock and Vibration Digest, **39**(2), 91-114 (2007).

[29] Giurgiutiu, V., Zagrai, A. and Bao, J.: Damage Identification in Aging Aircraft Structures with Piezoelectric Wafer Active Sensors. Journal of Intelligent Material Systems and Structures, **15**(9-10), 673-687 (2004).

[30] Park, S., Yun, C.-B., Roh, Y. and Lee, J.-J.: Pzt-Based Active Damage Detection Techniques for Steel Bridge Components. Smart Materials and Structures, **15**(4), 957-966 (2006).

[31] Sohn, H., Park, G., Wait, J.R., Limback, N.P. and Farrar, C.R.: Wavelet-Based Active Sensing for Delamination Detection in Composite Structures. Smart Materials and Structures, **13**(1), 153-160 (2004).

[32] Kovacs, G.T.A.: Micromachined Transducers Sourcebook. McGraw-Hill: New York, NY (1998).

[33] Gardner, J.W.: Microsensors: Principles and Applications. John Wiley & Sons: West Sussex, England (1994).

[34] Gardner, J.W., Varadan, V.K. and Awadelkarim, O.O.: Microsensors, Mems and Smart Devices. John Wiley & Sons: West Sussex, England (2001).

[35] Glaser, S.D., Li, H., Wang, M., Ou, J.-P. and Lynch, J.P.: Sensor Technology Innovation for the Advancement of Structural Health Monitoring: A Strategic Program of Us-China Research for the Next Decade. Smart Structures and Systems, **3**, 221-244 (2007).

[36] Oppenheim, I.J., Jain, A. and Greve, D.W.: Mems Ultrasonic Transducers for the Testing of Solids. IEEE Transactions on Ultrasonics, Ferroelectrics, and Frequency Control, **50**(3), 305-311 (2003).

[37] Bhushan, B., ed.: Springer Handbook of Nanotechnology. Springer: Berlin, Germany (2003).

[38] Iijima, S.: Helical Microtubules of Graphitic Carbon. Nature, **354**(6348), 56-58 (1991).

[39] Klein, D.L., Roth, R., Lim, A.K.L., Alivisatos, A.P. and Mceuen, P.L.: A Single-Electron Transistor Made from a Cadmium Selenide Nanocrystal. Nature, **389**, 699-701 (1997).

[40] Donnet, J.-B., Bansal, R.C. and Wang, M.-J., ed.: Carbon Black. Marcel Dekker: New York, NY (1993).

[41] Turton, R.: The Quantum Dot: A Journey into the Future of Microelectronics. Oxford University Press: New York, NY (1996).

[42] Devreese, J.T.: Importance of Nanosensors: Feynman's Vision and the Birth of Nanotechnology. MRS Bulletin, **32**(9), 718-724 (2007).

[43] Saito, R., Dresselhaus, G. and Dresselhaus, M.S.: Physical Properties of Carbon Nanotubes. Imperial College Press: London (1998).

[44] Andrews, R., Jacques, D., Rao, A.M., Rantell, T., Derbyshire, F., Chen, Y., Chen, J. and Haddon, R.C.: Nanotube Composite Carbon Fibers. Applied Physics Letters, **75**(9), 1329-1331 (1999).

[45] Tsukagoshi, K., Yoneya, N., Uryu, S., Aoyagi, Y., Kanda, A., Ootuka, Y. and Alphenaar, B.W.: Carbon Nanotube Devices for Nanoelectronics. Physica B, **323**(1-4), 107-114 (2002).

[46] Kong, J., Franklin, N.R., Zhou, C., Chapline, M.G., Peng, S., Cho, K. and Dai, H.: Nanotube Molecular Wires as Chemical Sensors. Science, **287**(5453), 622-625 (2000).

[47] Wood, J.R., Zhao, Q., Frogley, M.D., Meurs, E.R., Prins, A.D., Peijs, T., Dunstan, D.J. and Wagner, H.D.: Carbon Nanotubes: From Molecular to Macroscopic Sensors. Physical Review B, **61**(11), 7571-7575 (2000).

[48] Baughman, R.H., Zakhidov, A.A. and De Heer, W.A.: Carbon Nanotubes - the Route toward Applications. Science, **297**(5582), 787-792 (2002).

[49] Salvetat, J.-P., Bonard, J.-M., Thomson, N.H., Kulik, A.J., Forro, L., Benoit, W. and Zuppiroli, L.: Mechanical Properties of Carbon Nanotubes. Applied Physics A (Materials Science Processing), **A69**(3), 255-260 (1999).

[50] Meyyappan, M., ed.: Carbon Nanotubes: Science and Applications. CRC Press: Boca Raton, FL (2005).

[51] Stampfer, C., Jungen, A., Linderman, R., Obergfell, D., Roth, S. and Hierold, C.: Nano-Electromechanical Displacement Sensing Based on Single-Walled Carbon Nanotubes. Nano Letters, **6**(7), 1449-1453 (2006).

[52] Nalwa, H.S.: Nanostructured Materials and Nanotechnology. Academic Press: San Diego, CA (2002).

[53] Meyer, G. and Rieder, K.-H.: Controlled Manipulation of Single Atoms and Small Molecules with the Scanning Tunneling Microscope. Surface Science, **377-379**, 1087-1093 (1997).

[54] Wiesauer, K. and Springholz, G.: Fabrication of Semiconductor Nanostructures by Nanoindentation of Photoresist Layers Using Atomic Force Microscopy. Journal of Applied Physics, **88**(12), 7289-7297 (2000).

[55] Roberts, G., ed.: Langmuir-Blodgett Films. Plenum: New York, NY (1990).

[56] Klein, L.C., ed.: Sol-Gel Technology for Thin Films, Fibers, Preforms, Electronics and Specialty Shapes. Noyes Publications: Park Ridge, NJ (1988).

[57] Gogotsi, Y., ed.: Nanomaterials Handbook. Taylor & Francis: Boca Raton, FL (2006).

[58] Decher, G. and Schlenoff, J.B., ed.: Multilayer Thin Films: Sequential Assembly of Nanocomposite Materials. Wiley-VCH: Federal Republic of Germany (2003).

[59] Xie, X.-L., Mai, Y.-W. and Zhou, X.-P.: Dispersion and Alignment of Carbon Nanotubes in Polymer Matrix: A Review. Materials Science and Engineering R: Reports, **49**(4), 89-112 (2005).

[60] Corr, S.A., Rakovich, Y.P. and Gun'ko, Y.K.: Multifunctional Magnetic-Fluorescent Nanocomposites for Biomedical Applications. Nanoscale Research Letters, **3**(3), 87-104 (2008).

[61] Veiseh, O., Sun, C., Gunn, J., Kohler, N., Gabikian, P., Lee, D., Bhattarai, N., Ellenbogen, R., Sze, R., Hallahan, A., Olson, J. and Zhang, M.: Optical and Mri Multifunctional Nanoprobe for Targeting Gliomas. Nano Letters, **5**(6), 1003-1008 (2005).

[62] Wight, J.K. and Macgregor, J.G.: Reinforced Concrete: Mechanics and Design. Prentice Hall: Upper Saddle River, NJ (2008).

[63] Dharap, P., Li, Z., Nagarajaiah, S. and Barrera, E.V.: Nanotube Film Based on Single-Wall Carbon Nanotubes for Strain Sensing. Nanotechnology, **15**(3), 379-382 (2004).

[64] Knite, M., Tupureina, V., Fuith, A., Zavickis, J. and Teteris, V.: Polyisoprene-Multi-Wall Carbon Nanotube Composites for Sensing Strain. Materials Science and Engineering C, **27**(5-8), 1125-1128 (2007).

[65] Jia, Z., Wang, Z., Xu, C., Liang, J., Wei, B., Wu, D. and Zhu, S.: Study on Poly(Methyl Methacrylate)/Carbon Nanotube Composites. Materials Science and Engineering A, **271**(1-2), 395-400 (1999).

[66] Lahiff, E., Minett, A.I., Curran, S., Ryu, C.Y., Blau, W.J. and Ajayan, P.M.: Controlling the Position and Morphology of Nanotubes within a Polymer Film. Proceedings of Materials Research Society Symposium, **782**, 153-158 (2003).

[67] Kotov, N.A.: Ordered Layered Assemblies of Nanoparticles. MRS Bulletin, **26**(12), 992-997 (2001).

[68] Decher, G.: Fuzzy Nanoassemblies: Toward Layered Polymeric Multicomposites. Science, **277**(29), 1232-1237 (1997).

[69] Paloniemi, H., Lukkarinen, M., Aaritalo, T., Areva, S., Leiro, J., Heinonen, M., Haapakka, K. and Luddari, J.: Layer-by-Layer Electrostatic Self-Assembly of Single-Wall Carbon Nanotube Polyelectrolytes. Langmuir, **22**(1), 74-83 (2006).

[70] Mamedov, A.A., Kotov, N.A., Prato, M., Guldi, D.M., Wicksted, J.P. and Hirsch, A.: Molecular Design of Strong Single-Wall Carbon Nanotube/Polyelectrolyte Multilayer Composites. Nature Materials, **1**(3), 190-194 (2002).

[71] Olek, M., Ostrander, J., Jurga, S., Mohwald, H., Kotov, N., Kempa, K. and Giersig, M.: Layer-by-Layer Assembled Composites from Multiwall Carbon Nanotubes with Different Morphologies. Nano Letters, **4**(10), 1889-1895 (2004).

[72] Rouse, J.H. and Lillehei, P.T.: Electrostatic Assembly of Polymer/Single Walled Carbon Nanotube Multilayer Films. Nano Letters, **3**(1), 59-62 (2003).

[73] Losche, M., Schmitt, J., Decher, G., Bouwman, W.G. and Kjaer, K.: Detailed Structure of Molecularly Thin Polyelectrolyte Multilayer Films on Solid Substrates as Revealed by Neutron Reflectrometry. Macromolecules, **31**(25), 8893-8906 (1998).

[74] Rodriguez, L.N.J., De Paul, S.M., Barrett, C.J., Raven, L. and Spiess, H.W.: Fast Magic-Angle Spinning and Double-Quantum H Solid State Nmr Spectroscopy of Polyelectrolyte Multilayers. Advanced Materials, **12**(24), 1934-1938 (2000).

[75] Yoo, D., Shiratori, S.S. and Rubner, M.F.: Controlling Bilayer Composition and Surface Wettability of Sequentially Adsorbed Multilayers of Weak Polyelectrolytes. Macromolecules, **31**(13), 4309-4318 (1998).

[76] Tan, Y. and Resasco, D.E.: Dispersion of Single-Walled Carbon Nanotubes of Narrow Diameter Distribution. Journal of Physical Chemistry B, **109**(30), 14454-14460 (2005).

[77] Loh, K.J., Kim, J., Lynch, J.P., Kam, N.W.S. and Kotov, N.A.: Multifunctional Layer-by-Layer Carbon Nanotube-Polyelectrolyte Thin Films for Strain and Corrosion Sensing. Smart Materials and Structures, **16**(2), 429-438 (2007).

[78] Moore, V.C., Strano, M.S., Haroz, E.H., Hauge, R.H. and Smalley, R.E.: Individually Suspended Single-Walled Carbon Nanotubes in Various Surfactants. Nano Letters, **3**(10), 1379-1382 (2003).

[79] Callister, W.D.: Fundamentals of Materials Science and Engineering: An Integrated Approach. John Wiley & Sons: Hoboken, NJ (2005).

[80] Smits, F.M.: Measurement of Sheet Resistivities with the Four-Point Probe. Bell System Technical Journal, **37**(3), 711-718 (1958).

[81] Vossen, J.L.: Non-Destructive Sheet-Resistivity Measurements with Two Point Probes. RCA Review, **33**(3), 537-542 (1972).

[82] Valentini, L., Armentano, I., Puglia, D., Lozzi, L., Santucci, S. and Kenny, J.M.: A Deeper Understanding of the Photodesorption Mechanism of Aligned Carbon Nanotube Thin Films by Impedance Spectroscopy. Thin Solid Films, **449**(1-2), 105-112 (2004).

[83] Hone, J., Liaguno, M.C., Nemes, N.M., Johnson, A.T., Fischer, J.E., Walters, D.A., Casavant, J.M., Schmidt, J. and Smalley, R.E.: Electrical and Thermal Transport Properties of Magnetically Aligned Single Wall Carbon Nanotube Films. Applied Physics Letters, **77**(5), 666-668 (2000).

[84] Zhang, Y. and Iijima, S.: Elastic Response of Carbon Nanotube Bundles to Visible Light. Physical Review Letters, **82**(17), 3472-3475 (1999).

[85] Lu, S. and Panchapakesan, B.: Photoconductivity in Single Wall Carbon Nanotube Sheets. Nanotechnology, **17**(8), 1843-1850 (2006).

[86] Chen, R.J., Franklin, N.R., Jing, K., Jien, C. and Tombler, T.W.: Molecular Photodesorption from Single-Walled Carbon Nanotubes. Applied Physics Letters, **79**(14), 2258-2260 (2001).

[87] Stein, P.K.: 1936 a Banner Year for Strain Gages and Experimental Stress Analysis - an Historical Perspective. Experimental Techniques, **30**, 23-41 (2006).

[88] French, P.J. and Evans, A.G.R.: Polycrystalline Silicon Strain Sensors. Sensors and Actuators, **8**(3), 219-225 (1985).

[89] Allsop, T., Sugden, K., Bennion, I., Neal, R. and Malvern, A.: A High Resolution Fiber Bragg Grating Resonator Strain Sensing System. Fiber and Integrated Optics, **21**(3), 205-217 (2002).

[90] Davis, M.A., Bellemore, D.G. and Kersey, A.D.: Distributed Fiber Bragg Grating Strain Sensing in Reinforced Concrete Structural Components. Cement & Concrete Composites, **19**(1), 45-57 (1997).

[91] Peng, S., O'keeffe, J., Wei, C., Cho, K., Kong, J., Chen, R., Franklin, N. and Dai, H.: Carbon Nanotube Chemical and Mechanical Sensors. Proceedings of 3rd International Workshop on Structural Health Monitoring, 1-8 (2001).

[92] Minot, E.D., Yaish, Y., Szaonova, V., Park, J.-Y., Brink, M. and Mceuen, P.L.: Tuning Carbon Nanotube Band Gaps with Strain. Physical Review Letters, **90**(15), 156401/156401-156404 (2003).

[93] Tombler, T.W., Zhou, C., Alexseyev, L., Kong, J., Dai, H., Liu, L., Jayanthi, C.S., Tang, M. and Wu, S.-Y.: Reversible Electromechanical Characteristics of Carbon Nanotubes under Local-Probe Manipulation. Nature, **405**(6788), 769-772 (2000).

[94] Maiti, A., Svizhenko, A. and Anantram, M.P.: Electronic Transport through Carbon Nanotubes: Effects of Structural Deformation and Tube Chirality. Physical Review Letters, **88**(12), 126805/126801-126804 (2002).

[95] Li, Z., Dharap, P., Nagarajaiah, S., Barrera, E.V. and Kim, J.D.: Carbon Nanotube Film Sensors. Advanced Materials, **16**(7), 640-643 (2004).

[96] Kang, I., Schulz, M.J., Kim, J.H., Shanov, V. and Shi, D.: A Carbon Nanotube Strain Sensor for Structural Health Monitoring. Smart Materials and Structures, **15**(3), 734-7486 (2006).

[97] Kang, I., Lee, J.W., Choi, G.R., Jung, J.Y., Hwang, S.-H., Choi, Y.-S., Yoon, K.J. and Schulz, M.J.: Structural Health Monitoring Based on Electrical Impedance of a Carbon Nanotube Neuron. Key Engineering Materials, **321-323**, 140-145 (2006).

[98] Qian, D. and Dickey, E.C.: In Situ Transmission Electron Microscopy Studies of Polymer-Carbon Nanotube Composite Deformation. Journal of Microscopy, **204**(1), 39-45 (2001).

[99] Ambat, R. and Dwarakadasa, E.S.: The Influence of Ph on the Corrosion of Medium Strength Aerospace Alloys 8090, 2091 and 2014. Corrosion Science, **33**(5), 681-690 (1992).

[100] Carino, N.J.: Nondestructive Techniques to Investigate Corrosion Status in Concrete Structures. Journal of Performance of Constructed Facilities, **13**(3), 96-106 (1999).

[101] Adhikari, B. and Majumdar, S.: Polymers in Sensor Applications. Progress in Polymer Science, **29**(7), 699-766 (2004).

[102] Macdiarmid, A.G., Chiang, J.-C., Huang, W., Humphrey, B.D. and Somasiri, N.L.D.: Polyaniline: Protonic Acid Doping to the Metallic Regime. Molecular Crystals and Liquid Crystals, **125**(1-4), 309-318 (1985).

[103] Coleman, J.N., Khan, U. and Gun'ko, Y.K.: Mechanical Reinforcement of Polymers Using Carbon Nanotubes. Advanced Materials, **18**(6), 689-706 (2006).

[104] Ward, I.M. and Sweeney, J.: An Introduction to the Mechanical Properties of Solid Polymers. John Wiley & Sons: New York, NY (2004).

[105] Anderson, T.L.: Fracture Mechanics: Fundamentals and Applications. CRC Press: Boca Raton, FL (1995).

[106] Klemann, B.M. and Devilbiss, T.: The Fracture Toughness of Thin Polymeric Films. Polymer Engineering and Science, **36**(1), 126-134 (1996).

[107] Irwin, G.R.: Onset of Fast Crack Propagation in High Strength Steel and Aluminum Alloys. Proceedings of Sagamore Research Conference, **2**, 289-305 (1956).

[108] Malik, S., Rosner, H., Hennrich, F., Bottcher, A., Kappes, M.M., Beck, T. and Auhorn, M.: Failure Mechanism of Free Standing Single-Walled Carbon Nanotube Thin Films under Tensile Load. Physical Chemistry Chemical Physics, **6**(13), 3540-3544 (2004).

[109] Ren, Y., Fu, Y.Q., Liao, K., Li, F. and Cheng, H.M.: Fatigue Failure Mechanisms of Single-Walled Carbon Nanotube Ropes Embedded in Epoxy. Applied Physics Letters, **84**(15), 2811-2813 (2004).

[110] Sinha, N., Ma, J. and Yeow, J.T.W.: Carbon Nanotube-Based Sensors. Journal of Nanoscience and Nanotechnology, **6**(3), 573-590 (2006).

[111] Loh, K.J., Lynch, J.P., Shim, B.S. and Kotov, N.A.: Tailoring Piezoresistive Sensitivity of Multilayer Carbon Nanotube Composite Strain Sensors. Journal of Intelligent Material Systems and Structures, (*published online*) (2007).

[112] Loh, K.J., Lynch, J.P. and Kotov, N.A.: Mechanical-Electrical Characterization of Carbon Nanotube Thin Films for Structural Monitoring Applications. Proceedings of SPIE Smart Materials and Structures, **61741Z**, 1-12 (2006).

[113] Stadermann, M., Papadakis, S.J., Falvo, M.R., Novak, J., Snow, E., Fu, Q., Liu, J., Fridman, Y., Boland, J.J., Superfine, R. and Washburn, S.: Nanoscale Study of Conduction through Carbon Nanotube Networks. Physical Review B, **69**(20), 201402/201401-201403 (2004).

[114] Li, X.-H., Wu, B., Huang, J.-E., Zhang, J., Liu, Z.-F. and Li, H.-L.: Fabrication and Characterization of Well-Dispersed Single-Walled Carbon Nanotube/Polyaniline Composites. Carbon, **41**(8), 1670-1673 (2003).

[115] Barsoukov, E. and Macdonald, J.R., ed.: Impedance Spectroscopy Theory, Experiment, and Applications. John Wiley & Sons: Hoboken, NJ (2005).

[116] Duda, R.O., Hart, P.E. and Stork, D.G.: Pattern Classification. Wiley: New York, NY (2001).

[117] Horowitz, P. and Hill, W.: The Art of Electronics. Cambridge University Press: New York, NY (1989).

[118] Paret, D.: Rfid and Contactless Smart Card Applications. John Wiley & Sons: West Sussex, England (2005).

[119] Lee, Y.: Rfid Coil Design. Microchip, AN678, 1-18 (1998).

[120] Dobkin, D.M.: The Rf in Rfid: Passive Uhf Rfid in Practice. Newnes: Oxford, UK (2008).

[121] Loh, K.J., Lynch, J.P. and Kotov, N.A.: Inductively Coupled Nanocomposite Wireless Strain and Ph Sensors. Smart Structures and Systems, **4**(5), 531-548 (2008).

[122] Liu, Y., Wang, Y. and Claus, R.O.: Layer-by-Layer Ionic Self-Assembly of Au Colloids into Multilayer Thin-Films with Bulk Metal Conductivity. Chemical Physics Letters, **298**(4-6), 315-319 (1998).

[123] Zhang, M., Su, L. and Mao, L.: Surfactant Functionalization of Carbon Nanotube (Cnts) for Layer-by-Layer Assembling of Cnt Multi-Layer Films and Fabrication of Gold Nanoparticle/Cnt Nanohybrid. Carbon, **44**(2), 276-283 (2006).

[124] Jiang, C., Markutsya, S. and Tsukruk, V.V.: Collective and Individual Plasmon Resonances in Nanoparticle Films Obtained by Spin-Assisted Layer-by-Layer Assembly. Langmuir, **20**(3), 882-890 (2004).

[125] Giurgiutiu, V. and Cuc, A.: Embedded Non-Destructive Evaluation for Structural Health Monitoring, Damage Detection, and Failure Prevention. Shock and Vibration Digest, **37**(2), 83-105 (2005).

[126] Brown, B.H.: Electrical Impedance Tomography (Eit): A Review. Journal of Medical Engineering & Technology, **27**(3), 97-108 (2003).

[127] Holder, D.S., ed.: Electrical Impedance Tomography Methods, History and Applications. The Institute of Physics: London (2005).

[128] Hou, T.-C., Loh, K.J. and Lynch, J.P.: Spatial Conductivity Mapping of Carbon Nanotube Composite Thin Films by Electrical Impedance Tomography for Sensing Applications. Nanotechnology, **38**(31), 315501/315501-351501/315509 (2007).

[129] Vauhkonen, M.: Electrical Impedance Tomography and Prior Information. Ph.D. Thesis, Kuopio University, Natural and Environmental Sciences, Kuopio, Finland (1997).

[130] Wolfson, R. and Pasachoff, J.M.: Physics with Modern Physics for Scientists and Engineers, 2nd Edn. HarperCollins College: New York, NY (1995).

[131] Borcea, L.: Electrical Impedance Tomography. Inverse Problems, **18**(6), (2002).

[132] Cook, R.D., Malkus, D.S., Plesha, M.E. and Witt, R.J.: Concept and Applications of Finite Element Analysis, 4th Edn. John Wiley & Sons: New York, NY (2002).

[133] Somersalo, E., Cheney, M. and Isaacson, D.: Existence and Uniqueness for Electrode Models for Electric Current Computed Tomography. SIAM Journal on Applied Mathematics, **52**(4), 1023-1040 (1992).

[134] Ahmad, S.: Reinforcement Corrosion in Concrete Structures, Its Monitoring and Service Life Prediction - a Review. Cement & Concrete Composites, **25**(4-5), 459-471 (2003).

[135] Yonemoto, N. and Shida, K.: Multi-Functional Sensing for High-Sensitivity Detection of Initial State of Iron Rust. Proceedings of IEEE Instrumentation and Measurement Technology Conference, **2**, 1145-1148 (1998).

[136] Mai, Y.-W., Xie, X.-L. and Zhou, X.-P.: Dispersion and Alignment of Carbon Nanotubes in Polymer Matrix: A Review. Materials Science and Engineering R: Reports, **49**(4), 89-112 (2005).

[137] Feng, Z. and Yan, F.: Preparation and Tribological Studies of Nanocomposite Films Fabricated Using Spin-Assisted Layer-by-Layer Assembly. Surface and Coatings Technology, **202**(14), 3290-3297 (2008).

[138] Elliott, J. and Han, Y.: Molecular Dynamics Simulations of the Elastic Properties of Polymer/Carbon Nanotube Composites. Computational Materials Science, **39**(2), 315-323 (2007).

[139] Okabe, T. and Chowdhury, S.C.: Computer Simulation of Carbon Nanotube Pull-out from Polymer by the Molecular Dynamics Method. Composites Part A, **38**(3), 747-754 (2007).